

ABSTRACT

Title of Dissertation: **THE LIVES AND TIMES OF
STARS AND BLACK HOLES IN THE
DISKS OF ACTIVE GALACTIC NUCLEI**

Alexander Joseph Dittmann
Doctor of Philosophy, 2024

Dissertation Directed by: **Professor M. Coleman Miller
Department of Astronomy**

Enormous disks of gas are thought to feed the supermassive black holes at the centers of active galaxies; these disks may capture stars from nuclear clusters, or form stars in situ after collapsing under their own gravity. Such stellar populations may enrich these accretion disks with fusion byproducts, cause giant flares in these active galaxies, and leave behind compact remnants detected on earth through gravitational waves emitted as they merge with one another. This dissertation charts a theoretical expedition into these phenomena, from studying the implications of star-forming accretion disks for the growth of black holes in the early universe, to simulating the flow of gas around black hole binaries to ascertain their orbital evolution.

After a brief observational and theoretical overview of stars and active galactic nuclei, this dissertation delves into the development of simplified models of accretion disk structure, including the effects of stars and black holes embedded within accretion disks. The ultimate goal of this chapter was to determine if gravitational instability in the outer regions of these

accretion disks might lead to the formation of large numbers of black holes, which might go on to merge with the central supermassive black hole; this process might decrease the effective radiative efficiency of accretion onto supermassive black holes, facilitating the rapid growth of black holes in the early universe, which defies conventional explanation. Along the way, this work developed a new flavor of model to describe these disks, accounting for the pressure support provided by feedback from disk-embedded stellar-mass black holes, developed a number of semi-analytical estimates for how stars might evolve within these accretion disks, and estimated the typical timescales for objects to move through the disk. Together, these estimates showed that accelerated supermassive growth in the early universe was indeed feasible, although this estimate hinged on a number of yet-untested assumptions.

Subsequently, this dissertation advances to the question of how stars evolve when embedded within hot, dense disks of gas accreting onto supermassive black holes. Moving beyond the semi-analytical models of the preceding section, the third chapter reviews simulations of stellar evolution subject to the extreme conditions within these accretion disks. Stellar evolution calculations, due to the enormous spatial and time-scales involved, are virtually always restricted to one spatial dimension. This chapter investigates a number of the ways to account for the deviations in spherical symmetry inherent to accretion disks in these calculations, before reviewing how stellar rotation and the chemical composition of these accretion disks can affect the evolution of stars embedded therein. This work developed analytical criteria governing different regimes in stellar evolution, such as the balance between the stellar accretion and nuclear burning timescales, the relationship between gas composition and gas opacity, and the limiting effect of the central supermassive black hole's gravity on stellar accretion as the two compete for gravitational influence on the gas within the disk. Ultimately, the precise, quantitative details of these simulations

depend on the specific 3D-inspired prescriptions implemented, but the overall trends identified are robust.

The final study presented in this dissertation investigates the feasibility of these accretion disks as the host sites for the stellar-mass black hole mergers detected by the Laser Interferometer Gravitational-Wave Observatory. One of the primary uncertainties of this scenario is whether binaries formed within the disk will tend to spiral inward after formation, or instead be driven via hydrodynamic interactions to spiral outward to the point where chaotic three-body interactions would separate the binary. To address the feasibility of this gravitational wave progenation channel, we conducted three-dimensional hydrodynamical simulations of black hole binaries embedded within these accretion disks, at orbital separations slightly smaller than the limit for dynamical instability. This chapter focused on initially circular binaries over a range of orbital inclinations with respect to the midplane of the disk, finding that binaries with orbits at all misaligned with the disk midplane are gradually realigned, and that retrograde binaries can inspiral appreciably faster than prograde ones. Although the simulations were physically incomplete, in particular neglecting magnetohydrodynamic and radiative effects, they suggest that AGN disks could indeed host the binary black hole mergers detected via gravitational waves.

The Lives and Times of Stars and Black Holes
in the Disks of Active Galactic Nuclei

by

Alexander Joseph Dittmann

Dissertation submitted to the Faculty of the Graduate School of the
University of Maryland, College Park in partial fulfillment
of the requirements for the degree of
Doctor of Philosophy
2024

Advisory Committee:

Professor M. Coleman Miller, Chair/Advisor
Dr. Matteo Cantiello
Professor Peter S. Shawhan
Professor Richard F. Mushotzky
Professor Christopher S. Reynolds

© Copyright by
Alexander Joseph Dittmann
2024

Preface

Chapter 2 is based on work published in the Monthly Notices of the Royal Astronomical Society as [Dittmann & Miller \(2020\)](#). Chapter 3 summarizes results presented in [Dittmann et al. \(2021\)](#), [Jermyn et al. \(2021\)](#), and [Dittmann et al. \(2023a\)](#), which were published in the Astrophysical Journal. Chapter 4 has been adapted from an article, [Dittmann et al. \(2024a\)](#), published in the Astrophysical Journal.

Over the course of my time in graduate school, I have had the privilege to work on numerous other fascinating projects. A substantial portion of my time has been spent working as part of NASA's NICER mission to measure the radii and masses of neutron stars to constrain the equation of state of dense matter ([Bogdanov et al., 2019, 2021](#); [Dittmann et al., 2024b](#); [Miller et al., 2019, 2021](#); [Salmi et al., 2022](#); [Wolff et al., 2021](#)). In addition to my study of binary black holes embedded in AGN disks, I have also studied the evolution of binary stars and black holes accreting from standard accretion disks ([Dittmann & Ryan, 2021, 2022, 2023](#); [Dittmann et al., 2023b](#); [Duffell et al., 2024](#)), which I plan to give particular focus during my time as a postdoctoral scholar. I am also incredibly thankful for the support I have received and the freedom granted to me to pursue a wide variety of other research interests, from developing new methods to solve differential equations ([Dittmann, 2020, 2021a](#)), to developing analytical models for the early stages of tidal disruption events ([Dittmann, 2021b](#)). Although most of these will only receive at most a passing reference throughout the remainder of this thesis, each project has contributed invaluable to my growth as a scientist throughout graduate school.

Descend from Heaven, Urania, by that name
If rightly thou art called, whose voice divine
Following, above the Olympian hill I soar,
Above the flight of Pegasean wing!
The meaning, not the name, I call: for thou
Nor of the Muses nine, nor on the top
Of old Olympus dwellest; but, heavenly-born,
Before the hills appeared, or fountain flowed,
Thou with eternal Wisdom didst converse,
Wisdom thy sister, and with her didst play
In presence of the Almighty Father, pleased
With thy celestial song. Up led by thee
Into the Heaven of Heavens I have presumed,
An earthly guest, and drawn empyreal air,
Thy tempering: with like safety guided down
Return me to my native element:
Lest from this flying steed unreined, (as once
Bellerophon, though from a lower clime,)
Dismounted, on the Aleian field I fall,
Erroneous there to wander, and forlorn.

-Paradise Lost, Book VII, Lines 1-20

Acknowledgments

Professionally, I am indebted to none more than Cole. Beyond instilling within me an appreciation for rigor and healthy skepticism (“the computer is wrong until it is proven right”), Cole’s humor and wit have brought some enjoyment to even the most trying moments in research. I am especially grateful for the time he devoted, particularly early in my graduate career, to indulging my curiosity. His honing of my writing and tempering of my temperament have been invaluable.

I am also incredibly grateful for my numerous mentors throughout graduate school. Geoff, beyond being a wonderful collaborator, has also been a fantastic teacher, helping to introduce me to the world of hydrodynamics. Adam and Matteo’s insights into stellar evolution have been invaluable, and I am particularly thankful for all of the effort they put towards making the most of my time at CCA, despite the contemporaneous worldwide crises. I have also been privileged to learn from Adam and Hui’s expertise in accretion disks, plasma physics, and code development while at Los Alamos.

Almost none of my scientific accomplishments would have been possible without the exceptional teachers I had during my time as a student, who left me thoroughly prepared for research. This is especially true of my fantastic graduate course instructors, particularly Peter, Tom, Bill, Charles, Doug, Paul, and Stuart. I am also thankful for my interactions with many other professors outside of the classroom, especially Alberto, Brad, Chris, Peter, Richard, Sasha,

and Sylvain.

Graduate school would have been a rather empty experience without the numerous students I encountered along the way, especially Chongchong, Drew, Erica, Isiah, Liz, Siddhant, Zeeve, and my former officemates: Ben, Julian, Sergio, Yvette, Weizhe, and Sasha.

Numerous friendships have enlivened my time in graduate school, including Matt, Sam, Jeff, and Think, among many others. I am incredibly lucky to have such a close and enduring group of friends; I cannot thank Jack, Jonathan, Logan, Mark, and Sam — the real MVPs — enough for being wellsprings of merriment and esoteric levity in my life.

And finally, I must thank my family for their perpetual support. From what began with childhood trips to the library to hunt for answers to my questions about black holes and lead into their continued support, their encouragement of my interest in science has been integral to my path in life. Furthermore, their cultivation of creativity and the emphasis on the arts has, if not left me a more well-rounded person, at least provided me with some decent beveling.

Table of Contents

Preface	ii
Table of Contents	vi
List of Tables	viii
List of Figures	ix
List of Abbreviations	xi
Chapter 1: Introduction	1
1.1 AGN Disks	3
1.1.1 Theoretical Considerations	5
1.1.2 Observational Considerations	9
1.1.3 AGN Disks as Gravitational Wave Nesting Grounds	12
1.2 This Dissertation	16
Chapter 2: Accretion Disk Models for Active Galactic Nuclei	17
2.1 Introduction	17
2.2 Disk Models	18
2.2.1 Example Accretion Disks Models	25
2.3 Star-Forming Accretion Disks	34
2.4 Star Formation in Accretion Disks and SMBH Growth	38
2.4.1 The Premise	38
2.4.2 Methods	39
2.4.3 Results	47
Chapter 3: Stellar Evolution in AGN Disks	50
3.1 Introduction	51
3.1.1 Timescales	51
3.1.2 Simplified Stellar Models	54
3.2 Methods	57
3.2.1 Accretion	58
3.2.2 Mass Loss	67
3.2.3 Mixing	69
3.2.4 The Accretion Stream	70
3.2.5 Angular Momentum	73

3.3	Results	75
3.3.1	Timescales	75
3.3.2	Prototypical Models	78
3.3.3	Accretion	83
3.3.4	Rotation	93
3.3.5	Composition	95
3.4	Astrophysical Implications	99
Chapter 4: Black Hole Binaries in AGN Disks		103
4.1	Introduction	103
4.2	Binaries in AGN Disks	106
4.2.1	Objects Embedded in AGN Disks	106
4.2.2	Binary Orbits in AGN disks	111
4.3	Numerical Methods	116
4.3.1	N-body Evolution	121
4.4	Results	123
4.4.1	Large-Scale Structures	123
4.4.2	Minidisks	128
4.4.3	Orbital Evolution	136
4.5	Discussion	140
4.5.1	Accretion	140
4.5.2	Orbital Evolution	143
4.5.3	The Observed $q - \chi_{\text{eff}}$ Correlation	144
4.6	Conclusions	145
Chapter 5: Conclusions		147
5.1	Summary	147
5.2	Future Work	149
5.2.1	Disk Models	149
5.2.2	Stellar Evolution in AGN Disks	150
5.2.3	Disk-Embedded Black Hole Binaries	151
Appendix A: Software Used in This Dissertation		152
Appendix B: Appendices for Chapter 4		153
B.1	Orbital Evolution Diagnostics	153
B.1.1	Evolution Equations	153
B.1.2	Simulation Diagnostics	154
B.1.3	Averaging Over Time	155
B.2	Softening Dependence	156
B.3	Quantitative Records of Orbital Evolution	160
Bibliography		161

List of Tables

2.1	AGN Growth From Star-Forming Disks	48
B.1	Tabulated Binary Orbital Evolution Results	160

List of Figures

1.1	AGN Disks Evidenced by the Iron $K\alpha$ Line	6
1.2	The Dusty Torus in NGC 1068	7
1.3	CRTS AGN Flares	9
1.4	AGN Metallicities	10
1.5	Who Ordered That?	14
1.6	Black Hole Binary Populations, Mass-Ratios, and Spins	15
2.1	Tabulated Opacities	26
2.2	“Standard” Disk Models Using Kramers’ Opacities	30
2.3	“Standard” Disk Models Using Tabulated Opacities	33
2.4	Star-Forming AGN Disk Models	36
2.5	Accretion Rates Through Star-Forming Disks	40
2.6	Characteristic Masses in Star-Forming Disks	44
3.1	Regimes of Accretion onto Stars in AGN Disks	65
3.2	Timescales in the Evolution of AGN Stars	76
3.3	A Fiducial Intermediate Star	79
3.4	A Fiducial Immortal Star	80
3.5	Example Chemical Yields	82
3.6	Stellar Evolution in AGN Disks Under a Wide Range of Assumptions	84
3.7	The Maximum Masses of Tidally Limited AGN Stars	88
3.8	The Final Masses of Tidally Limited AGN Stars	89
3.9	The Chemical Yields of Tidally Limited AGN Stars	90
3.10	The Maximum and Final Masses of Rotating AGN Stars	94
3.11	A Schematic Representing Evolutionary Outcomes for Rotating AGN Stars	95
3.12	Maximum and Final Masses for Stars in AGN Disks of a Variety of Compositions	97
3.13	The Critical Density for Intermediate Stellar Evolution	98
4.1	Example Disk Models	109
4.2	An Orbital Schematic	113
4.3	Binary Evolution in AGN Disks — A Schematic	117
4.4	Example 3-Body Evolution	120
4.5	Accretion Rates for Binaries Over a Range of Inclinations	124
4.6	Large-Scale Density Slices	125

4.7	The Accretion disks of an $i_b = 30^\circ$ Binary	129
4.8	Time-Averaged Streamlines in the Binary Frame	130
4.9	Time-Averaged Velocity Profiles in the Binary Frame	130
4.10	One-Dimensional Minidisk Profiles	133
4.11	Density Projections in the Vicinity of the Binary	135
4.12	The Rates of Change of Physical Binary Quantities	137
4.13	The Rates of Change of Binary Orbital Quantities	139
B.1	Density Projections in the Vicinity of the Binary: Larger Softening	157
B.2	The Rates of Change of Binary Orbital Quantities: Larger Softening	158

List of Abbreviations

ADIOS	Adiabatic Inflow-Outflow Solution
AGN	Active Galactic Nucleus
ALMA	Atacama Large Millimeter/submillimeter Array
ASCA	Advanced Satellite for Cosmology and Astrophysics
BH	Black Hole
BHB	Black Hole Binary
CNO	Carbon-Nitrogen-Oxygen
CSD	Circum-Single Disk
CRTS	Catalina Real-Time Transient Survey
GRB	Gamma-Ray Burst
EMRI	Extreme Mass Ratio Inspiral
EOS	Equation of State
HLLE	Harten-Lax-van Leer-Einfeldt
IAS15	Implicit Adaptive Stepsize (15th order)
JINA	Joint Institute for Nuclear Astrophysics
LIGO	Laser Interferometer Gravitational Wave Observatory
MESA	Modules for Experiments in Stellar Astrophysics
MCG	The Morphological Catalogue of Galaxies
NACRE	Nuclear Astrophysics Compilation of REactions
NASA	National Aeronautics and Space Administration
NICER	Neutron Star Interior Composition Explorer
PC	Potekhin and Chabrier
QPE	Quasi-Periodic Eruption
REACLIB	Reaction Library
RK2	Runge-Kutta (2nd order)
RK3	Runge-Kutta (3rd order)
SMBH	Supermassive Black Hole
TDE	Tidal Disruption Event
VL2	van-Leer (2nd order)
ZAMS	Zero Age Main Sequence
ZLK	von Zeipel-Lidov-Kozai

Chapter 1: Introduction

Active Galactic Nuclei (AGNs) are some of the most energetic entities in the Universe: they were originally described as quasi-stellar objects (QSOs, or quasars),¹ appearing in visible light similar to faint stars within the Milky Way, point-like specks of light but with spectral lines so extremely redshifted ($z \approx 0.46$ for 3C 295, for example; [Minkowski, 1960](#)) that they were thought to be rather peculiar stars.² Summarizing the December 1960 meeting of the American Astronomical Society, the magazine *Sky & Telescope* ([Matthews et al., 1961](#)) noted that there was a “remote possibility that it may be a distant galaxy of stars”, but that there was general agreement that it was “a relatively nearby star with most peculiar properties.” 3C 273, another “star-like object with large red-shift” (from the title of [Schmidt, 1963](#)), was soon identified ([Hazard et al., 1963](#)). Although it seemed reasonable at the time that these sources could be extremely compact stars, with commensurably extreme gravitational redshifts, the gas densities implied were incompatible with observed spectral features (e.g. [Greenstein & Matthews, 1963](#);

¹“Originally” is a bit inaccurate, since many quasars became known at earlier times, albeit somewhat indirectly, by their prominent jets, and many nearby active galactic nuclei were identified by peculiar features in their optical spectra. Concerning their prominent radio-emitting jets, the study of active galactic nuclei began unknowingly with the pioneering radio surveys of Grote Reber (e.g., [Reber, 1940](#)), particularly [Reber \(1944\)](#), which identified the prominent radio emission originating from the Cygnus constellation. In the optical range of wavelengths, astronomers identified a number of galaxies (this is somewhat anachronistic, as for much of this time other galaxies were often thought to be “spiral nebulae” within the Milky Way) which seemed to have strong emission and absorption lines, similar to those of galactic nebulae, superimposed upon more typical galactic spectra (e.g., [Fath, 1909](#); [Hubble, 1926](#); [Seyfert, 1943](#); [Slipher, 1917](#)).

²It is worth recalling the historic and foundational connections between stars, chemistry, and atomic physics, such as the discovery (and naming) of helium based on novel spectral lines observed during a solar prominence [Lockyer \(1868\)](#).

Oke, 1963; Schmidt, 1963).

Eventually consensus was reached that these objects, and the many others like them discovered subsequently, resided far beyond our own galaxy and that their redshifts were cosmological in origin. At such great distances, these sources were necessarily very luminous, producing more light than most galaxies. Furthermore, constraints from optical variability suggested that the light emitted by 3C 273, for example, was emitted from within a region roughly 1.2 pc in size (far smaller than the typical $\sim 10^3 - 10^5$ pc characteristic of most galaxies (Greenstein & Schmidt, 1964)). Early models suggested that these objects might be powered by chain reactions of supernovae (Burbidge, 1961), entire clusters of stars evolving together and undergoing supernovae in quick succession (Cameron, 1962), that dense star clusters might shrink through gravitational “evaporation,” leading to frequent stellar collisions (Spitzer & Saslaw, 1966), or that supermassive ($\sim 10^8 M_{\odot}$) stars might act as sources of the gravitational and thermonuclear energy required to power these objects (Hoyle & Fowler, 1963a,b). Shortly thereafter, Salpeter (1964) and Zel’dovich (1964) proposed that quasars could be powered by accretion onto supermassive black holes.^{3,4}

The notion that active galactic nuclei were powered by accretion onto supermassive black hole eventually caught on, seeming to be the least contrived explanation for the growing collection of observations, and popularized by works such as Lynden-Bell (1969).⁵ It is now thought

³Furthermore, Salpeter (1964) suggested quite presciently that some kind of turbulent angular momentum transport could allow matter to move closer and closer to the black hole.

⁴Insofar as a dissertation is a record of the time one has spent during graduate school, I would be remiss to go without mentioning the brilliantly creative theory of stellar metamorphosis (Wolynski, 2012; Wolynski & Taylor, 2019a,b), the core tenant of which is that planets are simply very old stars that have undergone extreme mass loss, which also holds that stars are powered by gravitational contraction (as they are not hot enough to undergo nuclear fusion), that active galactic nuclei are the only entities capable of creating the conditions necessary for fusion, and of course that black holes do not exist (the scientific community is driven to acquiescence through fear, as shown in Wolynski (2019)). Needless to say, this theory has caused me much mirth.

⁵This, of course, led to much elation amongst those studying the theory of general relativity. Although Schwarzschild and others found the first solution to the Einstein field equations in the mid-1910s (e.g., Droste, 1917;

that most galaxies harbor massive black holes in their centers (e.g., [Greene et al., 2020](#); [Kormendy & Ho, 2013](#)), and that these supermassive black holes have on average actively accreted for about $10^7 - 10^9$ years over the course of cosmic time (e.g., [Marconi et al., 2004](#); [Sołtan, 1982](#); [Yu & Tremaine, 2002](#)). Despite more than five decades of effort, the precise nature and mechanics of the gas fueling AGNs remains enigmatic, largely because the extreme distance and small size of these regions precludes direct observation. The remainder of this dissertation will focus on just one small puzzle presented by these objects: how they affect nearby stars and stellar-mass black holes.

1.1 AGN Disks

Astronomers of the current age have come to agreement that active galactic nuclei are fueled by large reservoirs of gas falling deep into the gravitational well of supermassive black holes, although precisely how that gas travels from larger, \sim galactic scales down to the central black hole is still a matter of uncertainty and debate (e.g., [Goodman, 2003](#); [Guo et al., 2023](#); [Hopkins et al., 2023](#); [Shlosman et al., 1989](#)). There is fairly direct observational evidence that the X-ray-emitting innermost gas takes the form of a fairly thin disk (see, for example, Figure 2 of [Tanaka et al., 1995](#), reproduced here in Figure 1.1), but also that thick, dusty⁶ tori⁷ orbit the central black hole at much larger distances, potentially obscuring the central regions (see,

[Schwarzschild, 1916](#)), a solution which featured a unidirectional membrane which causal influences could cross only in one direction ([Finkelstein, 1958](#)) and later took the name of a “black hole,” general relativity was, prior to the late 1960s, an abstruse theoretical pursuit without application to the known universe. Of course, the roughly contemporaneous discovery of pulsars by Jocelyn Bell Burnell ([Hewish et al., 1968](#)) was also quite timely.

⁶In this context, “dust” is taken to mean molecules and icy conglomerates, at temperatures $\lesssim 2000$ K.

⁷“Tori” here should not be taken literally, but in the sense that the obscuring dust blocks direct line-of-sight emission from the galactic nucleus and that light, in some radio-loud sources as suggested by polarized data, seems to escape parallel to the jet (e.g., [Miller et al., 1991](#)). See, for example, [Burtscher et al. \(2016\)](#) for impressions of the dusty structures surrounding AGN inferred from infrared interferometry.

for example, [Antonucci & Miller, 1985](#); [Miller & Antonucci, 1983](#); [Miller & Goodrich, 1990](#); [Miller et al., 1991](#), one result of which is reproduced here in [Figure 1.2](#)). Reverberation studies, which can be used to infer length scales from the timescales on which brightness fluctuations are correlated, suggest that the inner radii of dusty tori can fall around ~ 0.3 pc (taking Fairall 9 as an example, [Clavel et al., 1989](#)), although the dusty region likely extends quite a bit further (see also [Kishimoto et al., 2007](#); [Weigelt et al., 2012](#)).⁸ ALMA observations of NGC 1068 also indicate the presence of a ~ 200 pc circumnuclear disk with gas densities of $\rho \gtrsim 10^{-19}$ g cm $^{-3}$ and a surrounding starburst ring round ~ 1.3 kpc ([Viti et al., 2014](#)). Indeed, circumnuclear starbursts surrounding active galactic nuclei may be fairly generic (e.g., [González Delgado et al., 2001](#); [Watabe et al., 2008](#)).

We have thus seen, observationally, that star formation and supermassive black hole accretion go hand-in-hand. Furthermore, most quiescent galaxies are thought to harbor in their centers nuclear star clusters (e.g., [Neumayer et al., 2020](#)). Imagining some titanic cloud of gas approaching near to the galactic nucleus and forming an accretion disk, the orbits of objects in these nuclear star clusters will naturally intersect the accretion disk, interacting with it.⁹ Theoretical studies suggest that stars might fairly generically form within AGN disks, and a number of observational trends in AGN and gravitational wave observations may be related to the presence

⁸The mass inferred for the central black hole of Fairall 9 by [Peterson et al. \(2004\)](#) was $M_{\bullet} = 2.55 \pm 0.56 \times 10^8 M_{\odot}$, suggesting that the inner radius of the dusty torus falls around $\sim 2.5 \times 10^4 R_g$, where the gravitational radius is defined to be $R_g = GM_{\bullet}/c^2$.

⁹Of particular relevance is the relatively novel phenomenon of “quasi-periodic eruptions,” or QPEs. The study of these eruptive events has recently exploded, beginning with the report of quasi-periodic (with a recurrence time of ~ 9 hours) flares (the number of X-ray counts briefly increasing by more than two orders of magnitude) from the nucleus of low-mass active galaxy by ([Miniutti et al., 2019](#)). A number of other similar sources have since been discovered (e.g., [Arcodia et al., 2021, 2024](#); [Chakraborty et al., 2021](#); [Giustini et al., 2020](#); [Guolo et al., 2024](#)), typically in galaxies with fairly low masses (with stellar masses $\lesssim 10^{10} M_{\odot}$ [Miniutti et al., 2019](#)). One class of the models for these events invokes a stellar-mass object and an accretion disk, both orbiting a central SMBH, but on orbits misaligned with respect to one another (e.g., [Linial & Metzger, 2023](#); [Suková et al., 2021](#); [Tagawa & Haiman, 2023](#); [Xian et al., 2021](#)). In these models, orbital parameters such as the semi-major axis and eccentricity can be tuned to produce various periodicities.

of such objects and their remnants.

1.1.1 Theoretical Considerations

The classic model for accretion disks was developed in [Shakura & Sunyaev \(1973\)](#), where, as in many successful astronomical models, the uncertainties accompanying physical reality are hidden away in an α parameter.¹⁰ The essential innovation of [Shakura & Sunyaev \(1973\)](#) was that the transport of material through accretion disks onto accreting objects could be explained by an effective turbulent viscosity on large scales,¹¹ relating the effective viscosity ν to the sound speed (c_s) and scale height (H) of a given accretion disk (thought to characterize the largest turbulent eddies in the system) through an efficiency parameter α according to

$$\nu = \alpha c_s H. \tag{1.1}$$

Shortly after the [Shakura & Sunyaev \(1973\)](#) model was introduced, the realization occurred that it implied that these disks, in their outer regions, should collapse under their own gravity and form stars ([Kolykhalov & Syunyaev, 1980](#)). A number of subsequent authors have revisited

¹⁰As, for example, in [Tutukov & Yungelson \(1979\)](#) and [Toonen et al. \(2014\)](#) to name only a few somewhat representative works from the binary population synthesis community and its treatment of common-envelope evolution.

¹¹Physically, dissipation in astrophysical gasses takes place on atomic scales because of collisions between molecules. However, these collisions alone, in a smooth flow, would be many orders of magnitude too insignificant to explain things like the luminosities and active lifetimes of accreting objects (e.g., [Spitzer & Härm, 1953](#)).

¹²There is particular irony to the proposition of the α -viscosity model. Nikolai Shakura, when he wrote [Shakura & Sunyaev \(1973\)](#), worked at the Sternberg Astronomical Institute, a division of Moscow State University. A couple of blocks away, Evgeny Velikhov worked in (and led) the Moscow State University Physics Department. Velikhov, of course, appears to have been the first to discover what is now termed the “magnetorotational instability” ([Velikhov, 1959](#)), which was later discovered independently by Chandrasekhar ([Chandrasekhar, 1961](#)), and later popularized (or, peradventure, rediscovered, since they made no reference to the aforementioned works) by Balbus and Hawley ([Balbus & Hawley, 1991](#)), becoming the de facto mechanism assumed to transport matter, momentum, and energy astrophysical disks ([Balbus & Hawley, 1998](#)). This is neither the time nor place for a review of the theoretical or observational shortcomings of the α -viscosity model, but a great deal of time and ink might have been spared by slightly more interdepartmental discussion in Moscow.

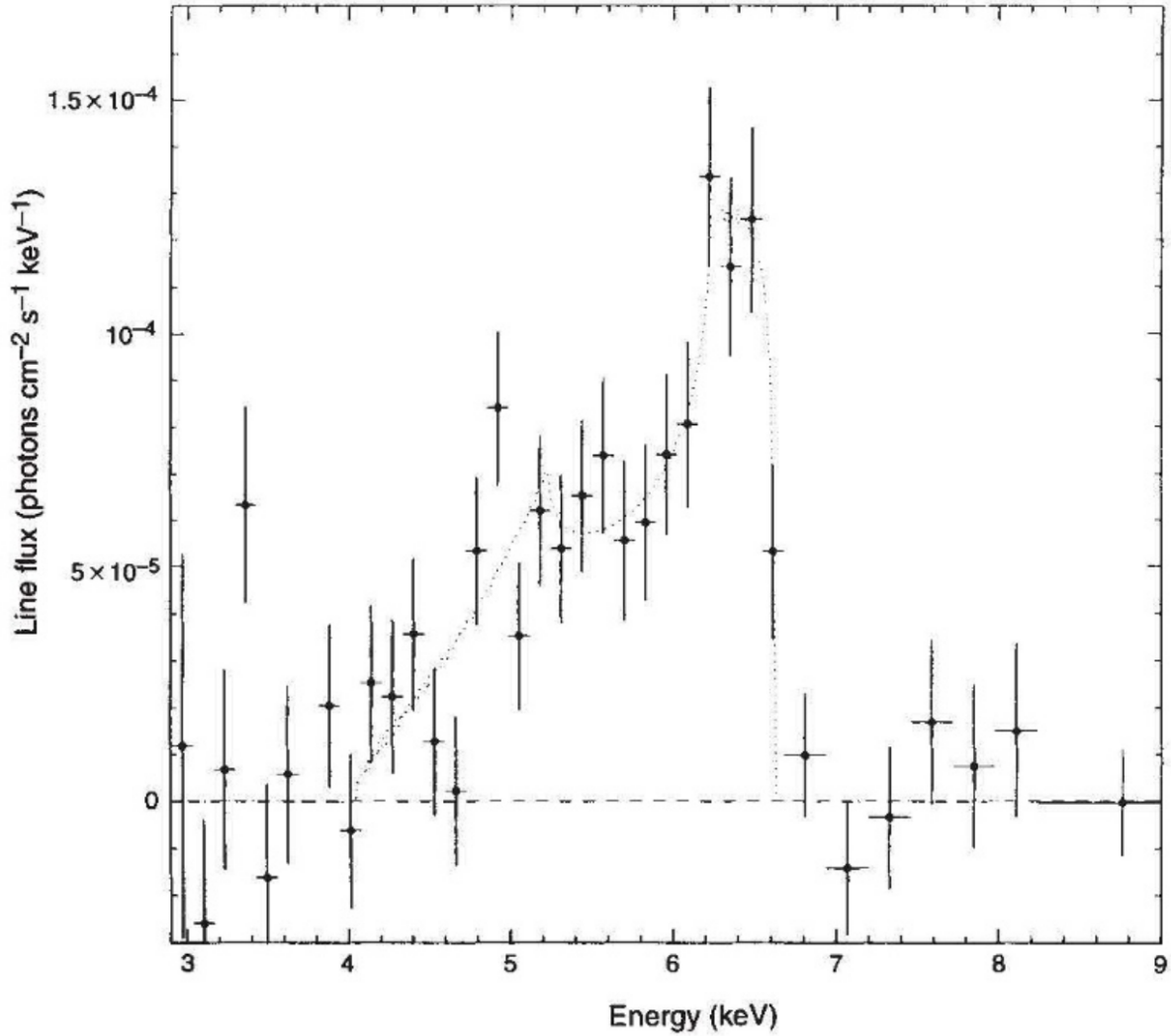


Figure 1.1: Iron $K\alpha$ line emission from MCG-6-30-15, with a rest-frame energy of ~ 6.4 keV, broadened to a width at zero intensity of $\sim 10^5$ km s $^{-1}$ (Tanaka et al., 1995). Continuum-subtracted data collected by the ASCA satellite are plotted using crosses, and the dotted lines plot the best-fit line profile produced by an externally-illuminated accretion disk orbiting a non-rotating black hole. The line profile, with its highly asymmetric redward shape, precludes gas distributions where appreciable matter is moving towards the observer, including quasi-spherical accretion flows; instead, the shape agrees with expectations of a nearly face-on disk, including the effects of transverse Doppler boosts and gravitational redshifts.

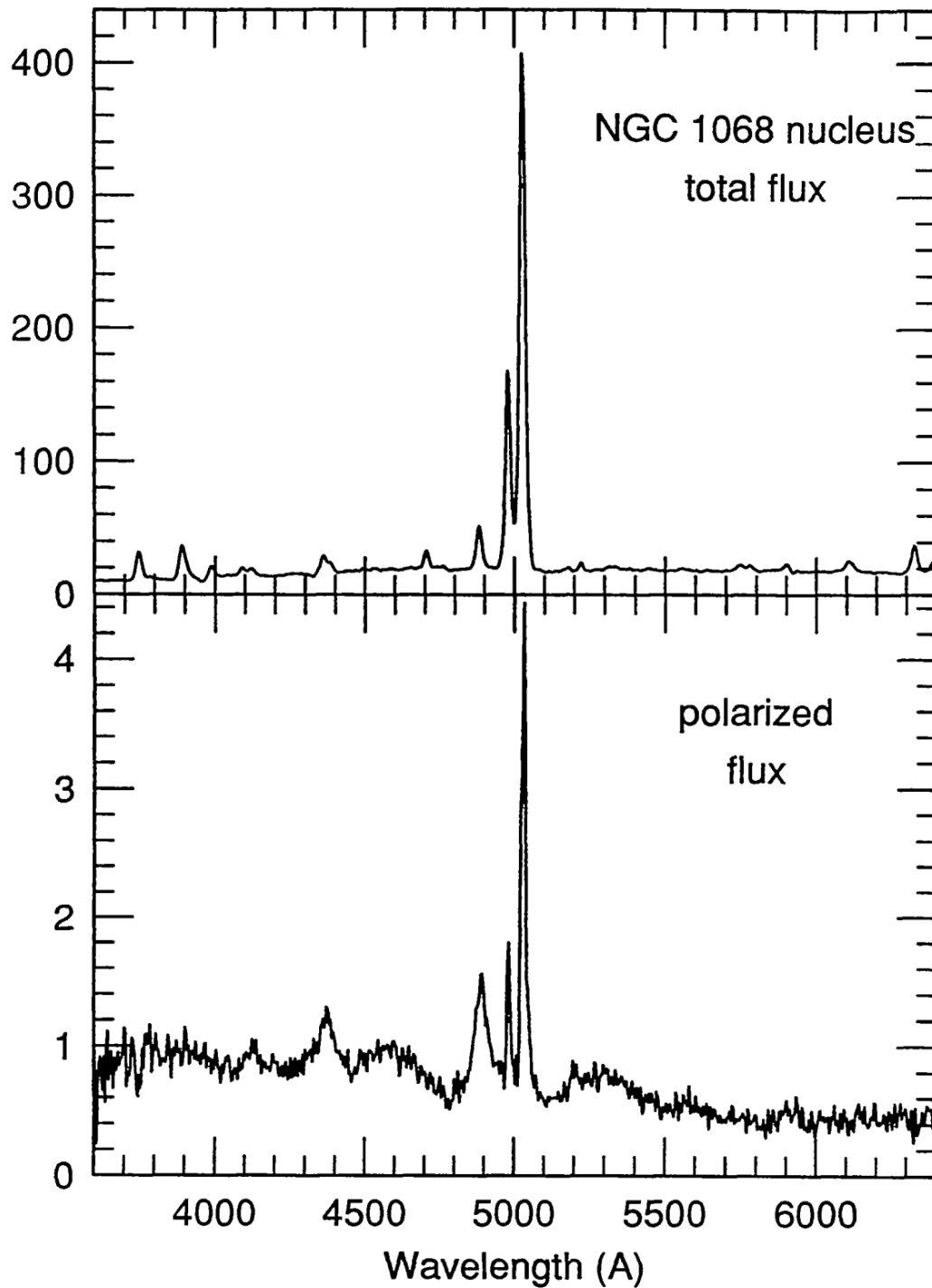


Figure 1.2: The flux spectrum (top) and polarized flux spectrum (bottom) of NGC 1068 presented in [Miller et al. \(1991\)](#). The narrow lines and flat continuum of the total spectrum are characteristic of low-velocity gas, and would classify the galaxy as “Type 2.” However, broad lines, indicative of an accretion disk nearer the central supermassive black hole are present in the polarized flux spectrum, suggesting a “Type 1” classification. The polarization position angle of these data was perpendicular to the radio jet of NGC 1068, indicative of scattering off of a conical (or biconical) plasma outflow.

this question, often using slightly different simplified disk models (e.g. [Goodman & Tan, 2004](#); [Inayoshi & Haiman, 2016](#); [Levin, 2003](#); [Thompson et al., 2005](#)), but the conclusion that stars should form at large distances follows naturally from the fact that the dynamical timescale of the disk at a given radius grows longer more quickly at large radii than does the free-fall timescale of the gas (see [Toomre, 1964](#), for a more precise derivation of the same conclusion, modulo a factor of order unity). Additionally, star formation (or at least gravitational collapse, short of actually reaching the densities necessary for “proper” star formation and the commencement of nuclear fusion) has been reproduced in numerical simulations of self-gravitating fluid disks (e.g., [Nayakshin et al., 2007](#)), of local shearing boxes (and sheets) of fluid (e.g., [Chen et al., 2023](#); [Gammie, 2001](#); [Jiang & Goodman, 2011](#), which are able to resolve the relevant physical processes with much higher fidelity), and of cosmologically-fed (and magnetically-supported) AGN disks ([Hopkins et al., 2023](#)).

It is also possible that stars may be brought into a newly-formed AGN disk from a preexisting nuclear star cluster. Stars may be removed from the nuclear star cluster into the disk through the excitation of density and bending waves, as well as through gas drag (e.g., [Artymowicz et al., 1993](#); [Rauch, 1995](#)). These interactions will tend to circularize orbits, and realign eccentric orbits with the AGN disk (e.g., [Fabj et al., 2020](#); [MacLeod & Lin, 2020](#); [Syer et al., 1991](#); [Tanaka & Ward, 2004](#)), although gravitational scattering events between objects in and around the disk can increase orbital inclinations (e.g., [Stewart & Ida, 2000](#); [Stone et al., 2017](#)).

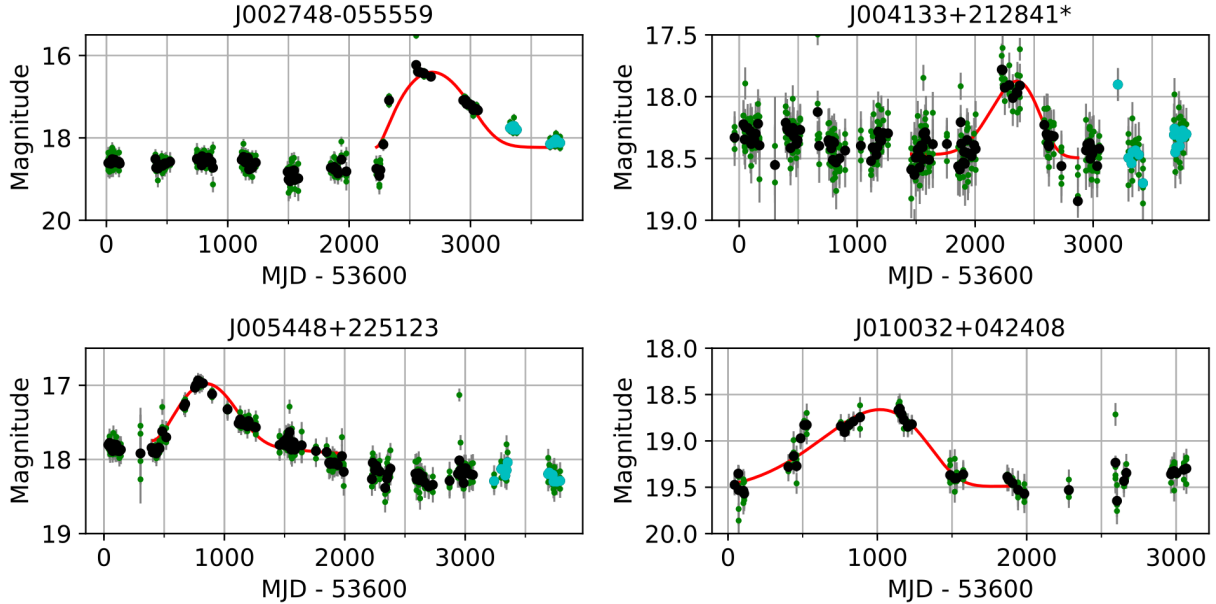


Figure 1.3: A small subset of the flares identified in CRTS data by [Graham et al. \(2017\)](#). In many cases, the flares last hundreds to thousands of days, and are far greater in magnitude than typical AGN variability, shown clearly by the scatter between individual observations. The black and cyan points plot data from the first and second CRTS data releases respectively. The red line in each panel plots a Weibull distribution fitted to each flare ([Weibull, 1951](#)).

1.1.2 Observational Considerations

A few different trends in AGN observations may be caused by stars either within AGN disks or in their immediate vicinity. One of the most glaring phenomenon is that of giant (“major”, “large-amplitude”) flares (e.g., [Frederick et al., 2021](#); [Graham et al., 2017](#)), during which AGN can brighten by up to ~ 3 magnitudes,¹³ temporarily (over ~ 100 s of days) increasing in average luminosity by an amount far exceeding their standard variability (as illustrated in Figure 1.3).

Possible causes of these flares include gravitational lensing of an AGN by some intermediate object ([Graham et al. \(2017\)](#) found that 11 of their 51 flares could be adequately described by a

¹³Here the magnitude is meant in the observational sense (that is to say, in base $10^{2/5}$), so that $\sim 2 - 3$ magnitudes amount to factors of about an order of magnitude (in base 10).

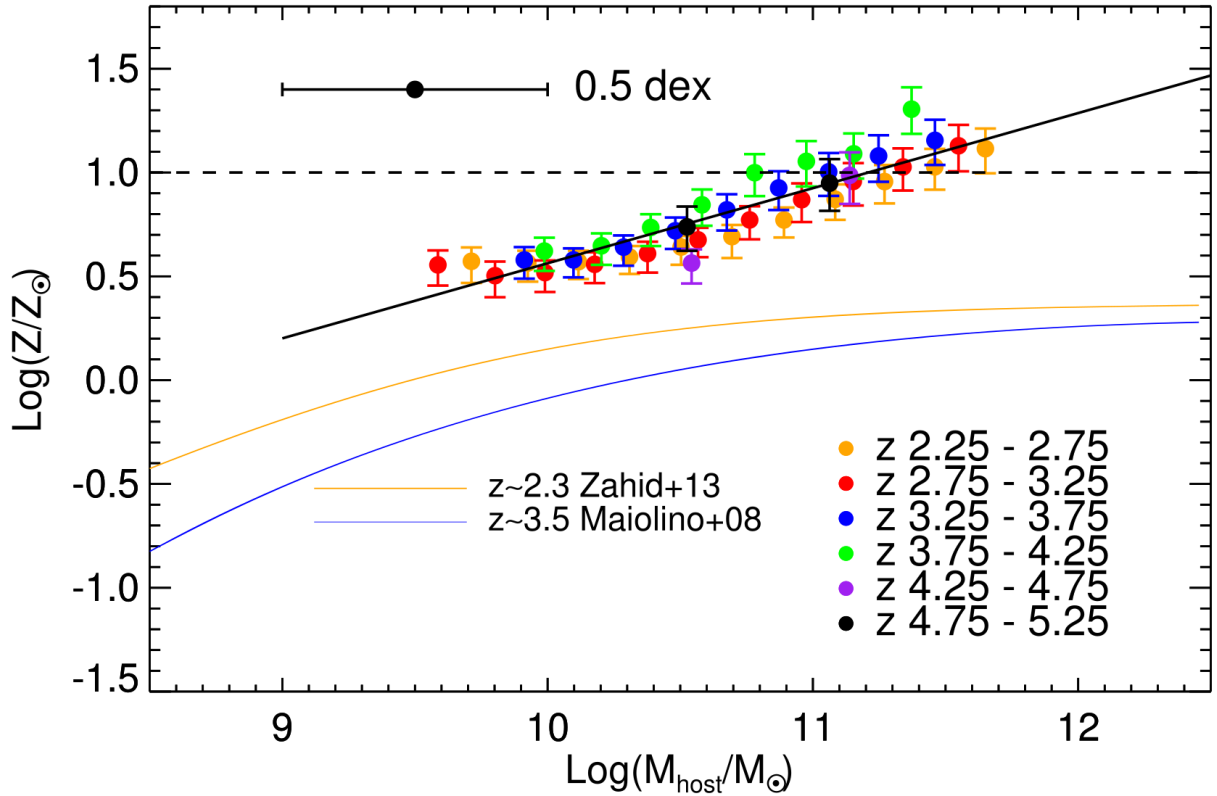


Figure 1.4: Metallicities inferred (using the average of the metallicities implied by the N V/C IV and (Si IV+O IV]/C IV line ratios) from averaged quasar spectra in a variety of SMBH mass and redshift bins, compared with an approximate host galaxy mass (the error bar in the top left corner indicates the typical scatter in the conversion from SMBH mass to host galaxy mass based on a pair of exquisitely imaged $z \sim 4$ quasars in [Targett et al. \(2012\)](#)). The blue and orange lines plot mass-metallicity relationships fit to star-forming galaxies at $z \sim 2.3$ ([Zahid et al., 2013](#)) and $z \sim 3.5$ ([Maiolino et al., 2008](#)). Irrespective of the uncertainty in the relationship between host galaxy and SMBH masses, the metallicities inferred for AGN are both well above those of star-forming galaxies and largely independent of redshift.

gravitational lensing model), superluminous supernovae, or tidal disruption events (TDEs).^{14,15}

Crucially, these flares are much greater in amplitude than typical AGN variability (on comparable timescales).

Active galaxies are also peculiar in their metal content, often seeming to have a much higher metallicity¹⁶ than galaxies as a whole (e.g. [Xu et al., 2018](#)), as illustrated in [Figure 1.4](#).¹⁷ Such inferences have a long history, dating back to at least the early 1990s when it was found that quasar metallicities of $\sim 3 - 14$ times solar seemed necessary to explain the observed N V/C IV line ratio ([Hamann & Ferland, 1992](#)). A complimentary line of evidence has been found in the analysis of Fe II/Mg II line ratio, which is thought to indicate the relative abundance of iron and alpha-capture elements generally (e.g. [Hamann & Ferland, 1999](#); [Maiolino & Mannucci, 2019](#)), and thus probe the relative roles of type Ia supernovae and core-collapse supernovae. Intriguingly, this ratio appears relatively constant over cosmic time (e.g., [Maiolino et al., 2003](#); [Sameshima et al., 2020](#); [Yang et al., 2021](#)), even out to $z \sim 7.5$ (e.g. [Onoue et al., 2020](#); [Yang](#)

¹⁴For the sake of completeness, [Graham et al. \(2017\)](#) also made the (in their words) “speculative” suggestion that some of these flares could result from the aftermath of black hole binary mergers within the disks of some AGNs, based on [Bartos et al. \(2017\)](#).

¹⁵A number of other TDE *candidates* have been identified in AGN (e.g. [Blanchard et al., 2017](#); [Jiang et al., 2019a](#); [Liu et al., 2018, 2020](#); [Zhang, 2024](#)). However, very few AGN flares are studied thoroughly enough to determine definitively whether they have been caused by tidal disruption events or some other phenomenon, because high-quality follow-up resources are scarce and AGN flares are plenty.

¹⁶The fraction (by mass) of gas constituted by elements other than hydrogen and helium.

¹⁷One must keep in mind that the metal content of these disks can not be measured directly, but is typically inferred from ratios of the strengths (frequency-integrated intensities) of various emission lines (e.g. [Hamann et al., 2002](#); [Nagao et al., 2006](#)). There are numerous uncertainties that preclude drawing definitive abundance inferences, from that of the underlying ionizing continuum to the numerous assumptions underlying radiative transfer calculations connecting gas abundances to synthetic spectra (e.g. [Ferland et al., 1998](#)). For example, there has long been debate over “nitrogen-rich” quasars, which exhibit anomalously strong nitrogen lines (typically N IV] and N III]) and constitute $\sim 1\%$ of quasars (e.g. [Bentz et al., 2004](#)), and whether or not they are truly overabundant in nitrogen (relative to, for example, solar abundances [Jiang et al., 2008](#)) or instead have anomalously high metallicities and are commensurately overabundant in nitrogen ([Batra & Baldwin, 2014](#)). As another example, in a sample of averaged AGN spectra across a range of binnings in SMBH mass and redshift from [Xu et al. \(2018\)](#), the line ratio between N V and C IV typically leads to a higher estimated metallicity than the (Si IV+O IV]) to C IV ratio. Moreover, [Xu et al. \(2018\)](#) found a consistent trend between NV/CIV-inferred metallicity and SMBH mass; however, [Sameshima et al. \(2017\)](#) found that no such correlations existed between the iron-to-hydrogen abundance ratio and SMBH mass, although they still inferred supersolar metal content.

et al., 2021) by which time very few type Ia supernovae should have occurred (the Universe being on the order of $\sim 7 \times 10^8$ years old, based on Planck Collaboration et al., 2020).¹⁸ One of the leading explanations for the apparent redshift-independence of these trends in metallicity and iron-to-alpha element ratio is that supernovae from stars captured into or formed within AGN disks could pollute the AGN environment (e.g. Artymowicz et al., 1993; Toyouchi et al., 2022).¹⁹

1.1.3 AGN Disks as Gravitational Wave Nesting Grounds

Gravitational waves were first observed directly on 14 September 2015,²⁰ when the Laser Interferometer Gravitational-Wave Observatory (LIGO) detected ripples in spacetime begotten by a pair of black holes (with detector-frame masses $m_1 = 38.7^{+5.3}_{-3.7} M_\odot$ and $m_2 = 32.5^{+3.7}_{-4.8} M_\odot$) merging 400^{+160}_{-180} Mpc away (Abbott et al., 2016a,b).²¹ Intriguingly, the participating black holes were fairly massive,²² and the implied volumetric event rate (noting the irreducibly small-number statistics) was $2 - 400 \text{ Gpc}^{-3} \text{ yr}^{-1}$ (Abbott et al., 2016c). Many origin stories have been spun for this event (and the many detected since, (e.g., Abbott et al., 2023a)), but the most enduring pur-

¹⁸Many analyses the X-ray spectra of accreting SBMHs have suggested that the inner regions of AGN disks may have iron abundances from a few to more than ten times the solar value (e.g., Nandra et al., 1997; Tanaka et al., 1995). Such analyses attempt to fit the shape of the iron $K\alpha$ fluorescence line, which typically shines from very near accreting black holes. The iron abundance is a free parameter in these models. However, systematic errors in these analyses can cause dramatic overestimation of the iron abundance, largely because current models do not properly describe high-density gas (e.g., García et al., 2018; Tomsick et al., 2018).

¹⁹In particular, Toyouchi et al. (2022) advocates for the formation of very top-heavy stellar populations within AGN disks, which may produce comparatively more iron as their lives terminate (Umeda & Nomoto, 2008).

²⁰Indirect evidence of gravitational waves was observed earlier, most prominently in the binary pulsar system PSR B1913+16, (e.g., Hulse & Taylor, 1975; Weisberg et al., 2010).

²¹Unless otherwise noted, throughout this thesis values quoted with uncertainties will be presented as the median value, along with the differences between the median, 95th percentile, and 5th percentile.

²²Qualitatively, more massive stars tend to leave behind more massive compact objects upon their deaths, although these trends may be nonmonotonic in initial stellar mass, and current studies suggest that the whether a star leaves behind a black hole or neutron star is a nontrivial function of progenitor mass (e.g., Burrows et al., 2024). Additionally, standard models of star formation (from the gravitational collapse of molecular clouds) predict far fewer stars at higher masses than at lower masses (e.g., Kroupa, 2001; Salpeter, 1955). Of course, more massive black holes emit higher-amplitude gravitational waves that are commensurately easy to detect. Given that such a population exists (which, notably, was not known a priori), it seems natural that these binaries would be detected (in perfect hindsight).

ported channels for producing the observationally implied binary black hole population include globular (or nuclear) star clusters (e.g., [Downing et al., 2010](#); [Sigurdsson & Phinney, 1993](#)), field binaries (e.g., [Broekgaarden et al., 2021](#); [Mapelli & Giacobbo, 2018](#)), and binaries within AGN disk (e.g., [McKernan et al., 2012](#); [Stone et al., 2017](#)).²³

AGN disks are promising locales for binary black hole mergers because the gravitational potential of the SMBH can help retain merger products, which can then undergo subsequent mergers; the accretion disk may help initially independent black holes form binaries; and the presence of gas enables the *possibility* of electromagnetic counterparts to merging black hole binaries (e.g., [McKernan et al., 2020a,b](#); [Stone et al., 2017](#); [Tagawa et al., 2020](#)). One particularly provocative gravitational event was GW190521, with constituent masses estimated to be $m_1 = 85_{-14}^{+21} M_\odot$ and $m_2 = 66_{-18}^{+17} M_\odot$ ([Abbott et al., 2020a](#)).²⁴ Both of these black hole masses are within the so-called “mass gap,” the range of black hole masses from $\sim 60 - 140 M_\odot$ ([Farag et al., 2022](#); [Mehta et al., 2022](#)) that stars are not thought to be able to leave behind via supernova,²⁵ suggesting that both constituent black holes had resulted from prior mergers. A flaring AGN was

²³I will not dedicate much ink to the preceding channels, but it is worth noting that essentially all of these formation channels can be contorted to “explain” virtually all of the observed gravitational wave events thanks to an abundance of astrophysical flexibility (e.g., [Ford & McKernan, 2022](#); [Rodriguez et al., 2021](#); [van Son et al., 2022](#)). Of course, in reality all of these may play some (or no) role, in addition to other possibilities I have neglected to list or that have not yet been imagined.

²⁴Notably, an independent analysis using an arguably more thorough sampling procedure inferred similarly large, but more disparate masses ([Nitz & Capano, 2021](#)).

²⁵Stars with masses on the order of $\sim 100 M_\odot$ at the time they initiate core hydrogen fusion (ZAMS, or Zero Age Main Sequence) typically reach central temperatures in excess of $\sim 7 \times 10^8$ K; at these temperatures, the photons released during fusion reactions are energetic enough to create electron-positron pairs ($\gamma + \gamma \rightarrow e^- + e^+$), which have negligible kinetic energy and provide negligible support against gravity; these reactions effectively remove pressure support, allow further collapse, increases in temperature (and the corresponding rate of nuclear reactions), and can lead to an explosive stellar detonation leaving behind no remnant (e.g., [Barkat et al., 1967](#); [Bond et al., 1984](#); [Fowler & Hoyle, 1964](#); [Glatzel et al., 1985](#); [Rakavy & Shaviv, 1967](#)). However, stars with ZAMS masses $\gtrsim 205 M_\odot$ can achieve central temperatures in excess of $\sim 6 \times 10^9$ K, leading to endothermic photodisintegration reactions that prevent the star from unbinding ([Bond et al., 1984](#); [Heger et al., 2003](#)), allowing the formation of black holes with masses $\gtrsim 140 M_\odot$. Massive stars shed a substantial fraction of their mass via winds throughout their lives, and there are significant uncertainties in nuclear reaction rates important for the aforementioned processes (most critically $^{12}\text{C}(\alpha, \gamma)^{16}\text{O}$, which governs the mass of the oxygen core that might eventually detonate), so there is substantial uncertainty in the precise range of black hole masses that can be produced as an outcome of stellar evolution (e.g., [Farag et al., 2022](#); [Farmer et al., 2019](#)).

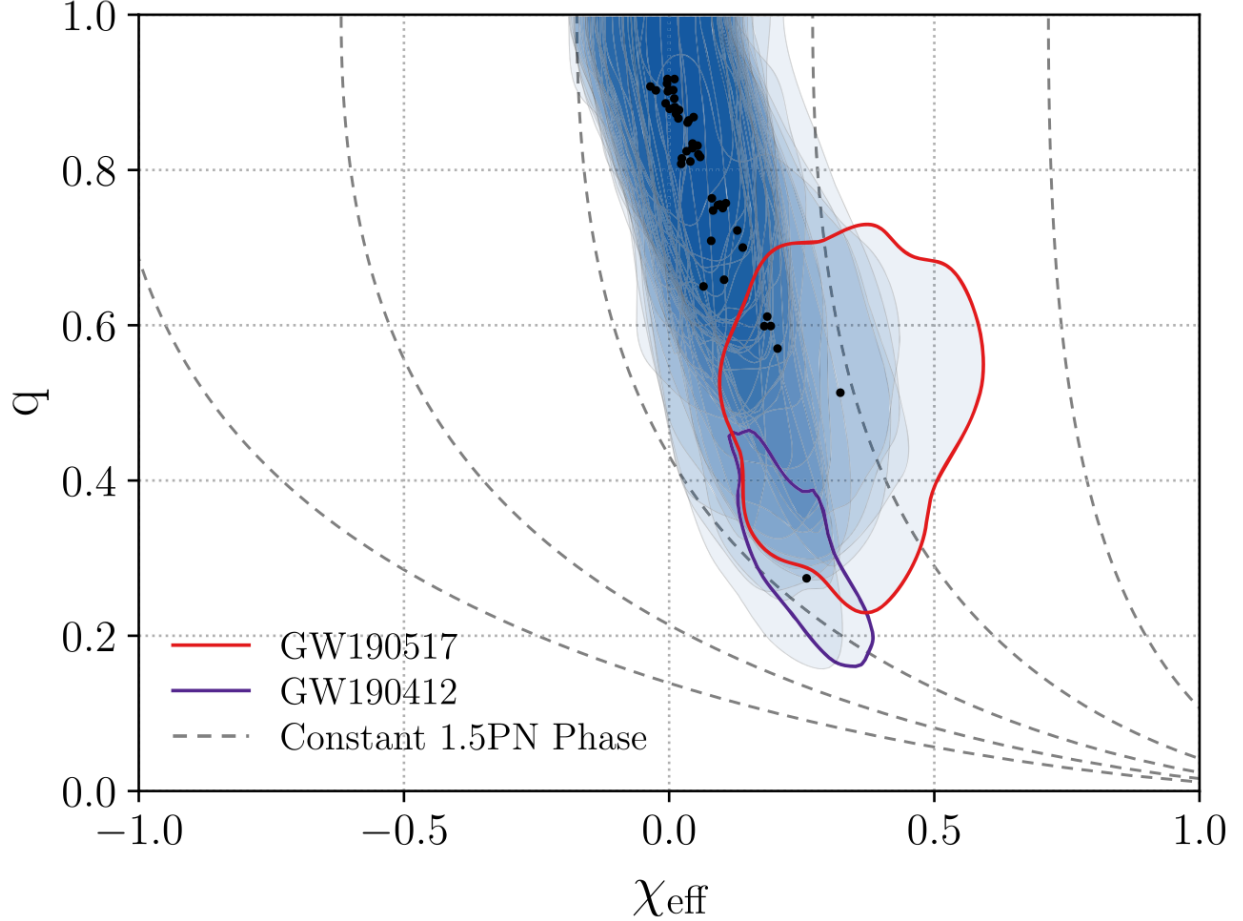


Figure 1.5: Effective spin and mass ratios, from [Callister et al. \(2021\)](#), using a model that allowed for linear correlations between the spin and mass ratio distributions for each event within in the GWTC-2 data set ([Abbott et al., 2021](#)). The 2D marginalized posterior distributions (minimum-area 90% credible regions) are shown in blue, and the median q and χ_{eff} values are marked using black dots.

also identified within a small corner of the localization error volume for GW190521 ([Graham et al., 2020](#)); similar flares have been roughly coincident with eight other gravitational wave events ([Graham et al., 2023](#)), although these associations are not statistically robust ([Nitz & Capano, 2021](#); [Palmese et al., 2021](#)).

Analyses of the gravitational wave event population as a whole have revealed an intriguing negative correlation between the mass ratio ($q \equiv m_2/m_1$) of these merging black hole binaries and their effective spins (χ_{eff} — the mass-weighted projections of the black hole spin angular

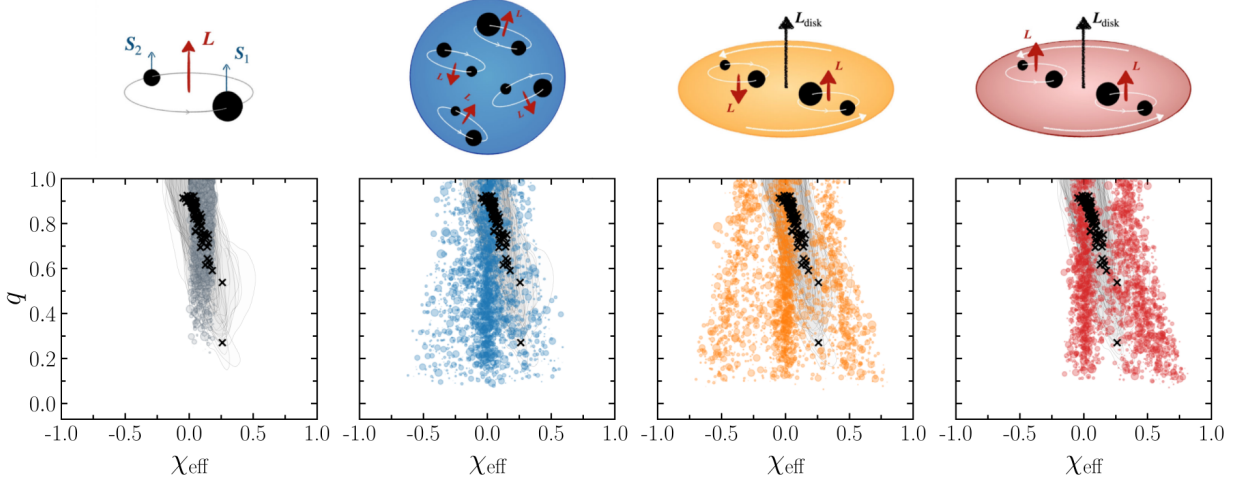


Figure 1.6: LIGO events (grey contours and black markings, from [Abbott et al. \(2023b\)](#)) and various population modes, as presented in ([Santini et al., 2023](#)). The gray circles show samples from a field binary model, and the colored circles show samples from different dynamical merger channels, each with different assumed symmetries. If the preferred direction of an AGN disk is able to influence binaries merging within it, qualitative agreement with the LIGO population can be achieved.

momenta projected into the plane of the binary orbit), along with a paucity of binaries with $\chi_{\text{eff}} < 0$ ([Adamcewicz et al., 2023](#); [Callister et al., 2021](#), see Figure 1.5). As illustrated in Figure 1.6, many formation channels predict χ_{eff} distributions symmetric about zero. It is worth noting that these trends have been identified as statistically significant under multiple prior assumptions about the black hole spin angular momenta, and while these trends were initially noted by [Callister et al. \(2021\)](#) analyzing the sample of gravitational wave events detected through the first half of Advanced LIGO’s third observing run ([Abbott et al., 2021](#)), they were later independently reproduced by [Adamcewicz et al. \(2023\)](#) using a data set with 35 additional events collected during the second half of Advanced LIGO’s third observing run ([Abbott et al., 2023a](#)). Although an anticorrelation between q and $|\chi_{\text{eff}}|$ is natural in any scenario where black holes undergo multi-

ple mergers,²⁶ the $\pm\chi_{\text{eff}}$ symmetry-breaking was unexpected.²⁷ AGN disks provide one of the more natural explanations for this symmetry breaking, providing a large reservoir of angular momentum which might affect both the spins and orbits of black holes (e.g., [Santini et al., 2023](#)), although particular common-envelope and mass-transfer scenarios can also accommodate such trends (e.g. [Adamcewicz et al., 2023](#)).

1.2 This Dissertation

The remainder of this thesis will detail my work to gain further insight into how AGN disks influence stars and stellar-mass black holes embedded within them. In [Chapter 2](#), I will review simple models of accretion disks and discuss some of my semi-analytical work using such models to understand the effects embedded stars and black holes might have on AGN disks, and how the formation of those objects may have accelerated SMBH growth in the early universe ([Dittmann & Miller, 2020](#)). In [Chapter 3](#), I will review stellar evolution, and in particular how the evolution of stars is altered by the dense environment of an AGN disk ([Dittmann et al., 2021, 2023a](#); [Jermyn et al., 2021](#)). In [Chapter 4](#), I will review my work on the evolution of binary black holes formed within AGN disks, the main goal of which has been to determine the circumstances under which binary formation in AGN disks might actually be viable as an origin for the binary black hole mergers observed by LIGO ([Dittmann et al., 2024a](#)). [Chapter 5](#) will conclude, offering reflections and comments concerning future studies along these lines.

²⁶In the vast majority of scenarios, black hole mergers will result in a spinning remnant black hole, even if the initial black holes were not spinning. Qualitatively, the binary orbit has a significant amount of angular momentum that must go *somewhere*. “Where” is split between gravitational wave emission and the spin of the remnant black hole, and the partition between these can be fairly reliably determined through simulations (see, for example, [Section 4.2.1 of Lehner & Pretorius, 2014](#), and the references therein). Then, if we imagine two black holes merging, one which is the product of an earlier merger and another that is not, the post-merger black hole will typically have a larger mass and higher spin than the other. A general anticorrelation between q and χ_{eff} follows.

²⁷As [Callister et al. \(2021\)](#) opens, “who ordered that?”

Chapter 2: Accretion Disk Models for Active Galactic Nuclei

2.1 Introduction

Models are widespread in the interpretation of observations of active galaxies. As discussed previously, there is ample observational evidence that gas in the vicinity of accreting SMBHs takes the form of a disk.¹ Even without considering general relativity, the evolution of fluids is highly complex and often chaotic, even under substantial simplifying assumptions (e.g., [Deissler, 1986](#); [Lorenz, 1963](#)). Accounting for the effects of stars and stellar-mass black holes on the fluid complicates things further, but that has not stopped people (myself included) from trying.

In [Section 2.2](#) I will briefly review how simplified disk models can be derived from the equations of hydrodynamics. In [Section 2.3](#) I will review some general approaches to adapting disk models to include some effects of stellar populations, and in [Section 2.4](#) I will review the variation of these models that I applied in the context of early-universe supermassive black hole growth.

¹Disk formation is a fairly generic astrophysical phenomenon (e.g., [Kant, 1755](#)), that follows naturally from the nature of central forces, which conserve angular momentum generically. Then imagining some collection of gas where thermal pressure and gravity counteract one another, radiative losses will often act to remove thermal energy from the gas, reducing its pressure support. On average however, these thermal losses will not appreciably change the angular momentum of the gas, if extant, resulting in some disklike geometry.

2.2 Disk Models

The equations governing the evolution of fluids can be written, ignoring energy transport for the time being, as

$$\partial_t \rho + \nabla \cdot (\rho \mathbf{v}) = 0, \quad (2.1)$$

$$\partial_t (\rho \mathbf{v}) + \nabla \cdot (\rho \mathbf{v} \mathbf{v}) + \nabla P = \mathbf{f}, \quad (2.2)$$

where ρ is the fluid density (at a certain time and place), \mathbf{v} is the fluid velocity, P is the fluid pressure, and \mathbf{f} is an external force per unit mass. Equation (2.1) enforces that matter is neither created nor destroyed, instead simply moving from one place to another. Equation (2.2) is analogous to Newton's 1st law, enforcing that the overall momentum of the fluid will be conserved in the absence of forces acting upon it (both external and owing to pressure gradients).

The above equations are intractable for general fluids varying in time and three spatial dimensions. In the following I will go through a number of common assumptions, all of which are objectionable at *some* level. Arguably the most common assumption in *disk* modeling is to ignore the vertical structure of the disk.² One could imagine integrating the above equations in a vertical direction, assuming some vertical profile of the fluid.³ Alternatively, one might imagine taking a power series of the above equations in the small parameter $H/R \ll 1$, where H is

²This is not, of course, universal. For example, much progress has been made in the study of warped disks, which are locally very thin but vary appreciably in three dimensions (e.g., [Ogilvie, 1999, 2018](#)); and others have developed detailed models for the local vertical structure of accretion disks (e.g., [Hubeny et al., 2000, 2001](#); [Hubeny & Hubeny, 1998a,b](#); [Meyer & Meyer-Hofmeister, 1982](#); [Milsom et al., 1994](#)). In all cases, however, some simplifying assumptions are made due to the geometrical symmetries (and asymmetries) of disks.

³Assuming a vertically constant sound speed (c_s , equivalent to assuming a vertically constant temperature) and a gravitational acceleration that varies linearly in the vertical direction (i.e. $g \propto z$) leads to a Gaussian profile, following from the equation of vertical hydrostatic equilibrium ($c_s^2 \partial_z \rho = -\rho g$).

the scale height of the disk and R is the cylindrical radius, and subsequently ignoring all terms proportional to H/R .^{4,5} It is also standard to assume the fluid's vertical velocity is zero, and that the azimuthal motion of the fluid satisfies approximate hydrostatic balance, i.e.

$$\Omega^2 R - \frac{1}{\rho} \partial_R P = \partial_R \Phi, \quad (2.3)$$

for some central gravitational potential $\Phi(r)$, where $\Omega \equiv v_\phi/R$. As H is often proportional to the sound speed c_s , and the pressure is often $P = c_s^2 \rho$, taking the limit $H/R \ll 1$ also renders the pressure gradient term but a small perturbation. It is also common to assume azimuthal symmetry ($\partial_\phi \rightarrow 0$), although not strictly necessary (as in the viscoelastic study of eccentric disks in [Ogilvie, 2001](#)).

Under such assumptions, and defining the surface density of the disk $\Sigma \equiv \int_{-\infty}^{\infty} \rho dz$ (in this context using the similarly vertically averaged velocities), Equation (2.1) becomes

$$R \partial_t \Sigma + \partial_r (R \Sigma v_R) = 0, \quad (2.4)$$

and the azimuthal term of Equation (2.2) becomes

$$R \partial_t (R^2 \Sigma \Omega) + \partial_R (R^3 \Sigma v_r \Omega) = 0, \quad (2.5)$$

where I have taken the radial component of \mathbf{f} to be $-\partial_R \Phi$. Note that $R^2 \Sigma \Omega = \Sigma R v_\phi$ is the

⁴The limit of a “razor-thin” disk.

⁵Throughout the disk literature H is defined in a few different ways, such as the half-width of the disk (for example, something like $H = \frac{1}{2} \rho^{-1} \int_{-\infty}^{\infty} \rho(z) dz$), or as the pressure scale height under the assumptions discussed in the third footnote of this chapter, leading to $H = c_s \sqrt{2|z/g|}$ (with or without the factor of $\sqrt{2}$ depending on the preference of a given author).

angular momentum per unit volume of the fluid, so (as long as $\Omega \neq R^{-2}$) the angular momentum of the fluid can only be conserved in a steady state if $v_r = 0$; otherwise stated, under the action of only a central force, matter cannot flow inward or outward through the disk.

It is certainly *popular* to describe transport through accretion disks using a viscous stress (e.g., Lynden-Bell & Pringle, 1974; Novikov & Thorne, 1973; Shakura & Sunyaev, 1973). This stress can be treated as an additional contribution to the fluid stress tensor, the divergence of which is taken on the right hand side of Equation (2.2), so that it reads

$$\partial_t(\rho\mathbf{v}) + \nabla \cdot (\rho\mathbf{v}\mathbf{v} - 2\nu\rho\sigma) + \nabla P = \mathbf{f} - \nabla \cdot \sigma, \quad (2.6)$$

where ν is the kinematic viscosity of the fluid (see Equation (1.1) and the preceding discussion), and σ is a velocity shear tensor (trace-free in d dimensions), the elements of which are defined as

$$\sigma_{ij} = \frac{1}{2} (\nabla_i v_j + \nabla_j v_i) - \frac{1}{d} \mathbf{g}_{ij} \nabla_k v^k, \quad (2.7)$$

for some metric tensor \mathbf{g} . Often, working in the axisymmetric, $v_z \approx 0$ limit, the most important of these terms (using cylindrical coordinates) is typically the $\sigma_{R\phi} = \sigma_{\phi R}$ term,

$$\sigma_{R\phi} = \sigma_{\phi R} = \frac{1}{2} \left(\partial_R v_\phi + \frac{v_\phi}{R} \right). \quad (2.8)$$

Most disk models progress under the additional assumption of a steady state, so that the mass current (or accretion rate) and angular momentum current through this disk are constant in time.⁶

⁶It was actually understood very early on that most accretion disks around black holes were not in a steady

The accretion rate through the disk can be defined as

$$\dot{M} \equiv - \int dz \int d\phi \rho v_R dz d\phi = -2\pi R \Sigma v_R, \quad (2.9)$$

which satisfies Equation (2.4) in the steady limit and has been defined such that the accretion rate is positive when the averaged radial velocity is negative.

Taking $\partial_t \rightarrow 0$ and the adding viscosity as in Equation (2.6) to Equation (2.5) implies that

$$R^2 \Sigma v_R v_\phi - R^2 \nu \Sigma (\partial_R v_\phi - \frac{v_\phi}{R}) = R^2 \Sigma \left[v_R v_\phi - \nu R \partial_R \left(\frac{v_\phi}{R} \right) \right] = -l_0 \frac{\dot{M}}{2\pi}, \quad (2.10)$$

for some constant angular momentum current defined in terms of the accretion rate and an arbitrary constant l_0 . The above expression can be rearranged as

$$\nu \Sigma \frac{R}{\Omega} \partial_R \Omega = -\frac{\dot{M}}{2\pi} \left(1 - \frac{l_0}{R^2 \Omega} \right). \quad (2.11)$$

In the Keplerian limit $\Omega^2 = GM_\bullet/R^3$ (where M_\bullet is the mass of the central SMBH), the preceding expression reduces to

$$\nu \Sigma = \frac{\dot{M}}{3\pi} \left(1 - l_0 (GM_\bullet R)^{-1/2} \right), \quad (2.12)$$

which reduces to $\dot{M} = 3\pi\nu\Sigma$ in the far reaches of the disk where $GM_\bullet R \gg l_0$. It is traditional

to set l_0 equal to the specific angular momentum of the disk at some characteristic (typically state (e.g., [Fitch et al., 1967](#)). The irreconcilability of viscous accretion disk models with AGN variability has been discovered and rediscovered numerous times (e.g., [Antonucci & Cohen, 1983](#); [Lawrence, 2018](#)).

innermost) radius (R_*),⁷ leading to

$$3\pi\nu\Sigma = \dot{M} \left(1 - \sqrt{\frac{R_*}{R}} \right). \quad (2.13)$$

Notably, if a central object instead drives a particular angular momentum current through the disk, or if the potential is appreciably non-Keplerian, the disk structure can be significantly affected.

The energy dissipated within the disk by viscosity (\mathcal{D}),⁸ to leading order, is given by

$$\mathcal{D} = 4\Sigma\nu\sigma_{r\phi}^2 = \Sigma\nu R^2(\partial_R\Omega)^2 = -\frac{\dot{M}}{2\pi}R\Omega\partial_R\Omega \left(1 - \frac{l_0}{R^2\Omega} \right). \quad (2.14)$$

Taking the Keplerian limit $l_0 = \sqrt{GM_*R_*}$, \mathcal{D} can be expressed as

$$\mathcal{D} = \frac{3}{4\pi}\Omega^2\dot{M} \left[1 - \sqrt{R_*/R} \right]. \quad (2.15)$$

Conveniently, this estimate of the dissipation does not depend on the assumed value of the kinematic viscosity.⁹ Assuming that this dissipated energy is radiated locally, which is a fairly reasonable assumption when $H/r \ll 1$ since the vertical direction is likely to provide the shortest path for radiation to take out of the disk, and that the amount of energy dissipated within the

⁷This condition amounts to a zero-viscous-torque boundary condition, sometimes confusingly and erroneously referred to as a zero-torque condition.

⁸In basic mechanics, the work done by some process is given by the product of a force and the distance over which it is applied. More generally, the rate of energy dissipation by viscosity is given by the product of the viscous stress and rate-of-strain tensors, which are in this case both proportional to the velocity shear tensor σ .

⁹The significance of this result is often dramatically overstated, as sometimes the absence of a ν is taken to imply that this result does not depend on the details of the turbulence model: “the major uncertainty of the theory — the viscosity — has vanished,” as [Pringle \(1981\)](#) puts it (this sentiment, of course, is endemic). Although the coefficient connecting the velocity shear tensor to the fluid stress tensor has vanished, this result still depends entirely on the form of the components of the stress tensor that has been assumed, as well as the negligibility of all but two components of that tensor. Furthermore, this form of the stress tensor effectively introduces parabolic terms to the fluid equations that are acausal and artificially local.

disk is equal to the amount of energy radiated (from both sides of the disk), the effective disk temperature (T_{eff}) can be approximated using

$$\mathcal{D} = 2\sigma_{\text{SB}}T_{\text{eff}}^4, \quad (2.16)$$

where σ_{SB} is the Stefan-Boltzmann constant, leading to

$$T_{\text{eff}} \approx \left[-\frac{\dot{M}}{4\pi} R\Omega \partial_R \Omega \left(1 - \frac{l_0}{R^2\Omega} \right) \right]^{1/4}. \quad (2.17)$$

These equations are often complemented by a number of others, such as a specific relationship between the (effective) kinematic viscosity within the disk, often

$$\nu = \alpha c_s H, \quad (2.18)$$

following the lead of [Shakura & Sunyaev \(1973\)](#). Some relationship between the physical and effective disk temperatures is often assumed as well, along the lines of

$$T^4 = \tau T_{\text{eff}}^4 \quad (2.19)$$

in the optically thick limit (e.g. [Shakura & Sunyaev, 1973](#)), or instead

$$T^4 = \left(\frac{3}{8}\tau + \frac{1}{2} + \frac{1}{4}\tau^{-1} \right) T_{\text{eff}}^4, \quad (2.20)$$

interpolating between the optically thick and thin limits as in ([Sirko & Goodman, 2003](#)).¹⁰ Some

¹⁰The 1/2 term follows from an Eddington (two-stream) approximation to the transfer equation as a boundary

equation of state that connects the sound speed to the temperature, pressure, and density, along the lines of

$$P = c_s^2 \rho = \rho k T / \mu + a T^4 / 3, \quad (2.21)$$

where ρ is the gas density, c_s is the sound speed, k is the Boltzmann constant, $a \equiv 4\sigma_{\text{SB}}/c$ is the radiation constant. In the preceding equation, μ is the mean molecular weight, defined as

$$\mu = m_H \frac{4}{3 + 5X - Z}, \quad (2.22)$$

where m_H is the mass of a hydrogen atom, X is the hydrogen mass fraction of the gas, and Z is the metal mass fraction of the gas. These equations are usually closed by some particular definition of H and relationship between Σ , H , and ρ , along with an opacity $\kappa(\rho, T)$ used to calculate relate the optical depth, often approximating

$$\tau = \rho H \kappa. \quad (2.23)$$

The approximate (virtually always Rosseland mean) opacities assumed can dramatically affect the disk models one calculates, as demonstrated in Section 2.2.1. Generally, the above equations, after choosing a few free parameters such as \dot{M} , l_0 , α , and $\Omega(r)$, can be solved algebraically at any radius using standard nonlinear root-finding techniques, or simple algebra in certain limits.

condition, and the other terms interpolate between the optically thin and optically thick limits. [Thompson et al. \(2005\)](#) derive a similar expression, differing by a factor of 2.

2.2.1 Example Accretion Disks Models

Now that we have gone through the preceding derivations, it will be useful to see some of these models in action, to examine some of their common features. To avoid confusion, within this subsection I will consider the following set of equations:

$$\sigma_{\text{SB}} T_{\text{eff}}^4 = \frac{3}{8\pi} \dot{M}' \Omega^2, \quad (2.24)$$

$$T^4 = \tau T_{\text{eff}}^4, \quad (2.25)$$

$$\tau = \kappa \rho H, \quad (2.26)$$

$$\alpha c_s^2 \Sigma = \frac{\dot{M}' \Omega}{3\pi}, \quad (2.27)$$

$$P = \frac{a}{3} T^4 + \frac{\rho k T}{\mu}, \quad (2.28)$$

$$\Sigma = 2\rho h, \quad (2.29)$$

$$c_s = H\Omega, \quad (2.30)$$

$$P = c_s^2 \rho, \quad (2.31)$$

$$\kappa = \kappa(\rho, T), \quad (2.32)$$

$$\dot{M}' = \dot{M}(1 - \sqrt{r_*/r}), \quad (2.33)$$

which are solved via nonlinear root-finding (Moré et al., 1980).¹¹ I will consider two functional forms for the opacity here: Case 1, a combination of electron scattering opacity and a simple Kramers' opacity (e.g., Kramers, 1923), approximately accounting for the opacity due to free-

¹¹<https://github.com/ajdittmann/agndisks>

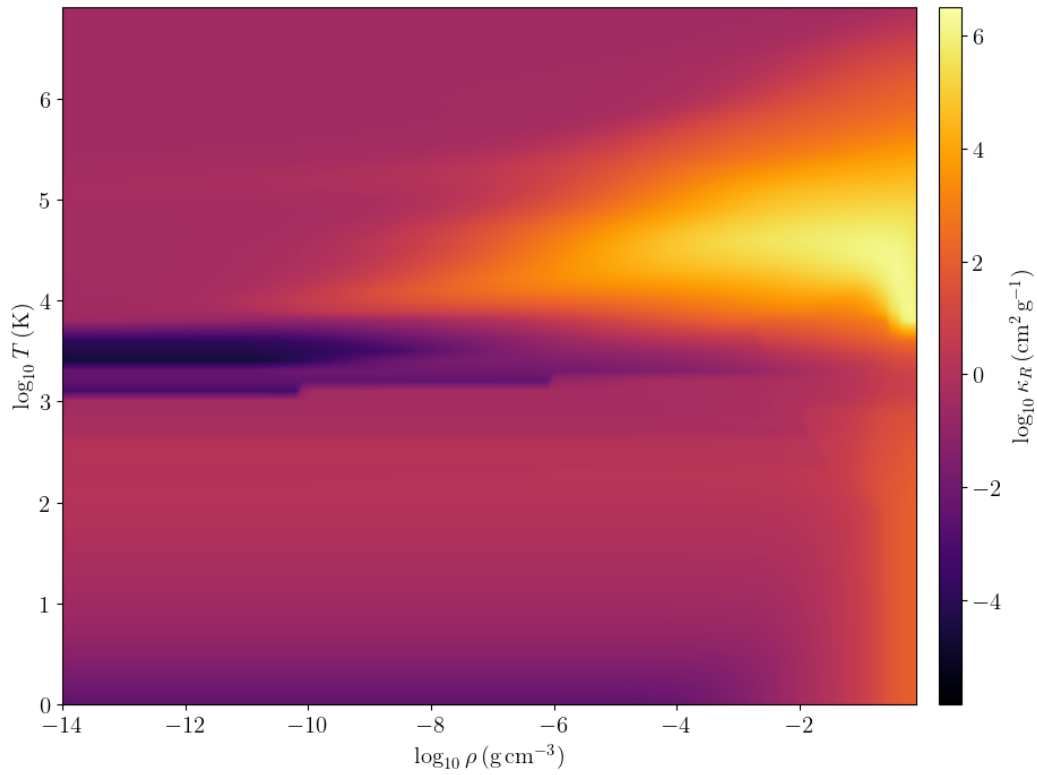


Figure 2.1: Tabulated opacities from [Zhu et al. \(2021\)](#). Notable features include the precipitous drop in opacities between $\sim 10^3$ and $\sim 10^4$ K, where various species of dust have sublimated but atomic opacities are not yet appreciable. At higher temperatures, in bands across a wide range of densities near $\sim 10^4$ K and $\sim 10^5$ K, the iron and H^- opacity bumps are visible.

free, bound-free, and bound-bound electronic transitions

$$\kappa = 0.2(1 + X) + 4 \times 10^{25}(X + 1)(Z + 0.001)\rho T^{7/2} [\text{cm}^2 \text{g}^{-1}]; \quad (2.34)$$

and Case 2, tabulated opacities compiled in [Zhu et al. \(2021\)](#), blending together molecular opacities from [Freedman et al. \(2014\)](#), atomic opacities from [Colgan et al. \(2016\)](#), and dust opacities following [Birnstiel et al. \(2018\)](#), which included water ice ([Warren & Brandt, 2008](#)), astronomical silicate ([Draine, 2003](#)), and refractory organics ([Henning & Stognienko, 1996](#)), using the dust sublimation temperatures in Table 3 of [Pollack et al. \(1994\)](#). I have used the publicly available implementation of this opacity blend,¹² which covers densities $10^{-14} \text{ g cm}^{-3} \leq \rho \lesssim 8 \times 10^{-1} \text{ g cm}^{-3}$ and temperatures from $1 \text{ K} \lesssim T \lesssim 8 \times 10^6 \text{ K}$, and is plotted in Figure 2.1.

One of the most challenging aspects of attempting to use more realistic or complete opacities is that the opacity may not be a particularly smooth function of density or temperature. For example, at temperatures between roughly $\sim 10^3 \text{ K}$ and $\sim 10^4 \text{ K}$, a variety of dust grain types sublimate dramatically decreasing the opacity of gas at those temperatures. When this occurs a few of the assumptions that were used to derive the above equations might break down.¹³ Regardless, these wildly varying opacities can lead to other disk parameters varying significantly as a function of radius.

In order for the assumption of a steady state to be valid, the resulting solutions must be stable. One important form of stability is thermal, as discussed, for example, by [Field \(1965\)](#). In

¹²<https://github.com/zhuzh1983/combined-opacity>

¹³For example, let us imagine that the disk is in fact vertically isothermal; even if density and temperature vary fairly smoothly with radius, κ may change rapidly. If the opacity plummets by $\sim 2 - 5$ orders of magnitude over a very short range in radius, the assumption that locally-generated heat escapes the disk vertically may break down. Additionally, deviations from vertical isothermality can lead to strongly varying opacity as a function of height within the disk, making the actual optical depth poorly characterized by a single (more or less characteristic) combination of opacity, temperature, and density.

the radiation-pressure dominated regime, $P \propto T^4$, $c_s \propto T^2$, so the heating rate varies $\mathcal{D} \propto c_s^2 \Sigma \propto T^6$. However, the cooling rate is simply $\propto T^4 \tau^{-1} \propto T^4 H^{-1} \kappa^{-1}$, which will be $\propto T^2$ if opacity is dominated by electron scattering, or $T^{11/2}$ if other Kramers-scaling opacity terms dominate. Because the heating rate varies more strongly with temperature than the cooling rate, any small temperature perturbation in radiation pressure dominated disks (under the above assumptions) will result in catastrophic collapse or expansion. One way to ameliorate this instability is to imagine the effective viscosity in the disk depends only on the gas pressure rather than the total pressure, $\nu = \alpha kT / (\mu \Omega)$ rather than $\nu = \alpha c_s^2 / \Omega$.

The instability concerning the remainder of this chapter is instead gravitational. Fluid disks will tend to collapse under their own weight when (Toomre, 1964)

$$Q \equiv \frac{c_s \Omega}{\pi G \Sigma} \approx \frac{\Omega^2}{2\pi \rho G} \lesssim 1. \quad (2.35)$$

Qualitatively, this criterion balances the dynamical timescale of the accretion disk at a given radius ($t_{\text{dyn}} \propto \Omega^{-1}$) with the gravitational free-fall timescale ($t_{\text{ff}} \propto (G\rho)^{-1/2}$): when the free-fall timescale is shorter (modulo constant factors of order unity) the disk collapses beneath its own weight. It is worth keeping in mind that other (for example, magnetohydrodynamic) effects may help support realistic disks (e.g., Kim & Ostriker, 2001).

With these considerations in mind, we are essentially ready to begin considering a few example disk models. But first, a few more definitions: I will specify r_* to be the innermost stable circular orbit of a nonrotating black hole, $r_* = 6r_g$, where

$$r_g \equiv \frac{GM_\bullet}{c^2}, \quad (2.36)$$

where c is the speed of light. I have also parameterized each accretion rate in terms of an Eddington ratio, such that

$$\dot{M} = \eta \dot{M}_{\text{Edd}}, \quad (2.37)$$

where

$$\dot{M}_{\text{Edd}} \equiv \frac{4\pi G M_{\bullet} m_H}{\epsilon c \sigma_T}, \quad (2.38)$$

where σ_T is the Thompson scattering cross section and ϵ is the fraction of the rest mass-energy of matter accreting onto the black hole that is transformed into radiation.¹⁴ For all of the models I'll calculate here, I have used an outer radius of $10^6 r_g$ for each disk, and fixed $\alpha = 0.1$, $\epsilon = 0.1$, $X = 0.72$, and $Z = 0.02$.

The first few of these models, using the simplified opacities of Equation (2.34), are shown in Figure 2.2. In one set of models, I have fixed $\eta = 0.1$ and used the SMBH masses $M_{\bullet} \in \{10^6, 10^7, 10^8\} M_{\odot}$. In the other set, I have fixed $M_{\bullet} = 10^7 M_{\odot}$ and instead varied $\eta \in \{0.01, 0.1, 1\}$.¹⁵ Before interpretation, a word of caution: in calculating these models, I have specified that (at fixed η) $\dot{M} \propto M_{\bullet}$. I have also plotted disk profiles as a functions of r/r_g , which includes an implicit factor of M_{\bullet} through r_g .

Examining the simple disk models in Figure 2.2, one striking observation is that the opacity appears nearly constant (as a function of M_{\bullet} and r/r_g , at fixed η). In fact, in the limit where radiation pressure and the electron scattering term in Equation 2.34 can be neglected, $\kappa \propto \dot{M}^{-1/2} M_{\bullet}^{-1/4} r^{3/4}$ (e.g., Frank et al., 2002),¹⁶ and thus in the present parameterization of \dot{M} ,

¹⁴This follows from balancing the force acting on gas due to gravity with that due to radiation pressure, in this case assuming electron scattering opacity.

¹⁵Active galactic nuclei are often inferred to accrete at rates between ~ 1 and $\sim 1/100$ times the Eddington limit (e.g., Shen et al., 2008).

¹⁶For what it's worth, the third edition of this book actually has a typo in the relevant equation, (5.53), although this result follows appropriately from their equations (5.49).

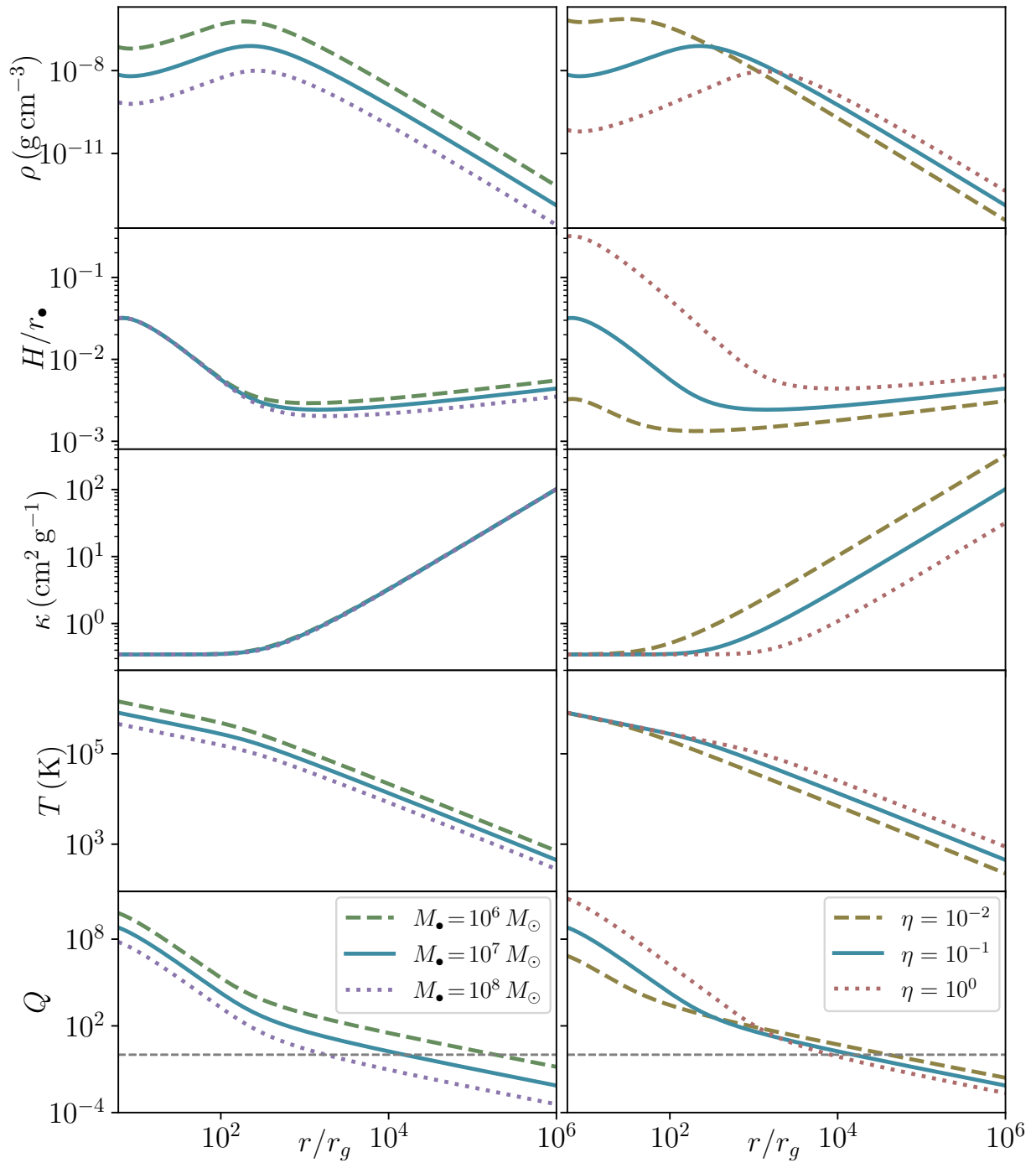


Figure 2.2: Disk models calculated using a combination of electron scattering and Kramers' opacities. Some important trends include the dependence of disk thickness of the accretion rate (η , relative to the Eddington rate), and the tendency of disks to become gravitationally unstable at large radii.

κ becomes constant as a function of r/r_g . It just so happens that for these disk parameters, radiation pressure becomes significant at around the same disk radii where scattering opacity begins to dominate, so the opacity appears approximately constant throughout. When M_\bullet is held fixed however, the dependence of κ on \dot{M} becomes evident.

Because T_{eff} is effectively determined by \dot{M} and Ω , and in the optically thick limit $T = T_{\text{eff}}\tau^{1/4}$, the variation of the temperature from model to model is fairly mild. In the gas pressure-dominated, Kramers' opacity case, the disk aspect ratio (H/r) is only weakly dependent on parameters such as the SMBH mass and accretion rate, varying as $H/r \propto \dot{M}^{3/20} M_\bullet^{-3/8} r^{1/8}$ (e.g., Frank et al., 2002). In the highest-temperature limit, where the opacity is dominated by electron scattering and radiation pressure dominates, the system of equations (2.24, 2.25, 2.26, 2.28, 2.30, 2.31) is straightforward to solve algebraically, leading to $H \propto \dot{M}$; this then causes the disk aspect ratio to be constant as a function of M_\bullet while holding η fixed and $H/r \propto \eta$ at constant M_\bullet .¹⁷

At small radii, the dynamical timescale is very short and disks are universally Toomre stable. At larger radii however, the dynamical timescale becomes longer (at a faster rate than the free-fall timescale), and the disks become gravitationally unstable (a feature first explored by Kolykhalov & Syunyaev, 1980). In the gas-pressure dominated regime, assuming a Kramers' opacity law (which, notably, breaks down around $T \sim 10^4$ K), the gravitational stability parameter scales as $Q \propto M_\bullet^{3/8} \dot{M}^{-11/20} r^{-9/8}$, leading to gravitational instability at large radii. Plots such as the bottom panels of Figure 2.2 may give an unsuspecting viewer the idea that disks become more gravitationally unstable (or, gravitationally unstable over a wider range of radii) as M_\bullet increases. In a sense this is true, but only because I have scaled the radial coordinate proportionally

¹⁷Near the SMBH, especially at higher accretion rates, H/r approaches unity and the “disk” fails to be a disk. In this case, a Polish donut may be more appropriate (e.g., Abramowicz et al., 1978; Abramowicz, 1981; Abramowicz et al., 1980; Paczyński & Wiita, 1980).

to M_{\bullet} ; at a fixed radial location (in, say cm or pc), Q increases with M_{\bullet} . Other approaches to gravitationally unstable disks will be dealt with in the later sections of this chapter, but first we will examine these standard disk models when computed using more realistic, tabulated opacities, shown in Figure 2.3.

Many qualitative aspects of disk models using more realistic opacities are similar to those using simplified opacities: disks still become gravitationally unstable at large radii, disks tend to be thicker (in the sense of having a larger aspect ratio) at higher Eddington fractions (η), temperature remains a weak function of SMBH mass and Eddington fraction, etc. However, as the disk reaches temperatures of $\sim 10^4$ K, opacities plummet as atomic opacities become negligible but dust is yet sublimated. These sharp drops in opacity, by $\sim 2 - 3$ orders of magnitude, correspond to sharp changes in other disk parameters. Fundamentally, the effective temperature of the disk as a function of radius is set by Equation 2.24 and the related disk temperature varies fairly weakly with optical depth. Since $c_s^2 \rho H$ is also determined as a function of radius by Equation 2.27, the density and scale height must adjust much more so than the temperature in order to satisfy the system of equations. This results in sharp spikes and dips in H/r and ρ in regions where κ changes very sharply.¹⁸

¹⁸This of course begs the question of whether such features should be taken seriously. They are still, of course, valid solutions the equations derived earlier, under assumptions such as vertical isothermality. However, as mentioned earlier, one must wonder if the assumption of local vertical heat transport remains valid in the presence of such strong opacity gradients. If taken seriously, these sorts of features can imply regions of the disk where resonant torques can trap stellar-mass objects (e.g., [Bellovary et al., 2016](#)).

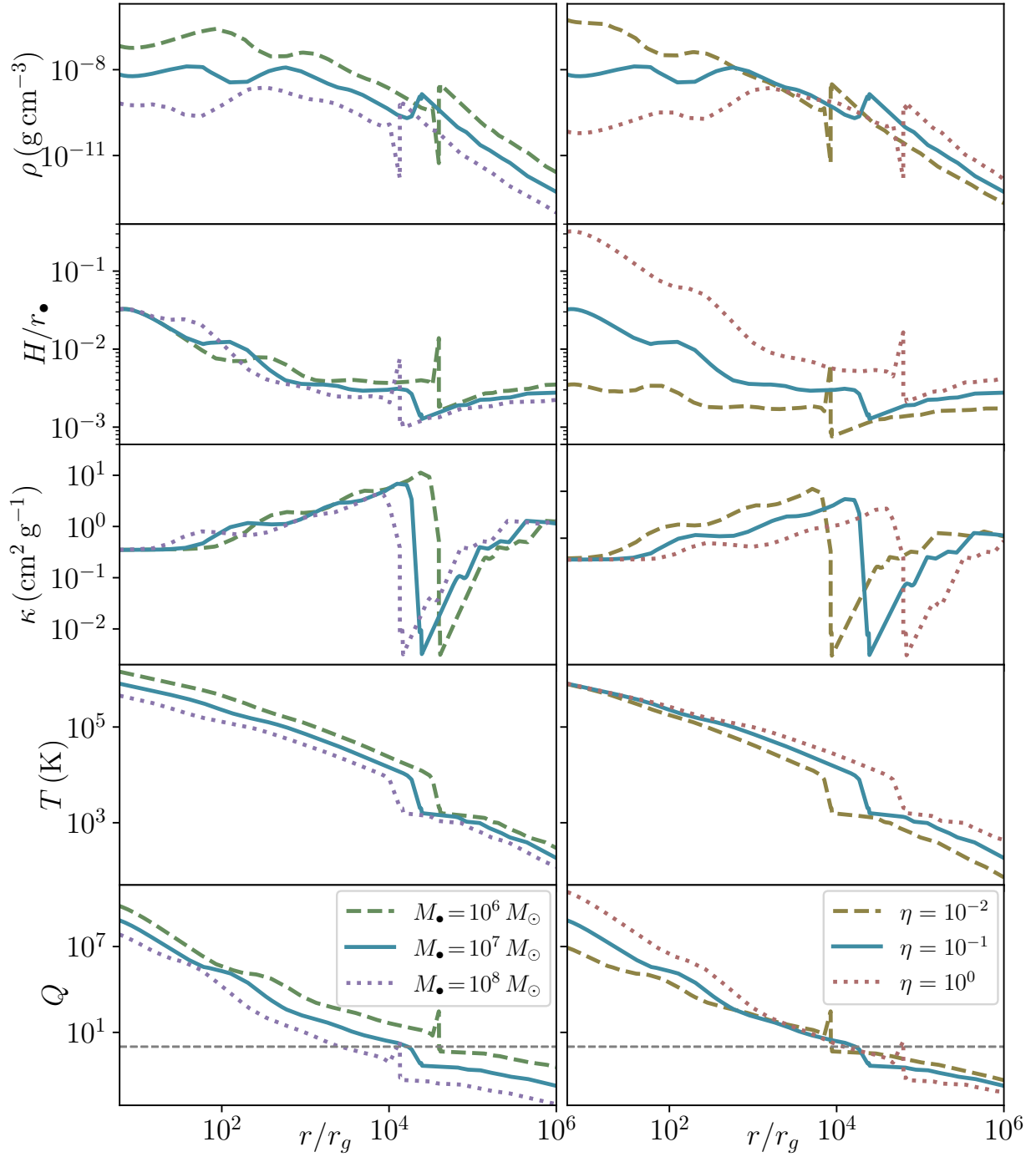


Figure 2.3: Disk models using the tabulated opacities from [Zhu et al. \(2021\)](#). Sharp variations in the opacity as a function of temperature lead to sharp variations in disk thickness and density, along with more subdued (but similarly sharp) changes in temperature.

2.3 Star-Forming Accretion Disks

Disks with vast regions satisfying $Q \ll 1$ should not last long. Simulations also confirm this analytical prediction (e.g., [Nayakshin et al., 2007](#); [Rice et al., 2005](#)).¹⁹ Thus, if one would like to construct a disk model for the purpose of comparing to observations, or any sort of steady-state disk, the disk ought to be gravitationally stable throughout.

One model for marginally stable (or better) disks was developed in [Sirko & Goodman \(2003\)](#), invoking an additional source of heating within the disk in order to maintain at least marginal gravitational stability, presumably from a population of stars formed within the disk during some unstable transient epoch. A later study took things one step further, self-consistently adjusting the (gas) accretion rate through the disk based on the amount of gas consumed during star formation, and tracking the feedback from star formation through both radiation pressure and shocks and its effect on disk structure, attempting to construct a unified model of accretion disks from a nuclear starburst down to an SMBH ([Thompson et al., 2005](#)). My own work, which will be discussed in more detail in Section 2.4 built upon the models presented in [Thompson et al. \(2005\)](#) with the additional consideration that feedback from accretion onto embedded stellar-mass black holes could be more important than feedback from a stellar population, with the addition

¹⁹Somewhat more rigorously, $Q < 1$ is a necessary but not sufficient condition for star formation. Gravitationally unstable gas may become turbulent, generate spiral arms, form stars, or some combination of the above. A convenient criterion for gravitational collapse was proposed by [Gammie \(2001\)](#), which argued that when the dynamical timescale is shorter than the characteristic cooling timescale, the unstable gas can settle into a gravitoturbulent state, as the collapse of any given clump is terminated by some interaction or another; on the other hand, if the cooling timescale is sufficiently short, then the disk may continue to collapse, eventually fragmenting into bound objects. This certainly works well as a rule of thumb, but has led to some confusion. Specifically, the cooling timescale and dynamical timescale are not fundamentally physically meaningful to the problem, but rather the heating rate (which likely scales inversely to the dynamical timescale, to a good approximation) and the cooling rate. Furthermore, because the cooling timescale is typically defined along the lines of the ratio of the thermal energy of the fluid to the cooling rate, defining stability criteria in terms of timescales leads to disparate results for radiation pressure vs gas pressure dominated fluids (e.g., [Chen et al., 2023](#)).

of slightly more realistic opacities.²⁰ More recently, models have been developed which more consistently model the stellar and black hole populations along side the gas disk, in addition to taking into account the finite extent over which embedded objects are able to inject energy (Gilbaum & Stone, 2022), although I will not discuss these models further within this thesis. Some example modified disk models are collected in Figure 2.4.

Essentially, these models trade the assumption that energy balance is determined by local viscous dissipation and then radiated away, relating T_{eff} directly to \dot{M} and Ω , for one instead determining

$$\rho = \frac{\Omega^2}{2\pi G Q_{\text{crit}}} \quad (2.39)$$

for some fiducial $Q_{\text{crit}} \sim 1$. This makes the density very well behaved in the marginally stable region, but makes the temperature evolution of the disk less trivial. Qualitatively, these models inject additional energy into the disk, which increases the local temperature and sound speed relative to a “standard” accretion disk model, causing these models to have much larger aspect ratios at large radii than standard disks. If extrapolated to large enough distances, these disk models can quickly violate the “disk” assumption integral to these models.

Because the optical depths in these models can potentially drop below unity at temperatures where dust sublimates, these models use some form of Equation 2.20 to relate the physical and effective temperatures, give or take a factor of 2. In practice, these models are essentially equivalent to those presented in Section 2.2.1 in the inner regions of the disk where $Q > Q_{\text{crit}}$.

In the outer unstable regions, Sirko & Goodman (2003) simply replaced Equation (2.24) with

²⁰Thompson et al. (2005) used the tabulated dust opacities from Semenov et al. (2003), but above $T \gtrsim 10^4$ K switched immediately to a pure electron scattering opacity, with no atomic opacities in between.

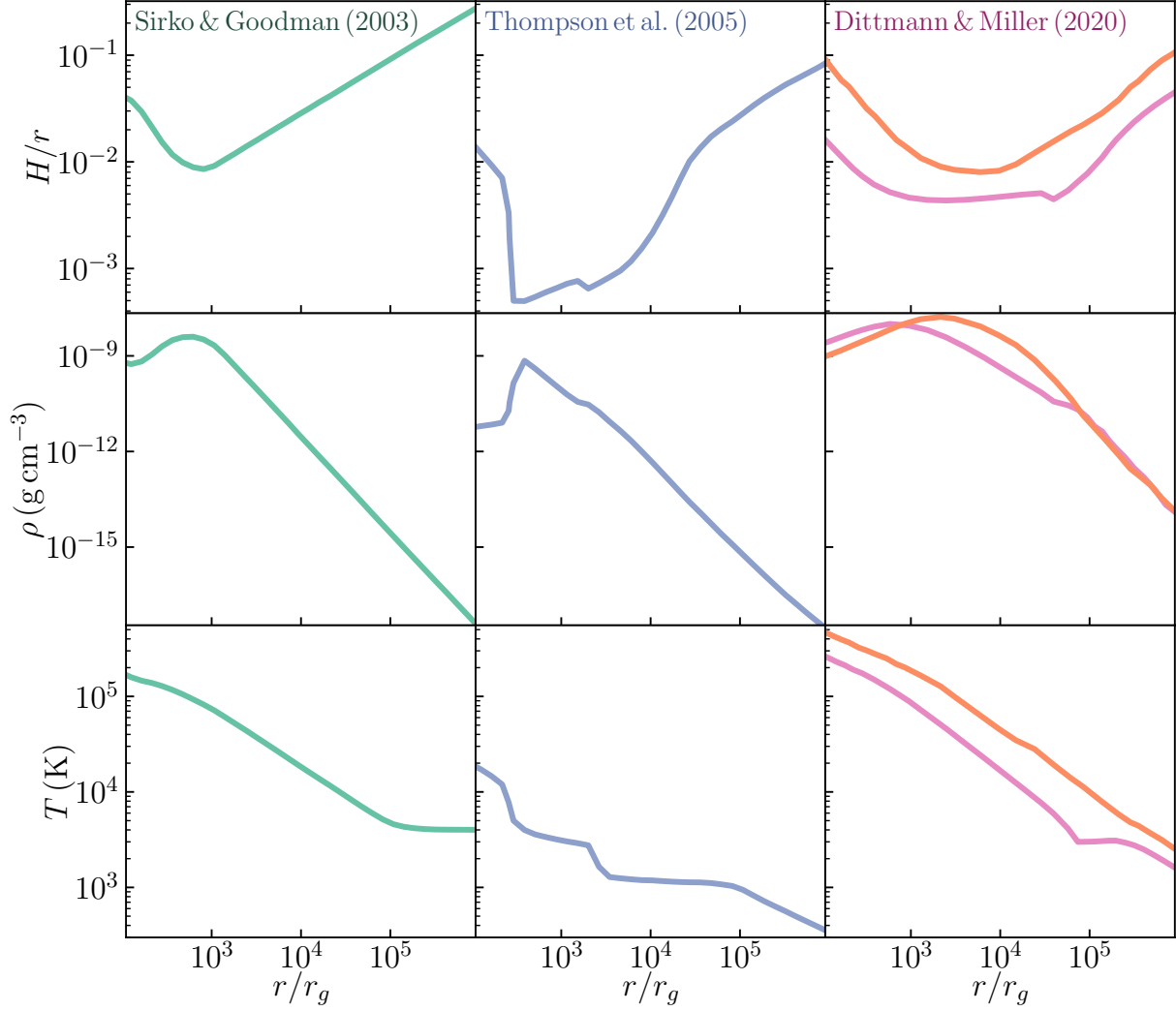


Figure 2.4: Four example AGN disk models, adopting various strategies for maintaining $Q > 1$: the left and center panels display AGN disk models (those of [Sirko & Goodman \(2003\)](#) and [Thompson et al. \(2005\)](#) respectively) around $M_{\bullet} = 10^8 M_{\odot}$ SMBHs computed in [Bellovary et al. \(2016\)](#); and the right column displays models for disks around $4 \times 10^6 M_{\odot}$ SMBHs computed in [Dittmann & Miller \(2020\)](#), based on [Thompson et al. \(2005\)](#) but making different assumptions about feedback and gas opacity. This figure has been adapted from [Dempsey et al. \(2022\)](#) and [Dittmann et al. \(2024a\)](#).

Equation (2.39),²¹ and used a modified radiation pressure, applicable in optically thin regions:

$$P = \frac{\rho k T}{\mu} + \frac{\tau a}{8} T_{\text{eff}}^4. \quad (2.40)$$

Thompson et al. (2005) take things a step or two further, introducing an additional pressure term

$$P = \frac{\rho k T}{\mu} + \frac{\tau a}{4} T_{\text{eff}}^4 + \epsilon \dot{\Sigma}_* c \left(\frac{1}{2} \tau + \xi \right), \quad (2.41)$$

where ϵ is the efficiency with which star formation transforms rest mass into energy for feedback (Thompson et al. (2005) uses $\epsilon = 0.001$, assuming a Salpeter initial mass function), $\dot{\Sigma}_*$ is the star formation rate surface density, and $\xi \sim 1$ characterizes kinetic feedback, i.e. that from supernovae. Their final equation relates the star formation rate to the accretion rate through the disk, $\dot{M}(r)$:

$$\dot{M}(r) = \dot{M}_{\text{out}} - \int_{R_{\text{out}}}^r 2\pi r' \dot{\Sigma}_* dr'. \quad (2.42)$$

One major consequence of this model is that when the optical depth is low (as it is in the range of temperatures over which dust sublimates) a great amount of star formation is necessary to support the disk, which can often transform a great majority of the accretion rate at large distances (\dot{M}_{out}) into stars, leaving a potentially very sub-Eddington accretion flow in the gravitationally stable region near the black hole. Another minor addition to the models presented in Thompson

²¹Sirko & Goodman (2003) also consider a variation of these disk models that is thermally stable in its innermost regions, taking the viscosity to be proportional to the gas pressure in addition to the radiation pressure, in addition to standard models making use of the total pressure.

²²In their Appendix C, Thompson et al. (2005) leave out the standard radiation pressure term, although judging from their 6th figure it appears to have been used in their calculations.

²³Thompson et al. (2005) also consider a disk model variation, with starburst galaxies in mind more than AGN disks, assuming a phenomenological inflow model inspired by globally-driven angular momentum transport, such as that by stellar bars or spiral waves. This alternative model replaces Equation (2.27) with an assumption of inflow at a constant radial Mach number.

et al. (2005), because they were designed to apply to much larger scales, further from the SMBH, is the consideration of a non-Keplerian potential, leading to an angular velocity along the lines of $\Omega^2 = GM_{\bullet}r^{-3} + 2\sigma^2r^{-2}$, to accommodate the gravitational influence of a dark matter halo or stellar bulge. Now, with these models introduced, we are prepared to consider star formation in AGN disks and SMBH growth.

2.4 Star Formation in Accretion Disks and SMBH Growth

This section reviews my application of the previously developed disk models to the problem of the rapid growth of some rare supermassive black holes at high redshifts, originally presented in [Dittmann & Miller \(2020\)](#).

2.4.1 The Premise

As discussed earlier, accretion disks around active galactic nuclei are potentially unstable to star formation at large radii. When the compact objects formed from some of these stars spiral into the central supermassive black hole, there is no radiative feedback and therefore the accretion rate is not limited by radiation forces. Using a set of accretion disk models, we calculated the gas and compact object accretion rate onto the central supermassive black hole. We found that the timescale for a supermassive black hole to double in mass can decrease by factors ranging from ~ 0.7 to as low as ~ 0.1 in extreme cases, compared to gas accretion alone. These results suggest that the formation of extremely massive black holes at high redshift (some reaching masses $M_{\bullet} \gtrsim 10^9 M_{\odot}$ at redshifts $z \gtrsim 7$ (e.g., [Mortlock et al., 2011](#))) may occur without prolonged super-Eddington gas accretion (e.g., [Toyouchi et al., 2019](#)) or very massive seed black

holes (e.g., [Begelman et al., 2006](#)).

2.4.2 Methods

2.4.2.1 Disk Models

As mentioned earlier, the two contribution of [Dittmann & Miller \(2020\)](#) to the disk models themselves were realizing that accretion onto stellar-mass black holes could provide stronger feedback (converting from $\sim 7\%$ to $\sim 40\%$ of the accreted rest mass into energy rather than $\sim 0.1\%$) and improvements to the opacities used by [Thompson et al. \(2005\)](#). I focused on SMBHs with lower masses in an attempt to understand the early growth of supermassive black holes. Because larger fractions of a given accretion disk will be gravitationally stable around less massive black holes, focusing on less massive SMBHs may also be a somewhat conservative approach. The rightmost column of [Figure 2.4](#) provides two examples of these disk models, which used $\dot{M}_{\text{out}} = 4\dot{M}_{\text{Edd}}$, $\epsilon = 0.1$ (the cooler, thinner disk) and $\dot{M}_{\text{out}} = 7\dot{M}_{\text{Edd}}$, $\epsilon = 0.4$ (the hotter, thicker disk). These values of ϵ are appropriate for accretion onto nearly-Schwarzschild black holes and maximally spinning black holes. Within this section, \dot{M}_{Edd} refers to the Eddington-limited accretion rate onto the SMBH with radiative efficiency ϵ_{\bullet} (taken here to be $\epsilon_{\bullet} = 0.1$). In each case, I have used an SMBH mass of $M_{\bullet} = 4 \times 10^6 M_{\odot}$ and used an outer disk radius of 5 pc.

[Figure 2.5](#) highlights a different aspect of these models: how the accretion rate through the disk varies as a function of radius due to star (and black hole) formation. Most importantly, the star formation rate increases dramatically in regions where dust has sublimated, dramatically decreasing the gas accretion rate through the disk. However, as these stars eventually die, the black

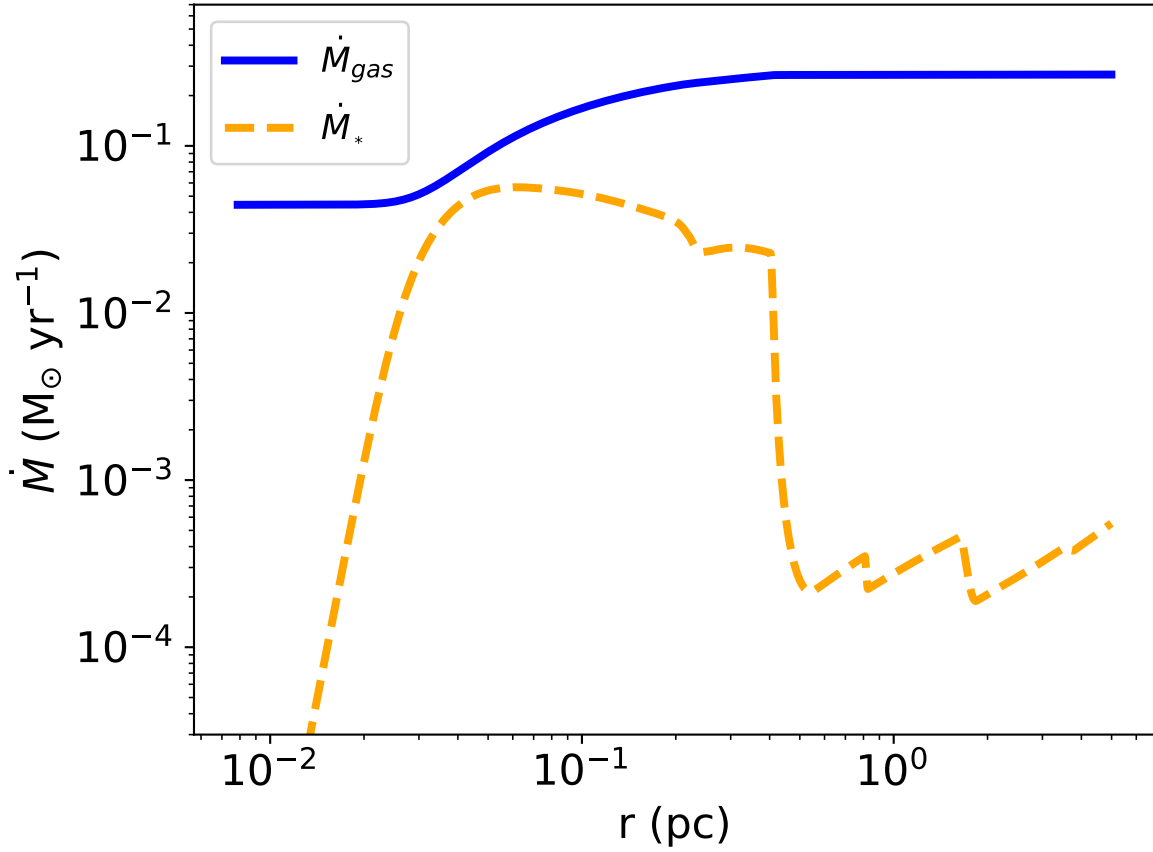


Figure 2.5: The gas accretion rate through the disk (\dot{M}) in blue, and the star formation rate in orange ($\dot{M}_{*} \equiv \pi r^2 \dot{\Sigma}_{*}$). As dust sublimates and the optical depth of the disk plummets, a great deal of star formation (or accretion onto embedded stellar-mass black holes) is necessary to support the disk.²⁴ This particular disk model used $\epsilon = 0.4$, $\alpha = 0.05$, and $\dot{M}_{\text{out}} = 3\dot{M}_{\text{Edd}}$.

holes they leave behind might help the SMBH grow without Eddington-limitation. However, the fate of stars formed within the disk is far from certain, and some studies have suggested that the migration of stars and black holes through AGN disks could stall at certain radii (e.g., [Bellovary et al., 2016](#)). These topics are explored in Sections [2.4.2.2](#) and [2.4.2.3](#) respectively.

2.4.2.2 Star Formation

In this study, short of simulating stellar evolution in AGN disks, we instead analytically estimated what sorts of stars might form within AGN disks and how they might end their lives. The first task was to estimate the masses of stars formed within the disk, as the disk fragments due to its gravitational instability and short cooling timescale. The initial mass of fragments in the disk can be roughly approximated roughly by the Jeans mass, $M_J \sim c_s^3 \rho^{-1/2}$. If cooling is efficient then as the initial fragments collapse $c_s^3 \rho^{-1/2}$ gradually decreases. As long as the thermal adjustment timescale is shorter than the free fall timescale for the fragment, the collapse remains approximately isothermal. Because density increases during collapse and the sound speed can be approximated at low temperatures by $c_s^2 = k_b T / \mu$, one expects each clump to fragment repeatedly until the assumption of isothermal collapse breaks down.

To make a rough estimate of the final fragment masses in our disk models, we applied the result of [Low & Lynden-Bell \(1976\)](#), which developed an approximation for when collapse should cease to be isothermal and the corresponding final fragment masses. The minimum Jeans mass can then be approximated by

$$M_{\text{frag}} \approx 1.54 \times 10^{-3} T_b^2 \frac{\kappa_f}{\kappa_0} M_{\odot}, \quad (2.43)$$

where κ_0 is the electron scattering opacity, κ_f is the final opacity of the fragment, and T_b is the effective temperature of the disk in Kelvin. This was appropriate for our disk models because fragments will be bathed in thermal radiation from the disk, and the disks in our models are optically thick to their own radiation. In the regions of our disks where we expect star formation, temperatures are typically between 100 and 1000 K and opacities only vary by factors of order unity. Accordingly, we assumed that κ_f is the same as the initial opacity before collapse. For the disk models here, typical fragment masses can range from hundreds to thousands of solar masses (see Figure 2.6).

As I will discuss in Section 2.4.2.3, the initial masses of stars formed within the disk are small enough that the stars themselves do not strongly affect the global disk structure. For simplicity, we assumed that accretion occurred in a spherically symmetric fashion, at a rate given by Bondi (1952):

$$\dot{M}_B \equiv \pi \rho G^2 m^2 / c_s^3, \quad (2.44)$$

for an accreting object of mass m .²⁵ The factor of m^2 essentially follows from the characteristic length scale at which the sound speed is comparable to the escape velocity from the object. Thus, if radiation pressure from the central object helps to counteract gravity, the accretion rate onto the star ($\dot{M}_{B,*}$) will be decreased according to

$$\dot{M}_{B,*} = \pi \rho G^2 m^2 (1 - \Gamma)^2 / c_s^3, \quad (2.45)$$

defining $\Gamma \equiv L_*/L_{\text{Edd}}$, where L_* is the stellar luminosity and the Eddington luminosity was

²⁵In reality, the accretion rate will decrease as the region of the star's gravitational influence becomes comparable to the scale height of the disk. The consequences of this variation in accretion rate is explored in Chapter 3.

approximated as $L_{\text{Edd}} \approx 1.3 \times 10^{38} (m/M_{\odot}) \text{ erg s}^{-1}$.

Massive stars are known to lose mass via winds (\dot{M}_w), which we approximated by the rate

$$\log(\dot{M}_w) \approx 1.738 \log(L_*) - 1.352 \log(T_{\text{eff}}) - 9.547, \quad (2.46)$$

empirically calibrated to O stars in [Lamers & Leitherer \(1993\)](#). We further employed the approximate expressions for $(1 - \Gamma)$, L/L_{\odot} , and T_{eff} from [Bond et al. \(1984\)](#) for Population I and II stars with masses between $\sim 100 M_{\odot}$ and $\sim 10^3 M_{\odot}$ to derive an approximate mass loss rate of

$$\dot{M}_W \approx 3.1 \times 10^{-10} \left(\frac{m}{M_{\odot}} \right)^{2.1} M_{\odot} \text{ yr}^{-1}. \quad (2.47)$$

Because this depends on mass more strongly than $\propto m^2$, and $1 - \Gamma$ decreases as the stellar mass increases, there is a well-defined equilibrium mass between this mass-loss rate (2.47) and the radiation-reduced Bondi accretion rate (2.45), which is plotted in [Figure 2.6](#) as M_{Bondi} . Qualitatively, this steady-state balance between accretion and mass loss seems to agree fairly well with stellar evolution simulations (e.g., [Cantiello et al., 2021](#); [Dittmann et al., 2021](#)) in the high-accretion-rate limit (to be discussed further in [Chapter 3](#)). We also argued, based on the analytical result from [Maeder & Meynet \(2000\)](#) that mass loss rates can become catastrophically large for stars with moderate rotation rates and $\Gamma \gtrsim 0.64$, that stars were likely limited to $m \approx 400 M_{\odot}$, using the expressions for Γ from [Bond et al. \(1984\)](#). We also assumed that stars would expire after lifetimes characteristic of such massive stars, a few Myr or so depending on their mass, implicitly assuming that the accretion onto and winds driven from the surface of the star would not affect their cores.

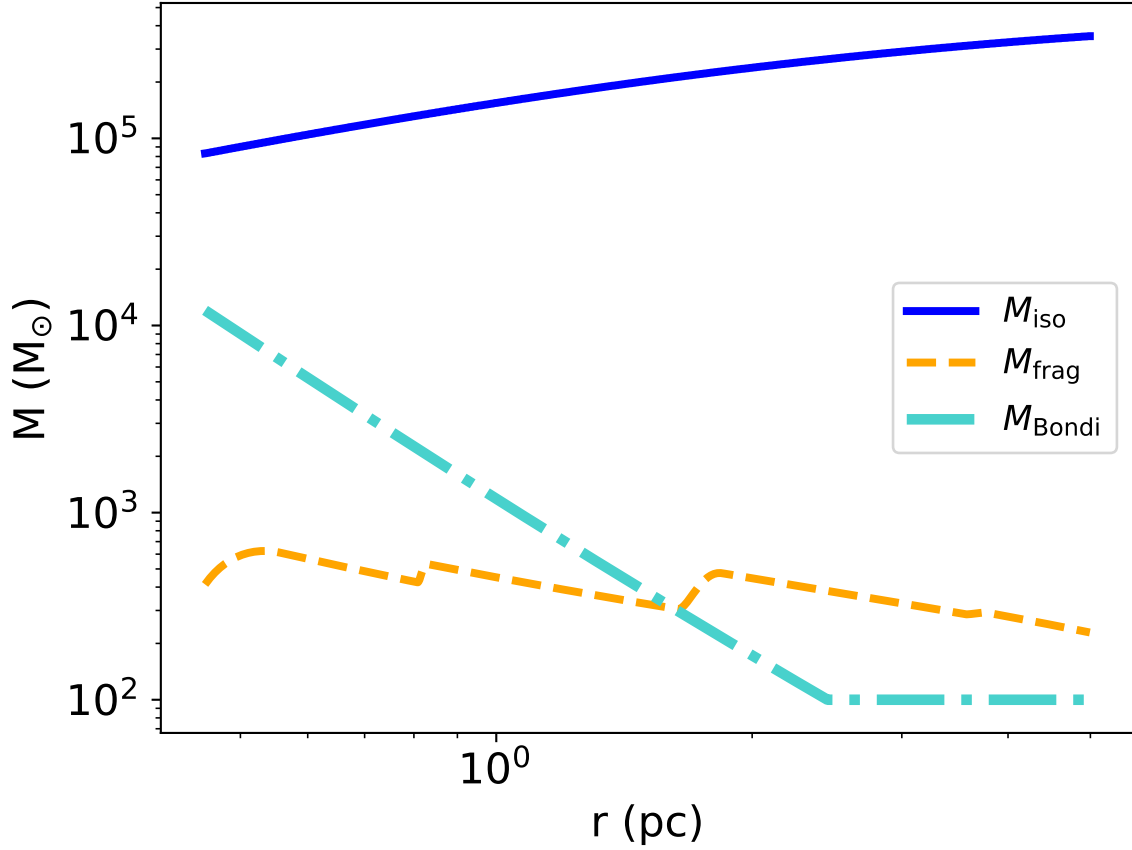


Figure 2.6: Some characteristic masses within the star-forming region of a disk model calculated using $\epsilon = 0.4$, $\alpha = 0.05$, and $\dot{M}_{\text{out}} = 3\dot{M}_{\text{Edd}}$, exterior to the dust sublimation region. M_{frag} is the characteristic mass of a fragment after gravitational collapse, given by Equation (2.43). M_{Bondi} is an estimate of the equilibrium mass reached by balancing a mass loss estimate for massive stars with a radiation-moderated (spherically symmetric) estimate of the accretion rate onto an embedded star. M_{iso} is the so-called “isolation mass,” at which embedded objects would begin to strongly disrupt the accretion disk.

2.4.2.3 Migration

Considering that stars and black holes embedded within AGN disks are likely to have masses from $\sim 10 M_{\odot}$ to $\sim 10^3 M_{\odot}$, and that the objects central to these disks have masses $M_{\bullet} \gtrsim 10^6 M_{\odot}$, from a birds-eye view the interactions between these embedded stars and black holes can be quite similar to planets. The first order of business was to determine how strongly the embedded objects gravitationally affect the AGN disk, and to this end we drew upon [Baruteau et al. \(2011\)](#).²⁶ Qualitatively, if the waves generated by the disk become sufficiently strong, they can clear open a gap in the disk, potentially reducing the accretion rate onto the planet to a significant degree; this occurs when the gravitational sphere of influence of the planet becomes comparable to (or exceeds) the scale height of the disk, or $H \lesssim r(q/3)^{1/3}$, where $q \equiv m/M_{\bullet}$. However, viscous spreading may cause this gap to close, resulting in a criterion for gap opening given by $g \lesssim 1$, where

$$g \equiv \frac{3}{4} \frac{H}{r} \left(\frac{q}{3}\right)^{-1/3} + 50 \frac{\alpha}{q} \left(\frac{H}{r}\right)^2. \quad (2.48)$$

Solving for m under the condition that $g = 1$ served to estimate the limiting mass for embedded stars and black holes above which they would open gaps in the disk, the so-called “isolation mass,” which is plotted in [Figure 2.6](#). The typical masses of objects embedded in AGN disks will often be below this limit, and the background disk will not be too disturbed by their presence.

In this limit, the average torque on an embedded object due to Lindblad and corotation

²⁶Although I did not realize it at the time, the first part of this treatment is unnecessary. The first term in Equation (2.48) is redundant (e.g., [Rafikov, 2002](#)). Rather, a sufficient condition can be derived by balancing the angular momentum flux due to propagating spiral density waves with the viscous angular momentum flux through the disk (e.g., [Lin & Papaloizou, 1986](#)). This results in a simpler criterion for gap opening, $q \gtrsim 5\alpha^{1/2}(H/r)^{5/2}$, which has been confirmed by hydrodynamic simulations (as pointed out by [Duffell & MacFadyen, 2013](#); [Kanagawa et al., 2015](#)).

resonances is, following [Paardekooper et al. \(2010\)](#),

$$\frac{\Gamma_{\text{iso}}}{\Gamma_0} = 1.1\psi - 0.9\beta - \delta - 2.5, \quad (2.49)$$

where

$$\psi \equiv -\frac{d \ln \Omega}{d \ln r}, \beta \equiv -\frac{d \ln T}{d \ln r}, \delta \equiv -\frac{d \ln \Sigma}{d \ln r}, \quad (2.50)$$

and $\Gamma_0 = (q/H)^2 \Sigma r^4 \Omega^2$. Largely due to the corotation torques, this can potentially result in outward migration over certain ranges of radii, as pointed out in [Bellovary et al. \(2016\)](#); [Lyra et al. \(2010\)](#).²⁷ However, gaseous torques are not the only things affecting the orbital evolution of embedded objects.

Gravitational waves, particularly at smaller radii near the central SMBH, can also play a crucial role in the evolution of orbiting objects. The leading-order post-Newtonian approximation is sufficient through nearly all of the disk, yielding a average torque (for objects on circular orbits) of ([Peters, 1964](#))

$$\Gamma_{\text{GW}} = -\frac{32}{5} \frac{G^{7/2} m^2 M_{\bullet}^2 (m + M_{\bullet})^{1/2}}{c^5 r^{7/2}}. \quad (2.51)$$

With this term included, the torque on migrating objects is negative throughout the entirety of each disk model I calculated, leading to unhindered inspiral towards the SMBH. Given that the angular momentum of an embedded object is $J = m\sqrt{GM_{\bullet}r}$, the rate of inspiral is then $\dot{r} = 2(\Gamma_{\text{GW}} + \Gamma_{\text{iso}})r/J$. We used this to calculate the migration timescale from the inner edge of each

²⁷This torque was derived under the assumption of a locally isothermal disk (i.e. $T = T(r)$). To be precise, we followed [Lyra et al. \(2010\)](#), interpolating between the locally isothermal and adiabatic limits based on the cooling timescale, although this was sufficiently short that the torques were essentially isothermal.

disk's gravitationally stable region as a function of mass, $\tau_m = \int \dot{r}^{-1} dr$. Having established that objects formed within these disks ought to march inexorably inwards, we are now a position to explore their influence on SMBH growth.

2.4.3 Results

As a reminder, the characteristic e-folding timescale for an SMBH accreting at an Eddington-limited rate, converting a fraction ϵ_\bullet of the accreted rest mass into energy, is $\tau \approx 4.5 \times 10^7 (\epsilon_\bullet / 0.1)$ yr. Assuming the first stars were born, subsequently expiring and leaving behind black holes, around a redshift of $z \sim 20$, in the ~ 500 Myr between $z \sim 20$ and $z \sim 7$ an Eddington-limited growth factor of only $\sim 6 \times 10^4$ could be achieved, requiring something along the lines of prolonged super-Eddington accretion, creating an SMBH of mass $M_\bullet \sim 10^4$ by $z \sim 20$, or a substantial number of black hole mergers in order to grow SMBHs to the masses inferred by some observations of high-redshift quasars (e.g., [Mortlock et al., 2011](#)). Physically, black holes descendant from stars formed within AGN disks migrating towards the SMBH and eventually merging presents a solution to this problem in the form of a large number of mergers. However, since the stellar-mass black holes formed from the accretion disk in the first place, this process can also be framed in terms of a reduced effective accretion efficiency.

One way to quantify the effective radiative efficiency is through the fraction of the accreted material that emits photons,

$$\Delta \equiv \frac{\min(\dot{M}_{\text{gas}}, \dot{M}_{\text{Edd}})}{\min(\dot{M}_{\text{gas}}, \dot{M}_{\text{Edd}}) + \dot{M}_{\text{BH}}}. \quad (2.52)$$

These values, along with the migration timescale for a $100 M_\odot$ embedded object, characteristic

ϵ	α	$\dot{M}_{\text{out}}/\dot{M}_{\text{Edd}}$	$M_{\text{frag}}/M_{\odot}$	τ_{100}/Myr	$\dot{M}_{\text{gas}}/\dot{M}_{\text{Edd}}$	$\dot{M}_{\text{bh}}/\dot{M}_{\text{Edd}}$	Δ
0.4	0.02	7.0	435.85	31.51	1.29	5.71	0.15
0.4	0.05	3.5	405.59	18.73	0.79	2.71	0.23
0.4	0.05	3.0	402.16	17.06	0.50	2.50	0.17
0.4	0.10	2.0	379.02	12.52	0.55	1.45	0.28
0.1	0.20	4.0	379.26	11.81	0.24	3.76	0.06
0.1	0.25	2.0	360.88	8.91	0.26	1.74	0.13
0.1	0.30	1.5	351.90	7.94	0.31	1.19	0.21
0.1	0.30	3.0	364.97	10.51	0.45	2.55	0.15

Table 2.1: Results for each model: ϵ is the efficiency parameter. α is the model viscosity parameter. \dot{M}_{out} is the gas accretion rate used as a boundary condition for the model at 5 pc. M_{frag} is the median fragment mass, using Equation (2.43), in the unstable region of the disk, save for the dust sublimation region. τ_{100} is the migration timescale for $m = 100 M_{\odot}$ objects. \dot{M}_{gas} is the gas accretion rate onto the central SMBH. \dot{M}_{bh} is the accretion rate, in black holes, onto the central SMBH. Δ is the fraction of the total Eddington-limited accretion rate comprised by gas.

fragment mass in the gravitationally unstable region, and the gas and compact object accretion rates onto the SMBH, are provided in Table 2.1, along with the parameters defining each disk model.

Qualitatively, Table 2.1 indicates that star-forming accretion disks have the potential to grow SMBHs in the early universe quite rapidly. Taking the most conservative model computed here as an example, that computed using $\epsilon = 0.4$, $\alpha = 0.1$, it could be possible for an SMBH to grow from $10^6 M_{\odot}$ to $10^9 M_{\odot}$ in only ~ 155 Myr,²⁸ while accreting gas at only $\sim 50\%$ of the Eddington-limited rate. If we assume Eddington-limited gas accretion (at $\epsilon_{\bullet} \sim 0.1$) for the first ~ 345 Myr, the overall growth factor would reach $\sim 2 \times 10^6$. Other models, such as the $\epsilon = 0.1$, $\alpha = 0.2$ model could result in growth factors over the same timeframe on the order of $\gtrsim 10^7$, easily facilitating the existence of $\sim 10^9 M_{\odot}$ SMBH by $z \sim 7$.

These models can also be used to make a rough estimate of the number of extreme mass

²⁸At lower SMBH masses, the mass ratio between embedded objects and the SMBH will be larger, making gap opening far more common and slowing migration. Additionally, lower-mass black holes will tend to have fractionally smaller gravitationally unstable regions. Thus, key model assumption break down at lower M_{\bullet} , and $10^6 M_{\odot}$ is a reasonably conservative lower limit for the applicability of these results.

ratio inspirals (EMRIs) that may be begotten by AGN disks. Dividing \dot{M}_{BH} by a characteristic migrating black hole mass, $m \sim 500 M_{\odot}$ for example, suggests $\sim 10^{-4}$ EMRIs per AGN per year, potentially detectable by future space-based gravitational wave detectors such as Taiji (e.g., [Hu & Wu, 2017](#); [Ruan et al., 2020](#)), TianQin (e.g., [Luo et al., 2016](#); [Wang et al., 2019](#)), and the Laser Interferometer Space Antenna (e.g., [Amaro-Seoane et al., 2017](#); [Robson et al., 2019](#)). Of course, this is something of an upper limit on the rate, since only a small fraction of these AGN will be sufficiently close for the mergers to emit distinguishable signals. Other, more focused works, have made similar predictions (e.g., [Derdzinski & Mayer, 2023](#); [Sigl et al., 2007](#)).

Beyond just the limitations intrinsic to steady-state disk models, this work had a few other major limitations. These included its treatment of stellar evolution, patching together various semi-analytical and empirical estimates; this is explored in more detail in Chapter 3. Another major uncertainty of this work was what might happen as multiple embedded objects mutually interact within the disk and each other, which was largely glossed over, assuming that black holes either merge or scatter as they approach one another maintaining a constant time-averaged accretion rate through the disk; some portion of this will be dealt with in Chapter 4, which deals with whether or not binary hole binaries formed within the disk are driven towards coalescence by hydrodynamical interactions with their surroundings.

Chapter 3: Stellar Evolution in AGN Disks

As discussed in Chapter 1, the disks of gas orbiting about and accreting onto SMBHs are expected both to form stars in situ and to capture stars from surrounding stellar clusters. Chapter 2, section 2.4.2.2 made a few semi-analytical estimates about the characteristic masses of stars formed within AGN disks based on studies of standard stellar evolution — that is to say of stars situated within the interstellar medium rather than within a dense accretion disk. Although some thought had been devoted to how stars orbiting near an SMBH might be affected by the strong radiation incident upon their surfaces (Tout et al., 1989),¹ the study of stellar evolution within AGN disks began only very recently (Ali-Dib & Lin, 2023; Cantiello et al., 2021; Dittmann et al., 2021, 2023a; Jermyn et al., 2021). In Section 3.1 I will review a few standard results in stellar evolution that will be particularly important for understanding stellar evolution in AGN disks. Afterwards, within Section 3.2 I will discuss some of the methods used to simulate stellar evolution within AGN disks, particularly the modifications made to standard stellar evolution codes. Finally, I will review our results in chapter 3.3.

¹Østby et al. (2000) comes to mind.

3.1 Introduction

In reviewing these standard analytical results, I have relied on [Kippenhahn & Weigert \(1990\)](#).

3.1.1 Timescales

Few even remotely pedagogical discussions of stellar evolution can go without a discussion of the relevant timescales, and this is no exception. Even better, it turns out that these will be crucial for understanding the outcomes of stellar evolution in AGN disks as well, as we will see in [Section 3.3](#).

Over the course of an average star's lifetime, it will change in mass very little, but change quite appreciably in radius. This consideration, along with the near-spherical nature of most stars, makes it convenient to chart the interior structure of stars in terms of mass rather than radius. For example, a derivative in radius can be substituted for a derivative in mass as $dm = 4\pi r^2 \rho dr$. The equation of motion for a given shell can be expressed as

$$\frac{1}{4\pi r^2} \frac{\partial^2 r}{\partial t^2} = -\frac{\partial P}{\partial m} - \frac{Gm}{4\pi r^4}, \quad (3.1)$$

where the first term on the right-hand side represents forces due to pressure gradients and the second term represents the gravitational pull of material within the shell. Hydrostatic equilibrium is satisfied when the acceleration vanishes, yielding

$$\frac{\partial P}{\partial m} = -\frac{Gm}{4\pi r^4}. \quad (3.2)$$

If we drop the pressure term in Equation (3.1), a characteristic timescale for collapse can be defined through $|\partial^2 r / \partial t^2| = R/t_{\text{ff}}^2$, leading to $t_{\text{ff}} \approx \sqrt{r^3/Gm} \approx 1/\sqrt{G\bar{\rho}}$, where $\bar{\rho}$ is the average density of the star within radius r . A characteristic explosive timescale can be defined by dropping the gravitational term, resulting in $t_{\text{exp}} \approx R\sqrt{\rho/P} \approx R/\bar{c}_s$, roughly the sound crossing time at some average sound speed \bar{c}_s . If the star is near hydrostatic equilibrium, these timescales will be roughly equal in magnitude, and can be characterized as a “hydrostatic” or “dynamical” timescale, on which deviations from hydrostatic equilibrium will be resolved by gravitational or acoustic adjustment. For concreteness,

$$t_{\text{dyn}} \approx \frac{1}{\sqrt{G\bar{\rho}}}, \quad (3.3)$$

and to use the surface of the Sun as an example, $t_{\text{dyn},\odot} \approx \sqrt{4r_{\odot}^3 G^{-1} M_{\odot}^{-1}} \approx 3200$ s.

Considering bodies in hydrostatic equilibrium, Equation (3.2) can be integrated from 0 to M , the total mass of the star, to yield

$$\int_0^M \frac{Gm}{r} dm = - \int_0^M 4\pi r^3 \frac{\partial P}{\partial m} dm = - [4\pi r^3 P]_0^M + \int_0^M 12\pi r^2 \frac{\partial r}{\partial m} P dm = 3 \int_0^M \frac{P}{\rho} dm. \quad (3.4)$$

The right-hand side is the gravitational energy of the star,

$$E_g = - \int_0^M \frac{Gm}{r} dm, \quad (3.5)$$

and the left-hand side is proportional the internal energy of the star (assuming here an ideal gas

with constant adiabatic index γ , $P/\rho = (\gamma - 1)u$, where u is the internal energy per unit mass),

$$3 \int_0^M \frac{P}{\rho} dm = 3(\gamma - 1) \int_0^M u dm = 3(\gamma - 1)E_{\text{int}}. \quad (3.6)$$

In this approximation then, $E_g = -3(\gamma - 1)E_{\text{int}}$, and the total energy of the star is

$$E = E_g \left[1 - \frac{1}{3(\gamma - 1)} \right]. \quad (3.7)$$

Crucially, we can use these to estimate a typical timescale for stellar structure to respond to energy losses (into the universe at rate L), according to

$$t_{\text{KH}} = \frac{|E_g|}{L} \approx \frac{GM^2}{2RL}, \quad (3.8)$$

after Hermann von Helmholtz and William Thompson, Baron Kelvin of Largs. Again using the sun as an example, $t_{\text{KH},\odot} \approx 5 \times 10^{14} \text{ s} \approx 1.5 \times 10^7 \text{ yr}$.

Another important timescale, for the time being, is that on which the reservoir of fuel within the star is expended as luminosity. For a fuel supply of mass m_f burnt at efficiency ϵ , the nuclear burning timescale for the star can be expressed as

$$t_{\text{nuc}} \approx \frac{\epsilon m_f c^2}{L}. \quad (3.9)$$

Taking the sun as an example, we can estimate a hydrogen-burning timescale based on the hydrogen mass fraction $X \sim 0.7$ and rest mass-energy released by hydrogen fusion $\epsilon \sim 0.007$, to find $t_{\text{nuc}} \approx 2 \times 10^{18} \text{ s} \approx 7 \times 10^{10} \text{ yr}$. Because only a fraction of the hydrogen within the sun will

reach high enough densities and temperatures to undergo fusion, this overestimates the lifetime of the sun by about a factor of $\sim 7 - 10$.

In most scenarios, $t_{\text{nuc}} \gg t_{\text{KH}} \gg t_{\text{dyn}}$. The relative brevity of the dynamical timescale indicates that most stars should be in, or quite near, hydrostatic equilibrium. Furthermore, structural and compositional changes due to nuclear burning should occur on timescales much longer than those required for a star to thermally adjust to imbalances in energy production or loss.

3.1.2 Simplified Stellar Models

The basic equations describing stellar structure and evolution can be expressed as

$$\frac{dr}{dm} = \frac{1}{4\pi r^2 \rho}, \quad (3.10)$$

$$\frac{dP}{dm} = -\frac{Gm}{4\pi r^4} \quad (3.11)$$

$$\frac{dl}{dm} = \epsilon_{\text{nuc}}(\rho, T, \mathbf{X}), \quad (3.12)$$

$$\frac{dT}{dm} = -\frac{3\kappa}{4acT^3} \frac{l}{16\pi^2 r^4}, \quad (3.13)$$

$$\left\langle \frac{dX_i}{dt} \right\rangle = R_i(\rho, T, \mathbf{X}), \quad (3.14)$$

where in addition to the relations introduced in Section 3.1.1, I've introduced an equation relating the luminosity at a given mass (or equivalently radius) l to the rate of energy (usually) injected at that location by nuclear reactions ϵ_{nuc} ; an equation expressing the temperature gradient through the star in terms of the luminosity, gas opacity κ , and temperature; and the time-averaged rate of creation or consumption of atomic species X_i at rate R_i due to nuclear reactions. These equations are closed by expressions for the opacity, $\kappa = \kappa(\rho, T, \mathbf{X})$ and an equation of state

$$P = P(\rho, T, \mathbf{X}).$$

With a few simple assumptions, it is straightforward to derive a scaling relation or two from the above equations that will be useful for understanding the evolution of stars embedded in AGN disks. First, we can focus on structure alone and neglect the time-evolution of the stellar composition. Furthermore, the equations can be greatly simplified by assuming a constant composition (and mean molecular weight μ), along with the assumption that radiation and degeneracy pressure are negligible. Then, expressing the opacity as $\kappa = \kappa_0 \rho^a T^b$ and the energy generation rate per unit mass as $\epsilon_{\text{nuc}} = q \rho T^n$, the thermal and energetic equations can be rewritten as

$$\frac{dl}{dm} = q \rho T^n, \quad (3.15)$$

$$\frac{dT}{dM} = -\frac{3\kappa_0 \rho^a T^{b-3}}{4ac} \frac{l}{16\pi^2 r^4}. \quad (3.16)$$

The structure equations can then be non-dimensionalized, substituting $m = xM$, $r(m) = f_1(x)R_*$, $P(m) = f_2(x)P_*$, $\rho(m) = f_3(x)\rho_*$, $T(m) = f_4(x)T_*$, and $l(m) = f_5(x)L_*$, in terms of characteristic values at some unspecified location x_* , leading to

$$\frac{df_1}{dx} = \frac{1}{4\pi f_1^2 f_3} \frac{M}{R_*^3 \rho_*}, \quad (3.17)$$

$$\frac{df_2}{dx} = \frac{x}{4\pi f_1^4} \frac{GM^2}{P_* R_*^4}, \quad (3.18)$$

$$\frac{df_4}{dx} = -\frac{3}{64\pi^2} \frac{f_3^a f_4^{b-3} f_5}{f_1^4} \frac{\kappa_0 \rho_*^a T_*^{b-4} L_* M}{ac R_*^4}, \quad (3.19)$$

$$\frac{df_5}{dx} = f_3 f_4^n \frac{q \rho_* T_*^n M}{L_*}, \quad (3.20)$$

$$f_2 = f_3 f_4 \frac{\rho_* k T_*}{\mu P_*}. \quad (3.21)$$

From these, we can read off a few scaling relations,

$$\rho_* \propto \frac{M}{R_*^3}, \quad (3.22)$$

$$P_* \propto \frac{GM^2}{R_*^4}, \quad (3.23)$$

$$L_* \propto \kappa_0 \frac{T_*^{4-b} R_*^4}{M \rho_*^a} \propto \kappa_0 \frac{T_*^{4-b} R_*^{4+3a}}{M^{1+a}}, \quad (3.24)$$

$$L_* \propto q \rho_* T_*^n M \propto q T_*^n \frac{M^2}{R_*^3}, \quad (3.25)$$

$$T_* \propto \mu \frac{P_*}{\rho_*} \propto \mu \frac{M}{R_*}. \quad (3.26)$$

If we assume a constant opacity, setting $a = b = 0$, it is straightforward to find that

$$L_* \propto \mu^4 M^3, \quad (3.27)$$

which will be useful later, and which follows from stars tending to burning slightly hotter as μ increases. After some algebra, one can also arrive at the scaling

$$T_* \propto \mu^{(4-n)/(3+n)} M^{4/(3+n)}, \quad (3.28)$$

where $n \gtrsim 13$ at higher temperatures (burning hydrogen via the CNO cycle). Qualitatively, it follows that massive stars should be dominated by radiation pressure rather than gas pressure, although in that regime the particular scaling relations written out here would break down and require replacement.

3.2 Methods

Although the above considerations will be useful for interpreting certain aspects of stellar evolution, they are far from able to describe the entire life of even an isolated star, let alone one embedded within an AGN disk. To achieve a more complete picture, simulations are necessary. The hierarchy of timescales discussed earlier helps somewhat, as throughout most of a given star's life hydrostatic equilibrium is a valid assumption and following the propagation of shocks or sound waves is unnecessary. However, virtually all stellar evolution calculations are limited to one spatial dimension,² save for a few pioneering works in the nascent field of 2D stellar evolution (Halabi et al., 2017; Mombarg et al., 2023).³ This leads to a great deal of uncertainty, and the necessity of simplified models for numerous physical processes crucial to stellar evolution such as convection. A number of the methods we have devised to study the evolution of stars embedded in AGN disks attempt to model intrinsically multidimensional processes in a 1D way. In this sense, the precise, quantitative results of our studies are somewhat dubious, but we have aimed to identify robust trends that are insensitive to these modeling uncertainties.

The era of modern stellar evolution calculations arguably began with the introduction of the Henyey relaxation method (Härm & Schwarzschild, 1964; Henyey et al., 1964; Hofmeister et al., 1964), which begins each iteration with an initial guess of each stellar structure parameter at each mass coordinate and gradually refines that initial guess until the stellar structure equations are satisfied to some precision before evolving the system in time and beginning the process

²Arguably, most stellar evolution calculations are effectively 2D because tracking tens to hundreds of isotopes might be necessary to correctly model various segments of a given star's life.

³Halabi et al. (2017) reported work in progress that does not seem to have amounted to much at this time. A number of other 2D works have solved the stellar structure equations, but neglected the chemical evolution of the star (e.g., Espinosa Lara & Rieutord, 2013; Rieutord et al., 2016).

anew. This process proved much more efficient than older methods, based on shooting,⁴ for example, and enabled stellar evolution calculations to proceed further than before (c.f. Härm & Schwarzschild, 1964; Schwarzschild & Härm, 1962).

A number of different codes can now compute stellar evolution quite accurately, such as the Dartmouth Stellar Evolution Program (e.g., Chaboyer et al., 1999), KEPLER (e.g., Weaver et al., 1978), and Modules for Experiments in Stellar Astrophysics (MESA; Jermyn et al., 2023; Paxton et al., 2011, 2013, 2015, 2018, 2019), to name a few.⁵ In addition to solving the stellar structure and evolution equations introduced above, these include nuclear reaction networks, strategies for treating convectively unstable regions, incorporating atmosphere models as an outer boundary condition, and incorporating hydrodynamics during periods in stellar evolution where the hydrostatic approximation breaks down. Below I'll review some of the additions to MESA that have been useful for modeling the evolution of stars within AGN disks.

3.2.1 Accretion

When the specific angular momentum of accreting material is low, and the radiation from the accreting star is sufficiently sub-Eddington, accretion may be modeled as a spherically sym-

⁴i.e. beginning each stage with guesses for the parameters at the mixed boundary conditions (m , r , l at the inner boundary, P , T at the outer), integrating, checking for consistency, updating one's guesses, and then iterating.

⁵These calculations would also not be possible without many years of work by researchers across the world bettering our understanding of the microphysics crucial to stellar evolution, from nuclear reaction rates to the equation of state of gasses in a variety of thermodynamic regimes. In particular, the MESA EOS is a blend of the OPAL (Rogers & Nayfonov, 2002), SCVH (Saumon et al., 1995), FreeEOS (Irwin, 2004), HELM (Timmes & Swesty, 2000), PC (Potekhin & Chabrier, 2010), and Skye (Jermyn et al., 2021) EOSes. Radiative opacities are primarily from OPAL (Iglesias & Rogers, 1993, 1996), with low-temperature data from Ferguson et al. (2005) and the high-temperature, Compton-scattering dominated regime by Poutanen (2017). Electron conduction opacities are from Cassisi et al. (2007). Nuclear reaction rates are from JINA REACLIB (Cyburt et al., 2010), NACRE (Angulo et al., 1999) and additional tabulated weak reaction rates Fuller et al. (1985); Langanke & Martínez-Pinedo (2000); Oda et al. (1994). Screening is included via the prescription of Chugunov et al. (2007). Thermal neutrino loss rates are from Itoh et al. (1996).

metric process occurring at the Bondi rate

$$\dot{M}_B = \eta\pi R_B^2 \rho c_s, \quad (3.29)$$

where η is an efficiency factor ($\eta \lesssim 1$), ρ and c_s are the density and sound speed of ambient gas,

$$R_B = \frac{2GM_*}{c_s^2} \quad (3.30)$$

is the Bondi radius, M_* is the mass of the star and G is the gravitational constant (Bondi, 1952).

These equations assume that the relative velocity between the star and ambient medium is much less than the sound speed. Retrograde stellar orbits have a relative velocity to the gas disk $\Delta v \gg c_s$, so Equations (3.29) and (3.30) are not applicable in this scenario (see, e.g. Hoyle & Lyttleton, 1939). For prograde orbits, the relative velocity comes from Keplerian shear and pressure gradients, and becomes larger than the sound speed when the Bondi radius is larger than the disk scale height, in which case the assumption of symmetry breaks down and Equation (3.29) is no longer appropriate.

To a good approximation, whether accretion from the AGN disk will have much of an effect on the evolution of a given star can be characterized by the initial mass-doubling timescale for that star,⁶ which for accretion at the Bondi rate is given by

$$\tau_2 = \frac{c_s^3}{8\pi\eta G^2 \rho M_0}, \quad (3.31)$$

⁶The mass-doubling timescale, due to its dependence on mass for Bondi accretion, is also half of the time required for runaway accretion in the absence of feedback.

where M_0 is the initial mass of the star. In terms of a characteristic density ($\rho_0 \equiv 10^{-18} \text{ g cm}^{-3}$) and sound speed ($c_{s,0} \equiv 10^6 \text{ cm s}^{-1}$) appropriate to the outer gravitationally unstable (or marginally stable) regions of AGN disks (e.g. [Cantiello et al., 2021](#); [Sirko & Goodman, 2003](#)), the mass-doubling timescale is approximately

$$\tau_2 \approx 2.2 \times 10^8 \text{ yr} \left(\frac{\rho}{\rho_0} \right)^{-1} \left(\frac{c_s}{c_{s,0}} \right)^3 \left(\frac{M_0}{M_\odot} \right)^{-1}. \quad (3.32)$$

If τ_2 is longer than the time spent by a given star on the main sequence, then the evolution of that star is minimally altered.⁷ However, as stars grow, the assumption of spherical accretion begins to break down. In addition to the Bondi radius, two other length-scales are important for stars in AGN disks. First, the scale height of the disk is given by

$$H \equiv \sqrt{2} \frac{c_s}{\Omega}, \quad (3.33)$$

where

$$\Omega = \sqrt{\frac{GM_\bullet}{r_\bullet^3}} \quad (3.34)$$

is the Keplerian angular velocity of the AGN disk, M_\bullet is the mass of the SMBH, and r_\bullet is the distance from the star to the SMBH. Second, the Hill radius ([Hill, 1878](#)) is

$$R_H = r_\bullet \left(\frac{M_*}{3M_\bullet} \right)^{1/3} = \left(\frac{GM_*}{3\Omega^2} \right)^{1/3}. \quad (3.35)$$

⁷However, see [Tout et al. \(1989\)](#) for an investigation of the effects of irradiation by AGNs on the evolution of non-embedded stars.

This is the radius of a sphere within which the gravity of the star dominates that of the SMBH. Note that with the above definitions $R_H/R_B \propto H^2/R_H^2$ and $H/R_H \propto hq^{-1/3}$, where $q \equiv M_*/M_\bullet$ is the mass ratio and $h \equiv H/r_\bullet$.

Hereinafter, we make the approximation that the gas accreting onto AGN stars has a uniform sound speed, and either a uniform density ($\rho = \rho_0$) or one that varies only as a function of height from the midplane ($\rho = \rho_0 f(z)$), where ρ_0 is the midplane gas density. Although this approximation should break down in most cases, especially as the length scale for accretion becomes large, it enables us to keep our investigation largely independent of the precise and highly uncertain structure of AGN disks (Chapter 2). We review below a few of the ways that deviations from a static uniform background can affect the accretion rate onto embedded stars.

3.2.1.1 Vertical stratification

It is common to assume that accretion disks are vertically isothermal. In such disks, vertical hydrostatic equilibrium leads to $\rho(z) = \rho_0 \exp[-(z/H)^2]$ when $r_\bullet \gg z$. For a star in the midplane of the disk this means that the average density of gas at the Bondi radius decreases with increasing Bondi radius, and so generally decreases as the star becomes more massive. Deviations from an isothermal structure or a more realistic treatment of radiation transport and opacities could lead to density inversions or more shallow density gradients (e.g. [Hubeny et al., 2000](#); [Jiang & Blaes, 2020](#); [Meyer & Meyer-Hofmeister, 1982](#); [Milsom et al., 1994](#)). Because these complications all reduce the effect of stratification, assuming a vertically isothermal disk allows us to approximate the maximum impact that vertical density variations could have on the evolution of AGN stars.

To account for how vertical density changes can decrease the accretion rate, we average the density in Equation (3.29) over a sphere with radius R_B centered on the star. We find that in this case, with $z = R_B \cos \theta$ in a polar coordinate system centered on the star,

$$\begin{aligned} \frac{\langle \rho \rangle}{\rho_0} &= \frac{1}{2} \int_0^\pi \sin(\theta) \exp \left[- \left(\frac{R_B}{H} \right) \cos^2(\theta) \right] d\theta \\ &= \frac{\sqrt{\pi}}{2} \frac{H}{R_B} \operatorname{erf} \left(\frac{R_B}{H} \right), \end{aligned} \quad (3.36)$$

where $\langle \dots \rangle$ denotes an average over the Bondi sphere, erf is the error function and ρ_0 is the density of the midplane of the disk. If we use $\langle \rho \rangle$ to compute the accretion rate we then find

$$\dot{M} = \dot{M}_B \frac{\sqrt{\pi}}{2} \frac{H}{R_B} \operatorname{erf} \left(\frac{R_B}{H} \right). \quad (3.37)$$

3.2.1.2 Shear

Shear in the accretion disk imbues accreting gas with net angular momentum in the frame comoving with the star, and can therefore limit accretion onto an embedded star. To leading order, at a distance Δs away from the star the linear velocity ($v = r_\bullet \Omega$) of the disk is different from that of the star by an amount

$$\Delta v = v(r_\bullet) - v(r_\bullet + \Delta s) \approx \frac{1}{2} v(r_\bullet) \frac{\Delta s}{r_\bullet} = \frac{1}{2} \Omega(r_\bullet) \Delta s, \quad (3.38)$$

where we have assumed a Keplerian rotation profile for simplicity. In a spherical coordinate system centered on the star, $\Delta s = R_B \cos(\theta) \sin(\phi)$ at a distance R_B from the star. Averaging the specific angular momentum relative to the star, $l = \Delta s \Delta v$, over the Bondi sphere, we find

that the average specific angular momentum is

$$\begin{aligned}\langle l \rangle &= R_B^2 \frac{\Omega(r_\bullet)}{8\pi} \int_0^{2\pi} \sin^2(\phi) d\phi \int_0^\pi \cos^2(\theta) \sin(\theta) d\theta \\ &= R_B^2 \frac{\Omega(r_\bullet)}{12}.\end{aligned}\tag{3.39}$$

Following [Krumholz et al. \(2005\)](#), we estimate the impact of angular momentum on the accretion. Let

$$\omega_* = \frac{\langle l \rangle}{c_s R_b},\tag{3.40}$$

where ω_* is a measure of the vorticity of the flow. Then this angular momentum reduces the accretion rate by a factor of

$$\frac{\dot{M}}{\dot{M}_B} = \min\{1, f_s(\omega_*)\},\tag{3.41}$$

where

$$f_s(\omega_*) = \frac{2}{\pi\omega_*} \sinh^{-1} [(2\omega_*)^{1/3}],\tag{3.42}$$

Equation (A7) of [Krumholz et al. \(2005\)](#). Note that in this case, $\omega_* = R_B \Omega / 12c_s = R_B / 6\sqrt{2}H$. Since this factor does not become significant until the Bondi radius is more than eight times the disk scale height, shear can be expected to affect accretion less than other factors such as vertical stratification.

3.2.1.3 Tidal effects

When the Bondi radius is much smaller than the disk scale height and Hill radius, disk geometry and the gravity of the SMBH have a negligible effect on accretion onto AGN stars.

However, because $R_B/R_H \propto M_*^{2/3}$, R_B naturally becomes larger than R_H as stars grow more massive. The reason this alters the accretion rate onto stars can be understood by considering the case where $R_B \gtrsim R_H$. In this case, the motion of gas at $R_B > R > R_H$ is controlled by the gravity of the SMBH with only minor influences from the star. To incorporate this effect we replace the Bondi radius with the smaller out of the Hill and Bondi radii when calculating accretion rates

$$\dot{M} = \dot{M}_B \min \left\{ 1, \left(\frac{R_H}{R_B} \right)^2 \right\}, \quad (3.43)$$

along the lines of [Rosenthal et al. \(2020\)](#).⁸ We illustrate these effects in [Figure 3.1](#)

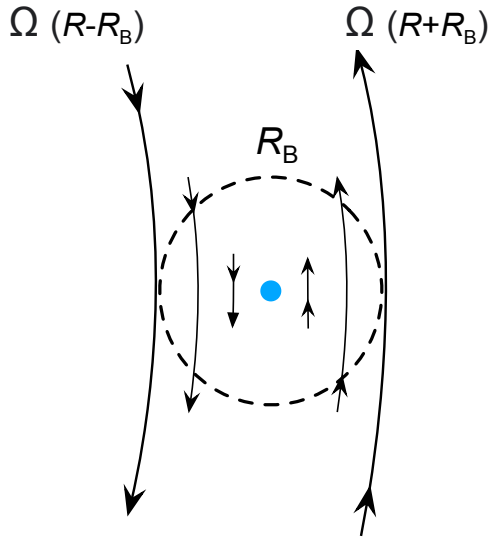
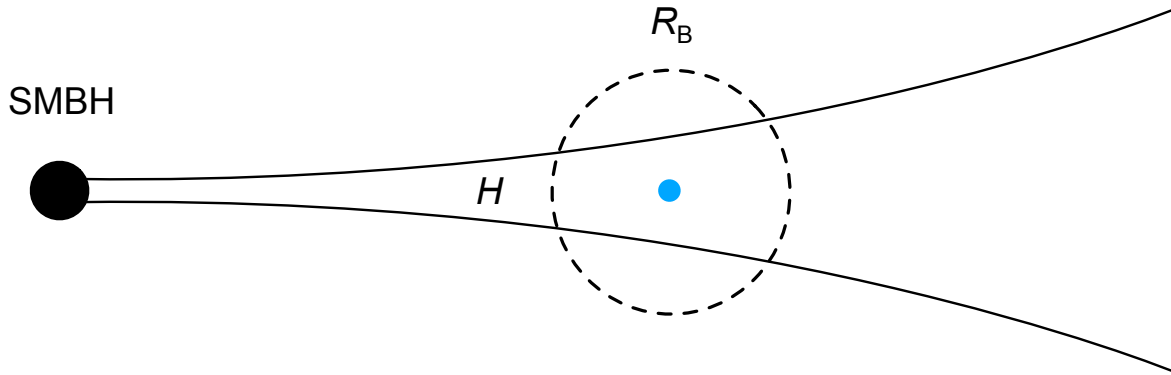
3.2.1.4 Radiative feedback

As stars become more massive, their luminosity (L_*) can increase rapidly, $L_* \propto M_*^3$ ([Böhm-Vitense, 1992](#)). As this radiation impinges on ambient gas, it causes a specific force on gas a distance r away of $f_g = F\kappa/c$, where κ is the opacity of the gas, c is the speed of light, and F is the radiative flux, given for a spherically symmetric radiation field by $L_*/4\pi r^2$. The net acceleration of a gas parcel due to radiation and gravity is thus

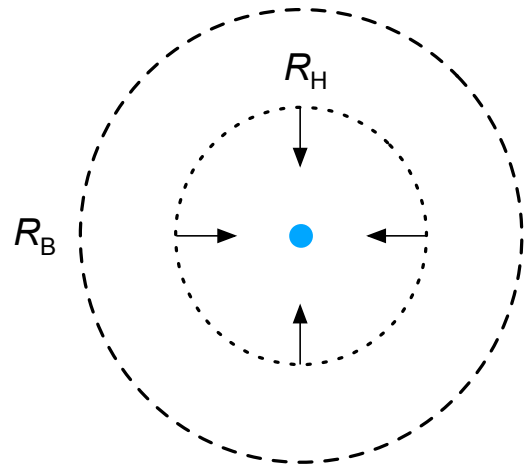
$$f = \frac{1}{r^2} \left(\frac{L_*\kappa}{4\pi} - GM_* \right) = -\frac{GM_*}{r^2} \left(1 - \frac{L_*\kappa}{4\pi GM_*c} \right). \quad (3.44)$$

⁸As I have introduced it, this essential assumes that the accretion rate is given by a characteristic density (ρ_0) traveling with a characteristic velocity (c_s) through a surface of area $\propto R_H^2$. [Rosenthal et al. \(2020\)](#) actually argues that the area through which gas accretes onto the embedded object should be $\sim HR_H$, but that the characteristic velocity should be ΩR_H ; the two routes reach the same destination. [Stone et al. \(2017\)](#) also developed a similar, smooth interpolation between these limits.

A. Rarefaction



B. Shear



C. Tides

Figure 3.1: Accretion onto an AGN star (blue circle) orbiting a supermassive black hole can be limited by geometric and tidal effects. Geometric effects include rarefaction (A), which is important when the Bondi radius R_B becomes comparable to or larger than the disk's scale height H , and shear (B), which is due to the Keplerian rotation of the disk. Tidal effects (C) are caused by the gravity of the SMBH, which becomes important when the Hill radius is smaller than the Bondi radius.

The luminosity where the net acceleration becomes zero is the Eddington luminosity

$$L_{\text{Edd}} = 4\pi GM_*c/\kappa. \quad (3.45)$$

Moreover, from Equation (3.44), it can be seen that the *effective* mass of the star as experienced by ambient gas is reduced by a factor of $(1 - L_*/L_{\text{Edd}})$. As $R_B \propto M_*$, the *effective* Bondi radius is reduced by the same factor. Similarly, the accretion rate onto a star is modified according to

$$\dot{M} = \dot{M}_B \left(1 - \frac{L_*}{L_{\text{Edd}}}\right)^2 \quad (3.46)$$

in the spherical limit. Notably, the effective Hill radius of the star is reduced by a factor of $(1 - L_*/L_{\text{Edd}})^{1/3}$, reducing the accretion rate in the tidally-limited regime as well, only by a factor of $(1 - L_*/L_{\text{Edd}})^{2/3}$.

This picture is entirely one dimensional, which is a drastic simplification of reality. For example, rotating stars are more luminous at their poles than their equators (Lucy, 1967; von Zeipel, 1924), and density perturbations can lead to channels of accretion through the Rayleigh-Taylor instability (Davis et al., 2014; Krumholz & Thompson, 2013). Cantiello et al. (2021) attempted to account for deviations from spherical symmetry by using, instead of Equation (3.46), the following phenomenological prescription:

$$\dot{M} = \dot{M}_B (1 - \tanh |L_*/L_{\text{Edd}}|). \quad (3.47)$$

This prescription is useful because it allows accretion at super-Eddington stellar luminosities, which can occur in geometries where radiation is able to escape in one direction while accretion primarily occurs along another, among other scenarios. I will present results computed using each prescription (Equations (3.46) and (3.47)) and show that they lead to quantitative, but not qualitative, changes in the overall picture.

3.2.2 Mass Loss

The core of our mass-loss treatment follows [Cantiello et al. \(2021\)](#), approximating that as L_* approaches L_{Edd} , near- or super-Eddington continuum-driven winds dominate stellar mass loss. Along the lines of previous work (e.g. [Paczynski & Prószyński, 1986](#); [Paxton et al., 2011](#); [Renzo et al., 2020](#)), we assume an outflow at the escape velocity from the surface $v_{\text{esc}} = (2GM_*/R_*)^{1/2}$ and an associated phenomenological mass loss rate

$$\dot{M}_{\text{loss}} = -\frac{L_*}{v_{\text{esc}}^2} \left[1 + \tanh \left(\frac{L_* - L_{\text{Edd}}}{0.1L_{\text{Edd}}} \right) \right]. \quad (3.48)$$

By default we employ this mass loss scheme along with an Eddington luminosity computed assuming only electron scattering opacity in a pure hydrogen gas. We have additionally tested the extent to which our results change when we adopt composition- and rotation-dependent mass loss rates.

3.2.2.1 Composition

As embedded stars accrete from the AGN disk, their composition becomes strongly influenced by that of the surrounding gas. Ignoring metallicity, the mean molecular weight (μ) of a fully ionized gas is given by $\mu = (2 - 5Y/4)^{-1}$, such that a higher helium mass fraction in the disk, and hence in the star, leads to a higher stellar mean molecular weight. At a fixed stellar mass, L_* increases with mean molecular weight, e.g. $L_* \propto \mu^4 M^3$ for a simplified stellar model with uniform molecular weight and constant opacity as derived earlier. Thus, AGN stars in higher- Y disks will tend to be more luminous at a given mass, potentially driving stronger outflows and

halting accretion at lower masses.

However, changes in the composition of AGN stars and the disk can change gas opacities and thus the Eddington luminosity, as impingement of radiation upon more opaque gas can more easily overcome the pull of gravity. Considering just electron scattering opacity, $\kappa \approx 0.2(2 - Y) \text{ cm}^2 \text{ g}^{-1}$. Thus, increases in Y can decrease gas opacity enough to increase L_{Edd} by up to a factor of 2 compared to the value corresponding to pure hydrogen gas. In more helium-rich AGN disks, then, it may be more difficult for stars to drive outflows and stave off accretion. However, the electron scattering opacity may also severely underestimate the actual opacity due to features such as the iron opacity peak, or the potentially stronger opacity peaks due to helium recombination (e.g. [Cantiello & Braithwaite, 2019](#); [Jiang et al., 2015, 2018, 2016](#)), so we present results using both opacity formulas and caution that there is still uncertainty in the opacities relevant to mass loss and the accretion stream, even in this already simplified gray opacity treatment.

3.2.2.2 Rotation

When modeling the rotation of the star (to be described in more detail within [Section 3.2.5](#)), we modeled increased mass loss, along similar lines to that advocated for in [Section 2.4.2.2](#). In some simulations (denoted $\Gamma - \Omega$) we accounted for centrifugal accelerations reducing the effective escape velocity from the star, and thus the radiative acceleration needed to unbind material from its surface ([Maeder, 2009](#); [Sanyal et al., 2015](#)), scaling the Eddington Luminosity by a factor

of $1 - \langle \Omega \rangle^2 / \Omega_c^2$, where $\langle \Omega \rangle$ is the mean angular velocity of the star and

$$\Omega_c \equiv \sqrt{\frac{GM_*}{R_*}} \quad (3.49)$$

is the critical angular velocity for a rotating sphere. This choice is likely to somewhat overestimate the effects of rotation on mass loss, since gravity darkening (which our 1D models do not include) will increase the stellar luminosity near the poles and decrease it towards the equator, leading to a net decrease in the surface-averaged stellar luminosity (Glatzel, 1998; Maeder & Meynet, 2000).

3.2.3 Mixing

As discussed in Section 3.1, as stars grow more massive they tend to become hotter, and thus radiation pressure plays a dominant role to radiation pressure in their support. Stars more massive than the sun also tend to predominantly burn hydrogen into helium via the CNO cycle, which depends sensitively on temperature, leading the energy generation rate to peak sharply in the innermost stellar regions. Such arrangements tend to be convectively unstable, leading to efficient mixing within the star. This convection, along with the radiation-pressure dominated nature of the star, brings these stars to adiabatic indices near $\gamma \sim 4/3$, the precipice of instability; in such a situation, even radiative regions (those stable against convection) can be strongly affected by instabilities that lead to enhanced mixing (e.g., Jiang et al., 2015, 2018).

In an attempt to account for the effects of these intrinsically three-dimensional effects in our one-dimensional stellar models, we incorporated an additional compositional diffusivity D

that increases with stellar luminosity as

$$D = H_* \left(\frac{F}{\rho} \right)^{1/3} \tanh \left(\frac{L_*}{L_{\text{Edd}}} \right)^\xi, \quad (3.50)$$

where F is the local heat flux through the star, H_* is the local pressure scale height,

$$H_* \equiv \frac{P}{\rho g}, \quad (3.51)$$

where g is the local gravitational acceleration. This form of the additional diffusivity is designed to only affect stars very near the Eddington limit through the exponent ξ , typically taken to be $\xi \sim 7$. This choice, on which our results depend very weakly for $\xi > 1$, ensures that stars only experience substantial mixing after approaching Eddington limit as a result of appreciable accretion, while stars that accrete to only a few solar masses are largely unaffected. The prefactor in Equation (3.50) is chosen to be on the order of what the effective convective diffusivity would be if the region happened to be convectively unstable.

3.2.4 The Accretion Stream

[Cantiello et al. \(2021\)](#) also developed a stellar boundary condition accounting for the affects of accreting material shocking against the stellar surface. The model assumes that:

- The accretion stream is spherically symmetric.
- The stream is in a steady state.
- Ram pressure dominates radiation and gas pressure within the stream.

- The stream primarily transports heat via radiative diffusion.
- The luminosity of the stream is spatially constant.
- The mass of the stream is negligible compared to the stellar mass.
- The opacity of the stream is spatially constant and equal to the electron-scattering value.

The last of these assumptions is arguably the most questionable, as we have seen the many orders of magnitude variations in opacity that can occur, particularly at lower temperatures (see, for example, Figure 2.1); however, as discussed in Section 3.2.1, the assumption of spherical symmetry should also break down for more massive stars.

In the spherically-symmetric limit, the continuity and momentum equations reduce to

$$\dot{M} = 4\pi r^2 \rho v = \text{const.} \quad (3.52)$$

$$\frac{\partial}{\partial r} \left(\frac{1}{2} v^2 \right) + \frac{GM}{r^2} = 0. \quad (3.53)$$

If the fluid is stationary at infinity, $v \approx \sqrt{GM/r}$, and

$$\rho = \frac{\dot{M}}{4\pi r^2} \sqrt{\frac{r}{GM}}. \quad (3.54)$$

From the equation of radiative thermal equilibrium,

$$\frac{dT}{dr} = -\frac{3\kappa\rho L}{64\pi r^2 \sigma T^3}, \quad (3.55)$$

under the assumptions that κ and L are constant, along with $\rho \propto r^{-5/8}$, $T \propto r^{-5/8}$ within the

stream.

As the material accreting from the AGN disk reaches the surface of the star, the two shock, converting the kinetic energy of the stream into luminosity with $L_{\text{shock}} \sim \dot{M}v^2$, which is then added to the stellar luminosity when determining the luminosity of the accretion stream. The optical depth between the accretion radius (the smaller of the Hill and Bondi radii, R_{acc}) is simply

$$\tau = \int_{R_{\text{acc}}}^r \kappa \rho dr, \quad (3.56)$$

leading to $\tau \approx \kappa \rho_0 R_{\text{acc}}^{3/2} r^{-1/2}$, for some background AGN gas density ρ_0 . The location of the photosphere can then be determined by finding the location between r and R_{acc} where $\tau \sim 1$, yielding a photospheric radius

$$R_{\text{ph}} \approx \min(R_{\text{acc}}, R_* + \kappa^2 \rho_0^2 R_{\text{acc}}^3) \quad (3.57)$$

To connect the optically thin and thick limits, the effective temperature of the stream is taken to be

$$T_{\text{eff}}^4 = T_0^4 + \frac{L}{4\pi R_{\text{ph}}^2 \sigma}, \quad (3.58)$$

where T_0 is the temperature of the background AGN disk, and which is related to the temperature at the stellar surface according to

$$T_* = T_{\text{eff}} \left(\frac{R_*}{R_{\text{ph}}} \right)^{-5/8}. \quad (3.59)$$

Finally, the pressure boundary condition modifies the standard Eddington atmospheric condition

$P_* = (1/3)aT_*^4 + g/\kappa$, where g and κ are the gravitational acceleration and opacity at the stellar surface, by the ram pressure of accreting material, as well as a similar term accounting for the force required to launch outflows, resulting in

$$P_* = \frac{1}{3}aT_*^4 + \frac{g}{\kappa} + \frac{GM\rho}{R_*} + \frac{\dot{M}_{\text{loss}}v_{\text{esc}}}{4\pi R_*^2}. \quad (3.60)$$

In practice, we smoothly introduced this boundary condition (as well as the heightened accretion rate onto the star) over a period of $\sim 10^7$ years, slow enough so that stellar structure could adapt in a numerically stable manner, but fast enough so that this initial blending only constituted a small fraction of the main sequence lifetime of each of our initial models.

3.2.5 Angular Momentum

In addition to accreting mass, a star may also accrete angular momentum, potentially increasing its rate of spin as it grows. Although most of our work focused on non-spinning stars, we also investigated the role of angular momentum in the evolution of disk-embedded stars in [Jermyn et al. \(2021\)](#). In this study, we did not track angular momentum as a function of enclosed stellar mass (or \sim equivalently, radius), but instead tracked the average angular momentum of the entire star, motivated by the expectation that as these stars grow to larger masses they will be almost fully convective and thus well-mixed (see also Section [3.2.3](#)).

In practice, the mean angular momentum of the star (J) evolved according to

$$\frac{dJ}{dt} = \dot{M}_{\text{gain}}j_{\text{gain}} - \dot{M}_{\text{loss}}j_{\text{loss}}, \quad (3.61)$$

where \dot{M}_{gain} is the accretion rate following from the considerations in Section 3.2.1, j_{gain} is the mean specific angular momentum of the accreted material, and j_{loss} is the mean specific angular momentum of the lost material.⁹ The average specific angular momentum within the accretion radius is determined by the shear profile of the AGN disk,

$$j_{\text{gain}} \approx R_{\text{acc}}^2 \frac{d(a\Omega)}{da} \approx \Omega R_{\text{acc}}^2. \quad (3.62)$$

Additionally, we assumed that any material with specific angular momentum greater than the Keplerian value at the stellar surface would necessarily shed that excess prior to accretion, capping j_{gain} at $\sqrt{GMR_*}$.¹⁰ We assume that material is lost from the star with the star's own specific angular momentum,

$$j_{\text{loss}} = \frac{J}{M} \left(\frac{MR_*^2}{I} \right), \quad (3.63)$$

where I is the stellar moment of inertia. In addition to these considerations, we additionally truncated the stellar angular momentum at the critical value for breakup

$$J_{\text{crit}} \approx \frac{I}{R_*^2} \sqrt{GMR_*}. \quad (3.64)$$

⁹The actual calculations modeled turbulent fluctuations and the variance in accreted angular momentum they are expected to cause. However, because the dynamical timescale of turbulent fluctuations was typically much shorter than stellar evolutionary timescales, this accounting was immaterial. Further details can be found in Section 3 and Appendix B of [Jermyn et al. \(2021\)](#).

¹⁰In retrospect, this truncation may have been overly lenient ([Dittmann, 2021b](#)), since angular momentum transport between the disk and star can become far less efficient at higher stellar spins.

3.3 Results

All of the files necessary to reproduce the calculations presented within this section are hosted on zenodo in [Dittmann et al. \(2021\)](#), [Jermyn et al. \(2021\)](#), and [Dittmann et al. \(2022\)](#). But before getting into the details of how rotation, different assumptions about accretion, and composition affect the evolution of stars in AGN disks, it will be useful to first get a sense for general trends in how such stars evolve.

3.3.1 Timescales

A first-order picture of the evolution of AGN stars can be gleaned from the balance between the main sequence lifetime of such a star in the absence of accretion and the typical accretion timescale onto that star due to Bondi accretion. The latter can be characterized by the initial mass-doubling timescale, τ_2 , of the star, introduced in Section [3.2.1](#).

If this timescale is initially shorter than the main-sequence timescale for a given star, the ultimate fate of that star will then depend on whether mass loss is able to eventually overcome or balance accretion. [Cantiello et al. \(2021\)](#) argued that when the nuclear burning timescale (τ_{nuc}) is shorter than, but comparable to, the accretion timescale, stars may accrete substantial mass before approaching the Eddington luminosity, driving extreme mass loss, and returning to moderate masses of $\sim 10 M_{\odot}$. We refer to such stellar models as “intermediate,” and the evolution of such a model is displayed in the upper panels of [Figure 3.2](#).

The upper panels of [Figure 3.2](#) illustrate the balance of various timescales more quantitatively, along with the stellar mass and core helium and hydrogen mass fractions, over the course of the evolution of an intermediate star. Therein we plot a rough estimate of the nuclear

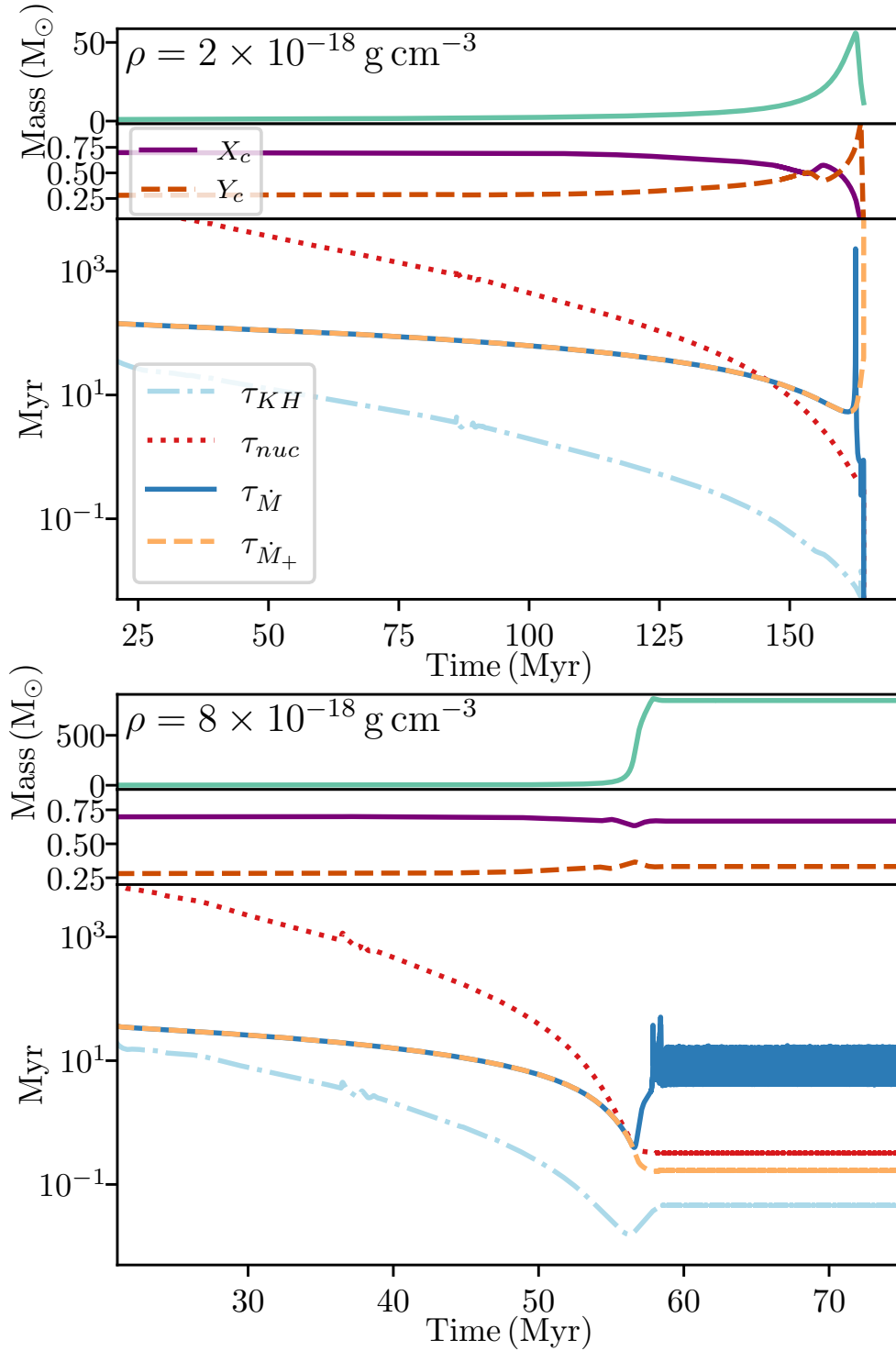


Figure 3.2: The evolution of fiducial intermediate (top panel trio, using a density of $\rho = 2 \times 10^{-18} \text{ g cm}^{-3}$) and immortal (bottom panel trio, using a density of $\rho = 8 \times 10^{-18} \text{ g cm}^{-3}$) stars. In each trio of panels, the upper plot shows the stellar mass over time, the middle plot shows the core hydrogen and helium mass fractions over time, and the lower plot shows the evolution of various timescales over time. All simulations used an ambient sound speed of $c_s = 10^6 \text{ cm s}^{-1}$. In both cases, the balance between the nuclear and accretion timescales determines the fate of the star, which hinges on whether or not the former becomes shorter than the latter.

burning timescale $\tau_{\text{nuc}} \sim 10^{10}(M/M_{\odot})(L/L_{\odot})^{-1}$ yr, the Kelvin-Helmholtz timescale $\tau_{\text{KH}} \sim 0.75GM_*^2R_*^{-1}L_*^{-1}$, the overall timescale for mass changes $\tau_{\dot{M}} \equiv M_*/|\dot{M}_{\text{acc}} - \dot{M}_{\text{loss}}|$, and the timescale for mass change due to accretion $\tau_{\dot{M}_+} \equiv M_*/\dot{M}_{\text{acc}}$. For the intermediate stellar model, the accretion timescale is initially shorter than the nuclear burning timescale. However, as the star grows more massive and luminous, the nuclear burning timescale shrinks more quickly than the accretion timescale, eventually becoming shorter. The star then becomes sufficiently luminous to stave off further accretion almost entirely, in this case ejecting roughly forty solar masses of material. Although the core becomes somewhat rejuvenated as hydrogen-rich material is mixed into it as the star climbs in mass, the supply of hydrogen in the core is eventually exhausted, followed shortly by the consumption of the core’s helium supply.

On the other hand, if the accretion timescale is sufficiently short, accretion and mass loss can balance one another, resulting in almost fully-convective stellar models with masses which are (on average) constant in time. Such stars are able to efficiently mix accreted material from the surface into their cores, and thus enrich their outer layers and winds with fusion byproducts, potentially enriching the disk with helium (Dittmann et al., 2021; Jermyn et al., 2022). We refer to such stellar models as “immortal,” and the evolution of such a model is shown in the bottom panels of Figure 3.2. In this case, although the nuclear burning timescale becomes much shorter as the star accretes, it is unable to outpace the shrinking of the accretion timescale. Once the star enters this quasi-steady stage of evolution, the core hydrogen and helium mass fractions become, on average, constant in time.

Of course, such stars cannot truly be immortal: the stars may migrate through the disk to regions where the accretion timescale is appreciably longer or the disk may dissipate, in which case the evolution of immortal stars proceeds similarly to intermediate models, losing most of

their accreted mass and reaching later stages of burning (see, e.g. Figures 10 and 11 in [Cantiello et al., 2021](#)).¹¹ Additionally, we note that if the accretion timescale is shorter than the Kelvin-Helmholtz timescale for massive stars ($\tau_{\text{KH}} \sim 3 \times 10^4$ yr, [Bond et al., 1984](#)), the luminosity of the star may not be able to adjust quickly enough to drive the star towards an equilibrium. Such stars may accrete all of the local disk mass (e.g. [Goodman & Tan, 2004](#)), and potentially reach the general relativistic limit of stellar stability ([Bludman, 1973](#); [Tooper, 1964](#)), although our models cannot probe this regime numerically.

3.3.2 Prototypical Models

A closer look at the typical evolutionary paths of intermediate and immortal stars will be instructive before moving to the interpretation of large grids of models.

This difference can be seen in Figures 3.3 and 3.4, which show cases of intermediate and immortal stellar evolution, in both cases beginning with a $1 M_{\odot}$ AGN star, embedded in gas with a sound speed of 10 km s^{-1} and ambient gas densities of $2 \times 10^{-18} \text{ g cm}^{-3}$ and $8 \times 10^{-18} \text{ g cm}^{-3}$ respectively.

The stars begin with a steep composition gradient, but become chemically homogeneous as they increase in mass, accreting fresh hydrogen and helium. Throughout most of its life, the $\rho = 2 \times 10^{-18} \text{ g cm}^{-3}$ model has a convective core and radiative envelope. From about $\sim 134 - 137 \text{ Myr}$, the hydrogen mass fraction in the core increases due to mixing of accreted material. After this, accretion is effectively halted by radiative feedback and the star loses its source of fresh hydrogen. The helium mass fraction then increases throughout the star until it is

¹¹However, [Ali-Dib & Lin \(2023\)](#) found that if mixing is sufficiently suppressed, then such a quasi-steady state cannot be maintained, and the stellar composition continues to evolve.

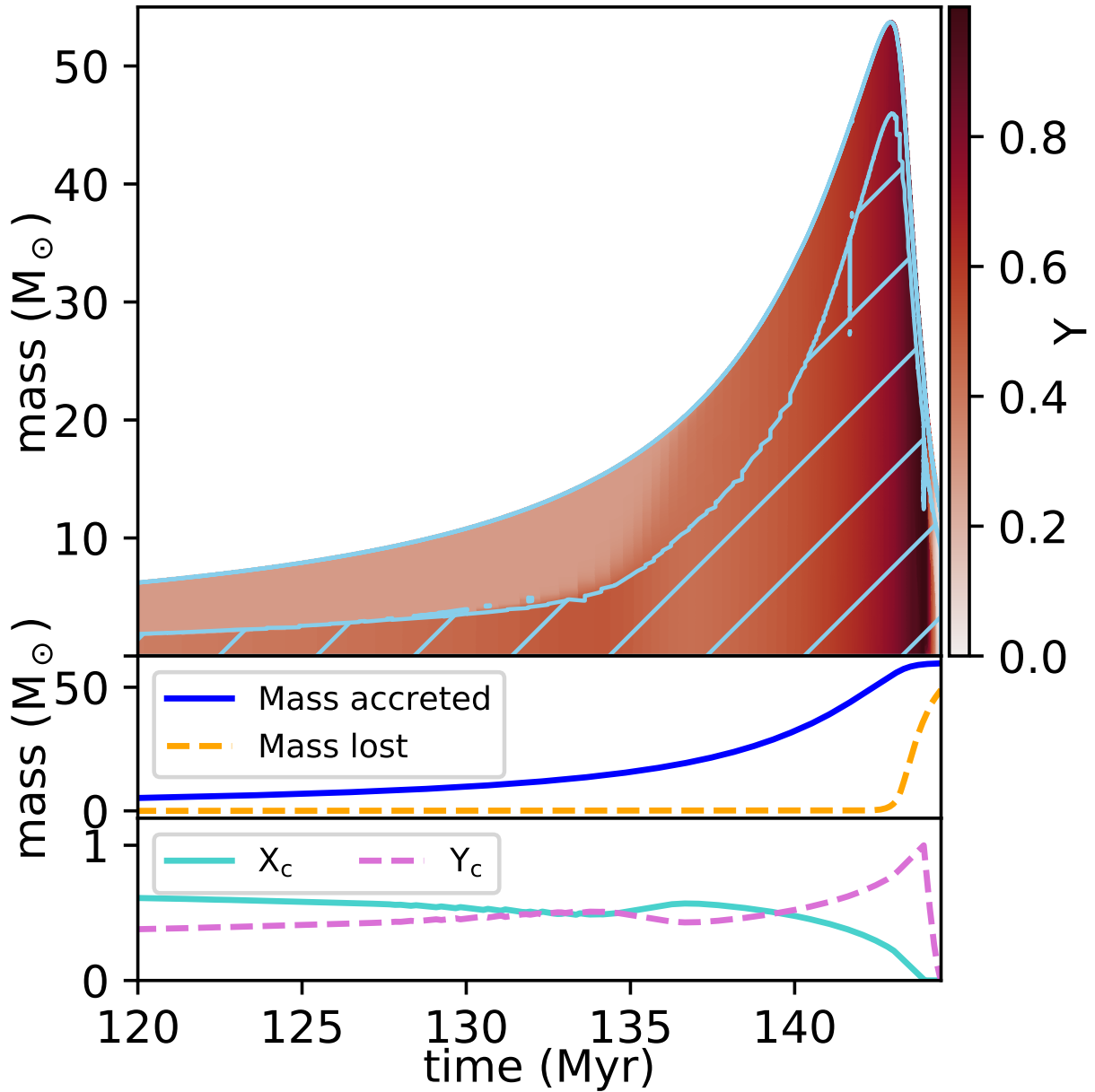


Figure 3.3: The evolution of a typical model in the intermediate accretion regime is shown. The ambient gas density is $2 \times 10^{-18} \text{ g cm}^{-3}$ and the sound speed is 10 km s^{-1} . The top panel shows the helium mass fraction in the star as a function of time and stellar mass coordinate. Convective regions are marked by light blue hatching. The middle panel displays the mass accreted and mass lost over time. The lower panel shows the core hydrogen and helium mass fractions throughout the star’s life.

eventually depleted through fusion into heavier elements. This general trend is followed by stars in the ‘intermediate’ accretion regime, where the nuclear burning timescale is shorter than, but comparable to, the accretion timescale.

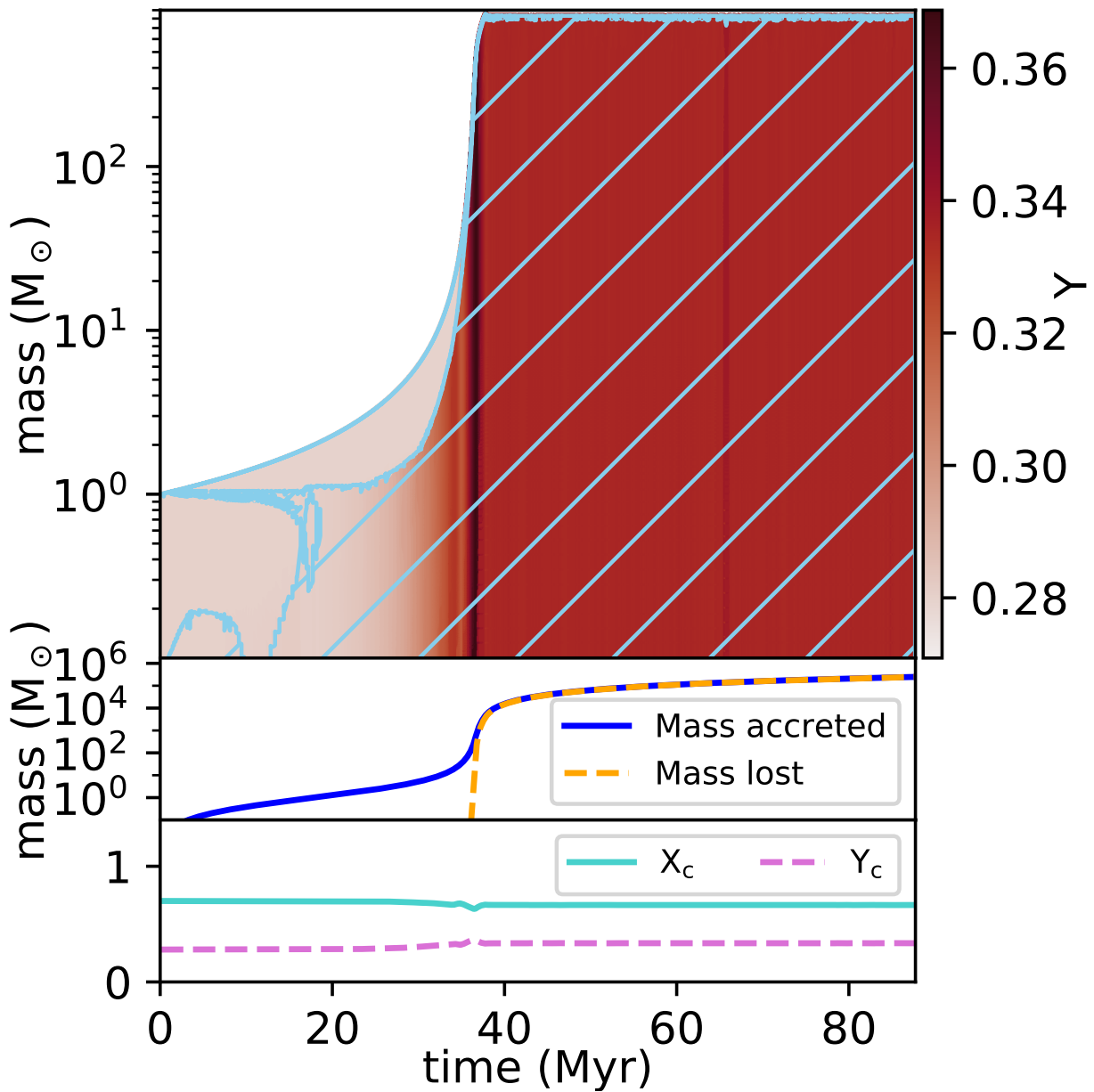


Figure 3.4: The evolution of a typical model in the runaway accretion regime, leading to an “immortal” AGN star. The ambient gas density is $8 \times 10^{-18} \text{ g cm}^{-3}$ and the sound speed is 10 km s^{-1} . The top panel shows the helium mass fraction in the star as a function of time and stellar mass coordinate. Convective regions are marked by light blue dashed lines. The middle panel displays the mass accreted and mass lost over time. The lower panel shows the core hydrogen and helium mass fractions throughout the star’s life.

Unlike the $\rho = 2 \times 10^{-18} \text{ g cm}^{-3}$ case, in the $\rho = 8 \times 10^{-18} \text{ g cm}^{-3}$ model mass loss and accretion come into approximate balance once the star nears the Eddington limit. As a consequence the mass of the model reaches an approximate steady state. The star is almost fully convective, so accreted material is rapidly mixed throughout. For the same reason, mass lost from the star is chemically enriched by the ashes of nuclear fusion occurring in the stellar core. Examining the mass loss and accretion budget, it is evident that this single star that began at $1 M_{\odot}$ is able to process well above $10^5 M_{\odot}$ worth of gas in $\sim 10^8$ of Myr (Figure 3.4, middle panel). Stars with higher initial masses or in higher-density (or lower-sound speed) environments are able to reach this evolutionary stage much more quickly, since $M/\dot{M}_B \propto M^{-1}\rho^{-1}$.

The chemical yields of mass lost from these models are shown in Figure 3.5. Although the immortal model loses mass at a rate $\sim 10^4$ times larger than the intermediate model, this material has a much lower metal content and so the overall yield of metals is lower. Thus, mass loss from immortal stars matters less for enriching the disk with metals than that lost from intermediate stars, although the large mass loss rates could play an important role in determining the overall structure of the AGN disk.¹² Additionally, stars may migrate through the disk, and the disk itself will dissipate over time. Thus, eventually ‘immortal’ stars will find themselves in lower-density environments and begin to evolve similarly to those in the intermediate accretion regime, reaching later stages of burning and losing most of their nuclear-processed material (e.g. Figure 10 and 11 in [Cantiello et al., 2021](#)).

¹²Recalling the disk model of [Thompson et al. \(2005\)](#) discussed in Chapter 2, ram pressure from the winds of very massive stars could play an important role in providing pressure support to the disk in the optically thin regime.

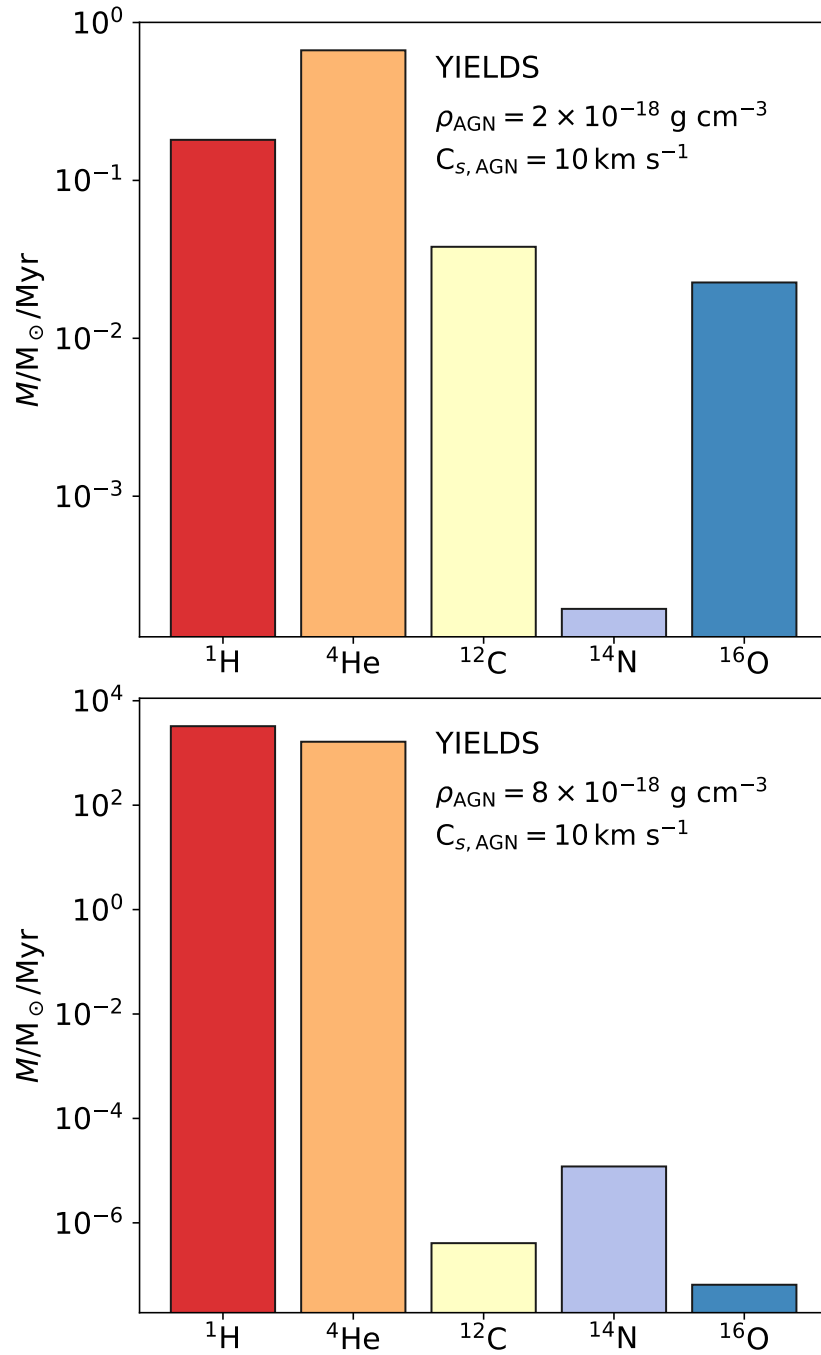


Figure 3.5: Chemical yields for archetypal ‘intermediate’ (figure 3.3, upper) and ‘immortal’ (figure 3.4, lower) models. For both cases, we have excluded the first 4×10^7 years of the star’s lives. Because the immortal model could fuse indefinitely, we have presented yields in terms of the mass lost per million years. Note that the yields from immortal stars contain very little metal content because these stars primarily fuse hydrogen, although their metal content is significantly enriched in nitrogen. As mortal stars lose mass and reach later stages of evolution they eventually produce significant amounts of carbon and oxygen as well.

3.3.3 Accretion

One of our first orders of business in delving deeper was to understand how the many possible modifications to accretion as stars grow more massive, discussed in Section 3.2.1, are most relevant. We present in Figure 3.6 a series of $M_*(t)$ diagrams for each of the accretion prescriptions discussed in Section 3.2.1. The prescriptions used by [Cantiello et al. \(2021\)](#) are taken as a baseline and shown in the first row. Each subsequent row demonstrates exactly one modification from baseline, with the exception of the fourth row which includes two modifications. In each panel we show a variety of values for Ω , ρ , the angular velocity and density of the gas at the stellar location in the AGN disk. Colors denote the ambient density, with lighter and yellower colors indicating stars in lower-density environments and darker and bluer colors indicating those in higher-density environments. The models in the left column are embedded in gas with a sound speed of 3 km s^{-1} , while the models in the right column are embedded in gas with a sound speed of 10 km s^{-1} . Line styles indicate the angular velocity Ω about the SMBH, and where necessary $M_\bullet = 10^8 M_\odot$ is used to calculate r_\bullet . Note that some models do not depend on Ω . This sparse grid of models elucidates the impact of the different modifications to accretion onto AGN stars.

We begin by considering the first and second rows, which show models computed using our baseline prescription and those computed using stronger radiative feedback (Equation (3.46)). The more severe reduction in accretion rate imposed by Equation 3.46 extends the range of densities leading to intermediate stellar evolution, as opposed to runaway, by about an order of magnitude.

Of the effects we consider, tidal forces from the SMBH are generally the most significant. Specifically, tidal effects slow accretion onto AGN stars enough to shift many from the runaway

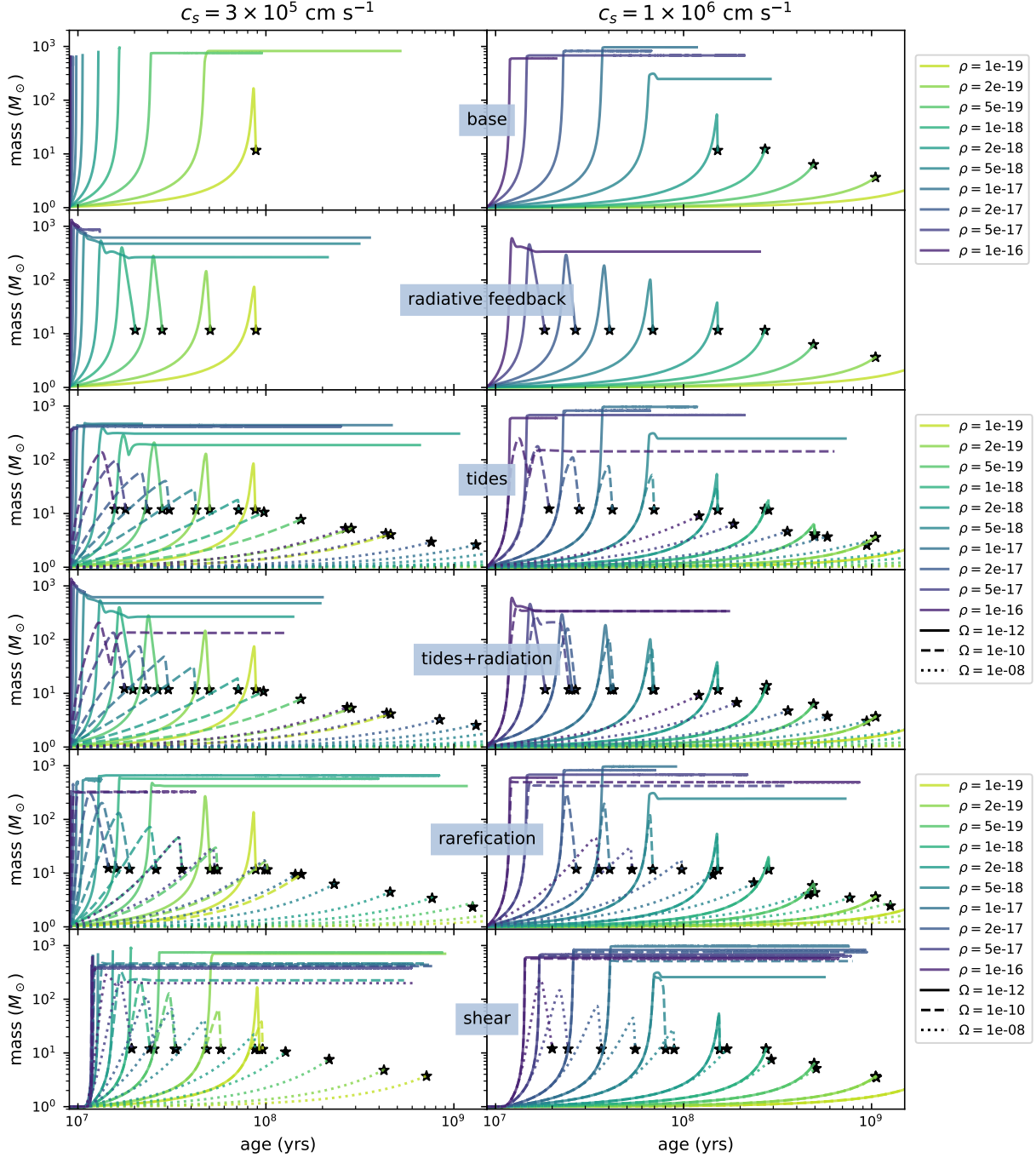


Figure 3.6: Evolutionary tracks of stellar mass over time for various accretion prescriptions. On the x-axes, the reported age includes the $\sim 10^7$ years over which the boundary conditions for each model were relaxed. We begin plotting results at the end of the relaxation process for each run. Each column corresponds to a different ambient sound speed, as indicated by the column headers. Each row presents results for a different accretion prescription, as indicated by the text boxes in each row. Line colors correspond to different ambient gas densities (given in g cm^{-3}), and line styles correspond to different AGN disk angular frequencies (given in s^{-1}) at the star’s location. Stars indicate the final masses of stars at the end of their lives. Recall that for $M_{\bullet} = 10^8 M_{\odot}$, $\Omega = \{10^{-12}, 10^{-10}, 10^{-8}\} \text{ s}^{-1}$ corresponds to distances from the SMBH $r_{\bullet} \approx \{7.67, 0.356, 0.0265\} \text{ pc}$.

regime to the intermediate regime, and to shift many from the intermediate regime into the regime of fairly standard stellar evolution. Because of its independence from disk structure, support from hydrodynamical simulations (e.g., [Li et al., 2021a](#)), and having the greatest efficacy of the standalone modifications to the models in [Cantiello et al. \(2021\)](#), the tidal accretion prescription is promising for general use. One feature of tidally-limited accretion is that the accretion rate becomes proportional to the sound speed, $\dot{M} \propto R_H^2 c_s \rho$, unlike Bondi accretion where $\dot{M}_B \propto c_s^{-3}$. Because of this, when tidal effects dominate, stars in disks with higher sound speeds tend to have larger final masses or maximum masses, as well as immortal-to-intermediate transitions at lower densities.

Because tidal effects depend on the ratio R_H/R_B , their impact may become less significant if R_B is reduced by radiation from the star. To test the extent to which this occurs, we carried out another suite of simulations using both modifications. For small Ω , tidal effects are minimal and stars evolve essentially identically to the models without tidal effects. However, at higher Ω , tidal effects dominate and evolution is largely the same as when only considering tidal effects. Thus we find that the evolution of AGN stars only depends significantly on radiative feedback assumptions for stars that are far from the SMBH, e.g. ~ 0.36 pc for a $10^8 M_\odot$ black hole.

Vertical stratification in the disk can also decrease the accretion rate onto AGN stars enough to cause qualitative deviations in their evolution. However, its effects are less significant than tidal effects because rarefaction only operates in one dimension in our models. This can be understood by considering the growth of the Bondi radius as the star accretes: although gas directly above and below the star decreases in density significantly, gas near the midplane is relatively unchanged. Still, smaller disk scale heights can lead to greatly reduced accretion. We find that rarefaction is also more significant for models accreting cooler gas. This can be understood by recalling

that $H \propto c_s \Omega^{-1}$, so while $\Omega = 10^{-10} \text{ s}^{-1}$ and $\Omega = 10^{-12} \text{ s}^{-1}$ models evolve very similarly at $c_s = 10^6 \text{ cm s}^{-1}$, model tracks diverge significantly at $c_s = 3 \times 10^5 \text{ cm s}^{-1}$.

We expect, however, that this investigation likely overestimates the effects of disk rarefaction on the evolution of AGN stars, since AGN disks are not perfectly vertically isothermal, which would lead to a less steep decline in density vertically. Similarly, radiation-MHD simulations of AGN accretion disks tend to develop vertical profiles that decline less rapidly from the midplane than would a vertically isothermal disk (e.g. [Jiang et al., 2019b](#)). Additionally, when taking into account realistic opacities, some disk models ([Hubeny et al., 2000](#)) and simulations ([Jiang & Blaes, 2020](#)) have shown that in the presence of opacity bumps, density inversions can occur in the disk, leading to an increase in density away from the midplane. Thus, the effects of rarefaction here are likely to be unrealistically strong.

We find shear to have a fairly negligible effect on the evolution of AGN stars. Because the effects of shear depend on the disk scale height, they lead to minor changes in the evolution of stars at $c_s = 10^6 \text{ cm s}^{-1}$ only fairly close to the SMBH, for $\Omega \gtrsim 10^{-8} \text{ s}^{-1}$. In cooler disks, with commensurately small scale heights, shear can be significant over a somewhat larger range in Ω . As discussed in Section 3.2.1.2, shear becomes significant at much larger R_B/H than for other effects such as tides or vertical stratification, so its lower efficacy at slowing accretion is natural.

3.3.3.1 Tide-mediated stellar evolution

Having identified tides as the most significant and generally applicable modification to Bondi accretion, of those considered here, we now turn to study their effects on the evolution of AGN stars. Recall that the Hill radius of a star can be written in terms of its mass and the angular

velocity of its Keplerian orbit. Similarly, the tide-limited accretion rate depends on, apart from stellar mass, $\rho c_s \Omega^{-4/3}$. Thus, to the extent that tides and accretion govern the evolution of AGN stars, we can study their evolution across a variety of disk characteristics and SMBH masses using only a few parameters. For this reason we perform the simulations in this section at a single AGN disk sound speed, $c_s = 10 \text{ km s}^{-1}$ and assume that outcomes of stellar evolution such as final masses and rate of mass loss scale with ρc_s . This is not completely correct, since changes in c_s *do* affect the stellar atmosphere, and the accretion rate scales as ρc_s^{-3} before accretion is limited by tides, which can have significant effects on evolution of stars while they are at lower masses. Thus, care must be taken when extrapolating these results to other sound speeds.

One of the most important features of the evolution of AGN stars is that initially low-mass stars can accrete enough gas from the disk and become massive stars, ending their lives as compact objects. Additionally, since these stars reach the Eddington luminosity, they also lose large amounts of processed material before reaching the end of their evolution. Thus, in Figure 3.7 we present the maximum masses achieved by AGN stars in our models, as well as the final masses in Figure 3.8.

To a good degree of accuracy, quantities such as maximum and final masses can be determined based on the mass-independent factors that control the accretion rate onto AGN stars. For sufficiently large Ω , such that tidal effects are significant, $\dot{M} \propto \rho c_s \Omega^{-4/3}$. Thus, a corresponding power-law contour in the $\rho - \Omega$ plane is given by $\rho = A c_s^{-1} \Omega^{4/3}$ for some constant A . One such curve for $M_{\text{max}} = 8 M_{\odot}$ is marked by a black dashed line in Figure 3.7 and is given by

$$\left(\frac{\rho}{\text{g cm}^{-3}} \right) \gtrsim 3.4 \times 10^{-6} \left(\frac{c_s}{10^6 \text{ cm s}^{-1}} \right)^{-1} \left(\frac{\Omega}{\text{s}^{-1}} \right)^{4/3}. \quad (3.65)$$

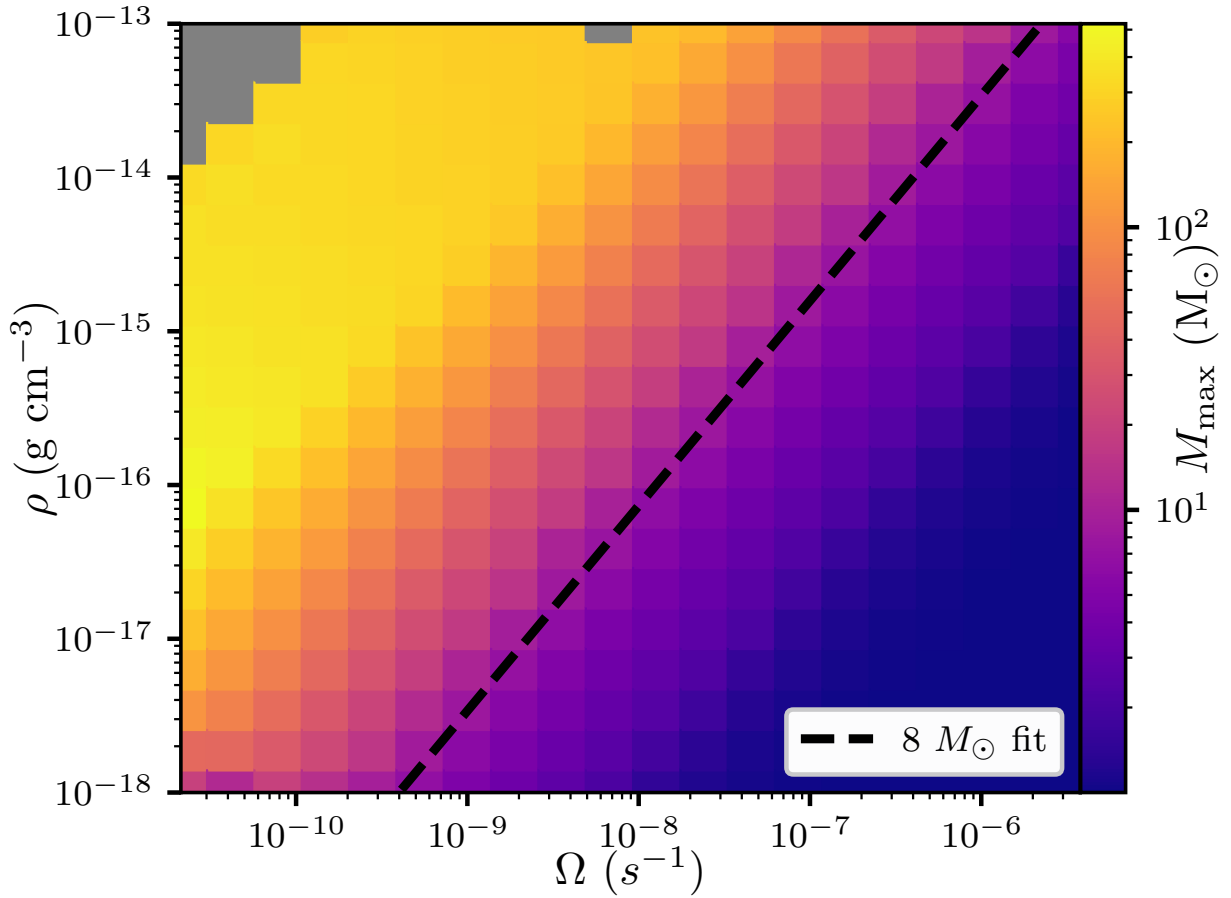


Figure 3.7: The maximum mass achieved by each model is shown as a function of ρ and Ω . Gray squares indicate models that failed during boundary condition relaxation. The dashed black line is the power-law fit to $M_{\max} = 8 M_{\odot}$ over this range, given by Equation 3.65. Note that all runs are calculated with $c_s = 10\ km\ s^{-1}$.

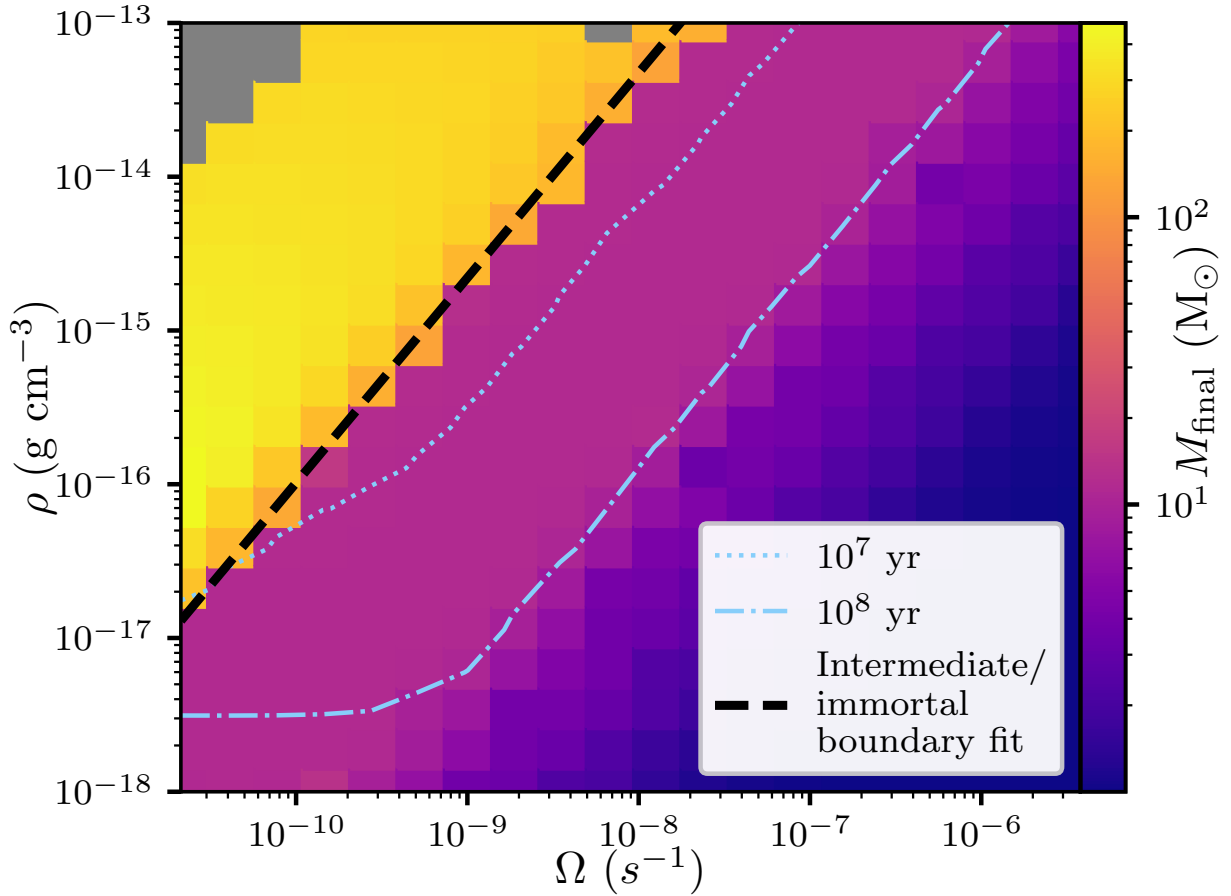


Figure 3.8: The final masses reached by each model is shown as a function of ρ and Ω . Gray squares indicate models that failed during boundary condition relaxation. The dashed black line is the power-law fit given by Equation 3.66 for the intermediate-immortal transition in ρ and Ω . The dashed thin blue line indicates models with final ages of 10^7 years, and the dot-dashed thin blue line indicates models with final ages of 10^8 years. Here, the reported age does not include time over which the boundary conditions were relaxed for each model. Note that all runs are calculated with $c_s = 10 \text{ km s}^{-1}$.

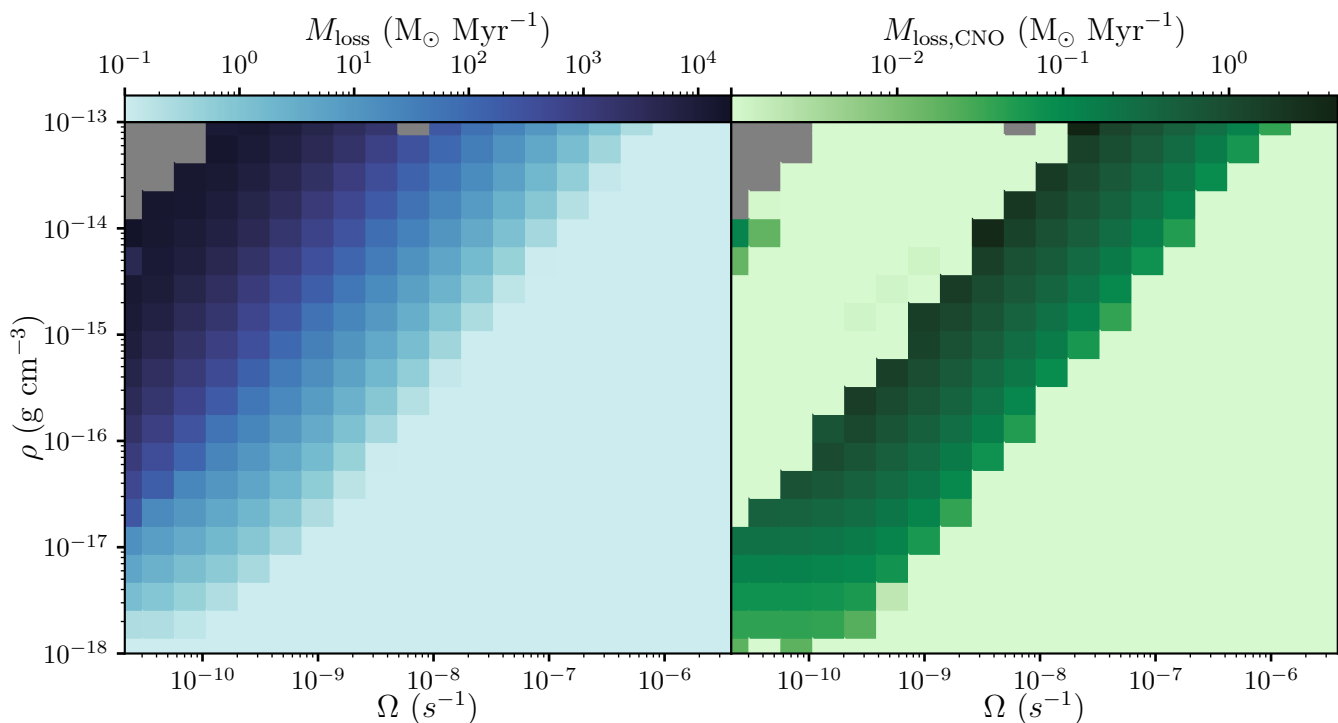


Figure 3.9: Average rates of mass (left: total, right: carbon, nitrogen, oxygen) loss from each model as a function of ρ and Ω . Gray squares indicate models that failed during boundary condition relaxation. The three models at high ρ and low Ω with unusually large CNO mass loss failed after boundary condition relaxation and significant accretion, but before much chemically homogeneous evolution. Note that all runs are calculated with $c_s = 10 \text{ km s}^{-1}$

In the low- Ω limit, as seen in Figure 3.6, quantities such as the maximum and final mass over the course of an AGN star's life become independent of Ω , and $\rho \gtrsim 5 \times 10^{-19} \text{ g cm}^{-3}$ at $c_s = 10^6 \text{ cm s}^{-1}$ is sufficient for stars to reach greater than $8 M_\odot$. Thus, Equation (3.65) can be used to predict in which regions of a disk stars will become massive before the end of their lives, subsequently they will forming compact objects. This result may be useful for studies of gravitational waves involving AGN disks, as well as interpretations of anomalous AGN flares.

The disk conditions where stars become 'immortal' can be seen in the high- ρ low- Ω area of Figure 3.7 where maximum masses begin to plateau. However, this distinction is easier to see in terms of the final mass of a star, or in the case of stars in the immortal regime, their asymptotic stellar mass. This quantity is plotted in Figure 3.8, which includes a power-law fit to the intermediate-immortal boundary, given by

$$\left(\frac{\rho}{\text{g cm}^{-3}} \right) \gtrsim 2.2 \times 10^{-3} \left(\frac{c_s}{10^6 \text{ cm s}^{-1}} \right)^{-1} \left(\frac{\Omega}{\text{s}^{-1}} \right)^{4/3}. \quad (3.66)$$

In the low- Ω limit, one can estimate based on Figure 3.6 that $\rho \gtrsim 2 \times 10^{-18} - 1 \times 10^{-16} \text{ g cm}^{-3}$ at $c_s = 10^6 \text{ cm s}^{-1}$ gives the location of the boundary, depending on ones assumption about radiative feedback. This expression may be useful for predicting the upper(lower) limits on $\rho(\Omega)$ where AGN stars may undergo supernova or other transient events at the end of their lives. We also include contours for stellar ages in Figure 3.8, which can be used to estimate whether or not a given AGN star would be able to reach its final mass within a disk lifetime. For disk lifetimes of $\sim 10 - 100 \text{ Myr}$, most intermediate stars will have time to reach the final stages of their evolution, even if initially only $1 M_\odot$. Additionally, as shown in Figure 3.5, both the rate of stellar mass loss and its composition can vary significantly for immortal stars.

We further investigate the mass loss rates of AGN stars and the metal content of the lost mass. From the left panel of Figure 3.9, we see that at low ρ or high Ω the total mass lost from a model is insignificant, while the opposite is true for stars that accrete more rapidly. This may be useful for gauging the kinematic impact of winds from AGN stars on accretion disks. For example, in the disk models of Thompson et al. (2005), there is a contribution to the pressure support from stellar feedback that is independent of disk opacity, there attributed to supernovae. However, the extreme mass loss rates from immortal stars could also provide significant pressure support and alter the disk commensurately. For example, consider an immortal star with $M_* \sim 400 M_\odot$, losing mass at a rate of $\sim 10^3 M_\odot/\text{Myr}$. We find that typical immortal stars have escape velocities in excess of 10^8 cm s^{-1} , not unlike massive OB stars (Lamers & Cassinelli, 1999; Smith, 2014). Using the escape velocity as a rough estimate of the outflow speed, this gives a ram pressure at the Hill radius ($R_H \sim 10^{16} \text{ cm}$ for $M_* \sim 400 M_\odot$) of $\sim 10^{-2} \text{ erg cm}^{-3}$. Depending on the accretion disk conditions, this can be well in excess of the ambient pressure of the AGN disk, ρc_s^2 , which ranges from 10^{-6} to $10^{-1} \text{ erg cm}^{-3}$ for the disk conditions explored in this study. Depending on the number of AGN stars within a given accretion disk, they may provide a significant fraction of the total pressure support.

Only the ejecta from intermediate stars is particularly metal rich, since those stars are able to progress through later stages of evolution, as demonstrated in the right panel of Figure 3.9. On the other hand, immortal stars have ejecta that is overall lower in metals, but is relatively more nitrogen rich (Figure 3.5), as their energy generation is dominated by the CNO cycle. Stars in the intermediate regime may also lose a significant amount of metal-enriched material during a supernova, but we have not included this contribution in our current analysis.

3.3.4 Rotation

Motivated by the above results, the investigation in [Jermyn et al. \(2021\)](#) took tidally-limited accretion as a baseline, additionally investigating the evolution of stellar spins. This came very naturally, as the angular velocity of the AGN disk at the location of the star determines both the Hill radius of the star and the degree of shear across the Hill or Bondi spheres. When using our fiducial mass-loss assumptions, not adjusting the definition of the Eddington limit, the evolutionary tracks presented in [Jermyn et al. \(2021\)](#) were essentially the same as those shown above in the tidally-limited case. However, by tracking the angular momentum of each model, [Jermyn et al. \(2021\)](#) was able to show additionally that the remnants left behind at the termination of intermediate stellar lives should be rapidly spinning.

However, when assuming that the stellar rotation rate affected the critical luminosity required to unbind the star, increasing the mass-loss rate, the outcomes of our stellar evolution calculations were strongly affected. The final and maximum masses for a grid of such models are shown in [Figure 3.10](#), and a schematic diagram linking various regions to parameter space to each outcome is shown in [Figure 3.11](#). The most significant difference in outcome, when modeling rotation-enhanced mass loss, is that many stars that might have been immortal instead expire — only immortal stars in the low-angular velocity high-density regime are spared.

The reason that many stars that might have been immortal instead expire is that they tend to spin up over time through accretion, at nearly constant mass. In principle, the gas these stars accrete might have specific angular momentum up to the Keplerian value, whereas the angular momentum lost by the star carries with it only the average specific angular momentum of the star. Thus, even if accretion and mass loss balance in time such that stellar masses remain roughly

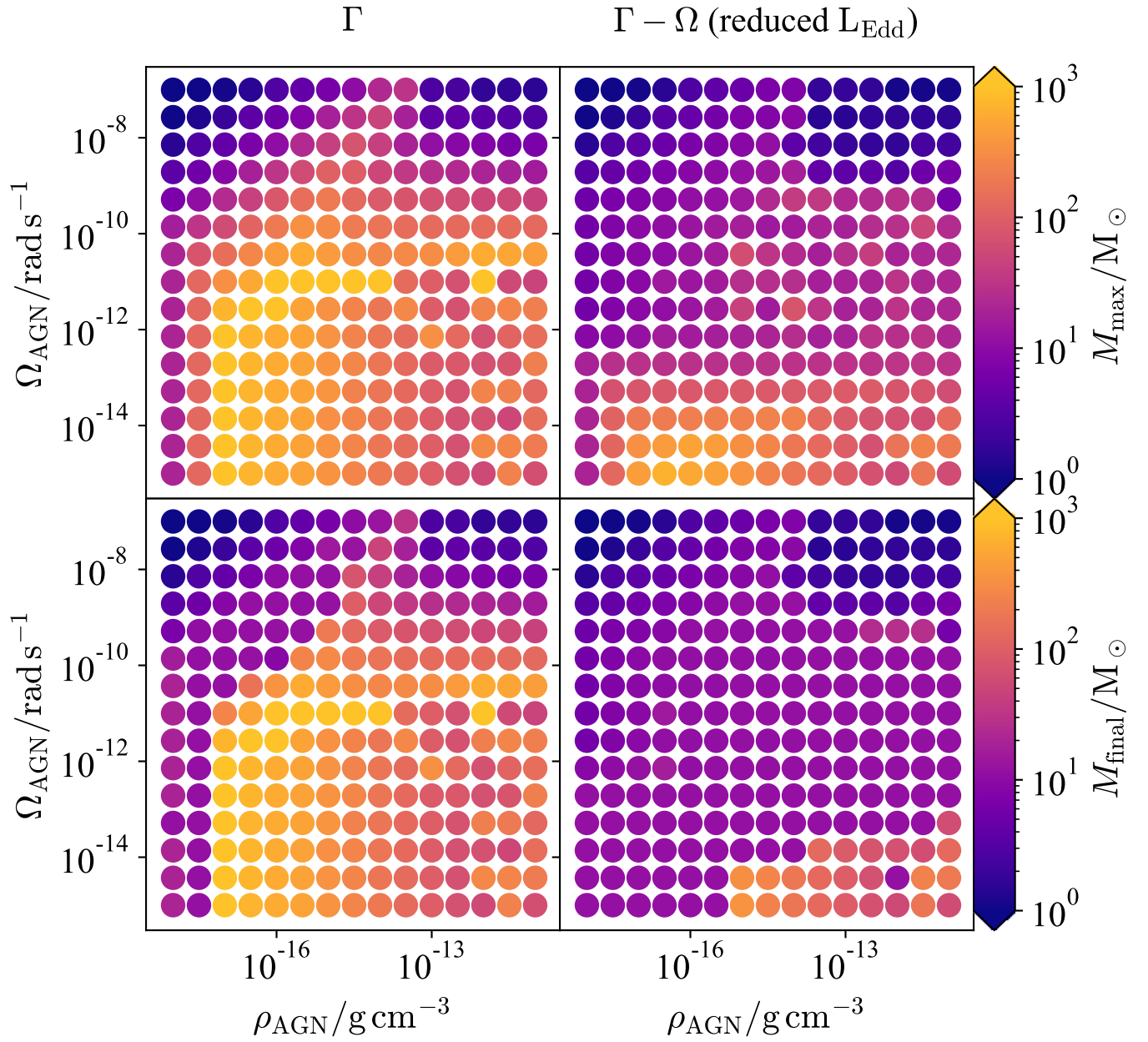


Figure 3.10: The peak mass (upper) and final mass (lower) in M_{\odot} is shown for each model with the Γ (left) and $\Gamma - \Omega$ (right) prescriptions as functions of the AGN density ρ_{AGN} and Keplerian angular velocity Ω_{AGN} .

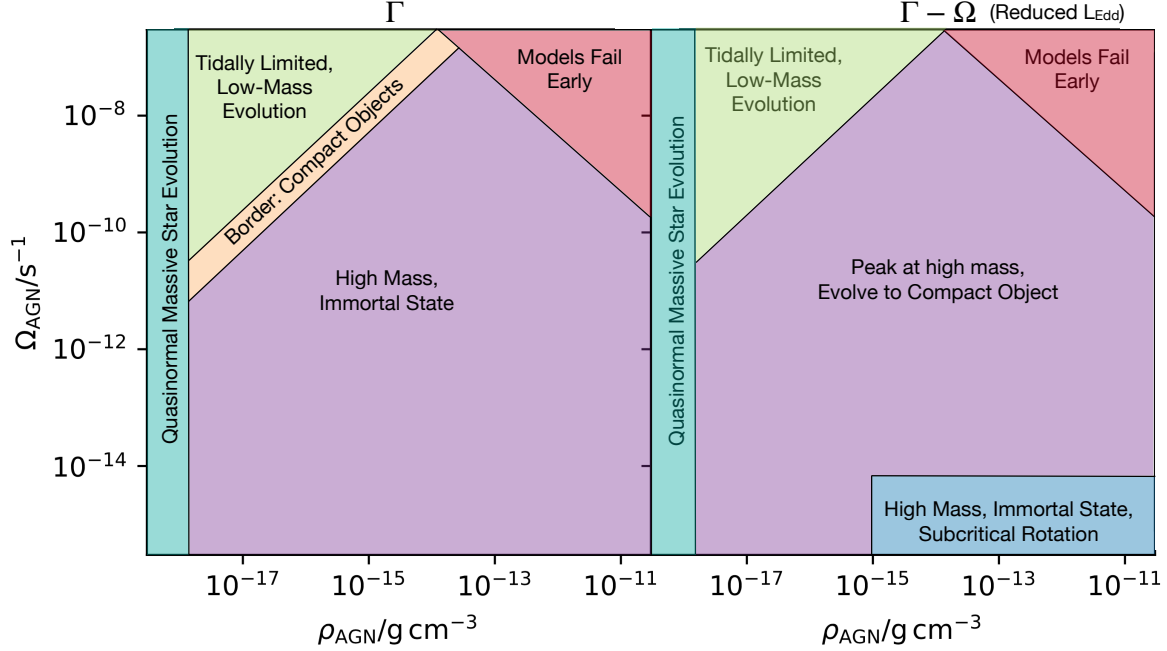


Figure 3.11: The boundaries between different kinds of evolution discussed in the text are shown for the grids with the Γ (left) and $\Gamma - \Omega$ (right) prescriptions as functions of the AGN density ρ_{AGN} and Keplerian angular velocity Ω_{AGN} .

constant, many stars can continue spinning up, eventually reaching sufficiently high spins that mass loss overtakes accretion, driving these stars towards core collapse.

3.3.5 Composition

Motivated by both the chemical yield results shown earlier in Figures 3.5 and 3.9, which suggest that a modest number of immortal stars might be able to convert a substantial — if not dominant — fraction of the mass flux through the AGN disk into helium (Jermyn et al., 2022), as well as some observations of active galactic nuclei (e.g., Dors et al., 2022),¹³ we undertook

¹³A few studies over the years have used spectroscopy to constrain the relative abundance of helium to hydrogen ($y \equiv n_{\text{He}}/n_{\text{H}}$) in active galaxies. For example, Bahcall & Oke (1971) estimated y in the range of 0.003 – 0.2 in a sample of 14 quasars, and Baldwin (1975) estimated y in the range of ~ 0.1 to ~ 0.3 in a sample of 14 quasars at redshifts $z \approx 0.2$. Naively estimating $Y \approx 4y/(1 + 4y)$, these measurements suggest values of Y ranging from ~ 0.012 to ~ 0.54 . However, these measurements may underestimate the helium abundance in these sources for reasons such as the steepness of the ionizing spectrum (Williams, 1971) or variability of the ionizing flux over time (Jura, 1973). Furthermore, modeling sufficiently reliable to determine the helium abundance from helium-to-

an investigation into the influence that disk composition would have on the evolution of stars embedded therein (Dittmann et al., 2023a).

As discussed in Section 3.2.2.1, an increased helium mass fraction for the accreting material should decrease the electron scattering opacity, increasing the Eddington luminosity, requiring the star to reach higher luminosities before driving appreciable mass loss. However, as discussed in Section 3.1.2, as the mean molecular weight in the interior of a star increases, that star will tend to become hotter and more luminous. We tested both effects somewhat independently by using both the helium-reduced opacity as well as a fiducial pure ionized hydrogen electron scattering opacity when defining the Eddington luminosity. Because we investigated a wide range of helium mass fractions, we limited our study by not including tidal reductions to the accretion rate in order to keep the number of simulations manageable.

Trends in the typical maximum and final masses (denoted M_{final} and M_{max} respectively) over the full range of densities and helium mass fractions investigated in this study are shown in Figure 3.12, in which the top row includes results from simulations which held κ fixed when calculating L_{Edd} , and the bottom row includes results from simulations which varied κ in concert with Y . The left column, which illustrates the maximum masses achieved by each model, demonstrates that at each constant density stars reach smaller maximum masses as Y increases, a natural result of their increased luminosity at constant mass. Similarly, for standard and intermediate stars, as well as transitioning between the intermediate and immortal regimes, maximum masses increase at constant Y as density increases.

hydrogen line ratios has remained elusive at the densities of quasar broad line regions due to factors such as the importance of three-body recombination (e.g Netzer, 1990).

Recently, Dors et al. (2022) measured Y in a sample of 65 Seyfert 2 narrow-line regions at redshifts $z \lesssim 0.2$, finding values of Y ranging from ~ 0.2 to ~ 0.46 . In contrast, the sample of 85 star forming regions studied in Dors et al. (2022) using the same methodology range in Y from ~ 0.18 to ~ 0.3 , suggesting significant helium enrichment in active galaxies.

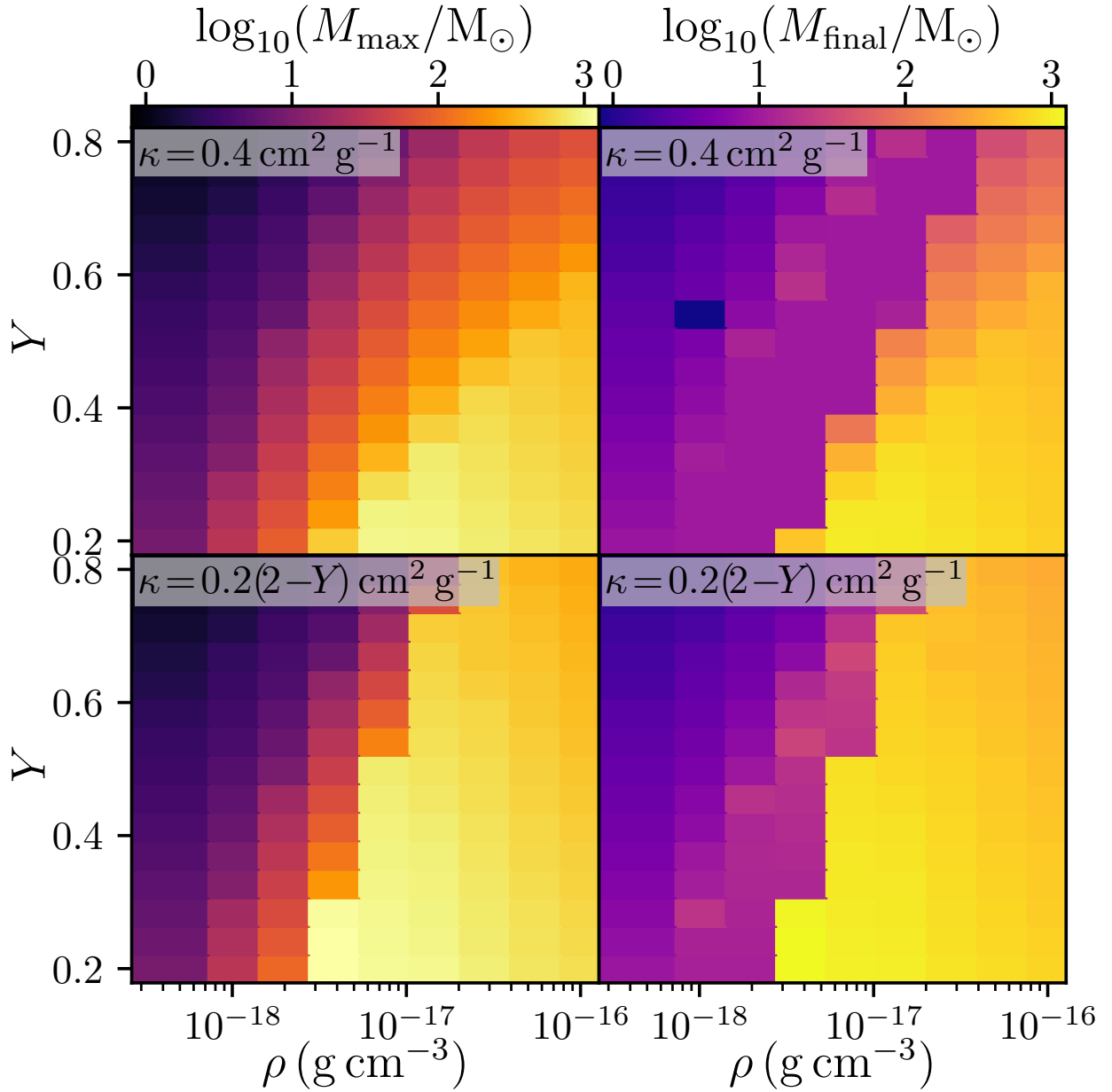


Figure 3.12: The maximum (left column) and final (right column) masses achieved by AGN stars as functions of ρ and Y , using both $\kappa = 0.4 \text{ cm}^2 \text{ g}^{-1}$ (top row) and $\kappa = 0.2(2 - Y) \text{ cm}^2 \text{ g}^{-1}$ (bottom row) when calculating L_{Edd} . All simulations used an ambient sound speed of $c_s = 10^6 \text{ cm s}^{-1}$.

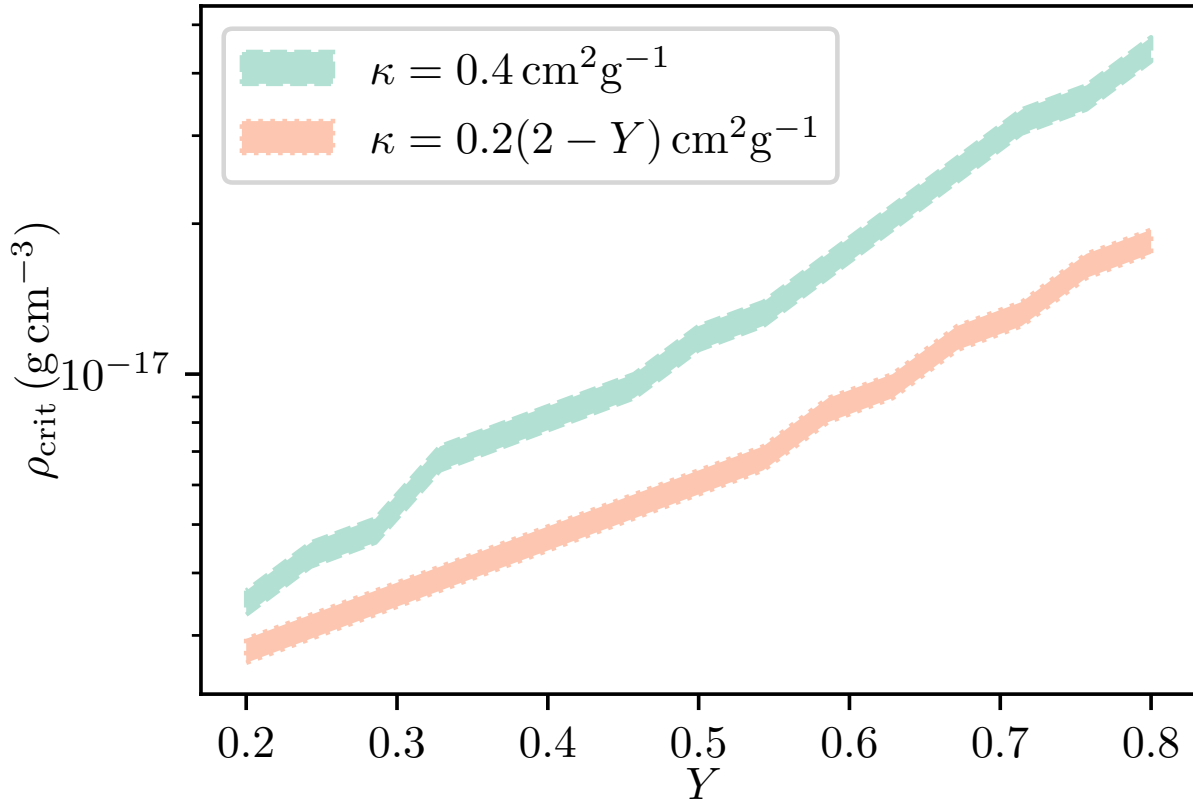


Figure 3.13: The constraints on the density at which AGN stars transition from intermediate to immortal (ρ_{crit}) from our simulations. The green dashed line and corresponding shaded region display results for simulations which used $\kappa = 0.4 \text{ cm}^2 \text{ g}^{-1}$ when calculating L_{Edd} , and the orange dotted lines and corresponding shaded region display results from our simulations using $\kappa = 0.2(2 - Y) \text{ cm}^2 \text{ g}^{-1}$ when calculating L_{Edd} .

The right column of Figure 3.12 shows the final masses of our stellar models, and is particularly useful for differentiating immortal and intermediate stars, where the former tend to have ‘final’ masses in excess of $100 M_{\odot}$ and the latter tend to have final masses around $\sim 10 M_{\odot}$. We investigated the transition between immortal and intermediate stars more closely by performing an additional set of simulations at each Y over the density range where the intermediate-to-immortal transition occurs, the results of which are shown in Figure 3.13. Following from the two opacity formulas differing most significantly at high Y and being identical at $Y = 0$, the critical densities required to support immortal stars, between the two opacity prescriptions, are closest at $Y = 0.2$, gradually growing further apart as Y increases. We also confirm the result gleaned from a more sparse sampling of the parameter space in Figure 3.12, although to a lesser extent in the $\kappa = 0.2(2 - Y) \text{ cm}^2 \text{ g}^{-1}$ case, that ρ_{crit} increases at higher helium mass fractions.

3.4 Astrophysical Implications

The results of stellar evolution in AGN disks depend strongly not only on the ambient gas density and temperature, but also the strength of the gravity of the SMBH on the gas surrounding a given star. This can lead to a complex radial dependence to how stars and accretion disks interact with one another. Although we do not yet have a comprehensive picture of how many immortal, intermediate, and standard stars ought to reside within a given AGN disk, the effects of individual intermediate and immortal stars are more clear.

Massive stars in AGN disks, and the near-Eddington mass loss they experience, can alter the accretion disk composition and structure significantly. As shown in Figure 3.9, AGN stars in the intermediate accretion regime can supply the disk with metals at rate of $\sim 0.1 - 2 M_{\odot}$ per Myr,¹⁴

¹⁴Arguably, the low rate quoted here might be somewhat misleading. Each star ejects metals into the disk during

even when accreting a mixture containing only hydrogen and helium. Additionally, as shown in Figure 3.8, many of these stars end their lives with masses $\gtrsim 10 M_{\odot}$, and may further enrich the disk and surrounding regions, as suggested by Artymowicz et al. (1993). Through both mass loss and supernovae, metallicity enrichment has a sensitive dependence on the disk properties ρ , c_s , and Ω . Metallicity enrichment could be further complicated by migration through the disk, (e.g. Lyra et al., 2010; Paardekooper et al., 2010; Tanaka et al., 2002), which can also be altered by the near-Eddington luminosities of AGN stars (e.g. Hankla et al., 2020). Detailed modeling along those lines is beyond the scope of the present work, but Equations (3.65) and (3.66) may prove useful to such efforts.

Despite these difficulties, AGN stars are a promising channel for producing the supersolar metallicities frequently inferred in both high- and low-redshift AGN (e.g. Hamann et al., 2002; Maiolino & Mannucci, 2019; Storch-Bergmann & Pastoriza, 1989; Xu et al., 2018), as discussed in Chapter 1. Additionally, if these stars undergo supernova explosions, they could significantly enhance the iron abundance in the disk, and could be partially responsible for the large iron abundances inferred from X-ray emission line analyses (e.g. Nandra et al., 1997; Tanaka et al., 1995, if these inferences turn out to be robust).

Although the mass lost from immortal AGN stars is not as metal-rich as that from their intermediate counterparts, nitrogen makes up a much larger fraction of the metal content of their winds, as shown in Figure 3.5. A large population of such stars may lead to an overabundance of nitrogen with comparatively little metallicity enhancement. This scenario bears some resemblance to nitrogen-rich quasars, a subset ($\sim 1\%$) of quasars that show anomalously strong nitro-

the later mass-loss-dominated stage of its life, which can last just a few Myr. However, the rate of metal enrichment quoted for each star includes the drawn-out accreting epoch of the star's life, which would be appreciably truncated if the initial star were more massive.

gen lines and elevated nitrogen-to-carbon abundance ratios (e.g. [Batra & Baldwin, 2014](#); [Bentz et al., 2004](#); [Bentz & Osmer, 2004](#); [Jiang et al., 2008](#); [Matsuoka et al., 2009](#)). In a subset of these quasars, variability in nitrogen-to-carbon line ratios has been demonstrated on timescales of \sim years, sometimes attributed to tidal disruptions of evolved stars ([Kochanek, 2016](#); [Liu et al., 2018](#)). The portion of the population not displaying variability may be linked to immortal stars within the accretion disk.

As shown in [Figure 3.8](#), there is a window in ρ and Ω where AGN stars are both in the intermediate accretion regime, and can potentially reach the end of their lives within an AGN disk lifetime. For stars that primarily undergo Bondi accretion ($R_B \ll R_H$ for most of the star’s growth) $\dot{M} \propto M_*^2$ and the accretion timescale is inversely proportional to the star’s mass. On the other hand, for stars in comparatively high- Ω disks where accretion is limited by tidal effects ($R_B \gg R_H$), $\dot{M} \propto M_*^{2/3}$ and the accretion timescale grows slowly with stellar mass. In these limits one can extrapolate the contours in [Figure 3.8](#) accordingly, but intermediate cases ($R_B \sim R_H$) are less straightforward. Notably, stellar rotation can alter this picture. If stellar rotation enhances mass loss as in our $\Gamma-\Omega$ prescription, many stars that might have been immortal instead reach the end of their lives after a period of rapid accretion. Overall, such a sequence would lead to supernovae during a given accretion episode with more regularity.

The results of our studies on rotation, particularly that stars within AGN disks may rotate quite quickly, suggest that long gamma ray bursts (GRBs) might occur within AGN disks following stellar deaths. The γ -ray emission in these events is believed to be produced by a relativistic jet (e.g., [MacFadyen & Woosley, 1999](#); [Tchekhovskoy et al., 2011](#)), a key ingredient in which is a black hole accreting high angular momentum material from the stellar carcass. However, GRBs occurring in AGN disks are likely to appear quite different to their near-vacuum counterparts, if

they can be observed at all. For example, if the stars are embedded within the AGN disk upon their death, the jet itself may be retained within the AGN disk photosphere, and light may finally diffuse out over periods of weeks to months (e.g., [Perna et al., 2021a](#); [Wang et al., 2022b](#)).

It is believed that the Milky Way experienced an AGN phase about 2-8 Myr ago ([Bland-Hawthorn et al., 2019](#); [Su et al., 2010](#)). With its directly available observations of stellar populations and stellar remnants, the Galactic Center (GC) is a prime target for testing the possible impact of AGN stars evolution ([Cantiello et al., 2021](#)). The central parsec contains an unexpected large number of young massive stars ([Alexander, 2005](#); [Ghez et al., 2003](#)), with O/WR stars confined to the inner 0.5 pc region ([Bartko et al., 2010](#); [Paumard et al., 2006](#)). The present day mass function of these stars is top-heavy ([Genzel et al., 2010](#)). Contrary to theoretical expectations ([Bahcall & Wolf, 1976, 1977](#)), the relative fraction of low-mass stars decreases moving towards the GC ([Do et al., 2017](#); [Genzel et al., 2010](#)). Spectroscopy reveals that some of the stars in the GC may be He-rich ([Do et al., 2018](#); [Habibi et al., 2017](#); [Martins et al., 2008](#)), which would follow naturally from formation in or accretion from a helium-enriched disk.

Chapter 4: Black Hole Binaries in AGN Disks

4.1 Introduction

As discussed in Chapters 1 and 2, the accretion disks around SMBHs, are a potential host site for merging stellar-mass black holes. Stellar mass black holes embedded in these disks will grow via gas accretion, and potentially through repeated mergers facilitated by the deep potential well of the SMBH (e.g. [Gerosa & Fishbach, 2021](#); [McKernan et al., 2012](#)). Thus, AGN disks are readily able to produce black holes within the pair instability mass gap, such as those inferred to have caused GW190521 ($85^{+21}_{-14} M_{\odot}$ and $66^{+17}_{-18} M_{\odot}$ at 90% confidence ([Abbott et al., 2020b](#)); however, see [Nitz & Capano 2021](#)). Additionally, the presence of gas introduces the *possibility* of electromagnetic counterparts to stellar-mass black hole binary mergers (e.g. [McKernan et al., 2019](#); [Stone et al., 2017](#); [Tagawa et al., 2023](#)). Flaring AGN have been associated with the localization error volumes of not only GW190521 ([Graham et al., 2020](#)), but also eight other gravitational wave events ([Graham et al., 2023](#)) during the third observing run of Advanced LIGO and Advanced VIRGO ([The LIGO Scientific Collaboration et al., 2021](#)), although these associations may not be statistically robust (e.g. [Nitz & Capano, 2021](#); [Palmese et al., 2021](#)).

Numerous investigations have estimated the rates of black hole binary mergers within AGN disks using semi-analytical methods or one-dimensional simulations (e.g. [Bartos et al., 2017](#); [McKernan et al., 2020a,b](#); [Stone et al., 2017](#); [Tagawa et al., 2020](#)), and it has been estimated that

up to $\sim 80\%$ of the black hole binary mergers detected by LIGO/VIRGO may occur within AGN disks (Ford & McKernan, 2022).

The progenitors of these gravitational wave events — stars and compact objects — may be captured into the disk from a nuclear star cluster through, for example, torques from the gaseous disk or dynamical friction (e.g. Artymowicz et al., 1993; MacLeod & Lin, 2020; Rauch, 1995; Syer et al., 1991). Additionally, gravitational instability in the outer regions of AGN disks may lead to star formation (e.g. Goodman, 2003; Kolykhalov & Syunyaev, 1980). Furthermore, as reviewed in Chapter 3, stellar evolution simulations suggest that most stars captured into or formed within AGN disks will leave behind black holes and neutron stars at the end of their lives (Ali-Dib & Lin, 2023; Cantiello et al., 2021; Dittmann et al., 2021, 2023a; Jermyn et al., 2021), and neutron stars within the disk will likely accrete from the disk to the point of collapse (e.g. Pan & Yang, 2021; Perna et al., 2021b).

A growing body of work has studied binary formation within AGN disks using multi-dimensional N-body simulations (e.g. Li et al., 2022a; Secunda et al., 2019, 2020) as well as hydrodynamical simulations (e.g. Li et al., 2023; Rowan et al., 2023a,b; Whitehead et al., 2023). An assumption that pervades the literature on black hole binary mergers within AGN disks is that gas-binary interactions help drive binaries towards inspiral. This assumption stems from early analytical (e.g. Artymowicz et al., 1991; Pringle, 1991) and numerical (e.g. MacFadyen & Milosavljević, 2008) work on isolated binary-disk interaction. However, subsequent higher-resolution and longer-duration simulations of circumbinary accretion have demonstrated that binary inspirals are far from universal (e.g. Dittmann & Ryan, 2021, 2022; Lai & Muñoz, 2023; Moody et al., 2019; Muñoz et al., 2020, 2019; Tiede et al., 2020; Wang et al., 2023).

Whether binaries inspiral or outspiral due to interactions with a circumbinary disk depends

on the binary eccentricity (e.g. [Miranda et al., 2017](#)), disk aspect ratio (e.g. [Dittmann & Ryan, 2022](#); [Tiede et al., 2020](#)), disk viscosity (e.g. [Dittmann & Ryan, 2022](#); [Miranda et al., 2017](#)), and binary mass ratio (e.g. [Dempsey et al., 2021](#); [Muñoz et al., 2020](#)).

Studies of viscous circumbinary disks inclined relative to their binaries have found that the binary and disk are typically brought into alignment in the circular case (e.g. [Lubow et al., 2015](#); [Moody et al., 2019](#)), but also that disks may equilibrate to a polar configuration about eccentric binaries (e.g. [Martin & Lubow, 2017](#)).

Compared to the study of isolated binaries, the study of embedded binaries is nascent. Early studies pursued global two-dimensional simulations, identifying the importance of resolution (c.f. [Baruteau et al., 2011](#); [Li et al., 2021b](#)), binary orientation ([Li et al., 2021b](#)), and disk thermodynamics ([Li et al., 2022b](#)). More recently, two-dimensional shearing-sheet simulations have surveyed binary eccentricity and mass ratio ([Li & Lai, 2022a](#)), typically finding that binaries shrink and eccentricities are damped. Recent two-dimensional studies have also surveyed the gas equation of state and binary separation ([Li & Lai, 2022b](#)).

Heretofore the only three-dimensional simulations of binary stellar-mass black holes embedded in AGN disks have been those presented in [Dempsey et al. \(2022\)](#). Using isothermal shearing-box simulations that directly evolve the three-body orbital evolution of the system, that work illustrated the dependence of binary orbital evolution on the binary separation; balance between gravitational forces and gas pressure; and the dimensionality of the problem, finding that three dimensional flows dramatically differ in structure compared to those found in two-dimensional simulations.

All previous simulations of binaries embedded in AGN disks have focused on binary orbits aligned or anti-aligned with the midplane of the SMBH disk, while in reality binaries may form

with a wide range of inclinations and eccentricities. In particular, the two-dimensional simulations of gas-assisted binary formation by [Li et al. \(2023\)](#) suggest that newly-formed binaries should form with high eccentricities, predominantly in retrograde configurations. Thus motivated, we focused in the present study on the orbital evolution of inclined embedded binaries, and investigated the evolution of eccentric binaries in a companion paper ([Calcino et al., 2023](#)), in both cases investigating both prograde and retrograde binaries.

We review AGN disk models and the orbits of embedded binaries in [Section 4.2](#), and describe our simulation methodology in [Section 4.3](#). We present the results of our simulations in [Section 4.4](#), including that retrograde binaries can inspiral more than four times faster than prograde binaries and binary inclinations are gradually driven to zero. We discuss some shortcomings of the present study, as well as its implications for mergers in AGN disks and various dynamical phenomena, in [Section 4.5](#). We conclude in [Section 4.6](#), and provide additional technical details in [Appendix B.1](#). We present some convergence tests in [Appendix B.2](#) and tabulate some of our results in [Appendix B.3](#).

4.2 Binaries in AGN Disks

4.2.1 Objects Embedded in AGN Disks

The accretion disks that fuel AGN are typically modeled by finding solutions to the equations of viscous hydrodynamics, often under the assumptions of azimuthal symmetry, a steady state, and the limit of a thin disk such that the disk pressure scale height H at a given radial distance r_{\bullet} is $H \ll r_{\bullet}$ (e.g. [Frank et al., 2002](#); [Novikov & Thorne, 1973](#); [Shakura & Sunyaev, 1973](#); [Sirko & Goodman, 2003](#); [Thompson et al., 2005](#)), although models which relax some of

these assumptions have also been developed (e.g. [Abramowicz et al., 1988](#); [Gilbaum & Stone, 2022](#); [Sądowski, 2009](#)). A common feature of many disk models is that at large distances from the center the free-fall timescale of the gas disk becomes shorter than the dynamical timescale leading to gravitational instability (e.g. [Toomre, 1964](#)) and the formation of stars (e.g. [Derdzinski & Mayer, 2023](#); [Kolykhalov & Syunyaev, 1980](#)). Some disk models have accounted for this by imposing marginal stability arbitrarily (e.g. [Sirko & Goodman, 2003](#)) or by invoking feedback from stars or black holes embedded in the disk (e.g. [Dittmann & Miller, 2020](#); [Gilbaum & Stone, 2022](#); [Thompson et al., 2005](#)).

We provide examples of several AGN disk models from the literature in [Figure 4.1](#) (see also [Figure 1](#) of [Dempsey et al. 2022](#)), specifically their aspect ratios H/r_\bullet , surface densities (Σ), the ratio of local disk mass to object mass, ratio of the Hill radius to disk scale height, and characteristic timescales for stellar mass objects to change their orbits.

Restricting ourselves to thin disks ($H \ll r_\bullet$) which are vertically isothermal, the density profile as a function of height above the disk midplane (z) at a given radius is $\rho(z) = \rho_0 \exp[-(z/H)^2/2]$, where ρ_0 is the density in the disk midplane and H is the pressure scale height of the disk. Furthermore, $H = c_s/\Omega$, where c_s is the sound speed within the disk at a given radius, $\Omega = \sqrt{GM_\bullet/r_\bullet^3}$ is the angular velocity of the disk, and M_\bullet is the SMBH mass. Considering objects¹ of mass $m \ll M_\bullet$ embedded within the AGN disk, the characteristic length scale within which gas is bound to the embedded object rather than the SMBH is the Hill radius ([Hill, 1878](#)),

$$R_H = r_\bullet \left(\frac{m}{3M_\bullet} \right)^{1/3}. \quad (4.1)$$

¹Within this subsection the difference between individual objects and tightly-bound binaries is immaterial so we use ‘object’ in place of either.

The local disk mass (M_d) within the Hill sphere of an object is given, assuming only vertical density variation, by

$$M_d = 2\pi\rho_0 H \left(\sqrt{\frac{\pi}{2}} (R_H^2 - H^2) \operatorname{erf} \left(\frac{R_H}{H\sqrt{2}} \right) + R_H H e^{-\frac{R_H^2}{2H^2}} \right). \quad (4.2)$$

The ratio R_H/H is a measure of the strength of gravitational forces relative to gas pressure, as well as the degree to which the disk is vertically stratified within the vicinity of the embedded object. In the limit $R_H \ll H$, the gas surrounding an embedded object has a near-constant density and the local disk mass is $M_d \approx 4\pi\rho_0 R_H^3/3$. In the limit $R_H \gg H$, the gas about an embedded object is strongly stratified and the local disk mass is $M_d \approx \sqrt{2\pi^3}\rho_0 R_H^2 H$. As illustrated in Figure 4.1, objects embedded in AGN disks can occupy both extremes. Previous studies have demonstrated that R_H/H significantly influences the orbital evolution of binaries embedded within accretion disks, with more-embedded binaries inspiraling more quickly at a given orbital separation (e.g. [Dempsey et al., 2022](#)).

The ratio M_d/m gauges whether the self-gravity of the gas disk is dynamically relevant to the orbital evolution of embedded objects. Throughout most of the AGN disk models shown in Figure 4.1 the self-gravity of the AGN disk should have a negligible effect on the dynamics of embedded objects, although it may be marginally important in the outer regions of the disks modeled in [Dittmann & Miller \(2020\)](#). Therefore, we are somewhat justified neglecting in our simulations the disk self-gravity and the back-reaction of gas upon the black holes.

The orbit of an embedded object about the SMBH can be characterized by a semi-major axis a , an eccentricity e , and an inclination angle relative to the disk midplane i . As embedded objects orbit within the disk, they excite waves that can transfer orbital energy and angular mo-

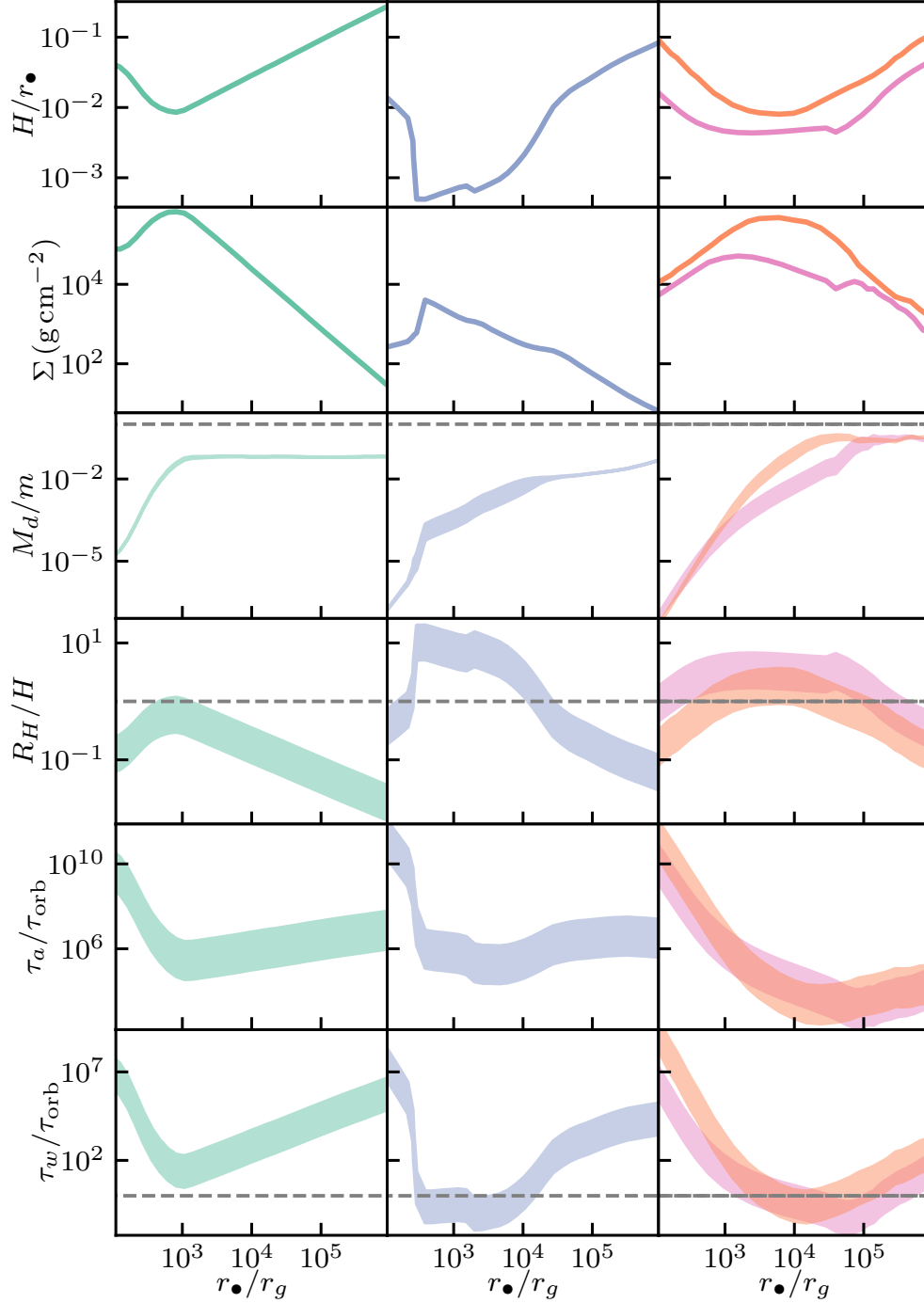


Figure 4.1: Four example AGN disk models: the left and center panels display AGN disk models (those of Sirko & Goodman (2003) and Thompson et al. (2005) respectively) around $M_{\bullet} = 10^8 M_{\odot}$ SMBHs computed in Bellovary et al. (2016); and the right column displays models for disks around $4 \times 10^6 M_{\odot}$ SMBHs computed in Dittmann & Miller (2020), based on Thompson et al. (2005) but making different assumptions about feedback and gas opacity. The first two rows display the disk aspect ratio and surface density. The bottom four rows display the range of M_d/m , R_H/H , τ_a/τ_{orb} , and τ_w/τ_{orb} for objects with masses ranging from $5 M_{\odot}$ to $300 M_{\odot}$. Horizontal dashed gray lines plot the line $y = 1$ where applicable.

mentum between the disk and object. Because the mass of an embedded object is typically much smaller than the mass of the corresponding SMBH, we approximate the timescales to change the orbital elements (τ_a for the semi-major axis and τ_w for the eccentricity and inclination) using the classical Type I values (Goldreich & Tremaine, 1980; Tanaka et al., 2002; Tanaka & Ward, 2004)

$$\tau_a \approx \left(\frac{M_\bullet}{\Sigma r_\bullet^2} \right) \left(\frac{H}{r_\bullet} \right)^2 q^{-1} \tau_{\text{orb}}, \quad (4.3)$$

$$\tau_w \approx \left(\frac{H}{r_\bullet} \right)^2 \tau_a \quad (4.4)$$

where $q \equiv m/M_\bullet$ and $\tau_{\text{orb}} \equiv \Omega^{-1}$ is the local orbital timescale. Because astrophysical disks generally have $H/r_\bullet < 1$, τ_w will generally be shorter than τ_a .

The ratio between τ_a and τ_{orb} measures the rate of change of the semi-major axis of an embedded object. If $\tau_a/\tau_{\text{orb}} \gg 1$, then the physical properties of the AGN disk are roughly constant on the orbital timescale of the embedded object. In this case the local AGN disk properties in the vicinity of an embedded objects are approximately constant, whereas if $\tau_a \sim \tau_{\text{orb}}$ the disk properties change relatively rapidly. In our simulations of embedded binaries, we assume that the properties of the AGN disk are constant in time, which is justified when $\tau_a/\tau_{\text{orb}} \gg 1$. Considering the disk models shown in Figure 4.1, the steady-state assumption in our simulations is reasonable in all AGN disk regions save for the outer regions of the disk models calculated in Dittmann & Miller (2020).

Objects formed within the disk will typically have inclinations $i \lesssim H/r_\bullet$, while objects captured into the disk may have larger initial inclinations ($i > H/r_\bullet$) that are eventually damped to $i \lesssim H/r_\bullet$. Additionally, gravitational scattering events between embedded objects may excite orbital eccentricities and inclinations over time (e.g. Stewart & Ida, 2000). For example, Stone

et al. (2017) estimated that over 10^8 years, typical inclinations exceeded H/r by factors of order unity far from the SMBH and more than an order of magnitude closer in. Assuming that binaries form within the disk with orbital separations $a_b \sim R_H$ (e.g., Li et al., 2023), in regions of the disk where $R_H/H \lesssim 1$ and $\tau_w/\tau_{\text{orb}} \gtrsim 1$ binaries may form with virtually any orientation relative to the disk midplane. On the other hand, where $\tau_w/\tau_{\text{orb}} \lesssim 1$, binaries will likely form in the disk midplane, either aligned or anti-aligned with the orbit of the binary about the SMBH, although the linear analysis performed in Tanaka & Ward (2004) breaks down in the $\tau_w/\tau_{\text{orb}} \lesssim 1$ limit. In regions with $\tau_w/\tau_{\text{orb}} > 1$, binary-single interactions may excite inclination even in binaries which are initially coplanar with the disk midplane (e.g. Tagawa et al., 2020).

4.2.2 Binary Orbits in AGN disks

In this section, we introduce basic definitions related to black hole binaries (BHBs) in AGN disks, drawing from Chapter 6 of Danby (1988). Subsequently, we briefly review relevant dynamical phenomena.

4.2.2.1 Definitions

The BHB is characterized by both its specific energy and its specific angular momentum vector,

$$\mathcal{E} = \frac{1}{2}\vec{v} \cdot \vec{v} - \frac{Gm_b}{|\vec{r}|}, \quad \vec{h} = \vec{r} \times \vec{v}, \quad (4.5)$$

where $m_b = m_1 + m_2$ is the binary mass, $\vec{r} = \vec{r}_2 - \vec{r}_1$ is the relative position vector and $\vec{v} = \vec{v}_2 - \vec{v}_1$ is the relative velocity vector. From \mathcal{E} and $h \equiv \sqrt{\vec{h} \cdot \vec{h}}$, we define the orbital semi-major axis, a_b ,

and eccentricity, e_b , using the well-known relations

$$a_b = -\frac{Gm_b}{2\mathcal{E}}, \quad e_b^2 = 1 - \frac{h^2}{Gm_b a_b}. \quad (4.6)$$

In addition to the scalar eccentricity, we also define the eccentricity vector which, in the orbital plane, points toward the periapse,

$$\mathbf{e} = \frac{\mathbf{v} \times \mathbf{h}}{Gm_b} - \frac{\mathbf{r}}{|\mathbf{r}|}. \quad (4.7)$$

Orienting an inclined and eccentric BHB in space requires three additional angles (i_b, ω_b, Ω_b) which are respectively the orbit inclination, argument of periapse, and longitude of the ascending node. For reference, we illustrate this connection in Figure 4.2. From the schematic, the orientation angles are related to \vec{h} and \vec{e} via,

$$\cos i_b = h_z/h, \quad (4.8)$$

$$\cos \Omega_b = -h_y/h_\perp, \quad (4.9)$$

$$\sin \Omega_b = h_x/h_\perp, \quad (4.10)$$

$$e_b \cos \omega_b = e_x \cos \Omega_b + e_y \sin \Omega_b, \quad (4.11)$$

$$e_b \sin \omega_b = -e_x \sin \Omega_b + e_y \cos \Omega_b, \quad (4.12)$$

where because ω_b and Ω_b are each confined to a plane they can be oriented without ambiguity, i_b simply takes values between 0 and π ,² and we have defined the magnitude of the in-midplane component of the binary angular momentum vector to be $h_\perp \equiv \sqrt{h_x^2 + h_y^2}$. We note that the role

²A number of textbooks on dynamics have included typos in their analogs to these expressions. See, for example, the list of known errors in Murray & Dermott (1999, <https://www.solarsystemdynamics.info/known-errors>).

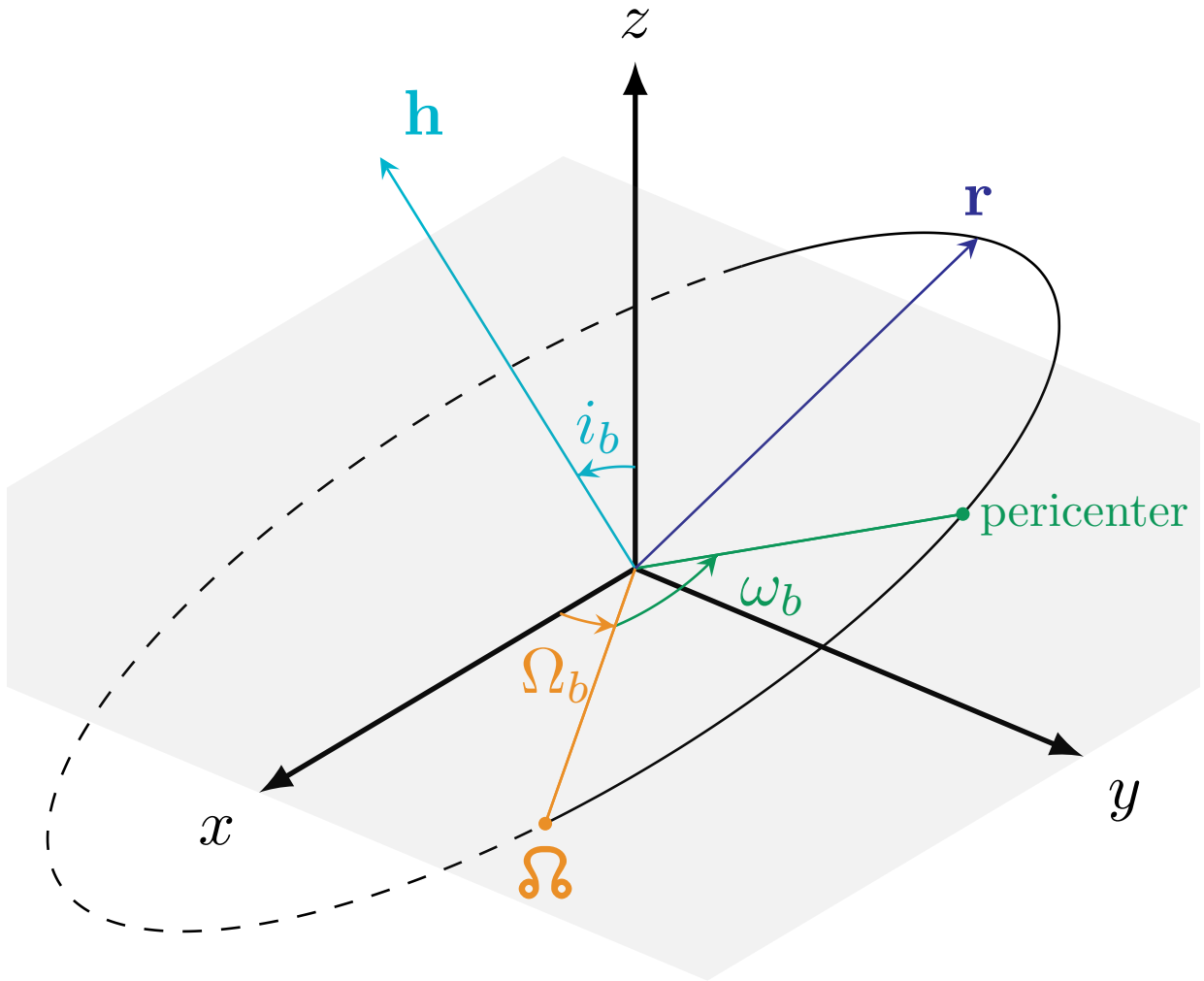


Figure 4.2: A schematic of a binary orbit oriented in three-dimensional space. The reference plane is shown in gray, and the portion of the orbit below the plane is plotted using a dashed line. The ascending node, the point at which \mathbf{r} passes from below to above the reference plane, is marked as Ω .

of Ω_b in the expressions for ω_b is simply a rotation in the $x - y$ plane, and that Ω_b is undefined when $h_\perp = 0$, in which case only $\Omega_b + \omega_b$ is a meaningful quantity and we set $\Omega_b = 0$.

Gravitational interaction with the surrounding gas changes the binary's total energy, E , and angular momentum, \vec{J} . These are related to the specific values through the reduced mass $\mu_b = m_1 m_2 / m_b$ such that,

$$E \equiv \mu_b \mathcal{E}, \quad \vec{J} = \mu_b \vec{h} \quad (4.13)$$

The power delivered to the binary, \dot{E} , and the total torque on the binary, $\dot{\vec{J}}$, together with the mass accretion rates $\dot{m}_{1,2}$, induce changes in a_b and e_b at the rates,

$$\frac{\dot{a}_b}{a_b} = \frac{\dot{m}_1}{m_1} + \frac{\dot{m}_2}{m_2} - \frac{\dot{E}}{E} \quad (4.14)$$

$$\frac{e_b \dot{e}_b}{1 - e_b^2} = \frac{\dot{m}_1}{m_1} + \frac{\dot{m}_2}{m_2} - \frac{1}{2} \frac{\dot{m}_b}{m_b} - \frac{\dot{J}}{J} - \frac{\dot{E}}{E}, \quad (4.15)$$

where $\dot{J} = \dot{\vec{J}} \cdot \vec{J} / J$. In addition to \dot{a}_b and \dot{e}_b , the orientation angles change with the rates

$$\dot{i}_b = \frac{\dot{h}_z h - h_z \dot{h}}{h \sqrt{h^2 - h_z^2}}, \quad (4.16)$$

$$\dot{\Omega}_b = \frac{\dot{h}_y h_x - \dot{h}_x h_y}{h_x^2 + h_y^2}, \quad (4.17)$$

$$\dot{\omega}_b = \frac{\dot{e}_b \cos \omega_b - (\dot{e}_x + e_y \dot{\Omega}_b) \cos \Omega_b - (\dot{e}_y - e_x \dot{\Omega}_b) \sin \Omega_b}{e_y \cos \Omega_b - e_x \sin \Omega_b}. \quad (4.18)$$

When $\sin(i_b) = 0$, neither Ω_b nor ω_b is well defined, while their sum, the longitude of periapsis

$\varpi_b = \Omega_b + \omega_b$, is. In this case the rate of precession of the orbit is given by

$$\dot{\varpi}_b = \frac{\dot{e}_y e_x - \dot{e}_x e_y}{e_b^2}. \quad (4.19)$$

In Appendix B.1 we provide further details on how we measure changes in the binary energy, angular momentum, and other quantities; how we derive average rates of change of binary orbital elements using these measurements; and list additional mathematical relations omitted here for brevity. In Section 4.4, we will make use of a coordinate system aligned with the BHB made up of the triad \vec{h} , \vec{r} , and $\vec{h} \times \vec{r}$.

4.2.2.2 Dynamics

We briefly draw attention to a few flavors of dynamical interactions between binaries, such as those described above, and a distant, perturbing third body. First, binaries with large separations ($a_b \gtrsim 0.4 R_H$) are known to evolve chaotically; tidal forces from the SMBH are likely to disrupt such loosely bound binaries (e.g. Eggleton & Kiseleva, 1995; Mardling & Aarseth, 2001). Another process that may operate, notable for functioning even in purely coplanar triple systems, is the evection resonance (Touma & Wisdom, 1994). This process relies on the orbital angular frequency of the outer black hole binary about the SMBH (n_\bullet) being commensurable to the rate of change of the longitude of periapsis $n_\bullet \approx \dot{\varpi}_b$. The resonance may be able to drive black hole binaries migrating inward through AGN disks towards high eccentricities (and thus faster gravitational wave-driven mergers, e.g. Peters, 1964), although this mechanism is thought to preferentially apply to binaries in AGN disks composed of an intermediate-mass black hole and a stellar-mass black hole (Bhaskar et al., 2022; Muñoz et al., 2022). If binaries acquire ap-

preciable eccentricities through the evection resonance or other processes, their inclination may also be excited through the eviction resonance (Touma & Wisdom, 1994) at the expense of the eccentricity of the binary.

The von Zeipel-Lidov-Kozai (ZLK) effect (Kozai, 1962; Lidov, 1962; von Zeipel, 1910, see also, e.g., Ito & Ohtsuka 2019 for a review) may induce high eccentricities in black hole binaries in AGN disks (e.g. Deme et al., 2020; Liu & Lai, 2018; Tagawa et al., 2020). This effect arises due to the equal precession rates of Ω_b and ϖ_b in Newtonian systems. For circular orbits with extreme mass ratios ($M_\bullet \gg m_b$), $\cos i_b \sqrt{1 - e_b^2}$ is effectively conserved, and binary inclination may be exchanged for eccentricity when $|\cos(i_b)| < \sqrt{3/5}$ (Kozai, 1962). Within this work we restrict ourselves to binaries with $|\cos(i_b)| > \sqrt{3/5}$, deferring binaries which undergo ZLK cycles to subsequent studies.

4.3 Numerical Methods

We simulate binaries embedded in AGN disks using the Athena++ code (Stone et al., 2020), generally following the procedure described in Dempsey et al. (2022). We assume that the gas is isothermal and inviscid, and use the shearing-box approximation (Hawley et al., 1995; Stone et al., 1996), which expands the equations of hydrodynamics about a reference point in the disk, in our case the BHB center of mass. We illustrate this methodology schematically in Figure 4.3, which highlights both the quasi-global features captured by our simulations, such as the horseshoe orbits followed by certain fluid elements and the spiral arms excited in the AGN disk, and the high fidelity with which the flow of gas around the binary is captured in three dimensions.

The equations of compressible, isothermal, inviscid hydrodynamics in the shearing box

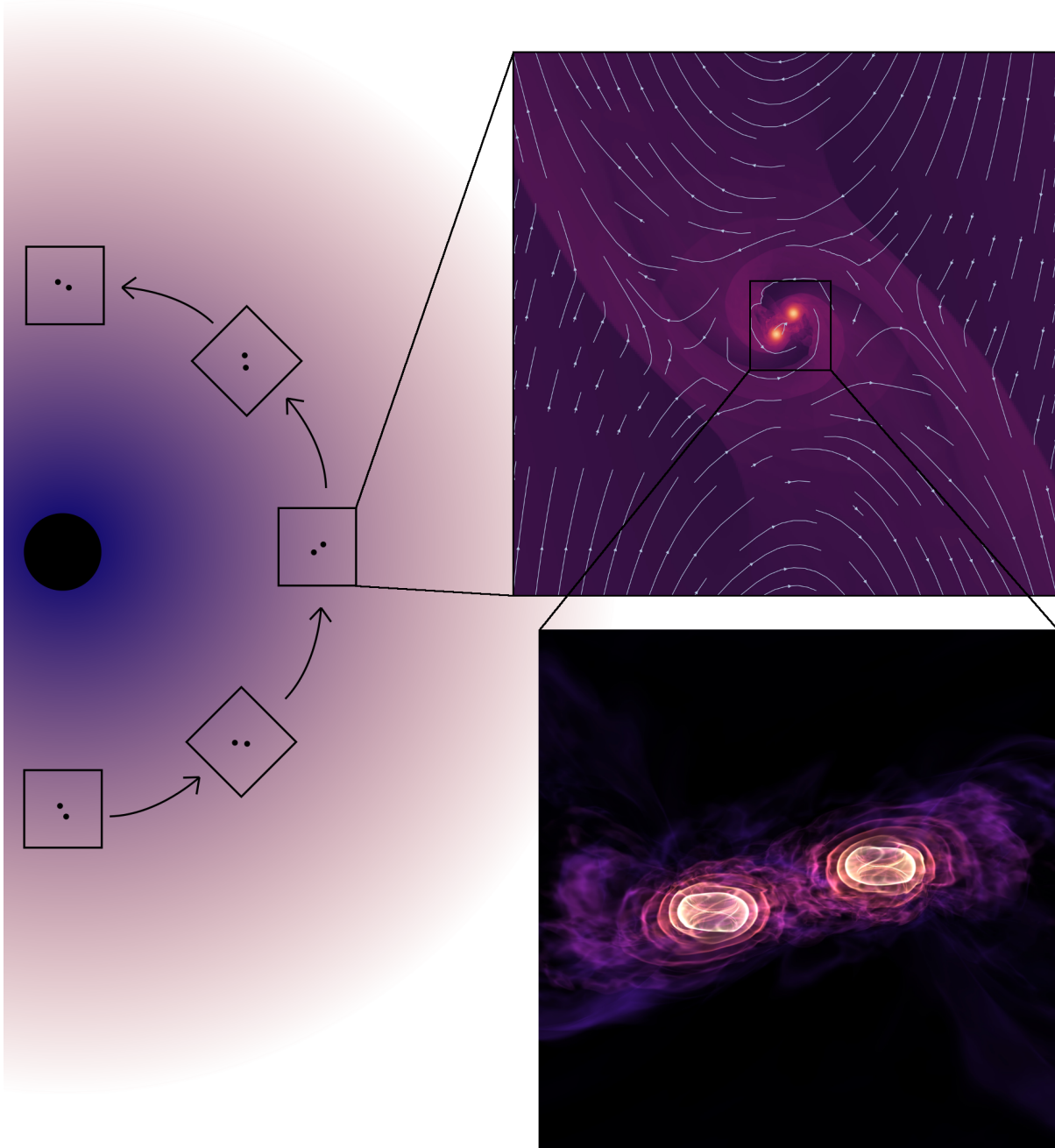


Figure 4.3: A schematic diagram of our simulation methodology. We do not simulate the global AGN disk (left), but instead consider a shearing box which orbits the SMBH along with the binary. The upper right panel plots a density slice through the midplane during a simulation of an inclination $i = 30^\circ$ binary, illustrating the quasi-global features captured by our simulation such as the excitation of spiral arms in the AGN disk and the horseshoe orbits of fluid elements which remain unbound from the binary. The bottom panel depicts opaque density iso-contours in the immediate vicinity of the binary in the same simulation, demonstrating that the flow of gas in three dimensions is resolved well by our methodology. In both plots of simulation outputs, brighter colors indicate higher densities, which are colored on a logarithmic scale.

frame, along with source terms describing the interaction between the fluid and the BHB, are

$$\frac{\partial \rho}{\partial t} + \nabla \cdot (\rho \mathbf{v}) = S_\Sigma, \quad (4.20)$$

$$\begin{aligned} \frac{\partial \mathbf{v}}{\partial t} + \mathbf{v} \cdot \nabla \mathbf{v} = & -\frac{\nabla P}{\rho} - \nabla \Phi + \frac{\mathbf{S}_p}{\rho} \\ & -2\Omega_0 \hat{\mathbf{z}} \times \mathbf{v} + 3\Omega_0^2 x \hat{\mathbf{x}} - \Omega_0^2 z \hat{\mathbf{z}}, \end{aligned} \quad (4.21)$$

where Φ is the gravitational potential of the BHB, S_Σ is a mass sink term, and \mathbf{S}_p is a momentum sink term. Each sink term $S_\Sigma = \sum_i S_{\Sigma,i}$, $\mathbf{S}_p = \sum_i \mathbf{S}_{p,i}$ is localized to the vicinity of the BHB point masses. As illustrated in Figure 4.3, we place the shearing-box at some orbital radius, R_0 , in the AGN disk. The coordinate basis vectors in this frame rotate in time and are $\hat{\mathbf{x}}$, which points from the SMBH to the center of the shearing-box; $\hat{\mathbf{z}}$, the direction normal to AGN disk midplane; and $\hat{\mathbf{y}}$ which is defined as $\hat{\mathbf{y}} = \hat{\mathbf{z}} \times \hat{\mathbf{x}}$ to complete the orthonormal triad. The rotation rate of the box is set to the Keplerian value, $\Omega_0 = \sqrt{GM_\bullet/R_0^3}$, and the binary center of mass is initially placed at the shearing box center, but we note that the binary center of mass is not fixed to this location. In the remainder of this chapter we use Ω_0 and n_\bullet interchangeably since n_\bullet does not change appreciably over the course of a simulation. We close the equations of motion with an isothermal equation of state such that $P = c_s^2 \rho$, where the sound-speed is $c_s = H_0 \Omega_0$, and H_0 is a scale height which we take to be constant throughout the domain. Feedback from accretion onto both black holes will likely heat the gas surrounding them, and this equation of state is not globally realistic; based on prior studies (e.g. Li & Lai, 2022b; Li et al., 2022b), we expect that our present choice will lead to more conservative binary inspiral predictions than variable-temperature alternatives. The $\Omega_0^2 z \hat{\mathbf{z}}$ term represents the vertical gravitational acceleration in the thin disk due to the SMBH. As discussed in Section 4.2, we neglect both the self-gravity of the

disk and the force of the disk on the black holes.

We model the gravitational potential of each black hole using a spline function which is exactly Keplerian outside of a softening radius r_s , within which the potential is softened to avoid singularities (Springel et al., 2001). We set the softening length to $r_s = 0.04a_b$.³ We apply torque-free sink terms S_Σ and S_p (Dempsey et al., 2020; Dittmann & Ryan, 2021) for gas within r_s from either point mass as described in Appendix A of Dempsey et al. (2022). We gradually introduce the black hole binary to the system over a timescale of $0.5n_\bullet^{-1}$, only allowing accretion after the conclusion of that period. We orient the binary as described in Section 4.2.2.1, using the simulation x -axis as a reference direction and $x - y$ plane as a reference plane for defining Ω_b , i_b , and ω_b .

Our simulation domain extends from $-24H$ to $24H$ in x and y , and from $-4H$ to $4H$ in z , resolving the scale height with five cells in each direction. Additionally, we utilize seven levels of static mesh refinement, allowing Athena++ to automatically place additional refinement regions in order to maintain that neighboring cells differ by at most one refinement level. Accordingly, we resolve the gas around the binary with more than 1200 cells per a_b . Our simulations used 2nd-order spatial reconstruction (van Leer, 1974), the HLLE approximate Riemann solver (Einfeldt, 1988; Harten et al., 1983), and a second-order strong stability preserving Runge-Kutta time integrator (RK2, Gottlieb & Shu, 1998). We found that the Runge-Kutta integrator leads to a much more stable time step than the 2nd-order van Leer integrator (Stone & Gardiner, 2009) used in Dempsey et al. (2022), enabling us to use much higher resolution and smaller softening lengths.

³The spline gravitational softening described in (Springel et al., 2001) is typically employed using a softening length ~ 2.8 times larger than a Plummer-softened potential because of the relative depths to which the potentials reach. The value used here is a factor of three smaller than in Dempsey et al. (2022), which we found to have appreciable consequences in our simulations of retrograde binaries.

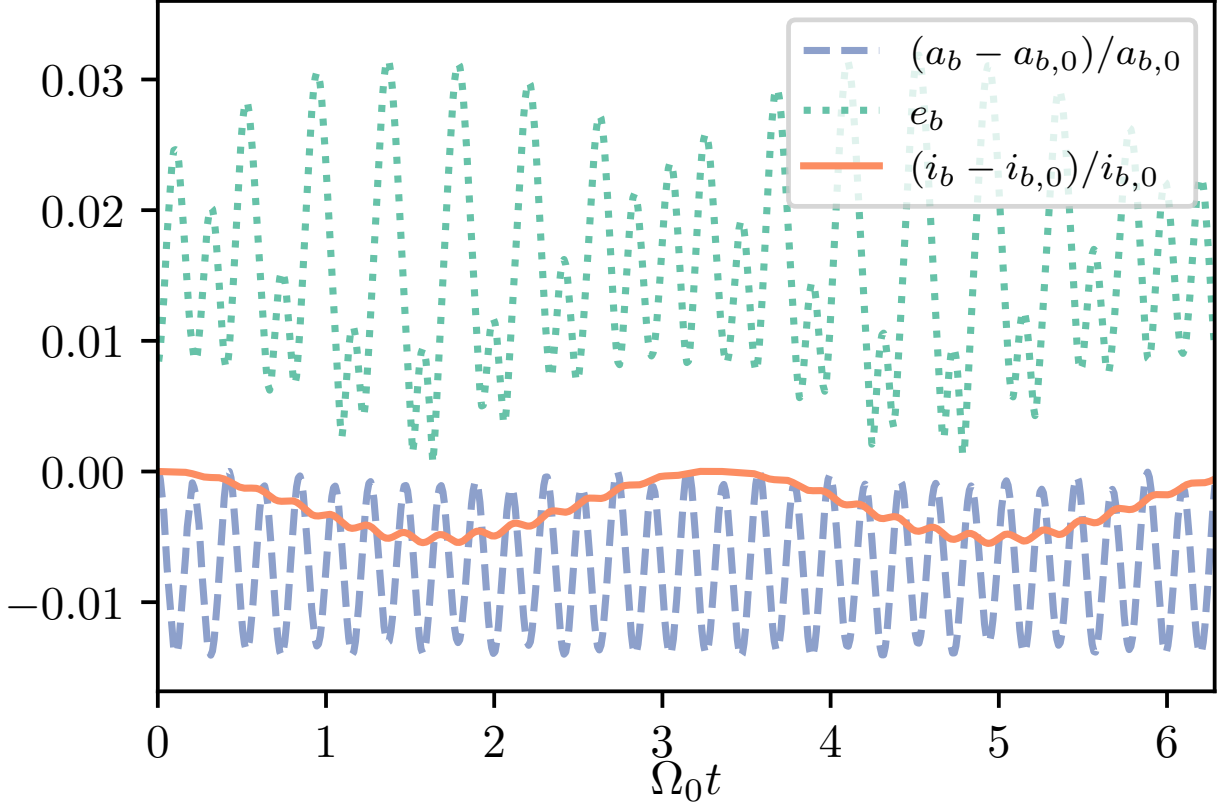


Figure 4.4: Evolution of the semi-major axis (blue dashed), inclination (orange solid), and eccentricity (green dotted) of our $i_b = 165^\circ$ binary over the course of one orbit about the SMBH.

Our simulations were initialized according to the background equilibrium solution, with $v_y = -3\Omega_0 x/2$, $v_x = v_z = 0$, and $\rho = \rho_0 \exp[-(z/H)^2/2]$. Because we neglect the self-gravity of the disk and disk-induced binary motion, our simulations are scale-free and the value of ρ_0 is set to unity without loss of generality.

We used shear-periodic boundary conditions in the x -direction and periodic boundary conditions in the y -direction. In the z -direction we applied standard outflow boundary conditions to the velocities, but extrapolated the density so that vertical hydrostatic equilibrium could be maintained.

4.3.1 N-body Evolution

Previous studies of embedded BHBs either use fixed binary orbits with ad hoc precession terms (e.g. [Li & Lai, 2022a](#)) or solved the 3-body equations of motion under simplifying assumptions ([Dempsey et al., 2022](#); [Whitehead et al., 2023](#)). We found that the approximate N-body evolution scheme employed in [Dempsey et al. \(2022\)](#), while sufficient for circular $i_b = 0$ binaries, did not properly conserve the angular momentum of inclined binaries and resulted in ZKL cycles of erroneous magnitude, motivating the present treatment. The difficulty lies in that fact that even for mildly hierarchical triples (e.g., $a_b \sim R_H/4$) such as the ones presented in [Section 4.4](#), the orbital evolution of the binary is non-trivial. We illustrate this by the evolution of the orbital elements of an $i_b = 165^\circ$ binary in [Figure 4.4](#).

To ensure that we evolve the BHB accurately, we have developed an N-body extension to `Athena++` that fully couples the evolution and interaction of N gravitating and accreting bodies to the hydrodynamics solver. Integration of the gravitational system is done with a full `REBOUND` ([Rein & Liu, 2012](#)) simulation embedded in `Athena++` and uses the IAS15 integrator, an implementation of a 15th-order Radau quadrature ([Radau, 1880](#); [Rein & Spiegel, 2015](#)). During one `Athena++` time step, `REBOUND` evolves the positions and velocities of all objects in the simulation to the appropriate end time of each stage of the integrator. For example, for the RK2 integrator used here, the two-stage update equations for the schematic system $dU/dt = F(U)$ are

$$U^{(1)} = U^{(0)} + \Delta t F(U^{(0)}) \quad (4.22)$$

$$U^{(2)} = \frac{1}{2} (U^{(0)} + U^{(1)}) + \frac{\Delta t}{2} F(U^{(1)}) \quad (4.23)$$

such that the final updated values are,

$$U^{(2)} = U^{(0)} + \frac{\Delta t}{2} (F(U^{(0)}) + F(U^{(1)})) \quad (4.24)$$

and where $U^{(0)}$, $U^{(1)}$, and $U^{(2)}$ are the values of U at the beginning of the step, at the end of the first stage, and at the end of the second stage, respectively. For our simulations U is the vector of conserved variables, as well as the position and velocities of all gravitating bodies in the REBOUND simulation.

During stage 1, we first measure the force between each body and the gas for the positions and velocities at the beginning of the step (i.e., evaluating $F(U^{(0)})$) and then evolve the N-body system to the end of the step. During stage 2, we measure the force between each BH and the gas for the positions and velocities at from the end of stage 1 (i.e, evaluating $F(U^{(1)})$). For each stage we add the force on each BH to a running time average with the appropriate weights. With this method we are able to achieve 2nd order in time coupling between rebound and Athena++ for the RK2 integrator. We have also tested our method with the forward Euler, VL2, and RK3 time integrators available in Athena++. The REBOUND simulation is always performed in the “global” frame of the AGN disk, but the Athena++ simulation is performed in the “local” shearing-box frame. We thus need to rotate the REBOUND results into the local frame when computing the gas forces.

With REBOUND taking care of the numerical integration of the N-body system between each hydrodynamical time step we are able to accurately model many systems of interest for embedded Black holes in AGN disks that were previously too numerically difficult to evolve. Examples include highly eccentric and inclined binaries, small clusters of objects, arbitrarily

complicated inner and outer binary configurations, and binary formation. Our sub-stage coupling method also allows for accurate book-keeping of the forces on the BHs allowing for high-fidelity time averages of orbital evolution quantities.

4.4 Results

We present six simulations over a range of binary inclinations, $i_b \in \{0, 15^\circ, 30^\circ, 150^\circ, 165^\circ, 180^\circ\}$. We focus on a single binary configuration, with mass ratio $m_b/M_\bullet = 1.536 \times 10^{-6}$, separation $a_b = R_H/4$ and a disk scale height of $H = 0.01R_\bullet$ such that $R_H/H = 0.8$ (c.f. [Dempsey et al., 2022](#)). In each case, the mean motion of the binary was $n_b \sim 13.9n_\bullet$. Each binary was initialized with $e_b = 0$, $\omega_b = 0$, and $\Omega_b = 0$. The simulations were run for at least $20n_\bullet^{-1}$, or ~ 3 orbits of the binary around the SMBH, which was sufficient for the accretion rates onto the binary to reach a quasi-steady state, as illustrated by [Figure 4.5](#). We perform all of our measurements of orbital evolution at times later than $14n_\bullet^{-1}$, well after initial transients have died out.

We focus first on somewhat large scales ($\sim R_H$) in [Section 4.4.1](#), at which the influence of the binary begins causing deviations in the flow compared to a single black hole of the same mass. We investigate the flow of gas through the accretion torus (minidisk or circum-single disk, ‘CSD’) surrounding each black hole in [Section 4.4.2](#), and binary orbital evolution in [Section 4.4.3](#).

4.4.1 Large-Scale Structures

On scales much larger than the binary semi-major axis, the presence of the binary has a negligible affect on the flow compared to a single black hole of the same mass. For example,

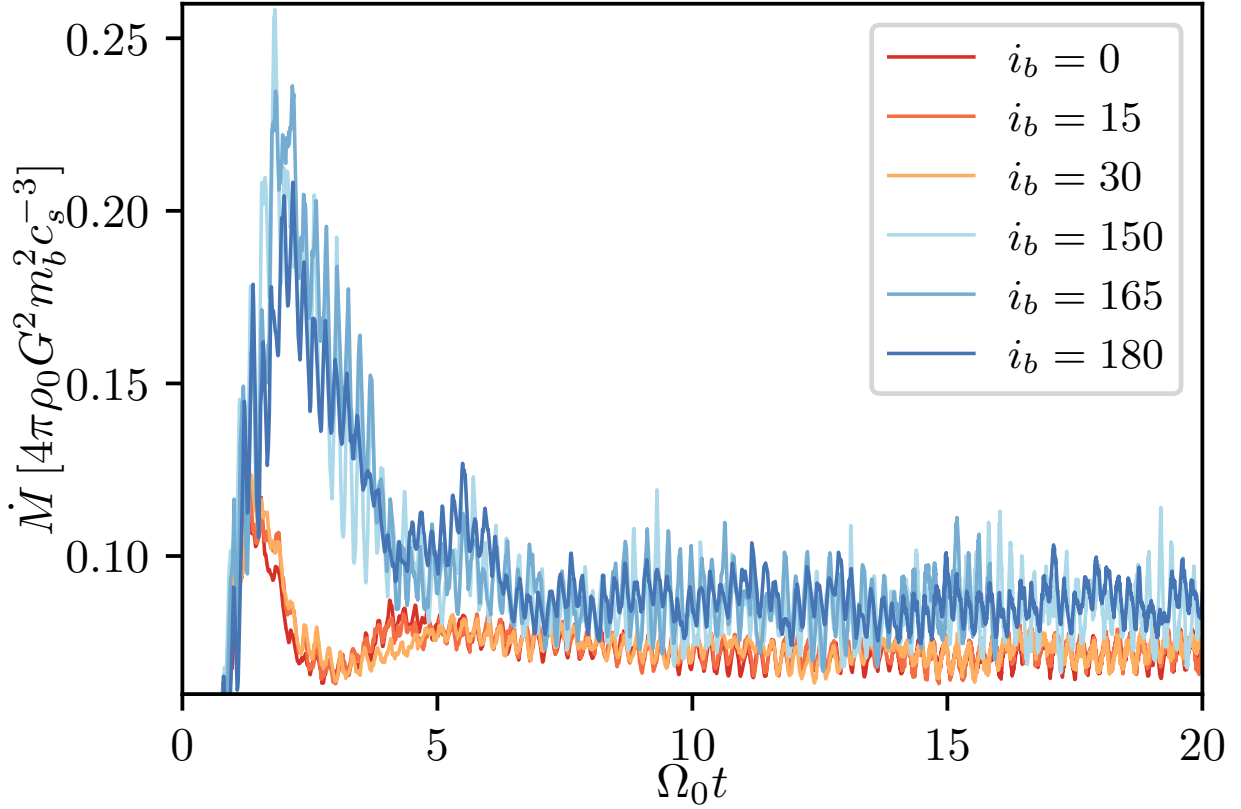


Figure 4.5: The accretion rate onto each binary, normalized to the Bondi accretion rate $\dot{M}_B = 4\pi\rho_0 G^2 m_b^2 / c_s^3$ (Bondi, 1952), over the course of our simulations. Retrograde ($i_b > 90^\circ$) binaries accrete at higher rates than prograde ($i_b < 90^\circ$) binaries. We use shades of red and orange to plot the accretion rate onto prograde binaries, while we plot the accretion rate for retrograde binaries using shades of blue, in each case using lighter shades for binaries closer to 90° .

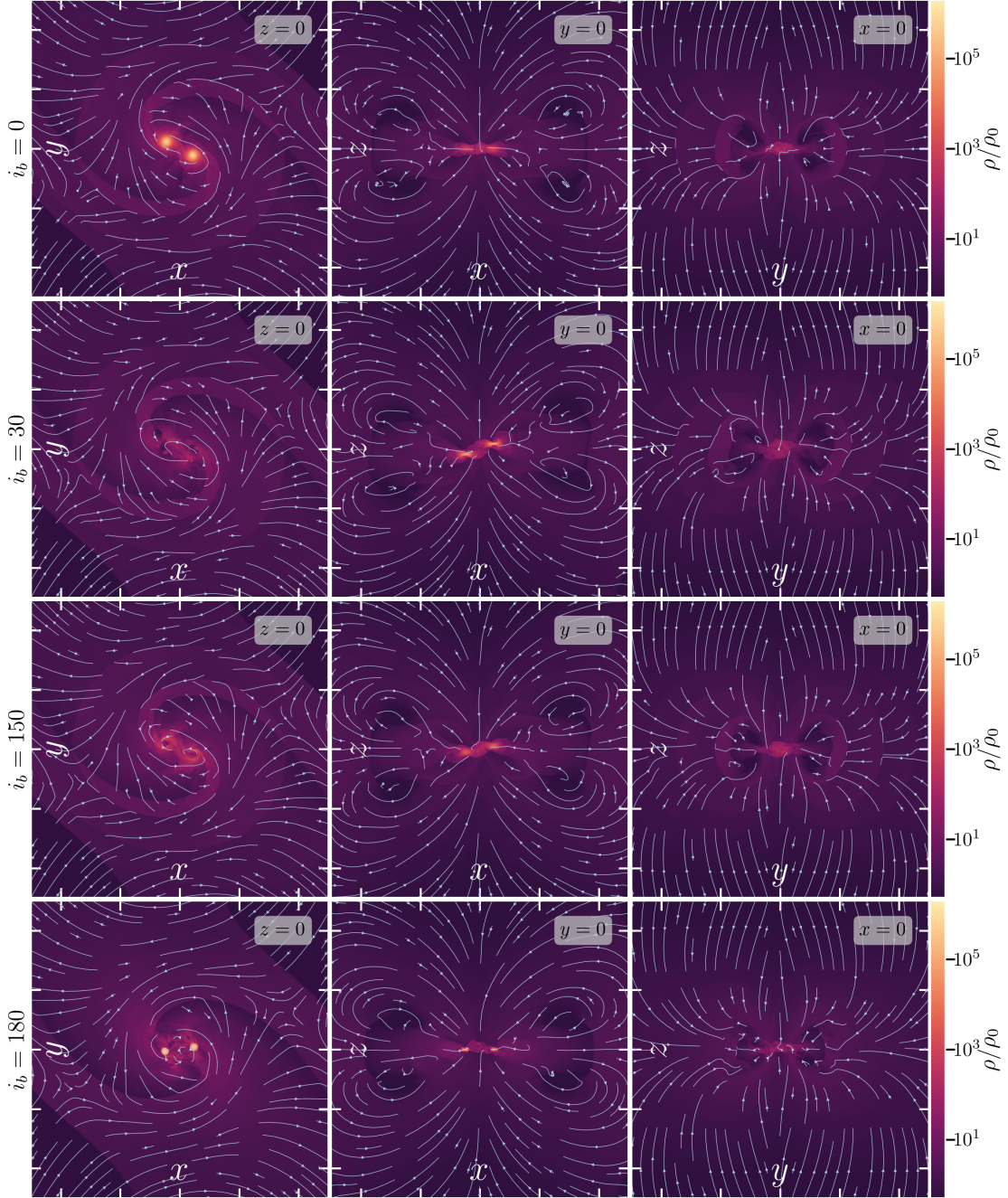


Figure 4.6: Slices of density along each coordinate plane, along with velocity streamlines, at $t = 14.5n_{\bullet}^{-1}$ in our $i_b = \{0^\circ, 30^\circ, 150^\circ, 180^\circ\}$ simulations. The first, second, and third columns plot data in the $x - y$, $x - z$, and $y - z$ planes respectively. Curved light blue arrows illustrate streamlines of the in-plane velocity field in each slice. In all cases, it is evident that accretion along the vertical direction plays a significant role. Additionally, there is evidence for an $m = 2$ spiral in each case, although these spirals are weaker when $i_b > 0^\circ$, and the deflection of fluid elements on approximate horseshoe trajectories is clearly visible through the streamlines in the $x - y$ plane. The axis ticks are spaced $2a_b = R_H/2$ apart, and each panel roughly encompasses a slice through the Hill sphere of each binary.

the fluid density slices in Figures 4.3 and 4.6 demonstrate the formation of a spiral arm in the larger disk. The streamlines in the aforementioned figures illustrate the horseshoe orbits followed by fluid elements that are deflected away from the binary, and the separatrices in the midplane velocity field where fluid is captured by the binary.

However, because the binary separation is a quarter of the binary Hill radius, the binary has a non-negligible influence on the gas within the Hill sphere, as illustrated for binaries at four different inclinations in Figure 4.6. Turning first to the density distribution in the disk midplane, it is clear that the binary creates $m = 2$ spirals at larger scales - while for prograde binaries these extend down and into the CSDs, these spirals are not as well defined within $r \sim a_b$ about retrograde binaries. Contrasting the simulations of aligned ($i_b = 0^\circ$) and anti-aligned ($i_b = 180^\circ$) binaries, while the gas just within the Hill sphere is prograde in both cases, the gas in the minidisks of the aligned binary orbits in a prograde sense while the minidisks of the anti-aligned binary orbit in a retrograde sense. The minidisks around retrograde binaries are significantly smaller than those of their prograde counterparts, largely due to the intense ram pressure experienced by gas orbiting along with the binary against gas falling in from larger scales in a prograde sense, which we investigate further in Section 4.4.2.

Turning to the slices through the $x - z$ and $y - z$ planes displayed in the second and third columns of Figure 4.6, we observe large-scale circulation, especially along the axis connecting the binary and SMBH. Although the precise dynamics depend on the binary inclination, matter more than $\sim 2a_b$ from the binary tends to be pushed away from the binary and subsequently lifted upwards to $|z| \gtrsim a_b$, joining the meridionally circulating flow which accretes onto the binary from higher latitudes. Much of the accretion onto the binary occurs along the vertical direction, necessitating three-dimensional study of these accretion flows. The circulation pattern

observed here is qualitatively similar to that observed in some three-dimensional simulations of planets embedded in circumstellar disks (e.g. [Fung & Chiang, 2016](#); [Szulágyi et al., 2014](#)), as well as the previous simulations of aligned embedded binaries ([Dempsey et al., 2022](#)).

One peculiar feature of retrograde binaries is their higher accretion rates relative to their prograde counterparts, as illustrated in [Figure 4.5](#): prograde binaries typically accrete at about 7.2% of the Bondi rate, whereas retrograde binaries typically accrete at about 8.6% of the Bondi rate. A similar trend was noted in ([Li & Lai, 2022a](#)), which attributed the increased accretion rate onto retrograde binaries to those binaries lacking CSDs, suggesting that the presence of minidisks around prograde binaries decreases the accretion rate. Unlike ([Li & Lai, 2022a](#)), we observe CSDs around retrograde binaries,⁴ so their existence or lack thereof cannot dictate these trends in accretion rate. Moreover, our $i_b = 150$ binary has both the smallest minidisks and *lowest* accretion rate out of the retrograde binaries studied here.

We have found that throughout the Hill sphere of each binary, to distances $\gtrsim R_H = 4a_b$, the average fluid density is lower and average radial velocity towards the binary barycenter is higher around retrograde binaries. Because gas typically enters the Hill sphere orbiting in a prograde sense, the prograde binaries will have, on average, longer-duration gravitational interactions with gas, potentially doing more work and hindering the binding of gas to the binary. Regardless, the higher accretion rates onto retrograde binaries begin at large distances from the binary and do not depend on the size of the minidisks.

⁴However, the CSD *size* in our simulations of retrograde is not converged. We illustrate this in [Appendix B.2](#), and show that this does not affect any of our other results.

4.4.2 Minidisks

The accretion disks that form around each black hole in our simulations display a number of notable characteristics: these mindisks exhibit meridional circulation, gas outflowing along the midplane and inflowing at higher latitudes, similar to the flows on the much larger scales of the Hill sphere shown in in Figure 4.6. The accretion disks that form around the black holes in prograde binaries orbit in a prograde sense, whereas the accretion disks that form around retrograde binaries form in a retrograde sense (that is, with the same handedness of the binary: $\mathbf{l}_b \cdot \mathbf{l}_{\text{gas}} > 0$); and the minidisks themselves are typically aligned with the AGN disk midplane - that is to say the angular momentum vector of gas in a minidisk around a prograde binary is nearly parallel to \vec{z} , and the angular momentum vector of gas comprising the CSD of a retrograde binary is nearly parallel to $-\vec{z}$.⁵ Particularly for inclined binaries, these CSD alignments could appreciably alter the effective spin distribution of AGN-channel black hole binary mergers (e.g McKernan & Ford, 2023).

As an example, a volume rendering of the minidisks of a $i_b = 30^\circ$ binary is displayed in Figure 4.7. Notably, while the gas most proximate to each black hole is aligned with the AGN disk midplane, the lower-density gas at larger distances, corresponding to the spirals and outflows seen in Figure 4.6, is more aligned with the orbital plane of the binary. We caution that this result does not hold at all binary inclinations: preliminary simulations of more misaligned binaries, which we presented in a subsequent paper, suggest that the minidisks of those binaries will align more with the binary orbital plane than do the minidisks of binaries in the present investigation.

⁵We also note that two-dimensional simulations of viscous thin disks accreting onto retrograde isolated binaries have instead found that each minidisk form instead with the same handedness as the larger circumbinary disk (and thus have $\mathbf{l}_b \cdot \mathbf{l}_{\text{gas}} < 0$) (Tiede & D’Orazio, 2024).

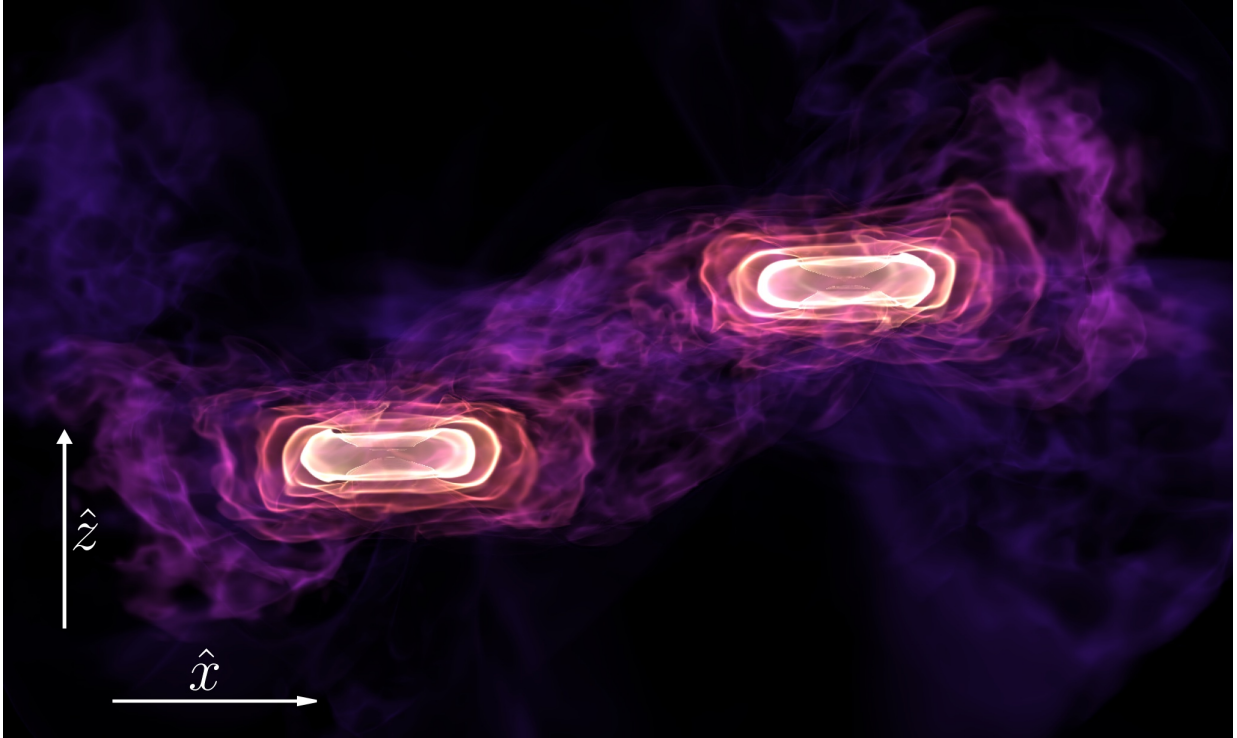


Figure 4.7: A volume rendering of the gas around the black holes in our $i_b = 30^\circ$ simulation at $t = 14.5n_\bullet^{-1}$. The darkest colors highlight gas at densities of $\rho \sim \rho_0/10$, and the brightest colors highlight gas at densities of $\rho \sim 10^4 \rho_0$, with intermediate colors spaced log-uniformly in density. Even though the orbit of the binary is inclined relative to the AGN disk midplane, the minidisks remain oriented along with the AGN disk rather than the plane of the binary orbit. Notably, the lower-density gas flowing away from the binary is in closer alignment with the binary orbital plane.

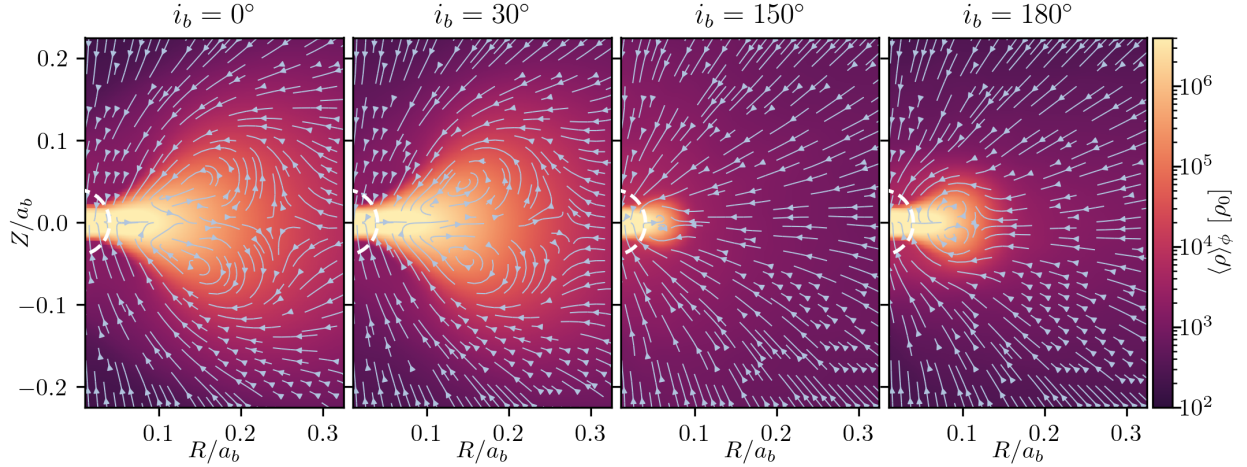


Figure 4.8: Profiles, averaged in time and azimuth, of the gas density and velocity in a cylindrical polar coordinate system in the frame of one of the black holes from each of our $i_b \in \{0^\circ, 30^\circ, 150^\circ, 180^\circ\}$ simulations. Streamlines illustrate meridional circulation in the mini-disks and vertical accretion onto the binary through the direction of the azimuthally-averaged velocity field, and color indicates the azimuthally-averaged fluid density. Time-averaging used 27 individual snapshots over the course of three binary orbits. The dashed white circle denotes the region where our sink particle operates and the gravitational potential is softened.

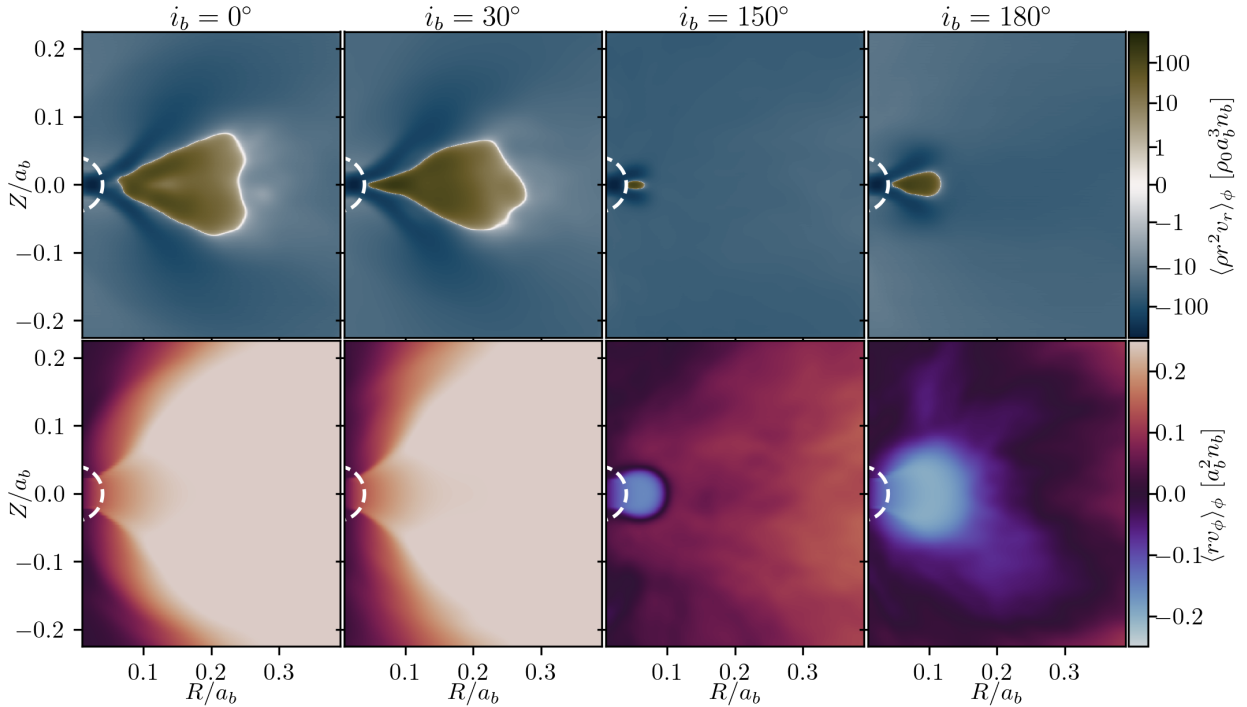


Figure 4.9: Azimuthally averaged profiles of radial mass flux (top row) and the specific angular momentum of the gas (bottom row) in a cylindrical polar coordinate system in the frame of one of the black holes from each of our $i_b \in \{0^\circ, 30^\circ, 150^\circ, 180^\circ\}$ simulations. Time-averaging used 27 individual snapshots over the course of three binary orbits. The dashed white circle denotes the region where our sink particle operates and the gravitational potential is softened.

It is worth comparing the alignment of these minidisks to the disk-binary alignment observed in earlier simulations of viscous, isolated circumbinary disks (e.g. [Moody et al., 2019](#)): in such simulations the binary accretes from a circumbinary disk much thinner than the orbit of the binary, and (in a frame oriented with the circumbinary disk) out-of-plane velocities in the circumbinary disk are negligible compared to the orbital motion of the binary. However, embedded binaries accrete gas vertically, and over the course of a binary orbital period just as much matter falls on from above as below. Gas flows onto isolated binaries from their circumbinary disks, whereas gas falls onto embedded binaries ballistically ([Dempsey et al., 2022](#)). Additionally, [Avara et al. \(2023\)](#) recently identified minidisk tilt oscillations on the order of the disk aspect ratio.

The gas constituting the minidisks of embedded binaries is also not particularly long-lived. While the typical viscous inflow timescale of material in the minidisks of isolated binaries can be tens to hundreds of binary orbital periods,⁶ we find that the mass-weighted average inflow timescales within the Roche lobe of each black hole are on the order of $\sim 0.2 - 4$ binary orbital periods t_{orb} in the minidisks themselves and $\lesssim 0.1t_{\text{orb}}$ in the polar regions around each black hole. We note, however, that for gas to form a CSD around a black hole, it must necessarily be moving with a similar bulk velocity to that black hole, lest it be left behind or captured by the other black hole; thus the gas forming each CSD has significantly torqued the black hole around which it orbits, even if the orbital plane of that gas does not align with the binary orbital plane.

The flow of gas onto and throughout the minidisks over a range of inclinations is illustrated in [Figure 4.8](#), which plots the azimuthally averaged gas density (in the frame of one of the

⁶A simplistic estimate follows from treating each CSD as a circular Keplerian disk with a radius matching the size of the Roche lobe of each black hole, in which case $r/v_r \approx 91n_{\bullet}^{-1} \approx 15t_{\text{orb}}$ for an unrealistically high viscosity of $\nu = 10^{-3}a_b^2\Omega_b$ and equal-mass binary.

black holes) along with velocity streamlines in the same frame. Although quasiballistic accretion occurs onto prograde binaries most prominently at higher latitudes, such accretion occurs over a wider range of angles in retrograde binaries until reaching the minidisk. Intriguingly, the CSDs surrounding the black holes comprising the $i_b = 150^\circ$ binary are visibly smaller than those around the $i_b = 180^\circ$ binary, which are in turn smaller than those of the black holes in prograde binaries. In fact, the CSD of the $i_b = 150^\circ$ binary is only about twice as large as the size of our sinks. However, the CSDs themselves display meridional circulation, with high-latitude inflows and midplane outflows, regardless of their size.

Another view of the flow of gas throughout and around the minidisks is provided in Figure 4.9, which plots the time- and azimuth-averaged profiles of the gas specific angular momentum and radial mass flux. Patterns of meridional circulation and midplane outflows are again evident in the distribution of radial mass flux, which also highlights accretion through the polar regions. Even though the CSDs around the black holes in the $i_b = 150^\circ$ binary are very small ($\lesssim a_b/10$ in extent), they still display the same circulation patterns. Although the specific angular momentum profile is not particularly informative for prograde binaries, around the black hole in retrograde binaries it very clearly demarcates which gas is flowing in a retrograde sense (and thus with the same handedness as the orbit of the binary) compared to gas orbiting in a prograde sense.

A slightly more condensed view of the velocity profile throughout the Roche lobe of each black hole is shown in Figure 4.10. The top panel therein illustrates the specific angular momentum profile in comparison to a reference Keplerian curve. Prograde binaries have sub-Keplerian disks at $r \gtrsim a_b/10$, and the time-averaged flow does not depend substantially on the binary inclination. The bottom panel illustrates the azimuthal and radial Mach numbers (\mathcal{M}_ϕ and \mathcal{M}_r respectively) of the gas around each black hole. As characteristic of a disk, the azimuthal flow is

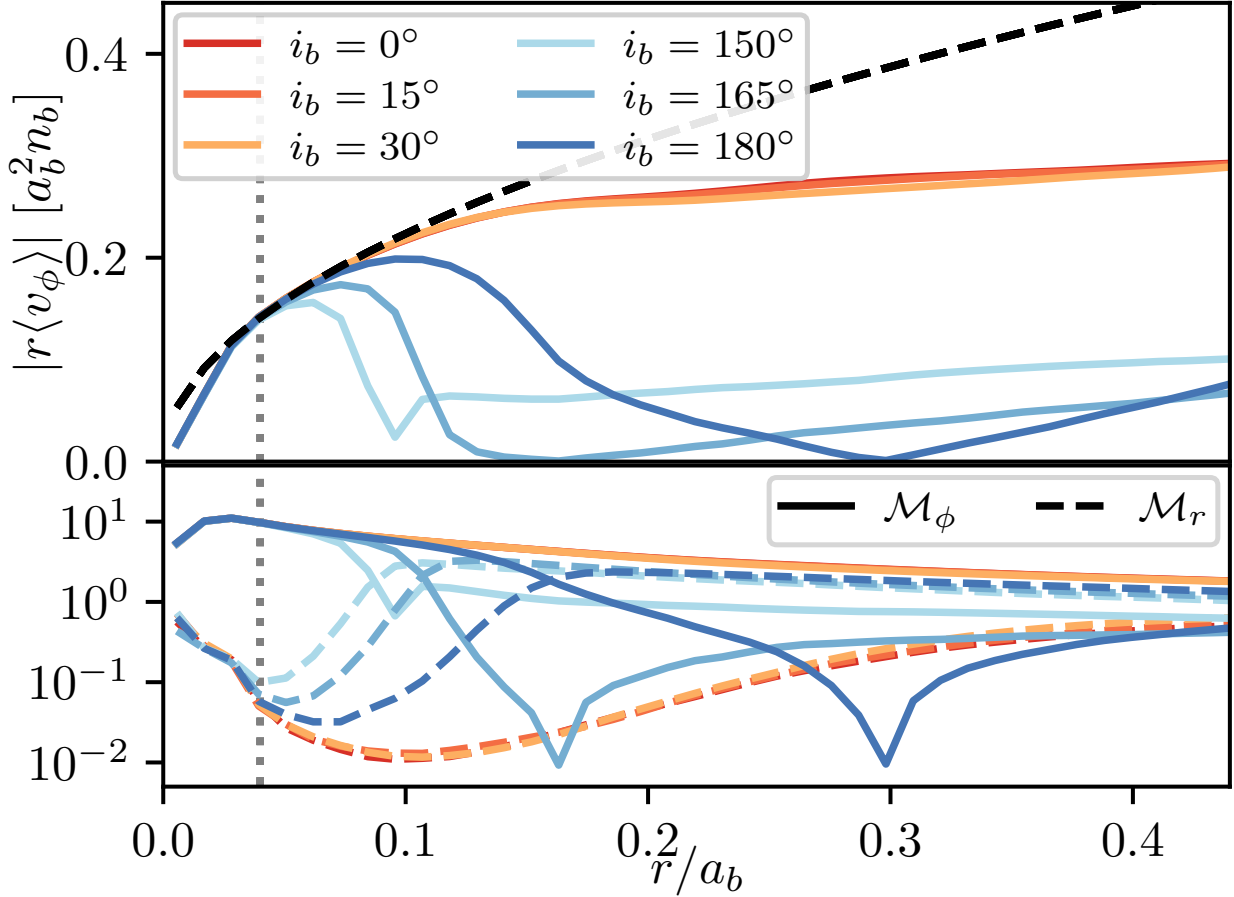


Figure 4.10: One-dimensional profiles, averaged over spherical shells centered on each black hole, of the fluid specific angular momentum (top panel) and both radial and azimuthal fluid Mach numbers (bottom panel). Warm colors display results for prograde binaries and cool colors display results for retrograde binaries. In the top panel, the dashed black line displays the specific angular momentum profile of a Keplerian disk. In the bottom panel the radial Mach number is plotted using dashed lines and the azimuthal Mach number is plotted using solid lines. We have calculated the characteristic Mach number at a given radius by integrating the radial and azimuthal momentum within each shell, dividing by mass in that shell and the sound speed, and taking the absolute value of the result. The vertical dotted line indicates the radius within which we apply sink terms and gravitational softening.

supersonic throughout, varying as $\mathcal{M}_\phi \propto r^{1/2}$, and in the prograde disks the radial Mach number is everywhere both below unity and orders of magnitude below the azimuthal Mach number. The Mach number profiles of CSDs around prograde binaries show very little variation with inclination.

The flow of gas around the black holes in retrograde binaries, however, is markedly different. The top panel of Figure 4.10 illustrates how the size of the CSD around each black hole varies with binary inclination, smallest for the $i_b = 150^\circ$ binary and largest for the $i_b = 180^\circ$ binary, and how the disks are still Keplerian at small radii despite their smaller size. The bottom panel shows how fluid motion is generally azimuthally subsonic prior to forming a disk, but plunges in a radially supersonic manner up until that point. The gas initially falls in ballistically, with $\mathcal{M}_r \propto r^{-1/2}$, before forming an accretion disk.

The flow of gas onto, off of, and between the minidisks in each binary is displayed in Figure 4.11, which plots a projection of the fluid density along the binary angular momentum vector. The CSDs around prograde binaries appear very similar to those observed in simulations of standard circumbinary disks (e.g. Dittmann & Ryan, 2021; Muñoz et al., 2019; Ryan & MacFadyen, 2017): spiral waves are present throughout the disks, some matter flows onto the binary from larger distances, and streams of gas flow between the two black holes. Although some very faint spirals can be seen in the CSDs of retrograde binaries, they are far less prominent (cf. Li et al., 2021b). As presaged by Figures 4.9 and 4.10, ample gas appears to be stripped away from the retrograde binaries, contributing to their smaller sizes; this trailing gas appears to be more substantial for the binaries that orbit outside of the AGN disk midplane, in line with the observed trends in CSD size.

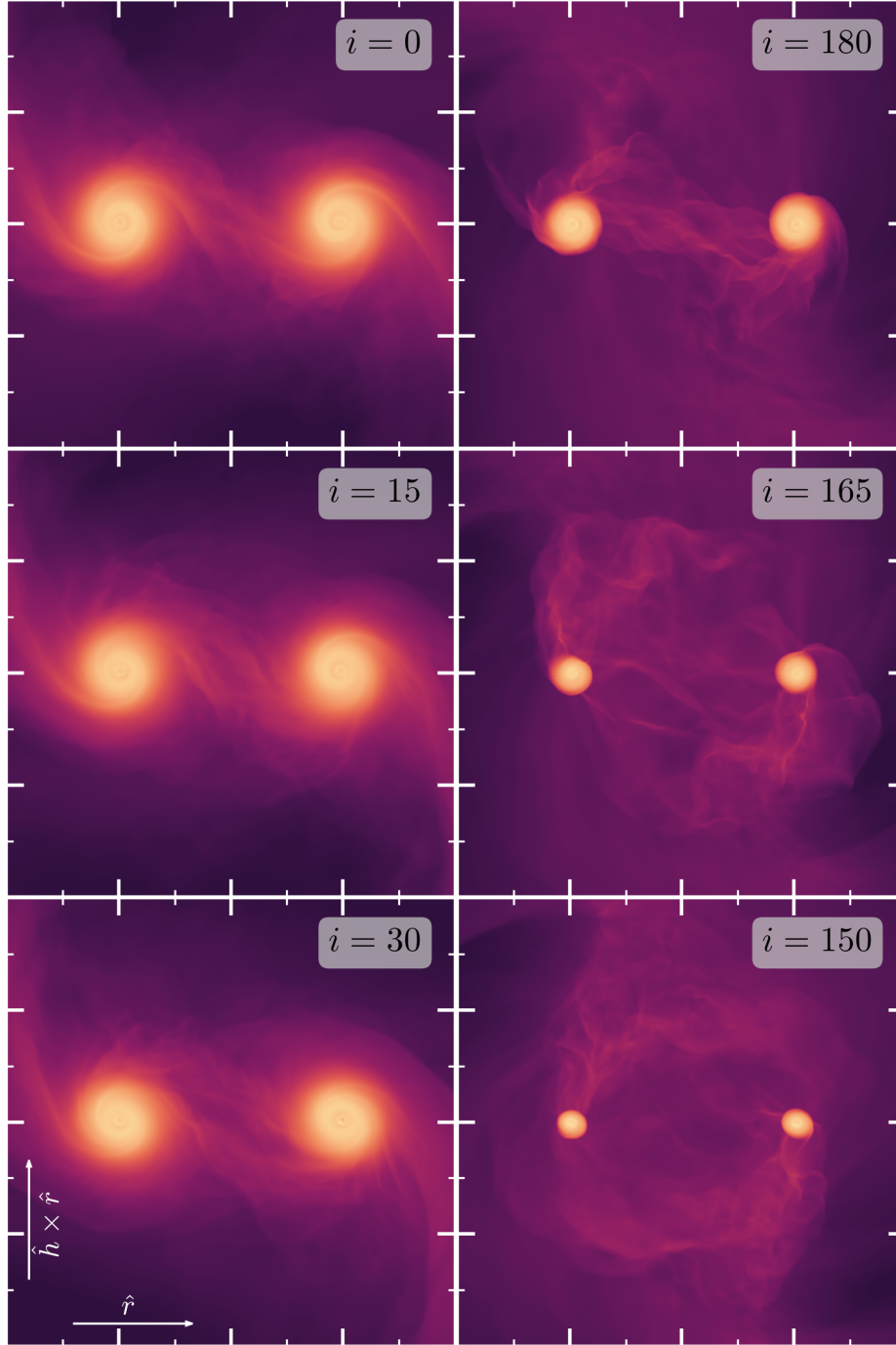


Figure 4.11: Projections of the fluid density along the orbital angular momentum vector of each binary at $t = 18.4n_{\bullet}^{-1}$; in each case the angular momentum vector of the binary is pointing out of the page, and in this frame the binary is moving in a counterclockwise sense. Because the CSDs are aligned with the AGN disk midplane rather than the orbital plane of the binary, the minidisks of inclined binaries appear slightly prolate in these projections. It is clear that retrograde binaries have smaller minidisks, and we can clearly see the streams of gas being stripped off of the retrograde binaries. Major ticks are placed $0.5a_b$ apart, with minor ticks every $0.25a_b$.

4.4.3 Orbital Evolution

Based on our examinations of the flow of gas onto the binary and around the black holes constituting it, we can draw a number of qualitative inferences. As a first approximation, we can assume that gas accreting onto each black hole does so on average with the same velocity as that black hole. Thus, the accretion of gas onto the binary should add to its specific energy largely through changing the mass of the binary and thus its specific gravitational binding energy, and for circular binaries with $|\vec{r}| \approx a_b$, $\dot{\mathcal{E}}/\mathcal{E} \approx 2\dot{m}_b/m_b$. However, gas must journey deep into the potential well of an individual black hole before accreting, potentially losing energy to the binary in the process and helping unbind it. For more tightly bound binaries, more work must be done on gas before it can accrete, and for sufficiently bound binaries this may cause binaries to outspiral as found in [Dempsey et al. \(2022\)](#).

The above reasoning is directly applicable to prograde binaries, but must be adapted slightly for retrograde binaries. For example, if CSDs do not form at all (e.g. [Li & Lai, 2022a](#)), then the assumption that gas accretes with the same velocity as a given black hole breaks down, and the kinetic contribution to the time derivative of the binary specific energy will become nonzero. On the other hand, if CSDs form around each black hole, as in our simulations, then the velocity of the gas must be significantly altered before it can accrete, as shown in Section 4.4.2, and thus the binary will do a significant amount of work on the gas. Similarly, as shown in Figure 4.9, the angular momentum of gas must change dramatically for it to become part of the minidisk, in which case the binary will experience a strong torque, greatly reducing the magnitude of its angular momentum, although it is not clear a priori if this will predominantly affect the binary eccentricity or semi-major axis. And similarly, for gas in the AGN disk which is on average aligned with the

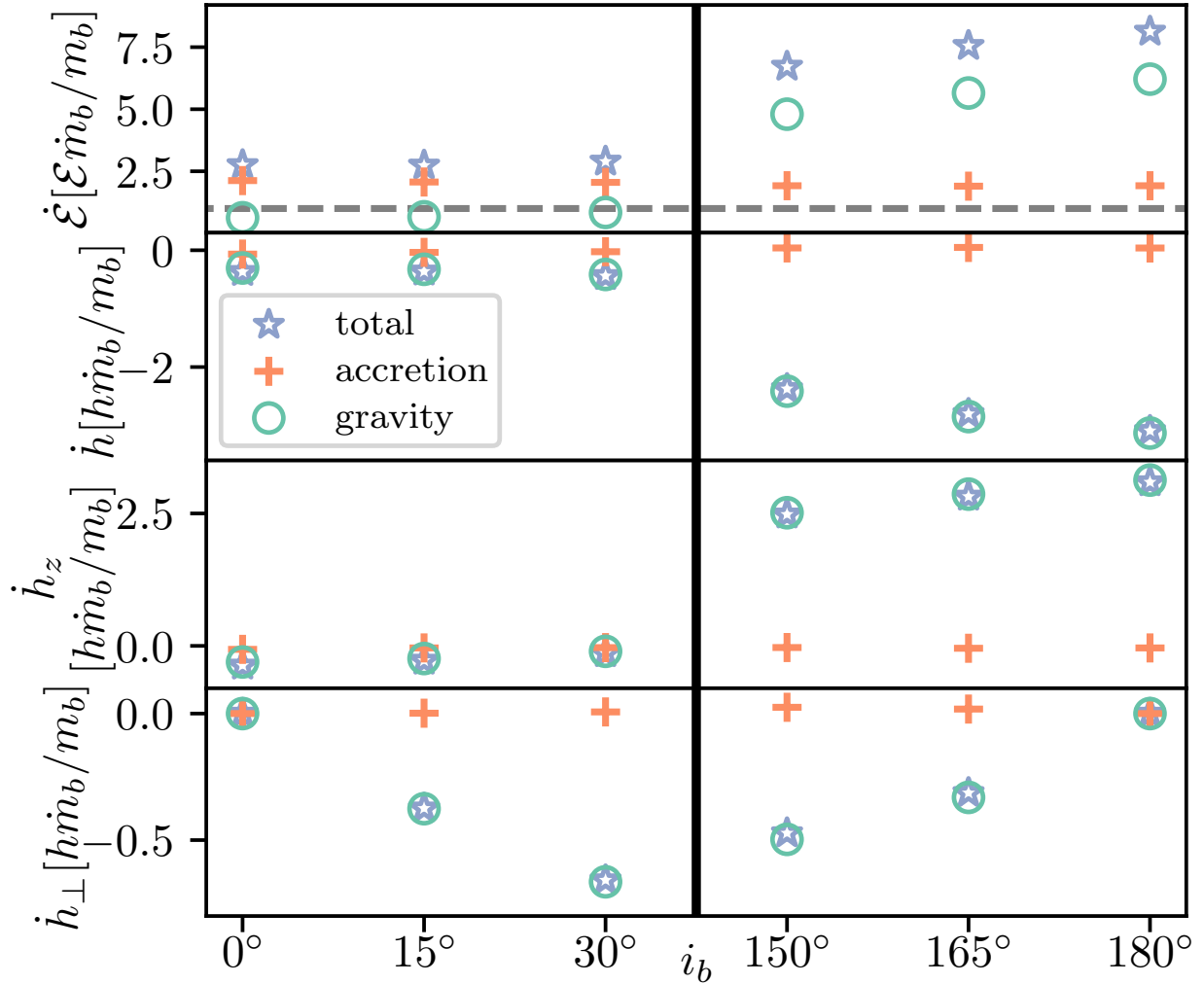


Figure 4.12: The top row plots the rate of change of the binary specific energy normalized by the average binary specific energy and accretion timescale m_b/\dot{m}_b for each of our simulations (the total rate shown by blue stars, the contribution due to accretion by orange crosses, and the contribution due to gravity by green circles). The second row plots the average rate of change of the magnitude of the binary specific angular momentum, the third the rate of change of the z-component, and the bottom row shows the rate of change of the perpendicular component, all normalized by the binary specific angular momentum and accretion timescale. In the first row, the gray dashed line indicates the critical value $\dot{\mathcal{E}}/\mathcal{E} = \dot{m}_b/m_b$ above which equal-mass binaries are driven to inspiral. All quantities were averaged in time between $14 n_\bullet^{-1}$ and $20 n_\bullet^{-1}$.

AGN disk midplane to accrete onto either black hole, that gas must gain significant out-of-plane angular momentum, and thus damp the inclination of the binary.

With the aforementioned notions in mind, we turn to our measurements of the rate of change of the specific energy and angular momentum of each binary in our simulations in Figure 4.12. Turning first to the energy, our prior expectations are confirmed: in all cases the contribution to $\dot{\mathcal{E}}/\mathcal{E}$ due to accretion is ~ 2 , and while the contribution due to gravity is small in the prograde case, it is quite large for retrograde binaries, suggesting that the binaries should inspiral rapidly. Also in line with our qualitative expectations, accretion does not change the specific angular momentum of any binary.⁷ As argued above, retrograde binaries experience significant torques, especially contributing to changes in the z -component of their angular momenta.

The orbital evolution of each binary follows from the above discussions. First, in the top row of Figure 4.13, we see that although all binaries contract (at this separation, see Dempsey et al. (2022)), retrograde binaries do so at a much higher rate. Similarly to previous studies we find that eccentricity is excited in retrograde binaries (e.g. Schnittman & Krolik, 2015; Tiede & D’Orazio, 2024), while eccentricity is damped in near-circular prograde binaries (Muñoz et al., 2019; Zrake et al., 2021). Although \dot{i}_b is not well-defined for $i_b = 0$ and $i_b = 180$, we see as expected that binary inclinations are damped. Otherwise put, this result suggests that any binary at all misaligned with the midplane of the AGN disk should be gradually aligned with the disk, in a prograde sense, over time. Thus, it appears that $i_b = 0$ is a stable equilibrium while $i_b = 180^\circ$ is unstable. If the trends we observe here continue to higher-inclination systems, initially near-retrograde binaries could realign with the AGN disk within a few mass-doubling timescales.

⁷Notably, if we used a naive sink prescription and allowed the sink particles to exert a torque on gas in the frame of each sink, then this would not be the case: fluid angular momentum would instead be transferred to both the spin and orbit of the black holes (Dempsey et al., 2020; Dittmann & Ryan, 2021).

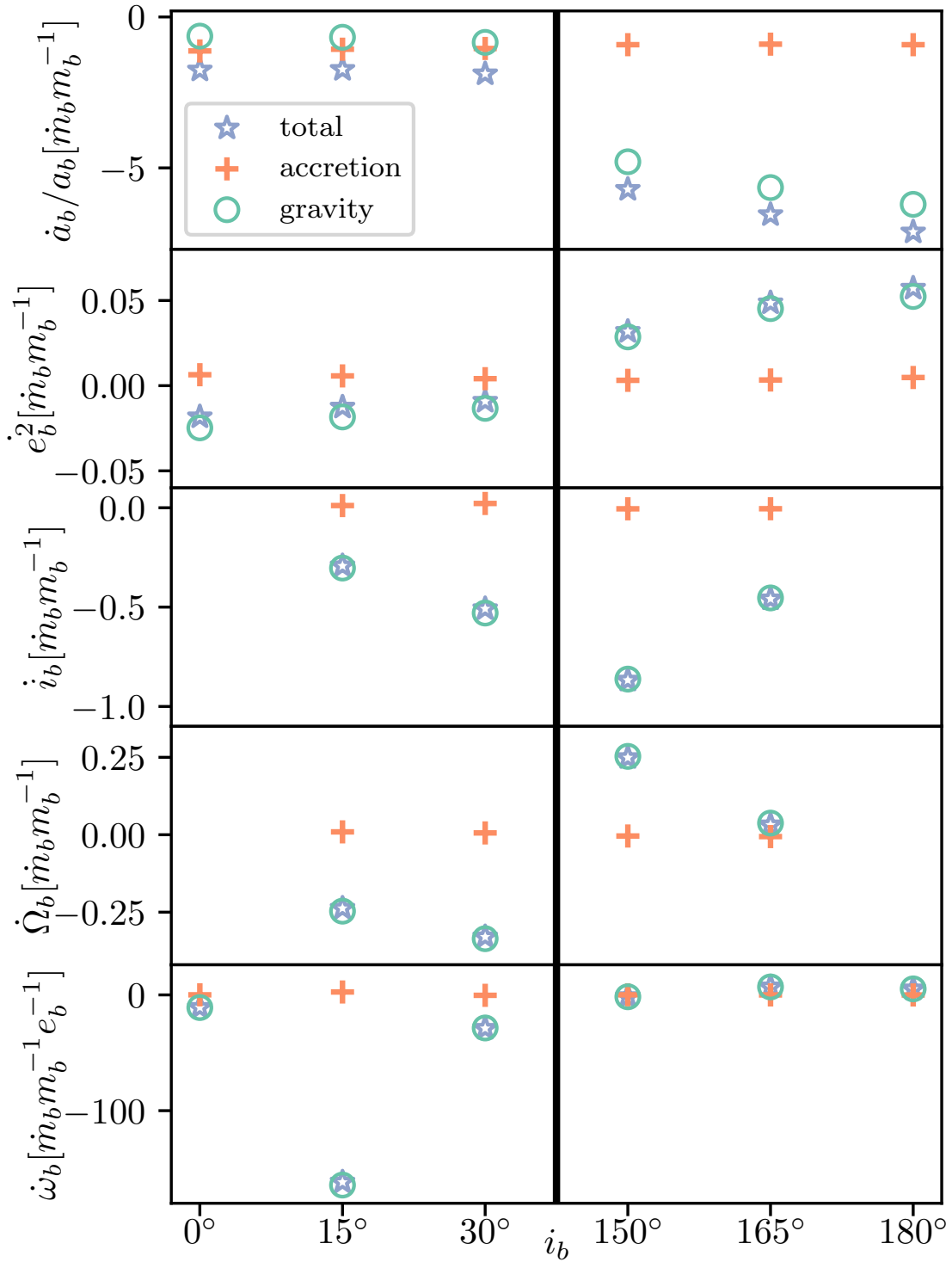


Figure 4.13: The rates of change (due to gravity, accretion, and in total) of the binary semi-major axis, squared eccentricity, inclination, argument of the ascending node, and argument of periastris. All quantities were averaged in time between $14 n_\bullet^{-1}$ and $20 n_\bullet^{-1}$. When reporting values of \dot{i}_b , $\dot{\omega}_b$, and $\dot{\Omega}_b$, we use radians rather than degrees. In the bottom row, for $i_b = 0^\circ$ and $i_b = 180^\circ$, we report $\dot{\varpi}$ rather than $\dot{\omega}$. We only report the contributions to orbital elements due to accretion and gravitational interactions with the surrounding gas, which are independent of choices like the reference plane for defining Ω_b .

The time derivative of $\dot{\omega}_b$ is not particularly well-defined for near-circular binaries (due to the terms in the denominator of Equation (4.18) that go to zero as $e_b \rightarrow 0$), so we have normalized those results by the time-averaged values of e_b ; for these nearly circular binaries, we simply emphasize that $\dot{\omega}_b$ is generally nonzero. The time derivative of Ω_b is more well defined, at least for binaries with $h_\perp \neq 0$, and we find that it is negative for prograde binaries and positive for retrograde binaries. These signs relate to the handedness of the binaries passage through the disk midplane and the background shear of the AGN disk, and as we discuss in Section 4.5.2, the important conclusion is that this disk-induced precession rate is nonzero.

4.5 Discussion

In this section, we briefly discuss the implications of our results on the manner in which accretion onto embedded black holes proceeds, the dynamics of jets which may be formed during the accretion process, and the orbital evolution of embedded BHBs. We caution that the present work has eschewed magnetic fields, the effects of radiation, gas self-gravity, and general deviations from isothermality, and thus some caution must be taken when applying our results to real AGN disks.

4.5.1 Accretion

Although the gravitational radii of embedded black holes were under-resolved by orders of magnitude in our simulations, our study achieved sufficient scale separation to observe that accretion onto each black hole does not occur in a spherically symmetric manner, but rather through an accretion disk. Additionally, accretion rates onto the embedded binaries in our simulations

are about $\sim 8\%$ of the Bondi accretion rate $\dot{M}_B = 4\pi\rho_0 G^2 m_b^2 c_s^{-3}$, which is reasonable given that our simulations are vertically stratified rather than uniform in density, and that the binary Hill radius is comparable to the Bondi radius $R_B = Gm_b/c_s^2$ such that tidal forces may limit accretion onto the binary. This is largely consistent with the results of previous three-dimensional simulations of accretion onto embedded binaries (Dempsey et al., 2022), but as noted in Section 4.4.1, retrograde binaries accrete at a slightly higher rate than prograde ones due to their disparate gravitational influence on gas entering the Hill sphere.

However, for typical gas densities in AGN disks such as those modeled in Figure 4.1, $\rho_0 \sim 10^{-18} - 10^{-9} \text{ g cm}^{-3}$, the Bondi accretion rate may be substantially larger than the Eddington accretion rate. Fixing R_H/H , as in our simulations, the Bondi accretion rate can be expressed as

$$\begin{aligned} \dot{M}_B = 12\pi \left(\frac{R_H}{H}\right)^3 \rho_0 G m_b \Omega^{-1} &\approx 1.18 \left(\frac{R_H}{H}\right)^3 \left(\frac{m_b}{10 M_\odot}\right) \\ &\left(\frac{\rho_0}{10^{-14} \text{ g cm}^{-3}}\right) \left(\frac{M_\bullet}{10^7 M_\odot}\right)^{-1/2} \left(\frac{r_\bullet}{1 \text{ pc}}\right)^{3/2} M_\odot \text{ yr}^{-1}. \end{aligned} \quad (4.25)$$

We can compare this to the Eddington-limited accretion rate onto a binary of the same mass,

$$\dot{M}_{\text{Edd}} = \frac{4\pi G m_b}{\kappa c \epsilon} \approx 2.2 \times 10^{-7} \left(\frac{0.1}{\epsilon}\right) \left(\frac{m_b}{10 M_\odot}\right) M_\odot \text{ yr}^{-1}, \quad (4.26)$$

where ϵ is the fraction of rest mass radiated during accretion onto the black holes, c is the speed of light, and κ is the opacity of the ambient gas. For brevity, we assume that $\kappa = 0.4 \text{ cm}^2 \text{ g}^{-1}$, the value for fully ionized hydrogen gas. Then, the ratio of the Bondi accretion rate to the Eddington accretion rate is

$$\frac{\dot{M}_B}{\dot{M}_{\text{Edd}}} \approx 5 \times 10^7 \left(\frac{R_H}{H} \right)^3 \left(\frac{\rho_0}{10^{-14} \text{ g cm}^{-3}} \right) \left(\frac{M_\bullet}{10^7 M_\odot} \right)^{-1/2} \left(\frac{r_\bullet}{1 \text{ pc}} \right)^{3/2} \left(\frac{\epsilon}{0.1} \right). \quad (4.27)$$

Thus, for a wide range of parameters, the accretion rates onto the binaries in our simulations, at $\sim 8\%$ of the Bondi rate, are highly super-Eddington. If the accretion rate onto each black hole is radially constant, the accretion process onto these embedded black holes may lead to significant feedback to larger scales in the form of jets and winds. However, such feedback would be driven on scales many orders of magnitude smaller than the smallest resolved in our simulations, and will be the subject of future work. Furthermore, thermodynamic effects neglected in our isothermal simulations may suppress the accretion rate (possibly as $\dot{M} \propto r^{1/2}$, see [Guo et al. 2023](#)), resulting in a much smaller accretion rate near the event horizon.

If either embedded black hole has an appreciable spin, jets will likely be launched into the AGN disk. Because jet efficiency strongly depends on the angular momentum of the gas accreting onto a given black hole (e.g. [Kwan et al., 2023](#)), it seems probable that prograde binaries could support jets; on the other hand, because the CSD size of retrograde binaries appears to depend strongly on softening, if they exist at all ([Li & Lai, 2022a](#)), retrograde binaries may not be able to launch strong jets. Although on small scales jets are typically aligned with the spin of the black hole by which they are launched, on larger scales jets can be aligned with the accretion disk surrounding them ([Liska et al., 2018](#); [McKinney et al., 2013](#)). It remains to-be-determined whether jets launched by embedded black holes would reach scales comparable to the size of their minidisks, although if they do they may be re-collimated and oriented along the normal to

the AGN disk midplane.

4.5.2 Orbital Evolution

The two most robust results, in terms of orbital evolution, of our study of stellar-mass black hole binaries embedded in AGN disks are that retrograde binaries inspiral more quickly and that binaries are gradually aligned AGN disk midplane. Specifically, anti-aligned binaries inspiral more than four times faster than aligned binaries. Furthermore, the rate at which binary inclinations decreases depends on how far out of the AGN disk midplane their orbital planes lie. Thus, binaries which form in a high-inclination retrograde configuration will both have their inclinations reduced and have their semi-major axes rapidly decreased through interactions with gas. Recent studies (e.g. [Li et al., 2023](#)) have suggested that a large fraction of binaries should form in retrograde configurations.

Additionally, we have observed that both ω_b and Ω_b precess due to interactions with the AGN disk. Although the former is not well-defined due to the low eccentricities in our simulations, and the latter is generally small, depending on the ambient gas density, the precession of these angles may affect various resonances which could operate on embedded binaries. It is well-known that precession of the argument of periapsis can both prevent ZLK cycles ([Holman et al., 1997](#)) and decrease the maximum achievable eccentricities in cases where ZLK cycles still occur ([Miller & Hamilton, 2002](#)). However, because of the small binary eccentricities in our simulations, the degree to which ZLK cycles will be affected is uncertain, although our results suggest that ZLK cycles should be less common for embedded binaries than those in vacuum. Evection resonances are more complicated still, due to their dependence on n_\bullet as well as $\dot{\omega}_b$.

Interactions with the gas disk may either help or hinder evection resonances, although our low- i_b , low- e_b simulations are not sufficient to predict how evection resonances should be affected in a general sense.

The comparative rates of change of the semi-major axis and inclination aside, we expect that all binaries with inclinations $i_b < 180^\circ$ will be gradually driven towards $i_b = 0^\circ$. Thus, our results suggest that many retrograde binaries will pass through the range of inclinations where ZLK cycles occur as their inclinations are gradually damped. Although the rate of orbital evolution depends strongly on disk properties, if it is slow compared to the timescale of ZLK cycles, the binary will undergo ZLK oscillations in inclination and eccentricity as long as they are not disrupted by disk-induced precession. Moreover, binaries near $i_b \sim 90^\circ$ may approach $e_b \sim 1$ via ZLK oscillations, in which case the dissipation of energy and angular momentum due to gravitational waves could become extreme near pericenter leading to a large population of merging black holes with polar alignment relative to the AGN disk.

4.5.3 The Observed $q - \chi_{\text{eff}}$ Correlation

The gravitational wave event population observed by LIGO and Virgo exhibits an intriguing negative correlation between BHB mass ratio $q \equiv m_2/m_1 \leq 1$ and the mass-weighted spin of each black hole projected onto the angular momentum of the binary orbit, χ_{eff} , as well as a paucity of BHBs with negative χ_{eff} . (Adamcewicz et al., 2023; Callister et al., 2021). Other dynamical gravitational wave event formation channels, such as stellar clusters, typically predict roughly symmetric χ_{eff} distributions, while the breaking of spherical symmetry in AGN disks may favor positive χ_{eff} mergers and lead to a negative correlation between q and χ_{eff} (McKernan et al., 2022;

Santini et al., 2023).

We found, as shown in Figure 4.9, that prograde binaries have prograde minidisks and retrograde binaries have retrograde minidisks. Accretion from these minidisks onto the black holes will naturally lead to binaries with positive effective spin. However, the minidisk sizes in our simulations of retrograde binaries appear to be resolution dependent, and it is not clear if they would persist at higher resolution and with smaller softening and sink length scales. Nevertheless, we also found that many retrograde binaries will be gradually reoriented to a prograde configuration, which might still lead to a preference for prograde binary mergers and positive effective spins.

4.6 Conclusions

We have conducted a series of three-dimensional hydrodynamical simulations of stellar-mass binaries embedded in AGN disks. Whereas previous three-dimensional studies of embedded binaries focused on those with prograde orbits aligned with the midplane of the AGN disk, we have explored a range of binary inclinations including both prograde and retrograde configurations. Our work has uncovered qualitatively new aspects to both the accretion flows around and orbital evolution of inclined embedded binaries. However, we caution that our simulations have used a simplified isothermal equation of state, neglected magnetic fields, and focused on nearly-circular binaries misaligned by not more than 30° from the AGN disk midplane.

Binaries with higher inclinations tend to accrete at higher rates, in all cases accreting at less than the Bondi rate. Retrograde binaries have substantially smaller minidisks, although the black holes constituting the $i_b = 180^\circ$ binary possessed larger minidisks than those constituting

the $i_b = 150^\circ$ or $i_b = 165^\circ$ binaries, due at least in part to ram pressure stripping. We find that the minidisks around each black hole are typically aligned with the AGN disk midplane. On the larger scales of the minidisks and AGN disk there are patterns of midplane outflows, meridional circulation, and accretion along the surface of gaseous tori. Some gas also flows directly onto each black hole along the polar directions.

Retrograde binaries inspiral up to four times as quickly as their prograde counterparts due to gravitational interactions with the disk. Additionally, we find that binaries with orbital planes outside of the AGN disk midplane experience inclination damping, which is small for binaries only slightly misaligned with the disk midplane, but grows larger for more misaligned binaries. We have also found that eccentricities can be excited in near-circular inclined binaries, although we cannot comment on the maximum eccentricities achievable through disk-binary interactions due to the limited range of orbital parameters surveyed herein. Similarly, we have found evidence for disk-driven precession of both the binary argument of periapsis and longitude of the ascending node, which may affect various the susceptibility of embedded binaries to various resonances. Because a significant fraction of binaries in AGN disks may form with retrograde configurations, our results paint an optimistic, albeit incomplete, picture of gas interactions assisting binary inspirals down to to scales where gravitational waves can drive their merger, resulting in gravitational wave signals such as those observed by LIGO/VIRGO.

Chapter 5: Conclusions

5.1 Summary

This dissertation has chronicled my investigations into how stars and stellar-mass black holes can interact with AGN disks. This work was motivated by, in addition to the numerous observations listed in the introduction, our general ignorance to the fundamental mechanics of active galactic nuclei. Along the way, my work has run the gamut of theoretical astrophysical activities, from developing semi-analytical models attempting to explain puzzling observations to simulating the interactions between black hole binaries and fluid disks, from the early universe to the center of our own galaxy.

In Chapter 2, I waded into the mire of AGN disk modeling, attempting to determine if gravitational instability in the outer regions of AGN disks could help explain the rapid growth of supermassive black holes in the early universe necessary to explain observations of high-redshift AGN (e.g., [Mortlock et al., 2011](#)). The general idea was that star formation in the outer reaches of these disks could eventually convert some accretion rate of gas into an accretion rate of compact objects, the latter of which would not be subject to the Eddington limit and could be seen as reducing the effective accretion efficiency onto the SMBH. The study answered in the affirmative: indeed, star formation in AGN disks could fairly reasonably explain the existence of high-redshift quasars, and the study made some lasting contributions to AGN disk models by

recognizing the efficacy of the feedback that accretion onto disk-embedded stellar-mass black holes could provide ([Dittmann & Miller, 2020](#)). However, in many ways that study begot more questions than answers, since its conclusions hinged on uncertain assumptions about how stars in AGN disks would evolve and expire, and how large populations of stars and black holes within the disk would interact with the disk and one another.

Chapter 3 detailed my studies on the evolution of stars within AGN disks. Although these models were necessarily one-dimensional, and required implementing approximate descriptions of intrinsically multidimensional processes such as accretion onto stars from a disk-like environment and internal mixing processes. In [Dittmann et al. \(2021\)](#) we investigated the various ways that factors such tides from the SMBH and the vertical stratification of the AGN disk could decrease the accretion rate onto embedded stars, finding that the most significant effect was that once stars accrete substantially, or if they are located closer to the central SMBH, their region of gravitational influence is characterized by the Hill radius rather than the Bondi radius, vying for influence against the gravitational pull of the SMBH. We also tested the degree to which our conclusions depended on our assumptions of radiative feedback on the accretion flow, concluding that the quantitative details, such as precisely which stars reach quasi-steady states between accretion and mass loss, vary but the general qualitative trends in stellar evolution in terms of sensitivity to the background angular velocity, density, and sound speed remained unchanged. Chapter 3 also discussed the results of two complementary studies, [Jermyn et al. \(2021\)](#) and [Dittmann et al. \(2023a\)](#), which investigated the role of importance of stellar rotation and the chemical composition of the AGN disk respectively. Together, these studies developed a more thorough understanding of how stars within AGN disks evolve, and identified useful semi-analytical criteria that may be useful for understanding stellar evolution in AGN disks without direct simulations.

In Chapter 4 my work moved into a third spatial dimension, moving to the study of newly formed (that is to say, at orbital separations just slightly smaller than the dynamical stability limit) black hole binaries within AGN disks. Although many previous studies had invoked effective drag forces on binaries to suggest that they could merge rapidly after forming within AGN disks (e.g., [Stone et al., 2017](#); [Tagawa et al., 2020](#)), fewer had actually studied the problem in any detail, only one of which ([Dempsey et al., 2022](#)) at all accounted for the three-dimensional structure of AGN disks. My work then extended these studies to the case of retrograde binaries, and those generally misaligned with the midplane of the AGN disk. We found that even slightly misaligned binaries would be driven towards alignment, and that retrograde binaries tend to lose energy and angular momentum at a higher rate. Additionally, we identified some hints that the orbital eccentricities of prograde binaries were damped, while the orbital eccentricities of retrograde binaries could be further excited, which was explored in more detail in [Calcino et al. \(2023\)](#). Although high eccentricities could lead to rapid inspirals, and significant gravitational wave emission at larger binary semi-major axes, these simulations also recorded accretion onto the binary at highly super-Eddington rates, calling into question their broader applicability.

5.2 Future Work

5.2.1 Disk Models

My future plans for accretion disk models are fairly limited; the more I have worked with them the more skeptical I have become. On the other hand, there is still great interest in disk models throughout the astronomical community, and it has also come to my attention that far more people are interested in using disk models than those who understand the assumptions

intrinsic to the models and the details of how disk models are constructed. Motivated thus, I have *very* slowly begun to develop a public code for the purpose of disk model calculation.¹ At the moment this code only solves [Shakura & Sunyaev 1973](#)-esque equations, without additional heating terms often invoked in the outer regions of AGN disks. Another active area of research in AGN disk models appears to be time-dependent extensions of the multi-fluid (gas, black holes, stars) disk models of [Gilbaum & Stone \(2022\)](#), although I am not personally involved.

5.2.2 Stellar Evolution in AGN Disks

I envisage two different strands of future work in stellar evolution in AGN disks. First, virtually none of the previously discussed stellar evolution calculations reached the point of core collapse. This is in part due to challenges of numerical stability and the smaller time steps required, but also the significant memory overhead and additional computational time required, since the nuclear reactions networks required to accurately model the late stages of stellar evolution typical involve hundreds of species, rather than the tens sufficient to produce accurate results for earlier stages of stellar evolution. Specifically, I would like to address whether we should expect neutron stars or black holes to form as the end products of stellar evolution in AGN disks, potentially leveraging recent insights from core-collapse supernova research (e.g., [Boccioli et al., 2023](#); [Wang et al., 2022a](#)). Another future direction of this research aims to make more direct comparison to observations. Specifically, we hope to leverage the results of these stellar evolution calculations, in combination with disk models and the expected numbers of stars we could expect to be formed in or captured into various regions of the AGN disk, to make more concrete predictions for the observable signatures of stellar populations in AGN disks.

¹<https://github.com/ajdittmann/agndisks>

5.2.3 Disk-Embedded Black Hole Binaries

I envision two distinct future studies of black hole binaries embedded in AGN disks: one extending our previous studies of inclined and eccentric binaries to the unequal mass case, and another attempting to model accretion and feedback from binary black holes in AGN disks.² Hopefully, these simulations of disk-embedded binaries of unequal mass will be able to support or rule out AGN disks as the host sites of the black hole binary mergers observed by LIGO by making more direct connection to the observed $q - \chi_{\text{eff}}$ anticorrelation. However, significant uncertainty remains as to how feedback from the potentially super-Eddington accretion onto these binary black holes will affect the larger-scale accretion flow. We have begun to develop a subgrid accretion prescription based on the ADIOS (adiabatic inflow-outflow solution) model (Blandford & Begelman, 2004), which might provide an improved model of gas flow between the resolution limit of our simulations and the much smaller scale of the black hole horizons.

²Work is also currently ongoing in the study of black holes (and binaries) in magnetohydrodynamically turbulent accretion disks.

Appendix A: Software Used in This Dissertation

- agndisks <https://github.com/ajdittmann/agndisks>
- Athena++ (Stone et al., 2020)
- ash <https://github.com/ajdittmann/ash>
- cmocean (Thyng et al., 2016)
- matplotlib (Hunter, 2007)
- MESA (Jermyn et al., 2023; Paxton et al., 2011, 2013, 2015, 2018, 2019, <http://MESA.sourceforge.net>)
- MESASDK (Townsend, 2019)
- numpy (van der Walt et al., 2011)
- PGF/TikZ (Tantau, 2013)
- REBOUND (Rein & Liu, 2012; Rein & Spiegel, 2015)
- scipy (Virtanen et al., 2020)
- yt (Turk et al., 2011)

Appendix B: Appendices for Chapter 4

B.1 Orbital Evolution Diagnostics

We detail hereinafter how we measure changes in binary properties such as angular momentum and energy; and how we use these quantities to calculate the average rates of changes of binary orbital elements reported in Section 4.4.3.

B.1.1 Evolution Equations

Expressions for the time evolution of the binary semi-major axis and eccentricity in terms of changes in the mass, energy, and angular momentum of the binary are given by Equations (4.14) and (4.15) respectively. Equations (4.16), (4.17), and (4.18) provide expressions for the rate of change of the binary inclination, longitude the ascending node, and argument of periapsis respectively. For completeness, we note that

$$\frac{\dot{\mu}_b}{\mu_b} = \frac{\dot{m}_1}{m_1} + \frac{\dot{m}_2}{m_2} - \frac{\dot{m}_b}{m_b}, \quad (\text{B.1})$$

$$\frac{\dot{J}_i}{J_i} = \frac{\dot{\mu}_b}{\mu_b} + \frac{\dot{h}_i}{h_i}, \quad (\text{B.2})$$

$$\frac{\dot{E}}{E} = \frac{\dot{\mu}_b}{\mu_b} + \frac{\dot{\mathcal{E}}}{\mathcal{E}}, \quad (\text{B.3})$$

and

$$\dot{\mathcal{E}} = \mathbf{a}_{\text{ext}} \cdot \mathbf{v} - \frac{G\dot{m}_b}{|\mathbf{r}|}, \quad (\text{B.4})$$

$$\dot{\mathbf{h}} = \mathbf{r} \times \mathbf{a}_{\text{ext}}, \quad (\text{B.5})$$

$$\dot{\mathbf{e}} = \frac{1}{Gm_b} \left(\mathbf{a}_{\text{ext}} \times \mathbf{h} + \mathbf{v} \times \dot{\mathbf{h}} - (\mathbf{v} \times \mathbf{h}) \frac{\dot{m}_b}{m_b} \right), \quad (\text{B.6})$$

where we have assumed a Keplerian binary orbit perturbed by external accelerations \mathbf{a}_{ext} and specific torques $\dot{\mathbf{h}}$.

B.1.2 Simulation Diagnostics

Every time the point masses in our simulations interact with the fluid through source terms (when using Runge-Kutta time integration schemes, as in this work, this simply occurs every sub-step), the point masses accrete some gas from within the sink region and gravitationally interact with the surrounding fluid. The gravitational force on each object ($\mathbf{F}_{g,i}$) is given by

$$\mathbf{F}_{g,i} = \int \rho \nabla \Phi_i dV, \quad (\text{B.7})$$

and the analogous contribution due to accretion, following from the sink term \mathbf{S}_p in Equations (4.20) and (4.21), is

$$\mathbf{F}_{a,i} = - \int \mathbf{S}_{p,i} dV, \quad (\text{B.8})$$

Similarly, the accretion rate onto the binary \dot{m}_b is simply

$$\dot{m}_b = - \int S_\Sigma dV. \quad (\text{B.9})$$

After measuring the force on each point mass, we can calculate their accelerations as $\mathbf{a}_{a,\text{ext}} = (\mathbf{F}_{a,2} - \mathbf{v}_2 \dot{m}_2)/m_2 - ((\mathbf{F}_{a,1} - \mathbf{v}_1 \dot{m}_1)/m_1)$ and $\mathbf{a}_{g,\text{ext}} = \mathbf{F}_{g,2}/m_2 - \mathbf{F}_{g,1}/m_1$.

B.1.3 Averaging Over Time

Although we averaged the force on each particle over every time step, we record derived quantities discretely using 452 samples per binary orbit. Measuring changes in orbital elements is complicated by the fact that even in the absence of feedback from the gas during accretion or through gravity, the orbital elements of the binary vary over time due to 3-body interactions with the SMBH (see, e.g. Figure 4.4). It is straightforward to calculate the average of a quantity Q in time as

$$\langle Q \rangle = \frac{1}{t_2 - t_1} \int_{t_1}^{t_2} Q dt. \quad (\text{B.10})$$

For example, one of our aims is to measure a characteristic rate of change of the binary semi-major axis, $\langle \dot{a}_b/a_b \rangle$. Instantaneously, it is straightforward to measure the change in semi-major axis in terms of the binary energy and masses of the binary components as

$$\frac{d \log a_b}{d \log m_b} = \frac{\dot{a}_b m_b}{a_b \dot{m}_b} = \left(\frac{\dot{m}_1}{m_1} + \frac{\dot{m}_2}{m_2} - \frac{\dot{E}}{E} \right) \frac{m_b}{\dot{m}_b} \quad (\text{B.11})$$

However, there is some ambiguity because a_b and E_b evolve in time through tidal interactions with the SMBH. Thus, instead of reporting $\langle \dot{a}_b/a_b \rangle$, we report quantities like $\langle \dot{a}_b \rangle / \langle a_b \rangle$, additionally

normalized by the accretion timescale $m_b/\langle\dot{m}_b\rangle$.

B.2 Softening Dependence

As mentioned in Section 4.4.2, we found that the size of the minidisks around each of the black holes in retrograde binaries were not converged, in the sense that the size of those CSDs appear to depend on length scale for our sink and gravitational softening regions. In the main body of the text, we reported results using a spline softening length of $0.04a_b$.¹

To illustrate how CSD size depends on the softening length, we plot in Figure B.1 projections of the gas density along the binary angular momentum vector analogous to Figure 4.11, except for simulations using sink and softening lengths of $0.12a_b$, the same settings as Dempsey et al. (2022). The minidisks are virtually unchanged for prograde binaries. However, the CSDs of retrograde binaries are visibly larger in Figure B.1 than in Figure 4.11; the minidisks in the $i_b = 180$ case are about the same size as those in the $i_b = 0$ case, and the minidisks of the $i_b = 165$ and $i_b = 150$ binaries are both about the same size as each other and appreciably larger than their smaller-softening counterparts.

Although the sizes of the minidisks appear to differ based on the gravitational softening length, we have found that this results in only very minor changes in binary orbital evolution. To illustrate this, we have plotted the time-averaged rates of change of the binary orbital elements from a suite of simulations using a softening length of $0.08a_b$, twice that used in the simulations comprising the main body of our study. The rates of change of the binary semi-major axis, eccentricity, and inclination are virtually identical to the results from smaller-softening simulations.

¹Because spline softening reduces to an exact Keplerian potential outside of the sink region, a roughly commensurate Plummer softening would have a softening length ~ 2.8 times larger (e.g. Springel et al., 2001).

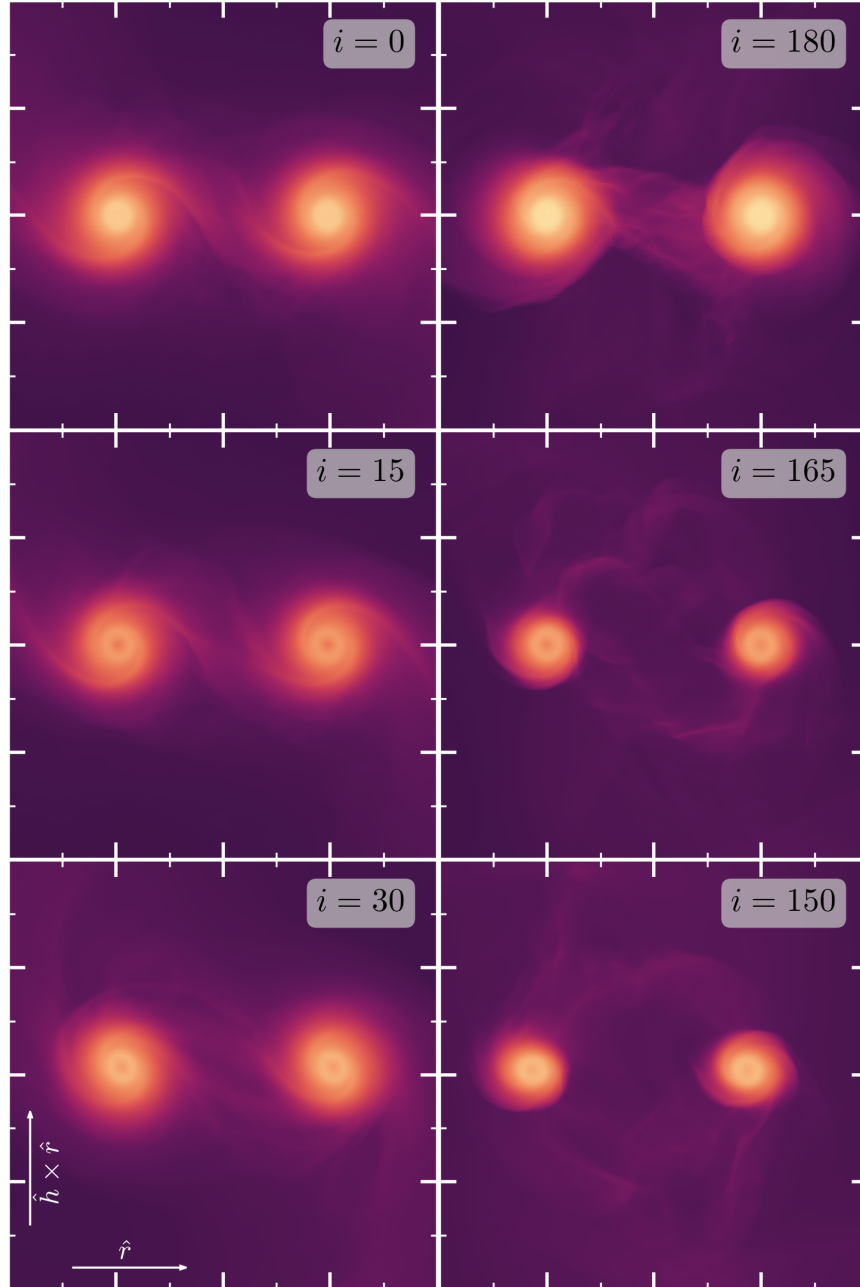


Figure B.1: Projections of the fluid density along the orbital angular momentum vector of each binary at $t = 18.4n_{\bullet}^{-1}$, in analogy to Figure 4.11. However, each point mass in the simulations pictured here has a gravitational softening length (and sink length) of $0.12a_b$, three times larger than the simulations presented in the main text. Many features on larger scales are completely consistent between these simulations, such as the streams of gas being stripped off of the retrograde binaries and gas flowing between the members of the prograde binaries. However, in these simulations the minidisks around the black holes in retrograde binaries are appreciably larger than in simulations using smaller softening lengths. Major ticks are placed $0.5a_b$ apart, with minor ticks every $0.25a_b$.

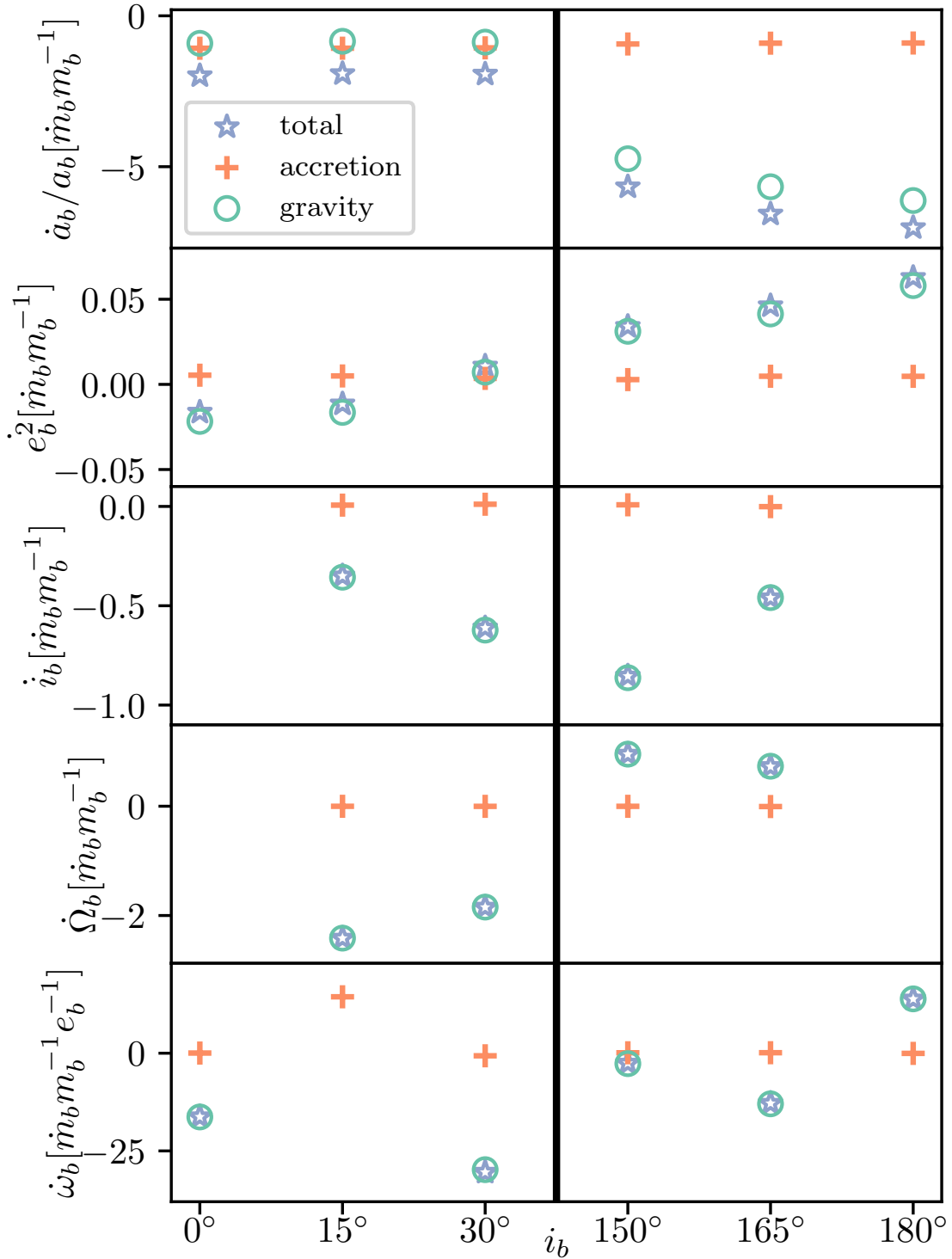


Figure B.2: The same quantities shown in Figure 4.13 for our simulations with the same resolution but gravitational softening parameters and sink rates twice as large, in this case $0.08a_b$ compared to the value of $0.04a_b$ used in the body of the paper.

However, we find that the time-averaged values of $\dot{\Omega}_b$ and $\dot{\omega}_b$ differ by factors of order unity between the $0.04a_b$ - and $0.08a_b$ -softening simulations, though in all cases these fluid-induced precession rates could hinder ZLK cycles.

Notably, the $i_b = 0$ simulations suggest an appreciably slower rate of inspiral for binaries with $a_b/R_h = 1/4$ binaries than the equivalent simulations in [Dempsey et al. \(2022\)](#): $\langle \dot{a}_b \rangle / \langle a_b \rangle \approx -1.76 \langle \dot{m}_b \rangle / m_b$ in our simulations compared to $\langle \dot{a}_b \rangle / \langle a_b \rangle \approx -3.1 \langle \dot{m}_b \rangle / m_b$ in [Dempsey et al. \(2022\)](#). However, [Dempsey et al. \(2022\)](#) used not only a softening length of $0.12a_b$ in comparison to the default value of $0.04a_b$ in this work, but also a different method of solving the equations of motion of the binary. Thus, we have repeated our $i_b = 0$ simulation using softening lengths of $0.12a_b$, $0.08a_b$, $0.04a_b$, and $0.02a_b$, using the same value for the sink length in each case. All of these simulations used our standard resolution settings except for the smallest-softening simulations, for which we added an additional level of refinement around the binary to achieve a resolution of ~ 2400 cells per a_b . Because of the great cost associated with the highest-resolution simulation, it was only carried out until $t = 5.5n_\bullet^{-1}$. Although not enough to reach a converged state or achieve robust statistics, this was sufficient for the binary to reach a quasi-steady accretion rate. Because the accretion contribution to the evolution of the semi-major axis is independent of softening length, we focus on the gravitational contribution to $\langle \dot{\mathcal{E}} \rangle / \langle \mathcal{E} \rangle$. For the aforementioned softening lengths, we found values of $\langle \dot{\mathcal{E}} \rangle / \langle \mathcal{E} \rangle$, averaged from $t = 4.5n_\bullet^{-1}$ to $t = 5.5n_\bullet^{-1}$, of $\sim 2.5, 0.78, 0.57, 0.76$. Thus, it appears that our fiducial softening choice is sufficiently converged, at least for prograde binaries, although our results can be assumed uncertain at the level of a few percent.

i_b	$\frac{\langle \dot{m}_b \rangle}{M_B}$	$\frac{\langle \dot{a}_b \rangle m_b}{\langle a_b \rangle \langle \dot{m}_b \rangle}$	$\frac{\langle \dot{a}_b \rangle m_b}{\langle a_b \rangle \langle \dot{m}_b \rangle} \Big _{\text{grav.}}$	$\frac{\langle e_b^2 \rangle m_b}{\langle \dot{m}_b \rangle}$	$\frac{\langle \dot{i}_b \rangle m_b}{\langle \dot{m}_b \rangle}$	$\frac{\langle \dot{\Omega}_b \rangle m_b}{\langle \dot{m}_b \rangle}$	$\frac{\langle \dot{\omega}_b \rangle m_b}{\langle e_b \rangle \langle \dot{m}_b \rangle}$	$\langle e_b \rangle$
0°	0.0712	-1.76	-0.634	-0.0183	-	-	-6.17	0.0157
15°	0.0722	-1.74	-0.671	-0.0126	-0.292	-0.237	-577.10	0.0155
30°	0.0725	-1.89	-0.842	-0.0092	-0.508	-0.329	-30.46	0.0155
150°	0.0844	-5.71	-4.80	0.0318	-0.868	0.249	-2.56	0.0170
165°	0.0873	-6.55	-5.65	0.056	-0.459	0.0316	-12.83	0.0134
180°	0.0863	-7.12	-6.21	0.0572	-	-	13.86	0.0131

Table B.1: Numerical values of the data plotted in Figure 4.13.

B.3 Quantitative Records of Orbital Evolution

We list in Table B.1 a number of the quantities plotted in Figure 4.13, as well as the accretion rate onto each binary, in all cases averaged from $t = 14n_{\bullet}^{-1}$ to $t = 20n_{\bullet}^{-1}$.

Bibliography

- Abbott, B. P., Abbott, R., Abbott, T. D., et al. 2016a, *Phys. Rev. Lett.*, 116, 061102
- . 2016b, *Physical Review X*, 6, 041014
- . 2016c, *ApJ*, 818, L22
- Abbott, R., Abbott, T. D., Abraham, S., et al. 2020a, *ApJ*, 900, L13
- . 2020b, *Phys. Rev. Lett.*, 125, 101102
- . 2021, *Physical Review X*, 11, 021053
- Abbott, R., Abbott, T. D., Acernese, F., et al. 2023a, *Physical Review X*, 13, 041039
- . 2023b, *Physical Review X*, 13, 011048
- Abramowicz, M., Jaroszynski, M., & Sikora, M. 1978, *A&A*, 63, 221
- Abramowicz, M. A. 1981, *Nature*, 294, 235
- Abramowicz, M. A., Calvani, M., & Nobili, L. 1980, *ApJ*, 242, 772
- Abramowicz, M. A., Czerny, B., Lasota, J. P., & Szuszkiewicz, E. 1988, *ApJ*, 332, 646
- Adamcewicz, C., Lasky, P. D., & Thrane, E. 2023, *ApJ*, 958, 13
- Alexander, T. 2005, *Phys. Rep.*, 419, 65
- Ali-Dib, M., & Lin, D. N. C. 2023, *MNRAS*, 526, 5824
- Amaro-Seoane, P., Audley, H., Babak, S., et al. 2017, arXiv e-prints, arXiv:1702.00786
- Angulo, C., Arnould, M., Rayet, M., et al. 1999, *Nucl. Phys. A*, 656, 3
- Antonucci, R. R. J., & Cohen, R. D. 1983, *ApJ*, 271, 564
- Antonucci, R. R. J., & Miller, J. S. 1985, *ApJ*, 297, 621
- Arcodia, R., Merloni, A., Nandra, K., et al. 2021, *Nature*, 592, 704

Arcodia, R., Liu, Z., Merloni, A., et al. 2024, arXiv e-prints, arXiv:2401.17275

Artymowicz, P., Clarke, C. J., Lubow, S. H., & Pringle, J. E. 1991, *ApJ*, 370, L35

Artymowicz, P., Lin, D. N. C., & Wampler, E. J. 1993, *ApJ*, 409, 592

Avara, M. J., Krolik, J. H., Campanelli, M., et al. 2023, arXiv e-prints, arXiv:2305.18538

Bahcall, J. N., & Oke, J. B. 1971, *ApJ*, 163, 235

Bahcall, J. N., & Wolf, R. A. 1976, *ApJ*, 209, 214

—. 1977, *ApJ*, 216, 883

Balbus, S. A., & Hawley, J. F. 1991, *ApJ*, 376, 214

—. 1998, *Reviews of Modern Physics*, 70, 1

Baldwin, J. A. 1975, *ApJ*, 201, 26

Barkat, Z., Rakavy, G., & Sack, N. 1967, *Phys. Rev. Lett.*, 18, 379

Bartko, H., Martins, F., Trippe, S., et al. 2010, *ApJ*, 708, 834

Bartos, I., Kocsis, B., Haiman, Z., & Márka, S. 2017, *ApJ*, 835, 165

Baruteau, C., Cuadra, J., & Lin, D. N. C. 2011, *ApJ*, 726, 28

Batra, N. D., & Baldwin, J. A. 2014, *MNRAS*, 439, 771

Begelman, M. C., Volonteri, M., & Rees, M. J. 2006, *MNRAS*, 370, 289

Bellovary, J. M., Mac Low, M.-M., McKernan, B., & Ford, K. E. S. 2016, *ApJ*, 819, L17

Bentz, M. C., Hall, P. B., & Osmer, P. S. 2004, *AJ*, 128, 561

Bentz, M. C., & Osmer, P. S. 2004, *AJ*, 127, 576

Bhaskar, H. G., Li, G., & Lin, D. N. C. 2022, *ApJ*, 934, 141

Birnstiel, T., Dullemond, C. P., Zhu, Z., et al. 2018, *ApJ*, 869, L45

Blanchard, P. K., Nicholl, M., Berger, E., et al. 2017, *ApJ*, 843, 106

Bland-Hawthorn, J., Maloney, P. R., Sutherland, R., et al. 2019, *ApJ*, 886, 45

Blandford, R. D., & Begelman, M. C. 2004, *MNRAS*, 349, 68

Bludman, S. A. 1973, *ApJ*, 183, 637

Boccioli, L., Roberti, L., Limongi, M., Mathews, G. J., & Chieffi, A. 2023, *ApJ*, 949, 17

Bogdanov, S., Lamb, F. K., Mahmoodifar, S., et al. 2019, *ApJ*, 887, L26

Bogdanov, S., Dittmann, A. J., Ho, W. C. G., et al. 2021, *ApJ*, 914, L15

Böhm-Vitense, E. 1992, *Introduction to Stellar Astrophysics*

Bond, J. R., Arnett, W. D., & Carr, B. J. 1984, *ApJ*, 280, 825

Bondi, H. 1952, *MNRAS*, 112, 195

Broekgaarden, F. S., Berger, E., Neijssel, C. J., et al. 2021, *MNRAS*, 508, 5028

Burbidge, G. R. 1961, *Nature*, 190, 1053

Burrows, A., Wang, T., & Vartanyan, D. 2024, *ApJ*, 964, L16

Burtscher, L., Hönl, S., Jaffe, W., et al. 2016, in *Society of Photo-Optical Instrumentation Engineers (SPIE) Conference Series*, Vol. 9907, *Optical and Infrared Interferometry and Imaging V*, ed. F. Malbet, M. J. Creech-Eakman, & P. G. Tuthill, 99070R

Calcino, J., Dempsey, A. M., Dittmann, A. J., & Li, H. 2023, arXiv e-prints, arXiv:2311.13727

Callister, T. A., Haster, C.-J., Ng, K. K. Y., Vitale, S., & Farr, W. M. 2021, *ApJ*, 922, L5

Cameron, A. G. W. 1962, *Nature*, 194, 963

Cantiello, M., & Braithwaite, J. 2019, *ApJ*, 883, 106

Cantiello, M., Jermyn, A. S., & Lin, D. N. C. 2021, *ApJ*, 910, 94

Cassisi, S., Potekhin, A. Y., Pietrinferni, A., Catelan, M., & Salaris, M. 2007, *ApJ*, 661, 1094

Chaboyer, B., Green, E. M., & Liebert, J. 1999, *AJ*, 117, 1360

Chakraborty, J., Kara, E., Masterson, M., et al. 2021, *ApJ*, 921, L40

Chandrasekhar, S. 1961, *Hydrodynamic and hydromagnetic stability*

Chen, Y.-X., Jiang, Y.-F., Goodman, J., & Ostriker, E. C. 2023, *ApJ*, 948, 120

Chugunov, A. I., Dewitt, H. E., & Yakovlev, D. G. 2007, *Phys. Rev. D*, 76, 025028

Clavel, J., Wamsteker, W., & Glass, I. S. 1989, *ApJ*, 337, 236

Colgan, J., Kilcrease, D. P., Magee, N. H., et al. 2016, *ApJ*, 817, 116

Cybur, R. H., Amthor, A. M., Ferguson, R., et al. 2010, *ApJS*, 189, 240

Danby, J. M. A. 1988, *Fundamentals of celestial mechanics*

Davis, S. W., Jiang, Y.-F., Stone, J. M., & Murray, N. 2014, *ApJ*, 796, 107

Deissler, R. G. 1986, *Physics of Fluids*, 29, 1453

Deme, B., Hoang, B.-M., Naoz, S., & Kocsis, B. 2020, *ApJ*, 901, 125

- Dempsey, A. M., Li, H., Mishra, B., & Li, S. 2022, *ApJ*, 940, 155
- Dempsey, A. M., Muñoz, D., & Lithwick, Y. 2020, *ApJ*, 892, L29
- Dempsey, A. M., Muñoz, D. J., & Lithwick, Y. 2021, *ApJ*, 918, L36
- Derdzinski, A., & Mayer, L. 2023, *MNRAS*, 521, 4522
- Dittmann, A., Cantiello, M., & Jermyn, A. 2021, Supporting information for "Accretion onto Stars in the Disks of Active Galactic Nuclei", Zenodo, doi:10.5281/zenodo.5071458. <https://doi.org/10.5281/zenodo.5071458>
- Dittmann, A. J. 2020, *MNRAS*, 496, 1217
- . 2021a, *Applied Numerical Mathematics*, 160, 205
- . 2021b, *MNRAS*, 508, 1842
- Dittmann, A. J., Cantiello, M., & Jermyn, A. S. 2021, *ApJ*, 916, 48
- Dittmann, A. J., Dempsey, A. M., & Li, H. 2024a, *ApJ*, 964, 61
- Dittmann, A. J., Jermyn, A. S., & Cantiello, M. 2022, Supporting information for "The Influence of Disk Composition on the Evolution of Stars in the Disks of Active Galactic Nuclei", Zenodo, doi:10.5281/zenodo.7246061. <https://doi.org/10.5281/zenodo.7246061>
- Dittmann, A. J., Jermyn, A. S., & Cantiello, M. 2023a, *ApJ*, 946, 56
- Dittmann, A. J., & Miller, M. C. 2020, *MNRAS*, 493, 3732
- Dittmann, A. J., & Ryan, G. 2021, *ApJ*, 921, 71
- . 2022, *MNRAS*, 513, 6158
- . 2023, arXiv e-prints, arXiv:2310.07758
- Dittmann, A. J., Ryan, G., & Miller, M. C. 2023b, *ApJ*, 949, L30
- Dittmann, A. J., Miller, M. C., Lamb, F. K., et al. 2024b, arXiv e-prints, arXiv:2406.14467
- Do, T., Kerzendorf, W., Konopacky, Q., et al. 2018, *ApJ*, 855, L5
- Do, T., Ghez, A., Morris, M., et al. 2017, in *IAU Symposium*, Vol. 322, *The Multi-Messenger Astrophysics of the Galactic Centre*, ed. R. M. Crocker, S. N. Longmore, & G. V. Bicknell, 222–230
- Dors, O. L., Valerdi, M., Freitas-Lemes, P., et al. 2022, *MNRAS*, arXiv:2206.09836
- Downing, J. M. B., Benacquista, M. J., Giersz, M., & Spurzem, R. 2010, *MNRAS*, 407, 1946
- Draine, B. T. 2003, *ARA&A*, 41, 241

- Droste, J. 1917, Koninklijke Nederlandse Akademie van Wetenschappen Proceedings Series B Physical Sciences, 19, 197
- Duffell, P. C., & MacFadyen, A. I. 2013, ApJ, 769, 41
- Duffell, P. C., Dittmann, A. J., D’Orazio, D. J., et al. 2024, arXiv e-prints, arXiv:2402.13039
- Eggleton, P., & Kiseleva, L. 1995, ApJ, 455, 640
- Einfeldt, B. 1988, SIAM Journal on Numerical Analysis, 25, 294
- Espinosa Lara, F., & Rieutord, M. 2013, A&A, 552, A35
- Fabj, G., Nasim, S. S., Caban, F., et al. 2020, MNRAS, 499, 2608
- Farag, E., Renzo, M., Farmer, R., Chidester, M. T., & Timmes, F. X. 2022, ApJ, 937, 112
- Farmer, R., Renzo, M., de Mink, S. E., Marchant, P., & Justham, S. 2019, ApJ, 887, 53
- Fath, E. A. 1909, Lick Observatory Bulletin, 149, 71
- Ferguson, J. W., Alexander, D. R., Allard, F., et al. 2005, ApJ, 623, 585
- Ferland, G. J., Korista, K. T., Verner, D. A., et al. 1998, PASP, 110, 761
- Field, G. B. 1965, ApJ, 142, 531
- Finkelstein, D. 1958, Physical Review, 110, 965
- Fitch, W. S., Pacholczyk, A. G., & Weymann, R. J. 1967, ApJ, 150, L67
- Ford, K. E. S., & McKernan, B. 2022, MNRAS, 517, 5827
- Fowler, W. A., & Hoyle, F. 1964, ApJS, 9, 201
- Frank, J., King, A., & Raine, D. J. 2002, Accretion Power in Astrophysics: Third Edition
- Frederick, S., Gezari, S., Graham, M. J., et al. 2021, ApJ, 920, 56
- Freedman, R. S., Lustig-Yaeger, J., Fortney, J. J., et al. 2014, ApJS, 214, 25
- Fuller, G. M., Fowler, W. A., & Newman, M. J. 1985, ApJ, 293, 1
- Fung, J., & Chiang, E. 2016, ApJ, 832, 105
- Gammie, C. F. 2001, ApJ, 553, 174
- García, J. A., Kallman, T. R., Bautista, M., et al. 2018, in Astronomical Society of the Pacific Conference Series, Vol. 515, Workshop on Astrophysical Opacities, 282
- Genzel, R., Eisenhauer, F., & Gillessen, S. 2010, Reviews of Modern Physics, 82, 3121
- Gerosa, D., & Fishbach, M. 2021, Nature Astronomy, 5, 749

Ghez, A. M., Duchêne, G., Matthews, K., et al. 2003, *ApJ*, 586, L127

Gilbaum, S., & Stone, N. C. 2022, *ApJ*, 928, 191

Giustini, M., Miniutti, G., & Saxton, R. D. 2020, *A&A*, 636, L2

Glatzel, W. 1998, *A&A*, 339, L5

Glatzel, W., Fricke, K. J., & El Eid, M. F. 1985, *A&A*, 149, 413

Goldreich, P., & Tremaine, S. 1980, *ApJ*, 241, 425

González Delgado, R. M., Heckman, T., & Leitherer, C. 2001, *ApJ*, 546, 845

Goodman, J. 2003, *MNRAS*, 339, 937

Goodman, J., & Tan, J. C. 2004, *ApJ*, 608, 108

Gottlieb, S., & Shu, C. W. 1998, *Mathematics of Computation*, 67, 73

Graham, M. J., Djorgovski, S. G., Drake, A. J., et al. 2017, *MNRAS*, 470, 4112

Graham, M. J., Ford, K. E. S., McKernan, B., et al. 2020, *Phys. Rev. Lett.*, 124, 251102

Graham, M. J., McKernan, B., Ford, K. E. S., et al. 2023, *ApJ*, 942, 99

Greene, J. E., Strader, J., & Ho, L. C. 2020, *ARA&A*, 58, 257

Greenstein, J. L., & Matthews, T. A. 1963, *Nature*, 197, 1041

Greenstein, J. L., & Schmidt, M. 1964, *ApJ*, 140, 1

Guo, M., Stone, J. M., Kim, C.-G., & Quataert, E. 2023, *ApJ*, 946, 26

Guolo, M., Pasham, D. R., Zajaček, M., et al. 2024, *Nature Astronomy*, arXiv:2309.03011

Habibi, M., Gillessen, S., Martins, F., et al. 2017, *ApJ*, 847, 120

Halabi, G. M., Izzard, R. G., Tout, C. A., Jermyn, A. S., & Cannon, R. 2017, *Mem. Soc. Astron. Italiana*, 88, 319

Hamann, F., & Ferland, G. 1992, *ApJ*, 391, L53

—. 1999, *ARA&A*, 37, 487

Hamann, F., Korista, K. T., Ferland, G. J., Warner, C., & Baldwin, J. 2002, *ApJ*, 564, 592

Hankla, A. M., Jiang, Y.-F., & Armitage, P. J. 2020, *ApJ*, 902, 50

Härm, H., & Schwarzschild, M. 1964, *ApJ*, 139, 594

Harten, A., Lax, P. D., & Leer, B. V. 1983, *SIAM Review*, 25, 35. <http://www.jstor.org/stable/2030019>

Hawley, J. F., Gammie, C. F., & Balbus, S. A. 1995, *ApJ*, 440, 742

Hazard, C., Mackey, M. B., & Shimmins, A. J. 1963, *Nature*, 197, 1037

Heger, A., Fryer, C. L., Woosley, S. E., Langer, N., & Hartmann, D. H. 2003, *ApJ*, 591, 288

Henning, T., & Stognienko, R. 1996, *A&A*, 311, 291

Heney, L. G., Forbes, J. E., & Gould, N. L. 1964, *ApJ*, 139, 306

Hewish, A., Bell, S. J., Pilkington, J. D. H., Scott, P. F., & Collins, R. A. 1968, *Nature*, 217, 709

Hill, G. W. 1878, *American journal of Mathematics*, 1, 5

Hofmeister, E., Kippenhahn, R., & Weigert, A. 1964, *ZAp*, 59, 215

Holman, M., Touma, J., & Tremaine, S. 1997, *Nature*, 386, 254

Hopkins, P. F., Grudic, M. Y., Su, K.-Y., et al. 2023, arXiv e-prints, arXiv:2309.13115

Hoyle, F., & Fowler, W. A. 1963a, *MNRAS*, 125, 169

—. 1963b, *Nature*, 197, 533

Hoyle, F., & Lyttleton, R. A. 1939, *Proceedings of the Cambridge Philosophical Society*, 35, 592

Hu, W.-R., & Wu, Y.-L. 2017, *National Science Review*, 4, 685. <https://doi.org/10.1093/nsr/nwx116>

Hubble, E. P. 1926, *ApJ*, 64, 321

Hubeny, I., Agol, E., Blaes, O., & Krolik, J. H. 2000, *ApJ*, 533, 710

Hubeny, I., Blaes, O., Krolik, J. H., & Agol, E. 2001, *ApJ*, 559, 680

Hubeny, I., & Hubeny, V. 1998a, in *American Institute of Physics Conference Series*, Vol. 431, *Accretion processes in Astrophysical Systems: Some like it hot! - eighth AstroPhysics Conference*, ed. S. S. Holt & T. R. Kallman, 171–174

Hubeny, I., & Hubeny, V. 1998b, *ApJ*, 505, 558

Hulse, R. A., & Taylor, J. H. 1975, *ApJ*, 195, L51

Hunter, J. D. 2007, *Computing in Science Engineering*, 9, 90

Iglesias, C. A., & Rogers, F. J. 1993, *ApJ*, 412, 752

—. 1996, *ApJ*, 464, 943

Inayoshi, K., & Haiman, Z. 2016, *ApJ*, 828, 110

Irwin, A. W. 2004, *The FreeEOS Code for Calculating the Equation of State for Stellar Interiors*, . . <http://freeeos.sourceforge.net/>

- Ito, T., & Ohtsuka, K. 2019, *Monographs on Environment, Earth and Planets*, 7, 1
- Itoh, N., Hayashi, H., Nishikawa, A., & Kohyama, Y. 1996, *ApJS*, 102, 411
- Jermyn, A. S., Dittmann, A. J., Cantiello, M., & Perna, R. 2021, *ApJ*, 914, 105
- Jermyn, A. S., Dittmann, A. J., Cantiello, M., & Perna, R. 2021, Supporting information for "Stellar Evolution in the Disks of Active Galactic Nuclei Produces Rapidly Rotating Massive Stars", vv1, Zenodo, doi:10.5281/zenodo.4562499. <https://doi.org/10.5281/zenodo.4562499>
- Jermyn, A. S., Dittmann, A. J., McKernan, B., Ford, K. E. S., & Cantiello, M. 2022, *ApJ*, 929, 133
- Jermyn, A. S., Schwab, J., Bauer, E., Timmes, F. X., & Potekhin, A. Y. 2021, *ApJ*, 913, 72
- Jermyn, A. S., Bauer, E. B., Schwab, J., et al. 2023, *ApJS*, 265, 15
- Jiang, L., Fan, X., & Vestergaard, M. 2008, *ApJ*, 679, 962
- Jiang, N., Wang, T., Mou, G., et al. 2019a, *ApJ*, 871, 15
- Jiang, Y.-F., & Blaes, O. 2020, *ApJ*, 900, 25
- Jiang, Y.-F., Blaes, O., Stone, J. M., & Davis, S. W. 2019b, *ApJ*, 885, 144
- Jiang, Y.-F., Cantiello, M., Bildsten, L., Quataert, E., & Blaes, O. 2015, *ApJ*, 813, 74
- Jiang, Y.-F., Cantiello, M., Bildsten, L., et al. 2018, *Nature*, 561, 498
- Jiang, Y.-F., Davis, S. W., & Stone, J. M. 2016, *ApJ*, 827, 10
- Jiang, Y.-F., & Goodman, J. 2011, *ApJ*, 730, 45
- Jura, M. 1973, *ApJ*, 181, 627
- Kanagawa, K. D., Tanaka, H., Muto, T., Tanigawa, T., & Takeuchi, T. 2015, *MNRAS*, 448, 994
- Kant, I. 1755, *Allgemeine Naturgeschichte und Theorie des Himmels, nach Newtonischen Grundsätzen abgehandelt*. <https://books.google.com/books?id=zBFDAAAAcAAJ>
- Kim, W.-T., & Ostriker, E. C. 2001, *ApJ*, 559, 70
- Kippenhahn, R., & Weigert, A. 1990, *Stellar Structure and Evolution*
- Kishimoto, M., Hönig, S. F., Beckert, T., & Weigelt, G. 2007, *A&A*, 476, 713
- Kochanek, C. S. 2016, *MNRAS*, 458, 127
- Kolykhalov, P. I., & Syunyaev, R. A. 1980, *Soviet Astronomy Letters*, 6, 357

Kormendy, J., & Ho, L. C. 2013, *ARA&A*, 51, 511

Kozai, Y. 1962, *AJ*, 67, 591

Kramers, H. A. 1923, *The London, Edinburgh, and Dublin Philosophical Magazine and Journal of Science*, 46, 836. <https://doi.org/10.1080/14786442308565244>

Kroupa, P. 2001, *MNRAS*, 322, 231

Krumholz, M. R., McKee, C. F., & Klein, R. I. 2005, *ApJ*, 618, 757

Krumholz, M. R., & Thompson, T. A. 2013, *MNRAS*, 434, 2329

Kwan, T. M., Dai, L., & Tchekhovskoy, A. 2023, *ApJ*, 946, L42

Lai, D., & Muñoz, D. J. 2023, *ARA&A*, 61, 517

Lamers, H. J. G. L. M., & Cassinelli, J. P. 1999, *Introduction to Stellar Winds*

Lamers, H. J. G. L. M., & Leitherer, C. 1993, *ApJ*, 412, 771

Langanke, K., & Martínez-Pinedo, G. 2000, *Nuclear Physics A*, 673, 481

Lawrence, A. 2018, *Nature Astronomy*, 2, 102

Lehner, L., & Pretorius, F. 2014, *ARA&A*, 52, 661

Levin, Y. 2003, arXiv e-prints, astro

Li, J., Dempsey, A. M., Li, H., Lai, D., & Li, S. 2023, *ApJ*, 944, L42

Li, J., Lai, D., & Rodet, L. 2022a, *ApJ*, 934, 154

Li, R., & Lai, D. 2022a, *MNRAS*, 517, 1602

—. 2022b, arXiv e-prints, arXiv:2207.01125

Li, Y.-P., Chen, Y.-X., Lin, D. N. C., & Zhang, X. 2021a, *ApJ*, 906, 52

Li, Y.-P., Dempsey, A. M., Li, H., Li, S., & Li, J. 2022b, *ApJ*, 928, L19

Li, Y.-P., Dempsey, A. M., Li, S., Li, H., & Li, J. 2021b, *ApJ*, 911, 124

Lidov, M. L. 1962, *Planet. Space Sci.*, 9, 719

Lin, D. N. C., & Papaloizou, J. 1986, *ApJ*, 309, 846

Linial, I., & Metzger, B. D. 2023, *ApJ*, 957, 34

Liska, M., Hesp, C., Tchekhovskoy, A., et al. 2018, *MNRAS*, 474, L81

Liu, B., & Lai, D. 2018, *ApJ*, 863, 68

Liu, X., Dittmann, A., Shen, Y., & Jiang, L. 2018, *ApJ*, 859, 8

Liu, Z., Li, D., Liu, H.-Y., et al. 2020, *ApJ*, 894, 93

Lockyer, J. N. 1868, *Proceedings of the Royal Society of London Series I*, 17, 131

Lorenz, E. N. 1963, *Journal of the Atmospheric Sciences*, 20, 130

Low, C., & Lynden-Bell, D. 1976, *MNRAS*, 176, 367

Lubow, S. H., Martin, R. G., & Nixon, C. 2015, *ApJ*, 800, 96

Lucy, L. B. 1967, *ZAp*, 65, 89

Luo, J., Chen, L.-S., Duan, H.-Z., et al. 2016, *Classical and Quantum Gravity*, 33, 035010

Lynden-Bell, D. 1969, *Nature*, 223, 690

Lynden-Bell, D., & Pringle, J. E. 1974, *MNRAS*, 168, 603

Lyra, W., Paardekooper, S.-J., & Mac Low, M.-M. 2010, *ApJ*, 715, L68

MacFadyen, A. I., & Milosavljević, M. 2008, *ApJ*, 672, 83

MacFadyen, A. I., & Woosley, S. E. 1999, *ApJ*, 524, 262

MacLeod, M., & Lin, D. N. C. 2020, *ApJ*, 889, 94

Maeder, A. 2009, *Physics, Formation and Evolution of Rotating Stars*, doi:10.1007/978-3-540-76949-1

Maeder, A., & Meynet, G. 2000, *A&A*, 361, 159

Maiolino, R., Juarez, Y., Mujica, R., Nagar, N. M., & Oliva, E. 2003, *ApJ*, 596, L155

Maiolino, R., & Mannucci, F. 2019, *A&A Rev.*, 27, 3

Maiolino, R., Nagao, T., Grazian, A., et al. 2008, *A&A*, 488, 463

Mapelli, M., & Giacobbo, N. 2018, *MNRAS*, 479, 4391

Marconi, A., Risaliti, G., Gilli, R., et al. 2004, *MNRAS*, 351, 169

Mardling, R. A., & Aarseth, S. J. 2001, *MNRAS*, 321, 398

Martin, R. G., & Lubow, S. H. 2017, *ApJ*, 835, L28

Martins, F., Gillessen, S., Eisenhauer, F., et al. 2008, *ApJ*, 672, L119

Matsuoka, K., Nagao, T., Maiolino, R., Marconi, A., & Taniguchi, Y. 2009, *A&A*, 503, 721

Matthews, T., Bolton, J., Greenstein, J., Münch, G., & Sandage, A. 1961, *Sky & Telescope*, 21, 148

McKernan, B., & Ford, K. E. S. 2023, arXiv e-prints, arXiv:2309.15213

McKernan, B., Ford, K. E. S., Callister, T., et al. 2022, MNRAS, 514, 3886

McKernan, B., Ford, K. E. S., Lyra, W., & Perets, H. B. 2012, MNRAS, 425, 460

McKernan, B., Ford, K. E. S., & O’Shaughnessy, R. 2020a, MNRAS, 498, 4088

McKernan, B., Ford, K. E. S., O’Shaughnessy, R., & Wysocki, D. 2020b, MNRAS, 494, 1203

McKernan, B., Ford, K. E. S., Bartos, I., et al. 2019, ApJ, 884, L50

McKinney, J. C., Tchekhovskoy, A., & Blandford, R. D. 2013, Science, 339, 49

Mehta, A. K., Buonanno, A., Gair, J., et al. 2022, ApJ, 924, 39

Meyer, F., & Meyer-Hofmeister, E. 1982, A&A, 106, 34

Miller, J. S., & Antonucci, R. R. J. 1983, ApJ, 271, L7

Miller, J. S., & Goodrich, R. W. 1990, ApJ, 355, 456

Miller, J. S., Goodrich, R. W., & Mathews, W. G. 1991, ApJ, 378, 47

Miller, M. C., & Hamilton, D. P. 2002, ApJ, 576, 894

Miller, M. C., Lamb, F. K., Dittmann, A. J., et al. 2019, ApJ, 887, L24

—. 2021, ApJ, 918, L28

Milsom, J. A., Chen, X., & Taam, R. E. 1994, ApJ, 421, 668

Miniutti, G., Saxton, R. D., Giustini, M., et al. 2019, Nature, 573, 381

Minkowski, R. 1960, ApJ, 132, 908

Miranda, R., Muñoz, D. J., & Lai, D. 2017, MNRAS, 466, 1170

Mombarg, J. S. G., Rieutord, M., & Espinosa Lara, F. 2023, A&A, 677, L5

Moody, M. S. L., Shi, J.-M., & Stone, J. M. 2019, ApJ, 875, 66

Moré, J. J., Garbow, B. S., & Hillstom, K. E. 1980, Implementation guide for MINPACK–1, Technical Report ANL–80–68, Mathematics and Computer Sciences Division, Argonne National Laboratory, 9700 South Cass Ave., Argonne, IL 60439–4801

Mortlock, D. J., Warren, S. J., Venemans, B. P., et al. 2011, Nature, 474, 616

Muñoz, D. J., Lai, D., Kratter, K., & Miranda, R. 2020, ApJ, 889, 114

Muñoz, D. J., Miranda, R., & Lai, D. 2019, ApJ, 871, 84

Muñoz, D. J., Stone, N. C., Petrovich, C., & Rasio, F. A. 2022, arXiv e-prints, arXiv:2204.06002

- Murray, C. D., & Dermott, S. F. 1999, *Solar system dynamics*
- Nagao, T., Maiolino, R., & Marconi, A. 2006, *A&A*, 459, 85
- Nandra, K., George, I. M., Mushotzky, R. F., Turner, T. J., & Yaqoob, T. 1997, *ApJ*, 488, L91
- Nayakshin, S., Cuadra, J., & Springel, V. 2007, *MNRAS*, 379, 21
- Netzer, H. 1990, in *Active Galactic Nuclei*, ed. R. D. Blandford, H. Netzer, L. Woltjer, T. J. L. Courvoisier, & M. Mayor, 57–160
- Neumayer, N., Seth, A., & Böker, T. 2020, *A&A Rev.*, 28, 4
- Nitz, A. H., & Capano, C. D. 2021, *ApJ*, 907, L9
- Novikov, I. D., & Thorne, K. S. 1973, in *Black Holes (Les Astres Occlus)*, 343–450
- Oda, T., Hino, M., Muto, K., Takahara, M., & Sato, K. 1994, *Atomic Data and Nuclear Data Tables*, 56, 231
- Ogilvie, G. I. 1999, *MNRAS*, 304, 557
- . 2001, *MNRAS*, 325, 231
- . 2018, *MNRAS*, 477, 1744
- Oke, J. B. 1963, *Nature*, 197, 1040
- Onoue, M., Bañados, E., Mazzucchelli, C., et al. 2020, *ApJ*, 898, 105
- Paardekooper, S. J., Baruteau, C., Crida, A., & Kley, W. 2010, *MNRAS*, 401, 1950
- Paczynski, B., & Prószyński, M. 1986, *ApJ*, 302, 519
- Paczynsky, B., & Wiita, P. J. 1980, *A&A*, 88, 23
- Palmese, A., Fishbach, M., Burke, C. J., Annis, J., & Liu, X. 2021, *ApJ*, 914, L34
- Pan, Z., & Yang, H. 2021, *ApJ*, 923, 173
- Paumard, T., Genzel, R., Martins, F., et al. 2006, *ApJ*, 643, 1011
- Paxton, B., Bildsten, L., Dotter, A., et al. 2011, *ApJS*, 192, 3
- Paxton, B., Cantiello, M., Arras, P., et al. 2013, *ApJS*, 208, 4
- Paxton, B., Marchant, P., Schwab, J., et al. 2015, *ApJS*, 220, 15
- Paxton, B., Schwab, J., Bauer, E. B., et al. 2018, *ApJS*, 234, 34
- Paxton, B., Smolec, R., Schwab, J., et al. 2019, *ApJS*, 243, 10
- Perna, R., Lazzati, D., & Cantiello, M. 2021a, *ApJ*, 906, L7

Perna, R., Tagawa, H., Haiman, Z., & Bartos, I. 2021b, *ApJ*, 915, 10

Peters, P. C. 1964, *Physical Review*, 136, 1224

Peterson, B. M., Ferrarese, L., Gilbert, K. M., et al. 2004, *ApJ*, 613, 682

Planck Collaboration, Aghanim, N., Akrami, Y., et al. 2020, *A&A*, 641, A6

Pollack, J. B., Hollenbach, D., Beckwith, S., et al. 1994, *ApJ*, 421, 615

Potekhin, A. Y., & Chabrier, G. 2010, *Contributions to Plasma Physics*, 50, 82

Poutanen, J. 2017, *ApJ*, 835, 119

Pringle, J. E. 1981, *ARA&A*, 19, 137

—. 1991, *MNRAS*, 248, 754

Radau, R. 1880, *Journal de Mathématiques Pures et Appliquées*, 6, 283. <http://eudml.org/doc/235431>

Rafikov, R. R. 2002, *ApJ*, 572, 566

Rakavy, G., & Shaviv, G. 1967, *ApJ*, 148, 803

Rauch, K. P. 1995, *MNRAS*, 275, 628

Reber, G. 1940, *ApJ*, 91, 621

—. 1944, *ApJ*, 100, 279

Rein, H., & Liu, S. F. 2012, *A&A*, 537, A128

Rein, H., & Spiegel, D. S. 2015, *MNRAS*, 446, 1424

Renzo, M., Cantiello, M., Metzger, B. D., & Jiang, Y. F. 2020, *ApJ*, 904, L13

Rice, W. K. M., Lodato, G., & Armitage, P. J. 2005, *MNRAS*, 364, L56

Rieutord, M., Espinosa Lara, F., & Putigny, B. 2016, *Journal of Computational Physics*, 318, 277

Robson, T., Cornish, N. J., & Liu, C. 2019, *Classical and Quantum Gravity*, 36, 105011

Rodriguez, C. L., Kremer, K., Chatterjee, S., et al. 2021, *Research Notes of the American Astronomical Society*, 5, 19

Rogers, F. J., & Nayfonov, A. 2002, *ApJ*, 576, 1064

Rosenthal, M. M., Chiang, E. I., Ginzburg, S., & Murray-Clay, R. A. 2020, *MNRAS*, 498, 2054

Rowan, C., Boehholt, T., Kocsis, B., & Haiman, Z. 2023a, *MNRAS*, 524, 2770

- Rowan, C., Whitehead, H., Boekholt, T., Kocsis, B., & Haiman, Z. 2023b, arXiv e-prints, arXiv:2309.14433
- Ruan, W.-H., Guo, Z.-K., Cai, R.-G., & Zhang, Y.-Z. 2020, International Journal of Modern Physics A, 35, 2050075. <https://doi.org/10.1142/S0217751X2050075X>
- Ryan, G., & MacFadyen, A. 2017, ApJ, 835, 199
- Salmi, T., Vinciguerra, S., Choudhury, D., et al. 2022, ApJ, 941, 150
- Salpeter, E. E. 1955, ApJ, 121, 161
- . 1964, ApJ, 140, 796
- Sameshima, H., Yoshii, Y., & Kawara, K. 2017, ApJ, 834, 203
- Sameshima, H., Yoshii, Y., Matsunaga, N., et al. 2020, ApJ, 904, 162
- Santini, A., Gerosa, D., Cotesta, R., & Berti, E. 2023, Phys. Rev. D, 108, 083033
- Sanyal, D., Grassitelli, L., Langer, N., & Bestenlehner, J. M. 2015, A&A, 580, A20
- Saumon, D., Chabrier, G., & van Horn, H. M. 1995, ApJS, 99, 713
- Schmidt, M. 1963, Nature, 197, 1040
- Schnittman, J. D., & Krolik, J. H. 2015, ApJ, 806, 88
- Schwarzschild, K. 1916, Abh. Konigl. Preuss. Akad. Wissenschaften Jahre 1906,92, Berlin,1907, 1916, 189
- Schwarzschild, M., & Härm, R. 1962, ApJ, 136, 158
- Secunda, A., Bellovary, J., Mac Low, M.-M., et al. 2019, ApJ, 878, 85
- . 2020, ApJ, 903, 133
- Semenov, D., Henning, T., Helling, C., Ilgner, M., & Sedlmayr, E. 2003, A&A, 410, 611
- Seyfert, C. K. 1943, ApJ, 97, 28
- Shakura, N. I., & Sunyaev, R. A. 1973, A&A, 500, 33
- Shen, Y., Greene, J. E., Strauss, M. A., Richards, G. T., & Schneider, D. P. 2008, ApJ, 680, 169
- Shlosman, I., Frank, J., & Begelman, M. C. 1989, Nature, 338, 45
- Sigl, G., Schnittman, J., & Buonanno, A. 2007, Phys. Rev. D, 75, 024034
- Sigurdsson, S., & Phinney, E. S. 1993, ApJ, 415, 631
- Sirko, E., & Goodman, J. 2003, MNRAS, 341, 501

Sądowski, A. 2009, ApJS, 183, 171

Slipher, V. M. 1917, Lowell Observatory Bulletin, 3, 59

Smith, N. 2014, ARA&A, 52, 487

Sołtan, A. 1982, MNRAS, 200, 115

Spitzer, Lyman, J., & Saslaw, W. C. 1966, ApJ, 143, 400

Spitzer, L., & Härm, R. 1953, Physical Review, 89, 977

Springel, V., Yoshida, N., & White, S. D. M. 2001, New A, 6, 79

Stewart, G. R., & Ida, S. 2000, Icarus, 143, 28

Stone, J. M., & Gardiner, T. 2009, New A, 14, 139

Stone, J. M., Hawley, J. F., Gammie, C. F., & Balbus, S. A. 1996, ApJ, 463, 656

Stone, J. M., Tomida, K., White, C. J., & Felker, K. G. 2020, ApJS, 249, 4

Stone, N. C., Metzger, B. D., & Haiman, Z. 2017, MNRAS, 464, 946

Storchi Bergmann, T., & Pastoriza, M. G. 1989, ApJ, 347, 195

Su, M., Slatyer, T. R., & Finkbeiner, D. P. 2010, ApJ, 724, 1044

Suková, P., Zajaček, M., Witzany, V., & Karas, V. 2021, ApJ, 917, 43

Syer, D., Clarke, C. J., & Rees, M. J. 1991, MNRAS, 250, 505

Szulágyi, J., Morbidelli, A., Crida, A., & Masset, F. 2014, ApJ, 782, 65

Tagawa, H., & Haiman, Z. 2023, MNRAS, 526, 69

Tagawa, H., Haiman, Z., & Kocsis, B. 2020, ApJ, 898, 25

Tagawa, H., Kimura, S. S., Haiman, Z., Perna, R., & Bartos, I. 2023, ApJ, 950, 13

Tanaka, H., Takeuchi, T., & Ward, W. R. 2002, ApJ, 565, 1257

Tanaka, H., & Ward, W. R. 2004, ApJ, 602, 388

Tanaka, Y., Nandra, K., Fabian, A. C., et al. 1995, Nature, 375, 659

Tantau, T. 2013, The TikZ and PGF Packages. <http://sourceforge.net/projects/pgf/>

Targett, T. A., Dunlop, J. S., & McLure, R. J. 2012, MNRAS, 420, 3621

Tchekhovskoy, A., Narayan, R., & McKinney, J. C. 2011, MNRAS, 418, L79

The LIGO Scientific Collaboration, the Virgo Collaboration, the KAGRA Collaboration, et al. 2021, arXiv e-prints, arXiv:2111.03606

Thompson, T. A., Quataert, E., & Murray, N. 2005, *ApJ*, 630, 167

Thyng, K. M., Greene, C. A., Hetland, R. D., Zimmerle, H. M., & DiMarco, S. F. 2016, *Oceanography*. <https://doi.org/10.5670/oceanog.2016.66>

Tiede, C., & D’Orazio, D. J. 2024, *MNRAS*, 527, 6021

Tiede, C., Zrake, J., MacFadyen, A., & Haiman, Z. 2020, *ApJ*, 900, 43

Timmes, F. X., & Swesty, F. D. 2000, *ApJS*, 126, 501

Tomsick, J. A., Parker, M. L., García, J. A., et al. 2018, *ApJ*, 855, 3

Toomre, A. 1964, *ApJ*, 139, 1217

Toonen, S., Claeys, J. S. W., Mennekens, N., & Ruiter, A. J. 2014, *A&A*, 562, A14

Tooper, R. F. 1964, *ApJ*, 140, 434

Touma, J., & Wisdom, J. 1994, *AJ*, 108, 1943

Tout, C. A., Eggleton, P. P., Fabian, A. C., & Pringle, J. E. 1989, *MNRAS*, 238, 427

Townsend, R. H. D. 2019, MESA SDK for Linux, v20190503, Zenodo, doi:10.5281/zenodo.2669541. <https://doi.org/10.5281/zenodo.2669541>

Toyouchi, D., Hosokawa, T., Sugimura, K., Nakatani, R., & Kuiper, R. 2019, *MNRAS*, 483, 2031

Toyouchi, D., Inayoshi, K., Ishigaki, M. N., & Tominaga, N. 2022, *MNRAS*, 512, 2573

Turk, M. J., Smith, B. D., Oishi, J. S., et al. 2011, *ApJS*, 192, 9

Tutukov, A. V., & Yungelson, L. R. 1979, *Acta Astron.*, 29, 665

Umeda, H., & Nomoto, K. 2008, *ApJ*, 673, 1014

van der Walt, S., Colbert, S. C., & Varoquaux, G. 2011, *Computing in Science Engineering*, 13, 22

van Leer, B. 1974, *Journal of Computational Physics*, 14, 361

van Son, L. A. C., de Mink, S. E., Callister, T., et al. 2022, *ApJ*, 931, 17

Velikhov, E. P. 1959, *Soviet Journal of Experimental and Theoretical Physics*, 9, 995

Virtanen, P., Gommers, R., Oliphant, T. E., et al. 2020, *Nature Methods*, 17, 261

Viti, S., García-Burillo, S., Fuente, A., et al. 2014, *A&A*, 570, A28

von Zeipel, H. 1910, *Astronomische Nachrichten*, 183, 345
— . 1924, *MNRAS*, 84, 665

Wang, H.-T., Jiang, Z., Sesana, A., et al. 2019, *Phys. Rev. D*, 100, 043003

Wang, H.-Y., Bai, X.-N., Lai, D., & Lin, D. N. C. 2023, *MNRAS*, arXiv:2212.07416

Wang, T., Vartanyan, D., Burrows, A., & Coleman, M. S. B. 2022a, *MNRAS*, 517, 543

Wang, Y.-H., Lazzati, D., & Perna, R. 2022b, *MNRAS*, 516, 5935

Warren, S. G., & Brandt, R. E. 2008, *Journal of Geophysical Research (Atmospheres)*, 113, D14220

Watabe, Y., Kawakatu, N., & Imanishi, M. 2008, *ApJ*, 677, 895

Weaver, T. A., Zimmerman, G. B., & Woosley, S. E. 1978, *ApJ*, 225, 1021

Weibull, W. 1951, *Journal of Applied Mechanics*, 18, 293. <https://doi.org/10.1115/1.4010337>

Weigelt, G., Hofmann, K. H., Kishimoto, M., et al. 2012, *A&A*, 541, L9

Weisberg, J. M., Nice, D. J., & Taylor, J. H. 2010, *ApJ*, 722, 1030

Whitehead, H., Rowan, C., Boekholt, T., & Kocsis, B. 2023, arXiv e-prints, arXiv:2309.11561

Williams, R. E. 1971, *ApJ*, 167, L27

Wolff, M. T., Guillot, S., Bogdanov, S., et al. 2021, *ApJ*, 918, L26

Wolynski, J. J. 2012, viXra e-prints, viXra:1205.0107
— . 2019, viXra e-prints, viXra:1910.0637

Wolynski, J. J., & Taylor, B. J. 2019a, viXra e-prints, viXra:1905.0509
— . 2019b, viXra e-prints, viXra:1910.0472

Xian, J., Zhang, F., Dou, L., He, J., & Shu, X. 2021, *ApJ*, 921, L32

Xu, F., Bian, F., Shen, Y., et al. 2018, *MNRAS*, 480, 345

Yang, J., Wang, F., Fan, X., et al. 2021, *ApJ*, 923, 262

Yu, Q., & Tremaine, S. 2002, *MNRAS*, 335, 965

Zahid, H. J., Geller, M. J., Kewley, L. J., et al. 2013, *ApJ*, 771, L19

Zel'dovich, Y. B. 1964, *Soviet Physics Doklady*, 9, 195

Zhang, X.-G. 2024, *MNRAS*, 529, L169

Zhu, Z., Jiang, Y.-F., Baehr, H., et al. 2021, MNRAS, 508, 453

Zrake, J., Tiede, C., MacFadyen, A., & Haiman, Z. 2021, ApJ, 909, L13

Østby , T., Macaluso, J., Lande, J., Coven, R., & Olausson, M. 2000, Burn the Sun, CD, Favored Nations